CENTRO DE INVESTIGACIÓN Y DE ESTUDIOS
AVANZADOS DEL INSTITUTO POLITÉCNICO
NACIONAL
UNIDAD ZACATENCO

DEPARTAMENTO DE INGENIERÍA ELÉCTRICA SECCIÓN
ELECTRÓNICA DEL ESTADO SÓLIDO

Preparación y Caracterización de Capas Delgadas Grado Dispositivo para Celdas Solares basadas en CIGSe

Tesis que presenta

ONYEKACHI MICHAEL NWAKANMA

Para obtener el grado de

DOCTOR EN CIENCIAS

EN LA ESPECIALIDAD DE
INGENIERÍA ELÉCTRICA

Directores de Tesis:

Dr. Velumani Subramaniam
Dr. José Arturo Morales Acevedo

Ciudad de México Abril 2021

CENTRO DE INVESTIGACIÓN Y DE ESTUDIOS
AVANZADOS DEL INSTITUTO POLITÉCNICO
NACIONAL
ZACATENCO UNIT

DEPARTMENT OF ELECTRICAL ENGINEERING
SOLID STATE ELECTRONIC SECTION

Preparation and characterization of device grade films for CIGSe-based Solar Cells

Thesis presented by

ONYEKACHI MICHAEL NWAKANMA

To obtain the degree of

DOCTOR IN SCIENCES

SPECIALTY IN
ELECTRICAL ENGINEERING

Thesis directors:

Dr. Velumani Subramaniam
Dr. José Arturo Morales Acevedo

Mexico City April 2021

Acknowledgment

I would like to acknowledge the Consejo Nacional De Ciencia Y Tecnología (CONACYT), Mexico for the PhD scholarship, and CONACYT project No. 263043 SEP-CINVESTAV 200, and CeMIESol P-55 for funding the research project.

I want to express profound gratitude to my advisors, Dr. Velumani Subramaniam and Dr. Arturo Morales-Acevedo, for their support, guide, and inspiration in my studies for this degree. Special thanks to members of my examination committee, Dra. María de la Luz Olvera Amador, Dr. Ramón Peña Sierra, Dr. Mauricio Ortega López, and Dr. José Chávez Carvayar for the unquantifiable guide to make this work a success.

I wish to thank M. en C. Miguel Galván Arellano, M. en C. Adolfo Tavira Fuentes, Norma Iris González García, Erika Diana Serrano Andrade, Yesenia Cervantes Aguirre, Beatriz Urrutia Bohorquez, Ing. Miguel Angel Avendaño Ibarra, Ing. José Martín Jiménez Sarmiento, Dr. Gaspar Casados Cruz, Alvaro Guzman Campuzano, Rosa Maria Nava Sánchez, Ing. Miguel Ángel Luna Arias, Monica Davar Ocegueda, and all the staff and students in the SEES department and CINVESTAV community. Special thanks to Isaac Montes-Valenzuela, I am grateful for all your help.

Special thanks to Mrs. Malathy Velumani, I am grateful for all the support and advice. I thank all the past and present members of MREB group for their help and support; Pablo Reyes, Myriam Solís- Lopez, Christeena Theresa Thomas, Mercy Rani Babudurai, Araceli- Romero Nunez, Atzin Ferrel, Francisco Alvarado César, Ganesh Regmi, Ashok Adikari, Karthik Sekar, Jorge Rios Ramirez, Roberto Hernandez Maya, Jorge Narro, Alejandra, Fernanda, Dorian, Hugo, Francisco Javier, Javier covarrubias, Rohini Neendoor Mohan, Aruna Devi, Latha Marasamy, Ravichandran.

I wish to express my sincere gratitude to Prof. Rose Osuji, Prof. Fabian Ezema, Prof. Francisca Okeke, Prof. A.B.C. Ekwealor, Prof. Augustine Chukwude, Uloaku Omenihu, the entire staff and students of the Physics and Astronomy department, and the University of Nigeria, Nsukka community. I also wish to thank Mr. Gabriel Ezeabikwa, Mrs. Vera Chukwuemeka, Elijah Adesuji, Rita Ibudialo, Nathaniel Lartey, Chris Nwachioma, Srikanth Chakaravarthy, Stephanie Chukwuemeka, Jacqueline Chukwuemeka, Chioma Ahiwe, and all my friend.

I wish to thank my parents, Mr. Benjamin Nwakanma and Mrs. Beatrice Nwakanma, my siblings Emeka and Amara, to Ezinwanne Okeke and all my cousins, I love you all.

And to all the friends and fantastic people I met here in Mexico, it has been a fantastic sojourn. I appreciate your friendship and support. I am grateful for the opportunity to study in a beautiful country, *Viva Mexico!*

Agradecimientos

Quiero agradecer al Consejo Nacional De Ciencia Y Tecnología (CONACYT), México por la beca de doctorado, y al proyecto CONACYT No. 263043 SEP-CINVESTAV 200 y CeMIESol P-55 por financiar el proyecto de investigación.

Quiero expresar un profundo agradecimiento a mis asesores; el Dr. Velumani Subramaniam y el Dr. Arturo Morales-Acevedo, por su apoyo, guía e inspiración en mis estudios de doctorado. Un agradecimiento especial a los miembros de mi comité de examen, la Dra. María de la Luz Olvera Amador, el Dr. Ramón Peña Sierra, el Dr. Mauricio Ortega López y el Dr. José Chávez Carvayar por la guía no cuantificable para hacer de este trabajo un éxito.

Quiero agradecer a M. en C. Miguel Galván Arellano, M. en C. Adolfo Tavira Fuentes, Norma Iris González García, Erika Diana Serrano Andrade, Yesenia Cervantes Aguirre, Beatriz Urrutia Bohorquez, Ing. Miguel Ángel Avendaño Ibarra, Ing. José Martín Jiménez Sarmiento, Dr. Gaspar Casados Cruz, Álvaro Guzmán Campuzano, Rosa María Nava Sánchez, Ing. Miguel Ángel Luna Arias, Mónica Davar Ocegueda, y todo el personal y alumnos del departamento SEES y comunidad CINVESTAV. Un agradecimiento especial a Isaac Montes-Valenzuela por toda su ayuda.

Un agradecimiento especial a la Sra. Malathy Velumani, estoy agradecido por todo el apoyo y sus consejos. Agradezco a todos los miembros pasados y presentes del grupo MREB por su ayuda y apoyo; Pablo Reyes, Myriam Solís- Lopez, Christeena Theresa Thomas, Mercy Rani Babudurai, Araceli- Romero Núñez, Atzin Ferrel, Francisco Alvarado César, Ganesh Regmi, Ashok Adikari, Karthik Sekar, Jorge Ríos Ramírez, Roberto Hernández Maya, Jorge Narro, Alejandra, Fernanda, Dorian, Hugo, Francisco Javier, Javier Covarrubias, Rohini Neendoor Mohan, Aruna Devi, Latha Marasamy, Ravichandran.

Deseo expresar mi más sincero agradecimiento a la Prof. Rose Osuji, Prof. Fabian Ezema, Prof. Francisca Okeke, Prof. A.B.C. Ekwealor, el Prof. Augustine Chukwude, Uloaku Omenihu, a todo el personal y estudiantes del departamento de Física y Astronomía y a la Universidad de Nigeria, comunidad de Nsukka. También deseo agradecer al Sr. Gabriel Ezeabikwa, la Sra. Vera Chukwuemeka, Elijah Adesuji, Rita Ibudialo, Nathaniel Lartey, Chris Nwachioma, Srikanth

Chakaravarthy, Stephanie Chukwuemeka, Jacqueline Chukwuemeka, Chioma Ahiwe y a todos mis amigos.

Deseo agradecer a mis padres, el Sr. Benjamin Nwakanma y la Sra. Beatrice Nwakanma, mis hermanos Emeka y Amara, a Ezinwanne Okeke y a todos mis primos, los amo a todos.

Y para todos los amigos y gente fantástica que conocí aquí en México, ha sido una estancia fantástica. Agradezco su amistad y apoyo. ¡Estoy agradecido por la oportunidad de estudiar en un hermoso país, Viva México!

Dedication

To my family, friends, and teachers!

Table of Contents

List of figures

List of tables

Abstract

Photovoltaic cells offer a means of tapping solar energy and provide a viable "green" solution to the increasing global energy demand. In this regard, chalcopyrite thin-film solar cells have attracted great interest among researchers, especially the alkali metals' effects on copper-indium-gallium-selenide (CIGSe). Previous reports used vacuum deposition methods for Post Deposition Treatment (PDT) processes for introducing alkali metals on CIGSe absorber layers with good results for improving CIGSe solar cells.

This study focuses on the effects of surface post-deposition treatments (PDT) with heavy alkali metals using a non-vacuum method on the CIGSe layers. X-ray diffraction studies confirmed that no secondary phases forms after the PDT. Morphological studies using scanning electron microscopy after the PDT verified the grain's enlargement. Some atomic composition changes were measured with energy-dispersive X-ray (EDX), showing a slight copper-poor composition after PDT and a slight variation in the In/Ga ratios. The electrical measurements using the Hall effect characterization showed a substantial increase in the CIGSe absorbers carrier mobility after PDT due to the passivation of grain boundaries by the alkali metals, from 1.7 cm^2/V s to 78.6 cm^2/V s and 57.11 cm^2/V s for films with Cs and Rb PDTs, respectively. The surface topographical characterization using atomic force microscopy (AFM) showed reduced peak-to-peak values and other surface parameters. Raman spectroscopy characterization exhibited only the A1 characteristic mode of the chalcopyrite structures for all the CIGSe samples, with a shoulder after PDT attributed to ordered vacancies (OVC) caused by the alkali metals.

Molybdenum (Mo) has been used as a back-contact electrode in high-efficiency solar cells mainly due to its ohmic nature in contact with the absorber material (especially with chalcopyrites and kesterites), low resistivity, good reflectance and porosity to alkali atoms. Alone and in tandem with other materials, e.g., titanium, can also serve as an effective barrier for the diffusion of impurities from the substrates. Another part of this study focuses on the effects of the sputtering deposition conditions (i.e., working pressure and power) on Mo for back-contact applications. Depositions were carried out on soda-lime glasses (SLGs) and stainless-steel substrates using direct-current (dc) sputtering. Optimized deposition power and sputtering pressure were used to deposit a Mo bilayer thin film intended for solar cell application on SLG substrates. X-ray diffraction studies showed the (110) plane corresponding to the Mo body-centered cubic structure. Other deposited

films' parameters such as stress and dislocation density were estimated. These properties affect the potential diffusion of sodium (Na) through the soda-lime glass into the absorber layer that is important as Na inclusion improves cell efficiency. The deposited film's cross-section was analyzed using a field-emission scanning electron microscopy to confirm the bilayer's successful deposition. The surface of the films plays a vital role in the Mo interface with the absorber layer. Atomic force microscopy was used to acquire the topographical information from the sputtered bilayer film. The resistivity, as measured using a four-point probe for the Mo films deposited at different conditions, was in the order of 10^{-6} Ω m while the resistivity of the bilayer was 0.60×10^{-6} Ω m. On stainless-steel (SS), a comparative study analyzes the effectiveness of a titanium layer deposited using e-beam evaporation and a zinc oxide (ZnO) layer deposited using radio-frequency (RF) sputtering for barrier applications. Structural characterization of the optimized Mo films using XRD studies confirmed the presence of a preferential (110) plane corresponding to the body-centered cubic (bcc) structure. Estimated Mo film parameters (e.g., strain) for films deposited on barrier layers were compared against films deposited on SS substrate without any barriers. These properties also influence the diffusion of Fe and Cr into the absorber layer. SEM study of the morphology of films and energy-dispersive X-ray (EDX) helped identify elemental compositions and verify the impurities blockage from the SS to the film by the barrier layers. Secondary ion mass spectroscopy (SIMS) was employed to study the impurities' depth profiles through the back-contacts' barriers. We observed 40% more impurities reduction using an annealed ZnO barrier combined with an optimized Mo layer as compared to other barriers.

Additional studies focused on optimized Radio-Frequency (RF) sputtering parameters for depositing low-thickness (ca 100 nm) aluminum-doped zinc oxide (AZO) aimed at reducing the optical losses commonly associated with transparent conducting oxides (TCO). The optical losses reportedly cause a significant reduction in the solar cells' efficiencies. X-ray diffraction (XRD) analysis and high-resolution scanning electron microscopy (HR-SEM) aided in studying the structure and morphology variations with deposition parameters and temperature. The optical characterization using UV-Vis spectral measurements showed transmittance above 90%. We defined a quality factor (QF) to characterize the TCO layers' performance, considering equal weight for the conductance and transmittance as they are essential properties for their TCO applications. The reported parameters allowed films with low resistivities and high QF for the TCO applications in CIGSe solar cells.

Keywords

CIGSe solar cells, alkali metal deposition, post-deposition treatment (PDT), non-vacuum deposition, molybdenum, bilayer, dc sputtering, flexible substrates, diffusion barrier layer, quality factor (QF), aluminum-doped zinc oxide (AZO), rf sputtering, Transparent conducting oxide (TCO)

Resumen

Las celdas solares ofrecen un medio para aprovechar la energía solar y proveen una solución “verde” viable a la creciente demanda energética mundial. En este sentido, las celdas solares de capa delgada basadas en calcopiritas han causado gran interés entre los investigadores, y especialmente los efectos debidos a metales alcalinos en las capas absorbentes de Cobre Indio-Galio-Selenio (CIGSe). Estudios previos utilizaron métodos en vacío para introducir metales alcalinos mediante procesos post depósito (PDT) en capas de CIGSe con buenos resultados para mejorar celdas solares de CIGSe.

Este estudio se enfoca en los efectos debidos a tratamientos post-depósito (PDT) de CIGSe con metales alcalinos pesados utilizando un método sin vacío. La difracción de rayos X confirma que no se producen fases secundarias después del PDT. Los estudios morfológicos usando microscopía electrónica de barrido (SEM) después del PDT mostraron el incremento de tamaño de los granos cristalinos. Las mediciones eléctricas por efecto Hall mostraron un incremento de la movilidad de los portadores después del PDT con metales alcalinos; desde 1.7 cm^2/Vs a 78.6 cm^2/Vs y 57.11 cm^2/Vs para PDT con Cs y Rb, respectivamente. La caracterización topográfica por microscopía de fuerza atómica (AFM) mostró una reducción de las alturas pico a pico y mejora de otros parámetros superficiales en las capas con PDT. La espectroscopía Raman exhibió solo el modo característico A1 de calcopiritas para todas las muestras de CIGSe, con un hombro atribuido a Vacancias Ordenadas (OVC) causadas por los metales alcalinos.

El Molibdeno (Mo) se ha usado como contacto posterior en celdas solares de alta eficiencia debido a la naturaleza óhmica en contacto con el material absorbente (especialmente calcopiritas y kesteritas), baja resistividad, buena reflectancia y porosidad a los átomos alcalinos. Solo y en tándem con otros materiales como Ti, puede servir como una barrera efectiva para la difusión de otras impurezas desde los substratos. Otra parte de este estudio se enfoca en el efecto de las condiciones de depósito (potencia y presión de trabajo) por pulverización de Mo para su aplicación en contactos posteriores de celdas solares. Los depósitos se realizaron en substratos de vidrio soda-lima (SLGs) y de acero inoxidable usando pulverización catódica en corriente directa (DC). Se utilizaron condiciones optimizadas de potencia y presión de trabajo para depositar bi-capas sobre substratos SLG. La difracción de rayos X mostraron el plano (110) correspondiente a la estructura cúbica centrada en el cuerpo (BCC). Además, se estimaron otros parámetros tales como esfuerzos

y densidades de dislocaciones. Estas propiedades afectan la difusión de sodio y otras impurezas metálicas desde el substrato SLG hasta el absorbedor, y esto es importante porque el sodio en cantidades moderadas ayuda a mejorar la eficiencia en celdas solares. La sección transversal de las capas depositadas se analizó usando microscopía electrónica de barrido con emisión por campo (FE-SEM) para confirmar el depósito de las bi-capas. Las características de las superficies de estas capas juegan un rol muy importante en su interfaz con el material absorbedor de CIGSe. La resistividad, medida por 4 puntas, de las capas de Mo depositadas en diferentes condiciones fue del orden de 10^{-6} Ω m mientras que para las bi-capas fue de 0.60×10^{-6} Ω m. Sobre acero inoxidable (SS), se hizo un estudio comparativo para analizar la efectividad de una capa de Titanio (Ti) depositada por evaporación (e-beam) y una capa de ZnO depositada por pulverización catódica (RF) para su aplicación como barrera. La caracterización estructural usando difracción de rayos X (XRD) confirmó la presencia del plano preferencial en la orientación (110) de la estructura cúbica centrada en el cuerpo. Se estimaron parámetros (esfuerzos, por ejemplo) en las capas de Mo depositadas sobre las capas barrera en comparación con capas de Mo depositadas sobre SS sin capas barrera. Esto puede influir en la difusión de Fe y Cr hacia la capa absorbente (CIGSe). El estudio morfológico de las capas y la espectroscopía de dispersión de energía de rayos x (EDX) ayudaron a verificar el bloqueo de impurezas por las capas barrera. También se utilizó espectroscopia de masa de iones secundarios (SIMS) para estudiar los perfiles en profundidad a través de las capas barrera para los contactos posteriores. Se observó que usando capas barreras de ZnO recocidas combinadas con capas de Mo óptimas se redujo en un 40% más la difusión de impurezas comparadas con otras barreras.

Se hicieron otros estudios adicionales sobre el depósito óptimo de capas de óxido de zinc impurificado con aluminio (AZO) con bajo espesor (ca 100 nm), las cuales son usadas como óxidos transparentes conductores (TCO) con bajas pérdidas ópticas. Las pérdidas ópticas causan la reducción de eficiencia en celdas solares. XRD y HR-SEM ayudaron a estudiar las variaciones estructurales y morfológicas en función de los parámetros y temperatura de depósito. La caracterización óptica usando mediciones espectrales en el rango UV-Vis mostraron transmitancia arriba del 90%. Para optimizar las capas se definió un factor de calidad (QF) de las capas de AZO, dando un peso similar a la transmitancia y la conductancia de las capas pues ambas propiedades son importantes en su aplicación como TCO en celdas solares. Los parámetros de fabricación de las capas de AZO reportados permitieron bajas resistividades y altos factores de calidad.

Palabras clave

Celdas solares CIGSe, Depósito de metales alcalinos, Tratamiento posterior al depósito (PDT), Depósito sin vacío, Molibdeno, Bicapa, Pulverización catódica de CC, Substratos flexibles, Capa de barrera de difusión, Factor de calidad (QF), óxido de zinc dopado con aluminio (AZO), Pulverización catódica RF, óxido transparente conductor (TCO)

Chapter One: Introduction

1.1 World energy review and outlook

The world has experienced tremendous growth in the demand for energy since 1970, mainly supplied by fossil fuels and greatly influenced by advancements in technology and strategic energy policies [1]. This growth in energy demand is closely associated with the increase in the human population, technological advancements, urbanization, among other factors. Statistics from the World Population Prospects (2019) show that the world's population continues to grow. However, at a slowing rate (Fig. 1), this implies an accompanying growth in energy demands to meet the growing populace's requirements.

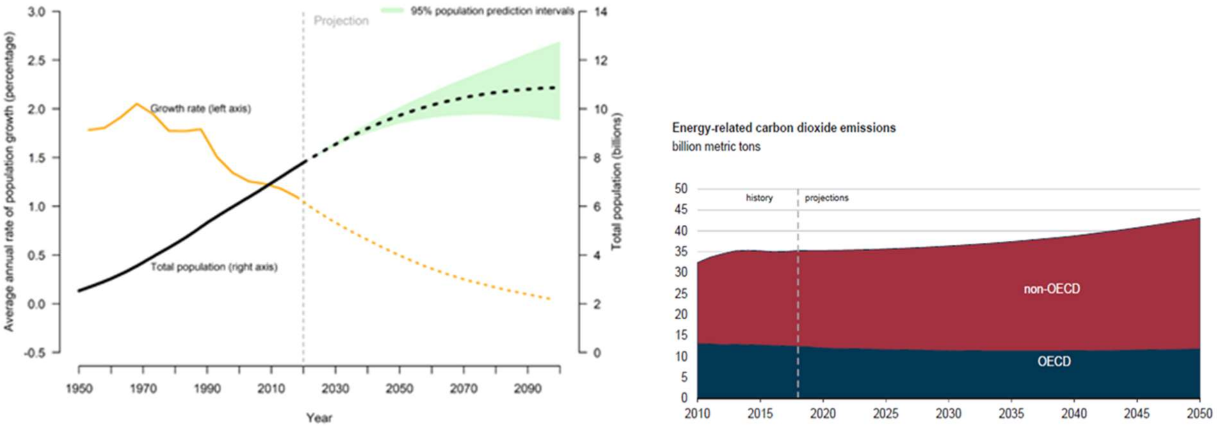

(a) (b)

Figure 1. 1 *(a) Population size and annual growth rate for the world projected between 1950-2020[2], (b) global energy-related* CO_2 *emissions in International Energy Outlook (IEO) 2019* [2]

The energy consumptions globally account for 82% of total greenhouse gases (GHG) emissions, with CO_2 from fuel combustion responsible for the most substantial fraction, up to 92% in most developing countries, albeit the percentage varies with the economic structure of the country [3]. With a projection that global energy-related CO_2 emissions grow at 0.6% per year from 2018 to 2050 (Fig. 1.1 b) [2], and the growth in the population (Fig. 1.2 a), these spell unprecedented pollution across the globe and massive dangers to lives.

Faced with the dangers of pollution posed by GHG and other nuisances, the decarbonization of the energy sector, especially in the developing world, is one of the most critical challenges facing the global energy system. The dangers posed by these pollutions also affect other areas of the environment, and not only the atmosphere [2,4,5]. In an age where the energy scenery is constantly changing, the participants should pay attention to many different change signals, facilitating a shared understanding of successful energy transitions. Among the strategies adopted by many world councils and stakeholders to combat pollution is electrification to reduce GHG from the energy sector. There is a flourishing abundance of emerging and competitive cost-efficient energy technologies, notably renewable energy, accelerating the transition towards carbon-free, decentralized, and digitalized energy systems.

According to the IEO report (2019), the world's energy consumption projects an increase from 2018 to 2050, reaching an approximate average of 911 quadrillion British thermal units (Btu) by 2050, and such energy demand poses an enormous challenge to limited natural resources found on earth. A report from the World Nuclear Association (2019) [6] shows that nuclear energy supplies about 10.5% of global demand and is the second-largest low carbon energy source after hydro, with the aim of 25% of global electricity in 2050 to be delivered by nuclear energy. These amounts of energy from nuclear energy sources signify a tremendous amount of energy, which goes a long way to supplement energy needs. However, atomic sources, although carbon-free, are not the safest form of energy. Many safety concerns are raised by nuclear power, including harmful radiations, especially from the waste products that are very hazardous to health, potential to be used as a source of nuclear weapons, and the possibility of a meltdown of the plants. The search for a clean, eco-friendly, and safe form of energy made solar energy the most viable alternative to address the world's energy crisis.

1.2 Photovoltaics

Photovoltaic (PV) comprises the science and technology and systems involved in the direct conversion of sunlight into electricity. The use of PV helps produce clean, reliable energy without any interference from heat engines, usually with semiconductors that exhibit the photovoltaic effect. They serve as a power source in various areas ranging from small-scale buildings to industrial capacities and even satellites, space vehicles, and megawatt-scale power plants. The PV panels' design comprising primarily of solar cells and traditionally guided by standard trackers, allows for the absorption of direct and diffuse light from the sky. The tracking functionality helps minimize the angle of incidence between the incoming light and the photovoltaic panel and possibly increases the amount of energy gathered from the incoming light's direct component.

These systems, rated in peak kilowatts (kWp), give the amount of electrical power that a system can potentially deliver when the Sun is in the sky on a clear day. The wide range of applications, decrease in PV panels' prices, and some aesthetic applications have continued to drive the increasing demand for photovoltaics every year and boosted the attractiveness to invest in these technologies [7,8].

Although the PV systems are relatively costly to install, the installations can function for many years with little maintenance after the facilities. Comparatively, the capital cost of constructing and operating any solar power plant is meager compared to existing power technologies [9]. Also, solar trackers have dramatically reduced the usual solar electricity problems not produced at night and significantly reduced in cloudy conditions [8,10,11]. According to Lawrence Berkeley National Laboratory (LBNL) [10,11], 80% of the new capacity in 2017 used tracking. The capacity factors have remained steady in recent years, even with the growth in less-sunny locales.

Considering the numerous potentials and advantages associated with PV [11,12], which largely depends on the tremendous amount of energy available from the Sun [13], several industries have sprung up over the decades to manufacture solar panels for PV applications. The division of the global photovoltaic market is along the lines of technology (thin films, Mono- and Multi Silicon), system (high concentrated PV (HCPV) and low concentrated PV (LCPV)), application (industrial, residential and commercial), and region (North America, Europe, Asia-Pacific, and Latin America, Middle East and Africa(LAMEA) [14]. However, the general classification of the PV cells and modules is by the absorber layer material. The silicon (Si) solar cells were among the first generation of solar cells that have dominated the PV market with the record power conversion efficiency (PCE) of 26.7 % [15] and the potentials to achieving a theoretical limit of 29.4% [16,17]. However, Si occurs mainly in the form of oxides. It requires tremendous energy(typically about 1500 to 2000 ºC) for purification, and such an amount of power limits the cost of production and adds to the emission of GHG. Another limitation is associated with the weight and rigidity of the Si solar cells, usually flat with heavy panels which are expensive to install, making it difficult to manufacture light-weight solar cells and unmanageable to be applied for aesthetic purposes. The PCE, η, of Si solar cells has also been tough to improve upon compared with the newer solar cell technologies [18] and the problem of long payback time, implying that initial costs must be reduced for solar to become more wholly embraced.

To combat the challenges facing the so-called first generation of solar cells, a new set of technologies, commonly referred to as the second generation of solar cells, was developed, mainly thin films. This new set of solar cells, characterized by a high optical absorption coefficient and some technological advancements on crystalline Si (c-Si), is geared towards improving the solar cells' PCE and reducing production cost. Some typical second-generation thin-film technologies commercially available and the certified η-values include the copper indium gallium selenide (CIGSe, η~23.35 [19,20]), cadmium telluride (CdTe, η~21.0 [20,21]), gallium arsenide (GaAs, η~27.6 [20,22]) and amorphous silicon (a-Si: H, η~10.2-11.9 [20,23,24]). A considerable advantage of these new sets of solar cells is that their direct bandgap. An example is a CIGSe bandgap, which can be tuned to match the solar spectrum by replacing indium with Ga such that a thin layer of approximately 2.0–2.5 µm is sufficient for the device [25]. Thus the wastage of raw material is reduced.

Further advancements in research and the quest to develop and improve solar cell efficiencies led to the 'emerging' of less commercially-advanced third-generation cell technologies. They can potentially overcome the Shockley–Queisser limit [16,17,26,27] of power efficiency for the single bandgap solar cells and multijunction solar cells. Among this generation of solar cells include organic photovoltaics (OPVs, η~11.2 [20]), copper zinc tin sulphide (CZTS, η~10.0 [20,28,29]) and the selenide version (CZTSSe, η~11.3 [20,30]), perovskite solar cells (η~20.9), dye-sensitised solar cells (DSSCs, η~11.9 [20,31]), and quantum dot solar cells (η~10.4 [32]). The certified efficiencies and properties of the solar cells, sub-, and mini-modules (Table 1.1), keep advancing with the advancement in research and the potentials of multijunction solar cells.

Table 1. 1 *Confirmed single-junction terrestrial cell and submodule efficiencies measured under the global AM1.5 spectrum (1000 W/m²) at 25°C* [33].

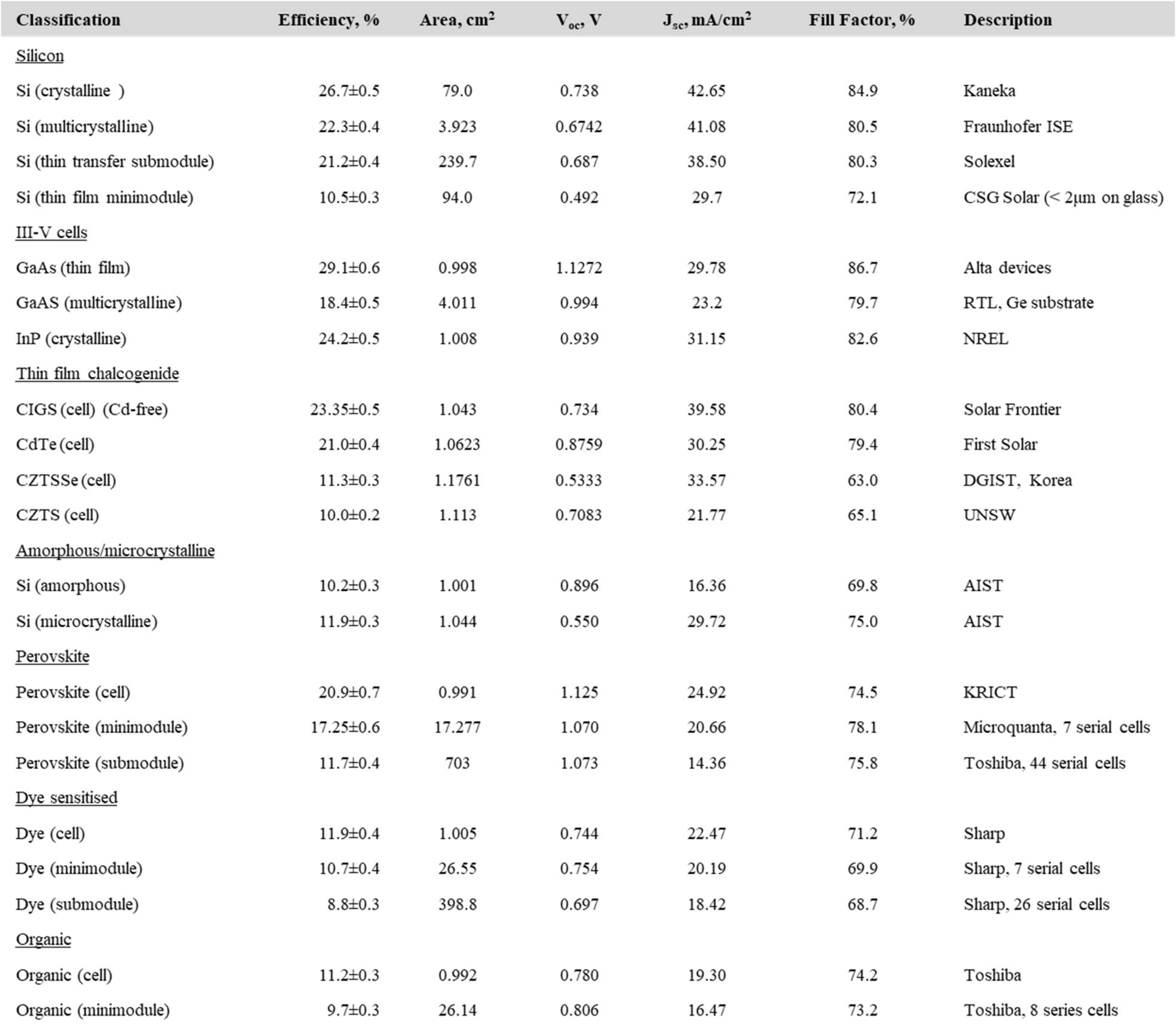

Classification	Efficiency, %	Area, cm²	V_{oc}, V	J_{sc}, mA/cm²	Fill Factor, %	Description
Silicon						
Si (crystalline)	26.7±0.5	79.0	0.738	42.65	84.9	Kaneka
Si (multicrystalline)	22.3±0.4	3.923	0.6742	41.08	80.5	Fraunhofer ISE
Si (thin transfer submodule)	21.2±0.4	239.7	0.687	38.50	80.3	Solexel
Si (thin film minimodule)	10.5±0.3	94.0	0.492	29.7	72.1	CSG Solar (< 2µm on glass)
III-V cells						
GaAs (thin film)	29.1±0.6	0.998	1.1272	29.78	86.7	Alta devices
GaAS (multicrystalline)	18.4±0.5	4.011	0.994	23.2	79.7	RTL, Ge substrate
InP (crystalline)	24.2±0.5	1.008	0.939	31.15	82.6	NREL
Thin film chalcogenide						
CIGS (cell) (Cd-free)	23.35±0.5	1.043	0.734	39.58	80.4	Solar Frontier
CdTe (cell)	21.0±0.4	1.0623	0.8759	30.25	79.4	First Solar
CZTSSe (cell)	11.3±0.3	1.1761	0.5333	33.57	63.0	DGIST, Korea
CZTS (cell)	10.0±0.2	1.113	0.7083	21.77	65.1	UNSW
Amorphous/microcrystalline						
Si (amorphous)	10.2±0.3	1.001	0.896	16.36	69.8	AIST
Si (microcrystalline)	11.9±0.3	1.044	0.550	29.72	75.0	AIST
Perovskite						
Perovskite (cell)	20.9±0.7	0.991	1.125	24.92	74.5	KRICT
Perovskite (minimodule)	17.25±0.6	17.277	1.070	20.66	78.1	Microquanta, 7 serial cells
Perovskite (submodule)	11.7±0.4	703	1.073	14.36	75.8	Toshiba, 44 serial cells
Dye sensitised						
Dye (cell)	11.9±0.4	1.005	0.744	22.47	71.2	Sharp
Dye (minimodule)	10.7±0.4	26.55	0.754	20.19	69.9	Sharp, 7 serial cells
Dye (submodule)	8.8±0.3	398.8	0.697	18.42	68.7	Sharp, 26 serial cells
Organic						
Organic (cell)	11.2±0.3	0.992	0.780	19.30	74.2	Toshiba
Organic (minimodule)	9.7±0.3	26.14	0.806	16.47	73.2	Toshiba, 8 series cells

1.3 Renewable energy prospects in Mexico

The earth's oblate spheroidal surface [34] receives an average energy density of approximately 1,000 W/m² [13] (also the air mass 1.5 (AM 1.5) standard or reference spectra used for PV cell performance measurements) for a surface perpendicular to the Sun's rays at sea level on a clear day. With this energy, Mexico, which has 1,964,375 square km [35], receives about 1.964 PW of solar energy [13]. Furthermore, listed among the countries in the sunbelt region (the countries within 35° of the Equator), which receives the most significant quantity of solar irradiation, Mexico holds the potential to be among the nations to attain the 405 GW solar PV capacity by 2030 [36].

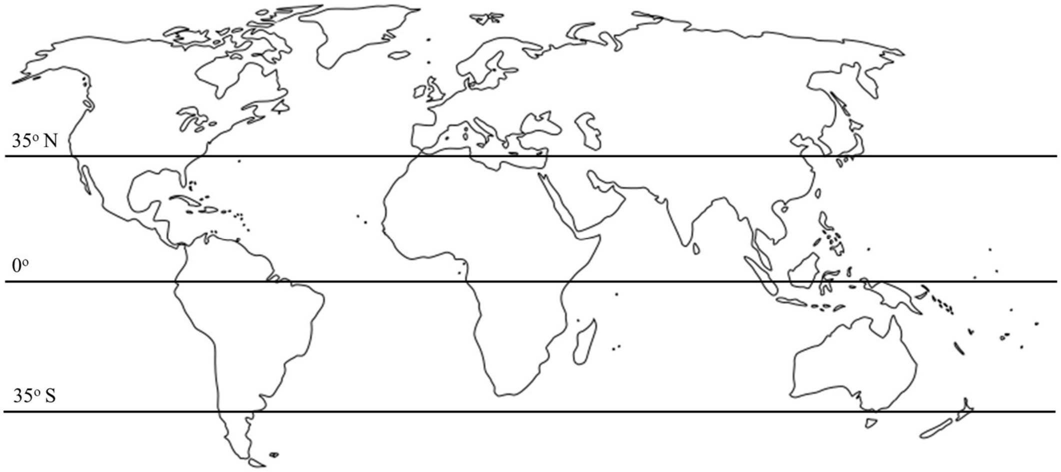

Figure 1. 2 *Simplified world map with modifications to show the Sunbelt zone regions located +/- 35° latitude around the Equator. Source:* *https://commons.wikimedia.org/wiki/File:Simplified_blank_world_map_without_Antartica_(no_borders).svg*

Although the country has embarked on reforms and the market for power generation expected to grow, due to the demand for efficient and cost-effective electricity, by an estimated 1.75 percent from 2019-2020, imports from the United States still find their way into the country, albeit flat or with a slight increase. Also, in compliance with the goals for sustainable development and reducing GHG, the power sector has the objective to generate about 50 percent of electricity from clean energy sources by 2050 at the lowest cost for the country since above 71 percent of the country's electricity comes from fossil fuels [37–39]. This move, however, may not be without some administrative hitches due to some economic considerations and policies [40].

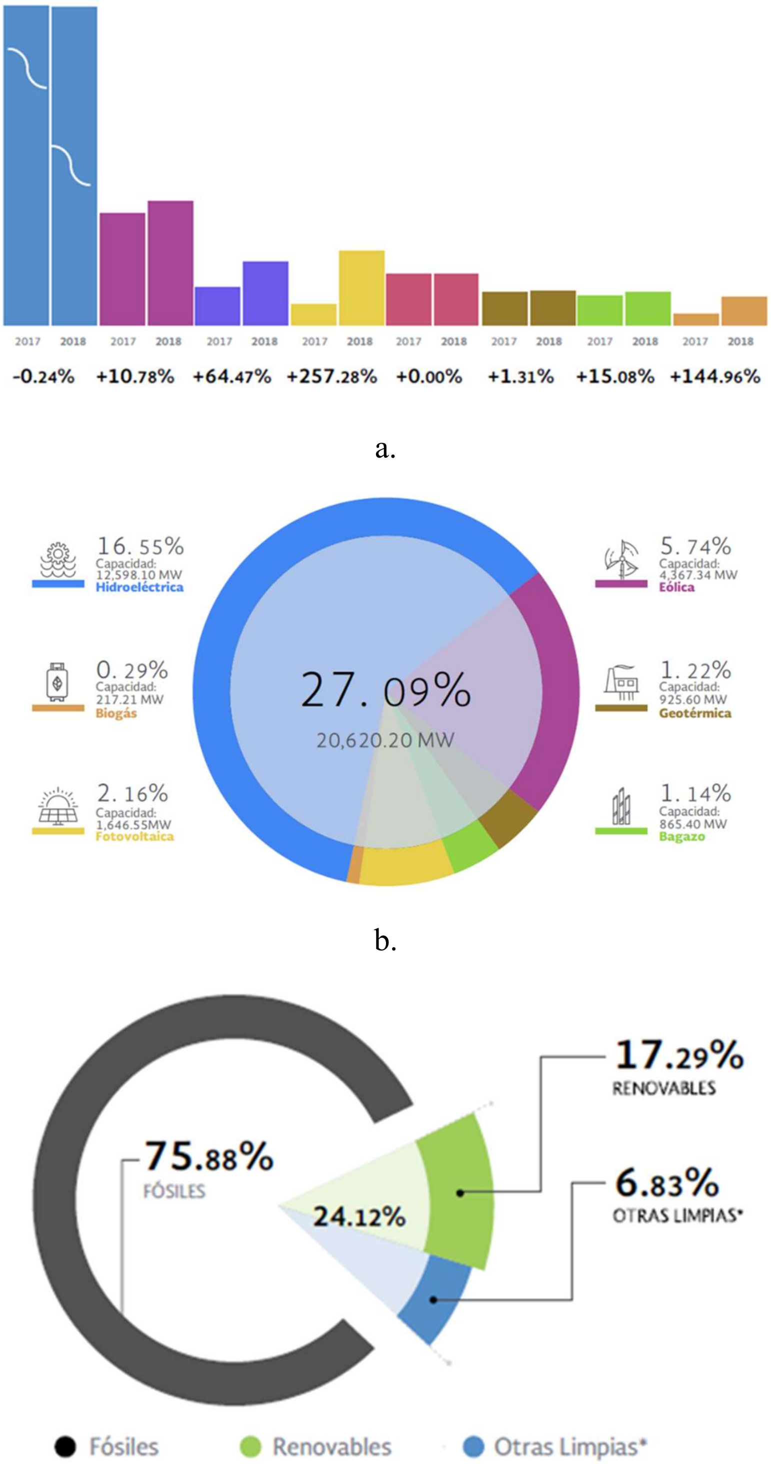

a.

b.

c.

Figure 1. 3 *Electricity generation associated with renewable and other sources of energies in México (a) percentage increase between 2017 and 2018, (b) percentage contributions from different renewable sources, and (c) comparison with fossil fuel and other sources* [38].

Although it is a massive increase in the percentage of installed PV capacity (Fig. 3a), the amount of energy compared with other energy (Fig. 1.3) remains very little despite the enormous potential. According to the Mexican energy secretary, the country projects to generate 470,431.7 GWh of electricity by 2029, a ~55% increase over the generated power in 2014 [41]. However, efficiently trapping a meager 1% over Mexico on bright noon is over 350 times this projected energy amount. Moreover, the countries in the sunbelt zones have potentially more solar insolation (above 1000W/m^2) than other regions outside the zone.

1.4 Motivation and objectives of the study

Due to the prevalent challenges posed by energy needs and the potentials offered by solar energy, we propose using the so-called three-stage co-evaporation method to deposition the copper-indium-gallium-selenium (CIGSe) absorber layer, with a non-vacuum post-deposition treatment (PDT) method for the solar cell fabrication. The deposition technique and the proposed PDT method commonly considered for solar cell fabrication are (but not limited):

1. Development and optimization of deposition parameters for efficient material utilization for each of the deposited layers
2. Improvement of deposition rates for better layer compositions affecting the properties, especially the absorber layer during the co-evaporation process
3. Understanding the effects of ambient parameters (e.g., deposition and annealing temperatures, presence of residual gases) which can influence layer parameters (e.g., layer formation and grain growth)
4. Study the deposited layers' properties that influence the interface of the heterojunctions and, therefore, the performance of the solar cells

This study focuses on optimizing the metal sources' temperatures, which affects the deposition rates and, therefore, the composition of the precursor materials and fabrication of the CIGSe absorber layer using the co-evaporation technique. We also explore using a spin-coating method for the optimized deposition of alkali metals during the PDT processes. The proposed method offers an alternative non-vacuum technique for alkali metal deposition. The study of the superficial properties and effects of the alkali metals on the absorber layers provides an understanding of the possible mechanisms involved.

The presence of alkali metals on the CIGSe absorber materials reportedly passivates the vacancies (e.g., V_{Cu}), among other things, within the bulk of the absorber material, and their relative location in-between the grains aids in passivating the grain boundaries. Although standard methods for the PDT involve thermal evaporation in a vacuum, the proposed spin-coating method will offer the opportunity to deposit the alkali metals, especially the heavier atoms, directly on the absorber layer's surface with controlled thickness. The relatively big ionic radii of the heavier alkali atoms and higher formation energy (e.g., Cs_{Cu}) already reduce the possibility of substituting the Cu vacancies. However, the proposed spin-on deposition of a thin layer of the alkali halide and subsequent thermal treatment will potentially remove the present halide and leaving behind the alkali atoms, aiding the possible formation of the alkali-In(Ga)-Se compound at the grain boundaries. The results from this PDT method will proposedly modify the absorber layer's surface (e.g., morphologically, electrically), although aimed not to create any structural modification on the CIGSe thin-film layer.

This thesis, organized in five chapters, has the preliminary chapter to discuss the introduction to photovoltaics, the overview from the global outlook, and the potentials to harness solar power. Chapter two presents a review of the CIGSe solar cell component layers and their material characterizations and the CIGSe solar cells and their tandem formations. A brief review of the different alkali metals provides an insight into the effects of their applications. The deposition processes and optimization conditions carried out for the layers and PDT are presented in chapter three of this study. Chapters four, five, and six focus on the results from the absorber layers' characterizations, effects of post-deposition treatments, and optimized deposition of the back-contact and transparent conducting oxide (TCO) layers. Finally, the conclusions and recommendations come in the last chapter of the work with a summary of the work.

References

[1] World Energy Council, World Energy Scenarios 2019. European Regional Perspective, (2019). https://www.worldenergy.org/publications/entry/world-energy-scenarios-2019-european-regional-perspectives.

[2] U.S. Energy Information Administration, International Energy Outlook 2019, Washington, 2019. https://doi.org/10.1080/01636609609550217.

[3] INTERNATIONAL ENERGY AGENCY, CO2 EMISSIONS FROM FUEL COMBUSTION 2019 EDITION, 2019. www.iea.org.

[4] J.H. Kim, B.S. Shim, H.S. Kim, Y.J. Lee, S.K. Min, D. Jang, Z. Abas, J. Kim, Review of nanocellulose for sustainable future materials, Int. J. Precis. Eng. Manuf. - Green Technol. 2 (2015) 197–213. https://doi.org/10.1007/s40684-015-0024-9.

[5] Y. Su, Y. Liang, L. Chai, Z. Han, S. Ma, J. Lyu, Z. Li, L. Yang, Water Degradation by China's Fossil Fuels Production: A Life Cycle Assessment Based on an Input–Output Model, Sustainability. 11 (2019) 4130. https://doi.org/10.3390/su11154130.

[6] World Nuclear Association, At Work 2019 Edition, (2019) 1–32. https://www.world-nuclear.org/getattachment/Our-Association/Publications/Annual-Reports-and-Brochures/At-Work-Annual-Report-2019/at-work-2019-may-edition.pdf.aspx.

[7] World Energy Council, World Energy Issues Monitor - Global and Regional Perspectives, (2019) 42. http://www.weltenergierat.de/world-energy-issues-monitor/.

[8] B. Parida, S. Iniyan, R. Goic, A review of solar photovoltaic technologies, Renew. Sustain. Energy Rev. 15 (2011) 1625–1636. https://doi.org/10.1016/j.rser.2010.11.032.

[9] S.C. Bhatia, Energy resources and their utilisation, in: Adv. Renew. Energy Syst., Elsevier, 2014: pp. 1–31. https://doi.org/10.1016/B978-1-78242-269-3.50001-2.

[10] J. Seel, M. Bolinger, Utility-Scale Solar: Empirical Analyses of Project Cost, Performance, and Pricing Trends in the United States, Intersolar 2016. (2016) 1–25.

[11] M. Bolinger, J. Seel, Utility-Scale Solar: Empirical trends in project technology, cost, performance, and PPA pricing in the United States, Lawrence Berkeley Natl. Lab. (2018) 62. https://emp.lbl.gov/sites/default/files/lbnl_utility_scale_solar_2018_edition_report.pdf%0

Ahttps://emp.lbl.gov/utility-scale-solar.

[12] BP Statistical Review of World Energy Statistical Review of World, Ed. BP Stat. Rev. World Energy. (2019). https://www.bp.com/content/dam/bp/business-sites/en/global/corporate/pdfs/energy-economics/statistical-review/bp-stats-review-2019-full-report.pdf.

[13] W. Is, S. Energy, D. Your, E. Needs, F.E. Use, A. Resources, The Sun' s Energy, (2020) 1–2. https://ag.tennessee.edu/solar/Pages/What Is Solar Energy/Sun's Energy.aspx (accessed January 20, 2020).

[14] E.P. Anil Chaudhary, Shruti Hariharan, Photovoltaic Market by Technology (Thin Film , Mono Si and Multi Si), System (High Concentration Photovoltaic (HCPV) and Low Concentration Photovoltaic (LCPV)), and Application (Industrial , Residential and Commercial): Global Opportunity Analysi, (2020). https://www.alliedmarketresearch.com/photovoltaic-market#toc (accessed January 16, 2020).

[15] K. Yoshikawa, H. Kawasaki, W. Yoshida, T. Irie, K. Konishi, K. Nakano, T. Uto, D. Adachi, M. Kanematsu, H. Uzu, K. Yamamoto, Silicon heterojunction solar cell with interdigitated back contacts for a photoconversion efficiency over 26%, Nat. Energy. 2 (2017). https://doi.org/10.1038/nenergy.2017.32.

[16] M.J. Kerr, A. Cuevas, P. Campbell, Limiting efficiency of crystalline silicon solar cells due to Coulomb-enhanced Auger recombination, Prog. Photovoltaics Res. Appl. 11 (2003) 97–104. https://doi.org/10.1002/pip.464.

[17] A. Richter, M. Hermle, S.W. Glunz, Reassessment of the limiting efficiency for crystalline silicon solar cells, IEEE J. Photovoltaics. 3 (2013) 1184–1191. https://doi.org/10.1109/JPHOTOV.2013.2270351.

[18] J. Carbeck, Solar power has big limitations. This wonder material could change that, (2016) 4–7. https://www.weforum.org/agenda/2016/06/perovskite-solar-cells/ (accessed January 20, 2020).

[19] S.F. K.K., Solar Frontier Achieves World Record Thin-Film Solar Cell Efficiency: 22.3 %, Online. (2015) 2–3. https://doi.org/http://www.solar-frontier.com/eng/news/2015/C051171.html.

[20] M.A. Green, E.D. Dunlop, D.H. Levi, J. Hohl-Ebinger, M. Yoshita, A.W.Y. Ho-Baillie, Solar cell efficiency tables (version 54), Prog. Photovoltaics Res. Appl. 27 (2019) 565–575. https://doi.org/10.1002/pip.3171.

[21] I. First Solar, First Solar Builds the Highest Efficiency Thin Film PV Cell on Record, (2015) 1–2. http://investor.firstsolar.com/releasedetail.cfm?ReleaseID=864426 (accessed January 20, 2020).

[22] B.M. Kayes, H. Nie, R. Twist, S.G. Spruytte, F. Reinhardt, I.C. Kizilyalli, G.S. Higashi, 27.6% Conversion efficiency, a new record for single-junction solar cells under 1 sun illumination, Conf. Rec. IEEE Photovolt. Spec. Conf. (2011) 000004–000008. https://doi.org/10.1109/PVSC.2011.6185831.

[23] H. Sai, K. Maejima, T. Matsui, T. Koida, M. Kondo, S. Nakao, Y. Takeuchi, H. Katayama, I. Yoshida, High-efficiency microcrystalline silicon solar cells on honeycomb textured substrates grown with high-rate VHF plasma-enhanced chemical vapor deposition, Jpn. J. Appl. Phys. 54 (2015) 0–6. https://doi.org/10.7567/JJAP.54.08KB05.

[24] T. Matsui, A. Bidiville, K. Maejima, H. Sai, T. Koida, T. Suezaki, M. Matsumoto, K. Saito, I. Yoshida, M. Kondo, High-efficiency amorphous silicon solar cells: Impact of deposition rate on metastability, Appl. Phys. Lett. 106 (2015) 0–5. https://doi.org/10.1063/1.4907001.

[25] J. Ramanujam, U.P. Singh, Copper indium gallium selenide based solar cells – a review, Energy Environ. Sci. 10 (2017) 1306–1319. https://doi.org/10.1039/C7EE00826K.

[26] W. Shockley, H.J. Queisser, Detailed balance limit of efficiency of p-n junction solar cells, J. Appl. Phys. 32 (1961) 510–519. https://doi.org/10.1063/1.1736034.

[27] F.H. Alharbi, S. Kais, Theoretical limits of photovoltaics efficiency and possible improvements by intuitive approaches learned from photosynthesis and quantum coherence, Renew. Sustain. Energy Rev. 43 (2015) 1073–1089. https://doi.org/10.1016/j.rser.2014.11.101.

[28] C. Yan, J. Huang, K. Sun, S. Johnston, Y. Zhang, H. Sun, A. Pu, M. He, F. Liu, K. Eder, L. Yang, J.M. Cairney, N.J. Ekins-Daukes, Z. Hameiri, J.A. Stride, S. Chen, M.A. Green, X. Hao, Cu2ZnSnS4 solar cells with over 10% power conversion efficiency enabled by heterojunction heat treatment, Nat. Energy. 3 (2018) 764–772. https://doi.org/10.1038/s41560-018-0206-0.

[29] F.A. Jhuma, M.Z. Shaily, M.J. Rashid, Towards high-efficiency CZTS solar cell through buffer layer optimization, Mater. Renew. Sustain. Energy. 8 (2019) 1–7. https://doi.org/10.1007/s40243-019-0144-1.

[30] DGIST Korea, Highest Efficiency For Flexible CZTSSe Solar Cell, (2020) 1–18. https://solarpowermanagement.net/article/108720/Highest_Efficiency_For_Flexible_CZTSSe_Solar_Cell (accessed January 21, 2020).

[31] S. Mathew, A. Yella, P. Gao, R. Humphry-Baker, B.F.E. Curchod, N. Ashari-Astani, I. Tavernelli, U. Rothlisberger, M.K. Nazeeruddin, M. Grätzel, Dye-sensitized solar cells with 13% efficiency achieved through the molecular engineering of porphyrin sensitizers, Nat. Chem. 6 (2014) 242–247. https://doi.org/10.1038/nchem.1861.

[32] Z. Yang, J.Z. Fan, A.H. Proppe, F.P.G. De Arquer, D. Rossouw, O. Voznyy, X. Lan, M. Liu, G. Walters, R. Quintero-Bermudez, B. Sun, S. Hoogland, G.A. Botton, S.O. Kelley, E.H. Sargent, Mixed-quantum-dot solar cells, Nat. Commun. 8 (2017) 1–8. https://doi.org/10.1038/s41467-017-01362-1.

[33] M. Green, E. Dunlop, J. Hohl-Ebinger, M. Yoshita, N. Kopidakis, X. Hao, Solar cell efficiency tables (version 57), Prog. Photovoltaics Res. Appl. 29 (2021) 3–15. https://doi.org/10.1002/pip.3371.

[34] M. Williams, What Is the Surface Area of the Earth?, Universe Today. (2017) 1–7. https://www.universetoday.com/25756/surface-area-of-the-earth/.

[35] Central Intelligence Agency, North America :: Mexico, (n.d.). https://www.cia.gov/library/publications/the-world-factbook/geos/mx.html (accessed January 23, 2020).

[36] A.T. Kearney, J. Hauff, M. Verdonck, H. Derveaux, L. Dumarest, J. Alberich, J.-C. Malherbe, Unlocking the Sunbelt potential of photovoltaics, 2010. https://www.mesia.com/wp-content/uploads/2017/09/EPIA-Unlocking_the_Sunbelt_Potential-of-PV.pdf.

[37] Mexico - Electricity Sector, (2020) 1–6. https://www.export.gov/article?id=Mexico-Electricity-Sector (accessed January 27, 2020).

[38] Secretaría de Energía, Reporte de Avance de Energías Limpias Primer Semestre 2018

Secretaría de Energía: Elaboración y Revisión, (2018) 21. https://www.gob.mx/cms/uploads/attachment/file/418391/RAEL_Primer_Semestre_2018.pdf.

[39] I. Renewable Energy Agency, REmap 2030, Renewable Energy Prospects: Mexico, summary, 2015. www.irena.org/remap (accessed March 12, 2021).

[40] M. Wattenbarger, Mexico blocks private renewables energy expansion, (2020). https://dialogochino.net/en/climate-energy/37327-mexico-blocks-private-renewable-energy-expansion/ (accessed March 12, 2021).

[41] Secretaría de Energía (SENER), Prospectiva del Sector Eléctrico 2015-2029, (2015) 166. https://www.gob.mx/cms/uploads/attachment/file/44328/Prospectiva_del_Sector_Electrico.pdf (accessed January 28, 2020).

Chapter Two: Copper-indium-gallium-selenide (CIGSe) Solar Cells State of the Art

2.1 A brief historical overview

An early work of literature on CIS (copper-indium-selenium) described binary components' reaction at higher temperatures and the crystallization in the chalcopyrite type ($CuFeS_2$). The structure's formation was associated with the subgroup element's high tendency to form atomic bonds with the chalcogens' tetrahedral coordination. However, its first application for photovoltaic purposes with CIS/CdS heterojunction reported 5% efficiency and subsequently optimized to give a 12% efficiency [1]. Subsequently, the success of photovoltaic converters made from semiconductor pairs attracted more scientific recognition. It led to further research for materials with more potentials, mostly having a PCE above 10%, with good lattice match, large bandgap, absence of interfacial potential "spike," and suitable electrical conductivities [1].

In contrast to Si solar cells, which have dominated the PV markets, CIS solar cells offer a thin film alternative to the large Si wafers. The comparable cost-to-efficiency ratio of Si solar cells has been an advantage due to the abundance of Si (the second most abundant element (27.7%) [2]). However, the volume of materials used for Si solar cell fabrication (~200 μm and above), and the sawed wafer from ingots, which presents material waste, will leave a significant burden on the ecosystem [3]. The degradation will also ultimately lead to the lifespan's termination, leading to 1 kg of silicon production, releasing approximately 1.58 kg of CO_2 into the atmosphere [4]. The materials used in thin-film technologies can pose some possible threats [5], coupled with the challenge of limited resources as they are not as abundant as Si. Nevertheless, the relatively small quantities of materials used for thin-films and the potential for being recycled offer a more alluring prospect.

For distinction, a thin film refers to materials built from the beginning through random nucleation and growth processes of independently condensing/reacting atomic/ionic/molecular species on a substrate. The properties of such material, structural, chemical, metallurgical, and physical, are greatly influenced by several deposition parameters and may probably be thickness-dependent [6]. These thin-films are direct bandgap materials with a high absorption coefficient of the order of 10^5 cm^{-1}, two orders of magnitude higher than that of silicon [7], which allows for better absorption of sunlight with ~2-4 μm thickness. They also have the advantage of flexibility. They can be grown on different substrates, rigid or flexible, and a monolithic integration technology, allowing connecting devices from the front of one cell to the back of the next one in the same plane [8]. These thin-film technology features also present the potential for reduced fabrication costs compared to Si-based technology [9]. The partial substitution of indium (In) with gallium (Ga) increases the bandgap from about 1.04 electron-volts (eV) for CIS to about 1.68 eV for copper gallium diselenide (CGS). The optimization of the bandgap can lead to a substantial increase in overall efficiency, and the solar cells are known as copper indium gallium diselenide [$Cu(In_xGa_{1-x})Se_2$], or CIGSe solar cells [10].

The continued interest in CIGSe solar cells from researchers as well from industries stems from the numerous advantages. Among these desirable features include (i) low-cost manufacturing process (non-vacuum/vacuum deposition, monolithic integration), (ii) relatively high efficiencies on glass [11], and flexible substrates [8] (iii) excellent stability exhibited in the energy output module degradation (%/yr) [12] (iv), and lesser use of toxic cadmium compare to CdTe solar cells, and Cd-free solar cells [13]. As the market for PV technologies continues to grow, there is a concern about these panels' potential hazards after the lifetimes had elapsed. Consequently, there is a need to recycle the materials or adequately dispose of the materials. The economic motivation to recycle most PV devices from studies does not outweigh the difference between recycling and landfill costs, making recycling an unfavorable economic option without appropriate incentives. However, landfilling over a long period can lead to accumulation and potential leaching of some toxic wastes into the environment, thereby posing potential hazards. Thus, although seemingly not economically favorable, recycling is the better option that can reduce the possible impact on the environment [14]. The recycled materials help make new solar cells, among other things. The recycling process of CIGSe solar cells involves putting the materials through a smelting process or acid baths to recover the metals, including selenium (Se), indium (In), and gallium (Ga). The glass is processed through thermal decomposition, solvent, or acid dissolution to remove any remaining PV layers and the glass materials recovered. Furthermore, the recycling of CIGSe proves to be more profitable than other PV materials [15].

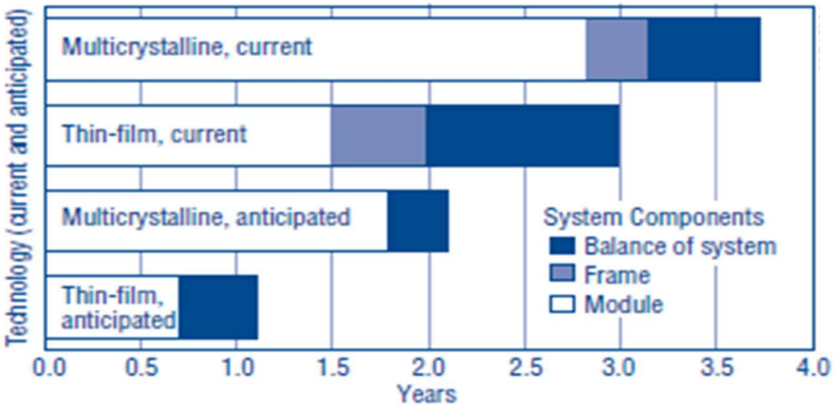

Figure 2. 1 *Energy Payback for Rooftop PV Systems. For a 30-year system life, PV systems will provide a net gain between 26 to 29 years of pollution-free and greenhouse-gas-free electrical generation* [16].

According to the global solar market, the solar PV reported a compound annual growth rate (CAGR) of 24% between 2010 and 2017, which gives it a decisive leading role as one of the fundamental pillars of the future global energy policy [17]. Also, an improvement in the energy-payback-time (EPBT) (Fig. 2.1) for the different solar technologies acts as a drive for more dependence. The EPBT, which serves as one metric adopted by several analysts in distinguishing the energy sustainability of different technologies, can be defined as the time necessary for a photovoltaic panel to produce the energy equivalent to that utilized to build it [16]. The thin-film PV gives an EPBT of fewer than 12 months in most parts of the world and six months in the SunBelt region. This value significantly improved over c-Si, which achieves an EPBT between 12 and 18 months [17]. Some major players in the PV industries manufacturing CIGSe solar cells include Solibro, Miasole, Solyndra, Soltecture, and Nanosolar.

2.2 CIGSe solar cell overview

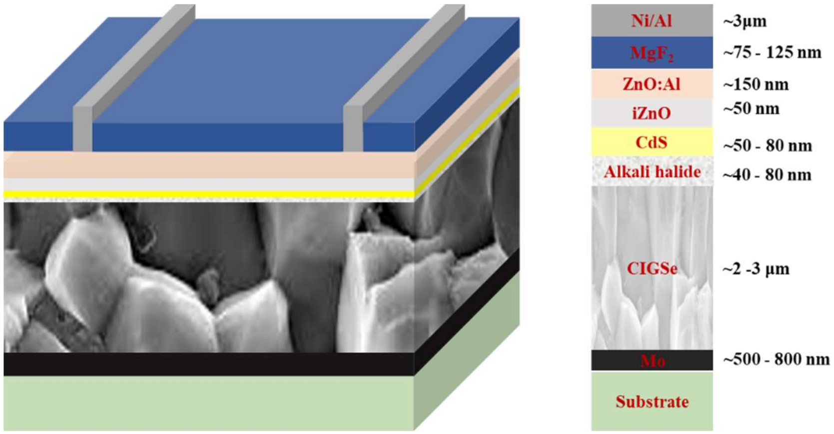

Figure 2. 2 *A schematic cross-section of the CIGSe based thin-film solar cells showing the different layers and approximate thicknesses*

The solar cell is a photovoltaic device that directly converts sunlight into electricity. The incident photons get absorbed if the energy is enough to excite the electrons. The absorbed photons in the p-type CIGSe absorber layer generate electron-hole pairs within the solar cell, migrate to the appropriate electrodes, and get collected to generate a current in the external circuit. The relation between the wavelength of the light (λ) of the absorbed photons and energy (E) given by

$$E = \frac{hv}{\lambda} = \frac{1240}{\lambda(nm)} eV \qquad \textbf{(Eqn. 2. 1)}$$

(c is the speed of light, h is Planck's constant). Furthermore, the number of photons per second per unit area, known as the photon flux defined as:

$$\Phi = \frac{no\ of\ photons}{sec\, m^2} \qquad \textbf{(Eqn. 2. 2)}$$

determine the number of electrons generated and hence the current generated from the solar cell. Other mechanisms play out within the device that determines the quantity of electric current generated within the solar cell device, such as the generated carriers' collection probability.

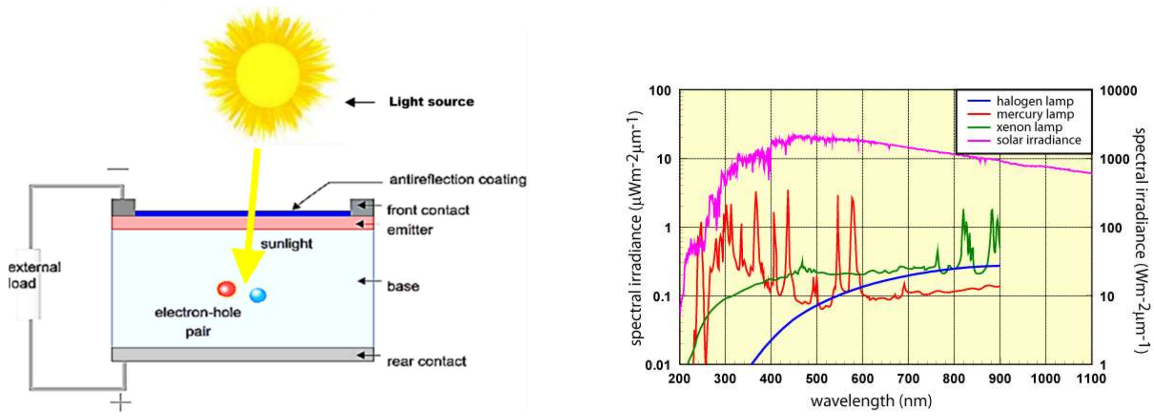

Figure 2. 3 *(a) A cross-sectional view of a single p-n junction solar cell indicating the necessary layers and connections to the external load* [18] *(b) comparison of the spectral irradiance of some artificial light sources (left axis) with the solar spectral irradiance (right axis)* [19]

The solar irradiance available at any location on the earth's surface depends on certain factors, such as time of the day, location (i.e., latitude). Other artificial sources can also serve to provide the irradiance for other functions, e.g., simulations. When the photons are incident on the solar cell, the "quantum efficiency" (QE) compares the ratio of the number of carriers collected (photon flux) by the solar cell to the number of incident photons of given energy on the solar cell. This comparison is similar to the spectral response, which considers the ratio of the generated current to the solar cell to the power incident. The collection of the generated currents reduces and ideally totally prevents the recombination of the hole-electron pairs leading to the flow of current through the external circuit. The collection of the generated carriers is a probability that depends on the diffusion length of the carriers. The total current through the circuit, assuming a diode model with zero series resistance and infinite shunt resistance, described as the short-circuit current, is given by:

$$I(V) = I_{dark} + I_{light} = I_o\left[exp^{qV/nk_BT} - 1\right] - I_L \qquad \textbf{(Eqn. 2. 3)}$$

where I_L light-generated current (same as the short-circuit current, I_{sc} for low series resistance < 10 Ω cm^2) and I_o is the reverse saturation current. ***n*** is the diode ideality factor (equals 1 for an ideal diode), while **T** is the absolute temperature, and **V** is the applied voltage.

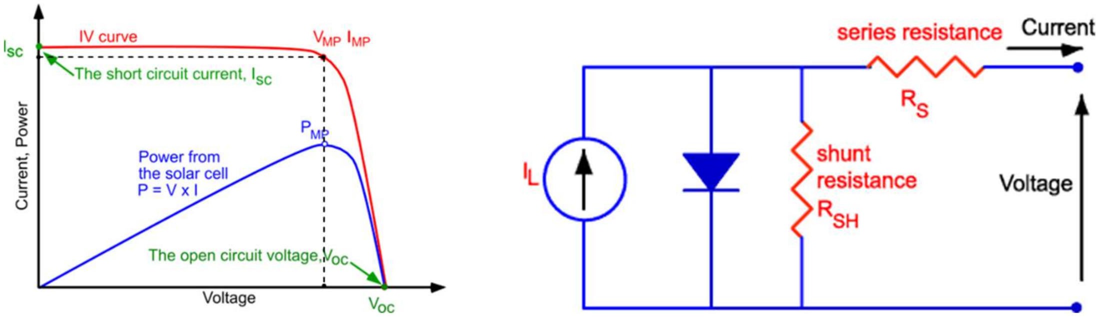

Figure 2. 4 *(a) Current-voltage (IV) curve showing some basic parameters, and (b) the equivalent circuit of a solar cell.*

The short-circuit current depends on some factors, including the surface area (A) of the solar cell, removed by calculating the current density (J_{sc} [mA/cm^2]=$^{I_{sc}}/_{A}$) instead, and the standardized spectrum for most solar cell measurements is the AM1.5 spectrum. The resultant open-circuit voltage, V_{OC}, represents the maximum voltage at zero current obtainable from a solar cell. With I(V) = 0, the equation for V_{OC} is given by:

$$V_{oc} = \frac{nk_BT}{q} \text{In}\left(\frac{J_{sc}}{J_o} + 1\right) \qquad \textbf{(Eqn. 2. 4)}$$

However, contrary to Eq. 2.4, the open-circuit voltage decreases with temperature. Instead, an increase in temperature increases the short-circuit current, $I_{sc,}$ due to the bandgap creation of more electron-hole pairs by the energetic photons. The V_{oc} depends on the saturation current of the solar cell and light-generated current, giving a measure of recombination. And so, the relationship between the current density and open-circuit voltage is;

$$J_{sc} = J_o\left(\exp^{\frac{qV_{oc}}{nk_BT}} - 1\right) \qquad \textbf{(Eqn. 2. 5)}$$

The presence of some resistive effects causes a dissipation of powers in the solar cell, which reduces the efficiency of the solar cell to convert photons of energy into electric current. The prevalent resistances encountered are series resistance (R_s) and shunt resistance (R_{sh}), which reduce the fill factor (FF) of the solar cell and depend on the geometry of the solar cell.

The series resistances are due to the effects of the metal contacts and the current flowing through the cell's emitter and base. The presence of low shunt resistance signifies alternative paths for the currents within the solar cell, typically due to some manufacturing defects. Incorporating both resistances, the current density through the device becomes

$$J(V) = J_{sc} - J_o\left(\exp^{\frac{q(V+JR_S)}{nk_BT}} - 1\right) - \frac{V+JR_S}{R_{sh}}$$ **(Eqn. 2. 6)**

The FF determines the maximum power from a solar cell since the value at operating points of the open-circuit voltage and short-circuits current from the solar cell is zero. The FF describes the ratio of the maximum power to the product of Voc and Isc from the solar cell and measures the "squareness" of the IV curve, given by:

$$FF = \frac{P_{MP}}{V_{OC} \times I_{SC}} = \frac{V_{MP} \times I_{MP}}{V_{OC} \times I_{SC}}$$ **(Eqn. 2. 7)**

The performance evaluation for a device by measuring the efficiency, η, gives output to the sun's input energy. This performance depends on the intensity of the incident light and the temperature of the solar cell. The efficiency measurement under AM1.5 conditions and a temperature of 25°C simulates the sun's effects on the earth's surface. The efficiency (η) is given by;

$$\eta = \frac{J_{SC} \cdot V_{OC} \cdot FF}{P_{in}}$$ **(Eqn. 2. 8)**

P_{in} is the input power for efficiency calculations taken as 1 kW/m^2 or 100 mW/cm^2.

2.3 Characteristics of the CIGSe absorber layer

Fabrication of the absorber layer using either the physical or chemical deposition methods is preferred in vacuum environments to improve the purity of the sources and minimize contamination and usually fitted with systems to contain and control pollution exhaust fumes. Although the preferred option is using vacuum systems in laboratories, the cost-to-efficiency ratio forms a frequent basis for most industrial applications [20].

Some deposition techniques in works of literature and industrially for the device grade absorber layer include [21,22]; stacked thermal evaporation technique, the novel co-evaporation technique, sputtering methods, electro-deposition, flash evaporation, spray pyrolysis, atomic layer deposition, and molecular beam epitaxy. The nanoparticles prepared from binary metallic precursors using physical methods such as ball-milling are converted to thin films of appropriate thicknesses using inkjet printing and doctor-blade techniques [23] or sintered into targets for sputtering [24]. The deposition parameters (e.g., deposition rates), and as well techniques (vacuum or non-vacuum), and temperatures (substrate and annealing temperatures) play vital roles in the composition and structure of the CIGSe layer, with all aimed at fabricating device grade deposition. These parameters influence the layer properties (e.g., crystal orientation primarily controlled by the deposition temperature) and compositional ratios and the solar cell parameters, including the minority-carrier lifetime, electron diffusion length, and charge-carrier mobilities [25].

2.3.1 Structure and phase properties

The CIGSe chalcopyrite (Fig. 2.5) structure is derived from the zinc blende structure and forms a regular tetrahedron with a chalcogen atom in the center. The deposition temperature of CIGSe precursors primarily controls the approximate lattice parameters [26] characteristic of a chalcopyrite structure, z = 4, a = 5.773 Å, and c = 11.55Å, and the density which varies between 5.65 and 5.77 g cm^{-3} [27]. The crystal orientations have pronounced influences on the carrier concentration and averaged Na composition, affecting V_{OC} and, consequently, the solar cell's efficiency [26]. Despite this close structural resemblance to zinc-blende semiconductors, they have reduced optical band gaps, more than 50% smaller. Their anomalous band-gap downshift ΔE_g places these ternary chalcopyrites among the most potent known absorbers in the solar spectrum (e.g., linear absorption coefficient at ***hv*** =1.5 eV of 10^5, 10^4, and approx.10 cm^{-1} for $CuInSe_2$, GaAs, and Si, respectively) [28].

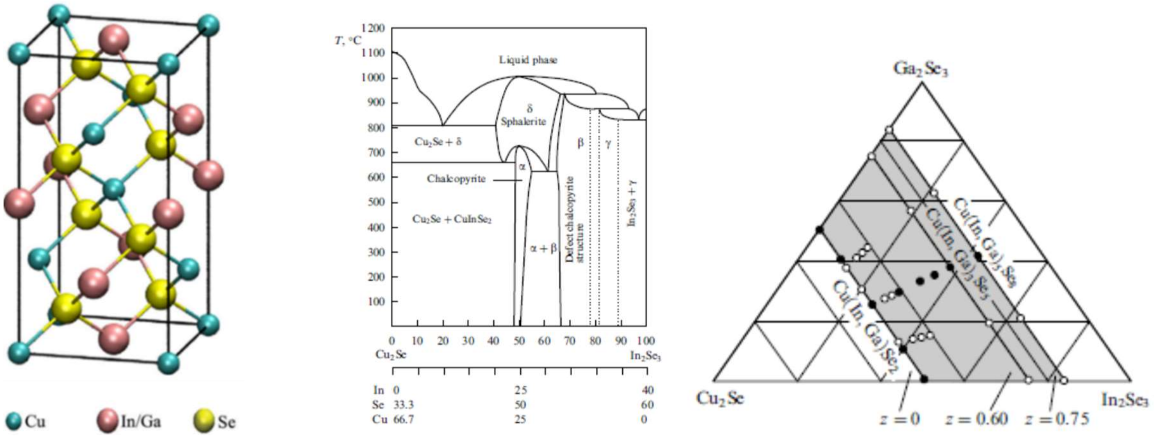

(a) (b) (c)

Figure 2. 5 *The crystal structure of a tetragonal chalcopyrite CIGSe unit cell with a lattice fixed ratio (c/a) approximating to 2 and any difference (known as tetragonal distortion, 2-c/a) resulting from different strengths of Cu–Se, In–Se, and Ga–Se bonds* [22], *(b) Phase diagram of the $Cu_2Se \pm In_2Se_3$ system, and (c) Pseudoternary diagram of Cu_2Se-In_2Se_3-Ga_2Se_3 system with the shaded region of $Cu_{1-z}(In_{1-x}Ga_x)_{1+z/3}Se_2$ existence* [27]

The phase diagram (Fig. 2.5 b) of the Cu_2Se-In_2Se_3 system shows the formation of CIS chalcopyrite structure (α) at stable temperatures (T) lower than 750 °C, which is a crucial phase for application in solar cells. There is a probable presence of sphalerite structure (δ) at T=750-1000 °C. Also, there can exist a defect chalcopyrite structure (β) at T below 950 °C caused by distributed arrays of defect pairs (Cu vacancies at V_{Cu} and In_{Cu} anti-sites), and the CIS melting temperature is around 990 °C [27]. However, the diffusion pattern does not always follow the connecting line between the Cu_2Se and In_2Se_3 pseudobinary system [29].

The pseudo-ternary phase diagrams of the Cu_2Se-In_2Se_3-Ga_2Se_3 system (Fig. 2.5 c) show the region of CIGSe existence (shaded area) [27] with reactions involving Cu_2Se and In_2Se_3 rendering a pseudobinary system, including the intermediate CIS phase [29]. The ternary system's diffusion path characteristically departs from the straight-line connecting path between the initial end members. It typically crosses the line to satisfy the mass balance. The diffusion path is invariant for steady-state conditions in an infinite system but changes with time in a finite system due to modification caused by interdiffusion [29].

The diffraction patterns of CIGSe films commonly exhibit the occurrence of peaks along (112), (220)/(204), and (116)/(312) directions, with the crystals generally having a (112) preferred orientation. An increase in (In, Ga) ratio may result in a decrease in (112) orientation and Cu/In+Ga (CGI) ratio and an associated increase in the (220/204) orientation [30]. This variation results in the grains becoming relatively more randomly oriented. The CIGSe-related peaks slightly shift to a higher 2θ value as the CGI value deviated from 1 (stoichiometric composition). The (112) preferred orientation peak of the CIGSe absorber also slightly shifts toward a higher diffraction angle with In/(In+Cu) ratio increases and a decrease of lattice constants a and c [31]. The stoichiometry of the ranges from Cu-poor (CGI <1) to Cu-rich (CGI > 1), with the optimal solar cells having the composition of CGI ~ 0.9 [32]. Careful consideration involves controlling the uniform composition distribution and solving challenges associated with Cu-poor composition for high-efficiency CIGSe solar cell [31].

During the growth process, the Cu-Se phase's presence is crucial to guarantee high-quality material with large grains, requiring high-performance devices. However, this Cu–Se phase is a degenerate p-type semiconductor and essentially controls the Cu-rich films' optoelectronic and surface properties. Their presence in the solar cell absorber is highly unfavorable, and the required final Cu-poor composition is necessary to prevent the segregation of these phases [33]. The Cu-poor composition, also known as ordered vacancy compound (OVC) at the absorber layer's surface, creates a suppressed homojunction and a downshift of the valence band maximum Fermi level [34]. Considering the Cu composition (≈ 0.35, 0.60, and 0.94), the existing different CIGSe phases (i) dominant OVC phases, (ii) coexistence of both OVC and chalcopyrite CIGSe, and (iii) dominant CIGSe phase [33].

The absorber layers' deposition processes using high temperatures enhance gallium diffusion towards the absorber/buffer interface, which probably produces better homogeneous gallium distribution within the absorber layer. The gallium accumulation at the molybdenum/absorber interface has a distinct impact on the solar cells' behavior and stability. However, gallium segregation towards the back-contact/absorber interface may introduce a gallium-depleted phase near the heterojunction, an unintentional gallium gradient in the chalcopyrite layer [35].

2.3.2 Morphology and composition

The morphology of the as-deposited CIG layer plays a crucial role in the resulting morphology and the overall quality of the final CIGSe film after selenization [36] in stoichiometric or copper-rich part of the film characterized by slightly large grains. In contrast, the crystallites on the (In, Ga)-rich part are noticeably smaller with different shapes [30]. The orientation relationship and structural similarity, as well as their relative diffusion and nucleation behavior, account for the development of the CIS dendritic morphology within the Cu_2Se matrix [37], and the precipitate of intergranular $Cu_{2-x}Se$ existing in the films with [Cu]/[In] > 1 [30]. The dendritic shape CIS phase formed within the Cu_2Se grains and at the grain boundaries show In as the active component in diffusion through Cu_2Se, following ionic lattice diffusion through the Cu vacancy sites of Cu_2Se the phase. The migrating path also shows the rapid transport of In in Cu_2Se, which yields the CIS product's precipitation within the Cu_2Se and the changing diffusion pathway signifying that the inter-diffusion reaction proceeds in a finite system which will be valuable in thin-film processing [37].

For sequential depositions, the uniformity of the composition and surface morphology of high-quality CIGSe thin films may depend on the precursors or the stacking method employed for the deposition. The surface morphology significantly influences surface roughness, so the CdS/CIGSe interface properties [38]. The different metallic precursors possess their separate diffusion properties and behavior under the influence of temperature, which affects the resulting depth profile of the Ga/(Ga+In) ratio and the resulting device performance. For sequential depositions, Cu layers reportedly have smooth morphology, with the layers deposited on the Cu layer influences the evolution of the films' final morphology [39]. Furthermore, overgrowing copper-rich material with an indium-rich top layer is necessary to achieve good quality material [30]. The Mo back-contact layer does not affect the morphology of the absorber layer, and the Ga segregation towards Mo improves the adhesion of the CIGSe films [39]. However, the structure of Mo controls the diffusion of Na into the absorber layer [40], and the presence of $NaInSe_2$ in the CIGSe structure modifies the film morphology, creating a preferred (112)-tetra orientation [41].

2.3.3 Optical properties

Several studies are dedicated to advanced bandgap engineering to control gallium and sulfur's spatial distribution in CIGSe to create a graded bandgap. The impact of the in-depth variation of the bandgap modeled using numerical simulations and some theoretical analysis has been verified experimentally on some graded solar cells [42].

The interference caused by multiple reflections within the CIGSe thin films causes the optical transmittance to increase predominantly between 1000-1400nm wavelengths and subsequently become stable at ~45% [31]. The calculation of the optical absorption coefficient (α) from the transmission (T) and reflection (R) data with the corresponding film thickness (d) allows for the estimation of the optical band gap (E_g) of these direct bandgap chalcopyrite compounds semiconductor [31]. The conventional CIS solar cell with a bandgap of 1.0 eV proves to be a low-optimal performance single-junction solar cell. However, the improvement of the bandgap with the partial substitution of In with Ga improves the bandgap to the ideal value ranging between 1.3 to 1.5 eV with approximate Ga composition (Ga/In+Ga) ratio between 0.4–0.75 and as well Ga improving adhesion by segregating to Mo back contact when $CuIn_xGa_{1-x}Se_2$ films [39].

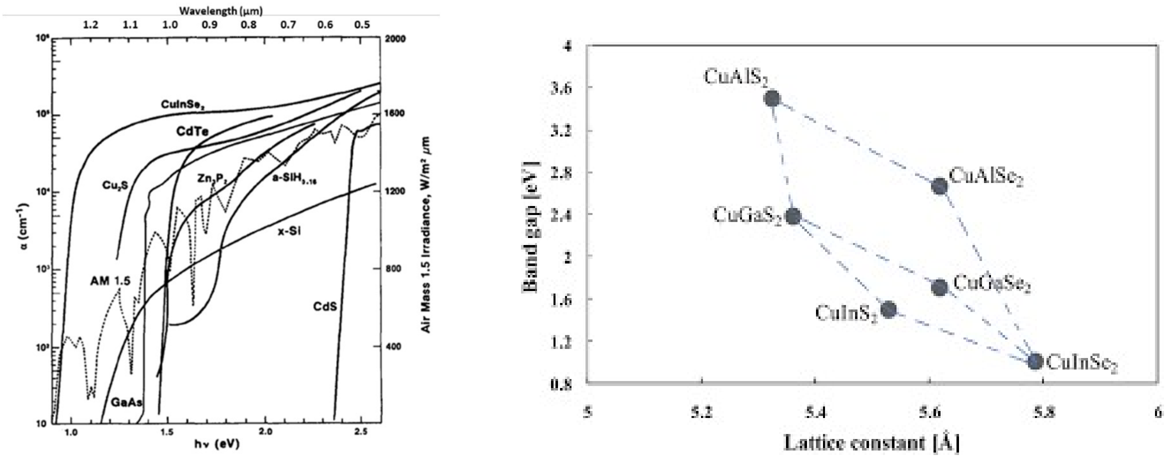

(a) (b)

Figure 2. 6 *The absorption spectrum of $CuInSe_2$ compared with other photovoltaic semiconductors compared to the solar emission spectrum for AM1.5(dashed line)* [43]. *(b) The bandgap as a function of lattice constant "a" of the $Cu(In, Ga, Al)(S, Se)_2$ alloy system with selenide based materials including a wide range of bandgap energies from 1.04 eV for $CuInSe_2$ to 2.7 eV for $CuAlSe_2$, and sulfide-based materials from 1.55 eV for $CuInS_2$ to 3.45 eV for $CuAlS_2$. The system incorporates a more significant part of the visible spectrum range* [22].

The theoretical bandgap can be estimated using the relation;

$$E_g = (1-x)E_g(CuInSe) + xE_g(CuGaSe) - bx(1-x) \qquad \textbf{(Eqn. 2. 9)}$$

$\boldsymbol{x}$ gives the gallium composition, and $\boldsymbol{b}$ is the bowing factor (ranging between 0.11eV and 0.25eV) taken to be 0.15 eV for CIGSe materials [44]. In the presence of sulfur, the estimated theoretical bandgap is;

$$E_g = 0.95 + 0.8x - 0.14x(1-x) + 0.7y - 0.05y(1-y) \qquad \textbf{(Eqn. 2. 10)}$$

where $\boldsymbol{x}$ is the Ga/(Ga+In) ratio, and $\boldsymbol{y}$ is the S/(S+Se) ratio [42].

Nevertheless, the record efficiencies in CIGSe solar cells possess an optimal bandgap of approximately 1.2eV. The Ga content, which can increase the bandgap to 1.45eV (optimal solar cell bandgap) [45], can also lead to more defects in the CuInSe lattice structure resulting in degradation of the solar cell.

The reduced bandgap's exact behavior less than the theoretical value when the bandgap reduces from 1.4 to 1.15 eV is due to the space charge region (SCR) in the solar cell. Also confirmed experimentally, it creates an increase in the open-circuit voltage concerning the case of solar cells where the CIGSe layer has a uniform bandgap of 1.15 eV [46]. The accumulation of Ga near the back-contact caused by the different reaction kinetics of In and Ga with Se results in lowering the bandgap in the SCR and V_{oc} of the solar cell [47]. Part of the proposed solution is the partial selenization of CIG precursor before annealing and sulfurization at a high temperature, forming a Ga's homogenous distribution. However, it increases the complexity and uncontrollability of the selenization process [42]. Another proposal to improve the Ga distribution is reducing the CIGSe absorber thickness, but reducing the absorber will decrease long-wavelength light absorption and short-circuit current (J_{sc}) [48]. The distribution of Ga, and thus the bandgap variation, is modified using various grading profile techniques.

Studies on the bandgap grading showed that it could reduce the recombination losses and increase the solar cell's carrier collection. The graded profile potentially broadens both the conduction band (C_B) and valence band (V_B) of the absorber layer, and that improves the carrier collection with an increased quasi-drift electrical field in the Space Charge Region (SCR) [49]. The grading profile can follow the standard pattern by gradually increasing the Ga content with a linear increase of the bandgap while linearly decreasing the electron affinity through the absorber [50]. This method allows the Ga concentration to produce a gradient in the electron affinity and a quasi-electrical field through the solar cell, associated with amplifying the electrons' diffusion length. The enhancement in the solar cell's efficiency in using this grading design comes from enhanced carrier collection and a decreased recombination rate, which increases the Open-Circuit Voltage (V_{OC}) of the cell due to a lower recombination saturation current in higher bandgap locations. However, the absorption position dependence causes the increasing bandgap to decrease the short-circuit current density steadily [49]. A reversal of the grading profile gradually reduces the bandgap, with an associated increase in the recombination rate but high V_{oc} due to broadened bandgap [51].

A combination of the grading profiles, either as doubly graded or multi-graded possible due to varying bandgap engineering techniques, allows for tuning the bandgap and improving solar cells' efficiency. Doubly graded profiles have the Ga content either decreasing from the front surface to an optimized minimum position and then increases to the back contact or vice versa, with both kinds of grading affecting the probability of carrier collection [52]. The optimized profile improves the carrier collection and the short-circuit current density and improves solar cell efficiency [53]. The Multi-graded bandgap structure delivers better performance than profiles with an improved V_{OC} and J_{SC}. Theoretically, the multi-graded profiles gave an efficiency of up to 19.83% and 18.8% for experimentally fabricated cells [53].

Using Raman spectroscopy, optical studies provide a non-contact monitoring method for the device layers, rendering information on the crystal structure, composition ratios, and phases [54]. The chalcopyrite structure possesses 24 modes of vibration, Γ_o (3 acoustic and 21 optical phonon branches), owing to the eight atoms, with each atom having three degrees of freedom. However, only 13 Raman active modes (Γ_{Raman}=A_1+$3B_1$+$3B_2$+6E) can be measured by Raman spectroscopy with optimized experimental conditions [55].

For the CIGSe compound, the most intense Raman peak at 175 cm^{-1} belongs to the A_1 (Γ_1) mode, which is related to two pairs of anion (Se) vibrations with Cu and In atoms at rest and exhibits the most energetic scattering intensity. It has the maximum intensity value at the ratio of Cu/In=1 and decreases rapidly with deviation from 1. The vibration of the anions occurs in the a-axis and the other in the b-axis [55]. Other Raman peaks at 213 cm^{-1} belong to the vibration mode E, while the peak near 232 cm^{-1} belongs to B_2 or E [56] and reaches a minimum near Cu/In = 1 [54].

With the partial substitution of In atoms with Ga, the Raman peaks shift linearly as a function of the Ga composition ratio, $\boldsymbol{x}$ expressed with the equation [57];

$$Raman\ shift\ (cm^{-1}) = ax + b \qquad \textbf{(Eqn. 2. 11)}$$

a = 13 [cm^{-1}/ratio], b = 175 [cm^{-1}] and the Raman peak positions of CIGSe thin films were blue-shifted linearly with increasing [Ga]/[In+Ga]. Increasing the x component from equation (2.11) increases A1(Γ1) frequency due to reducing oscillatory mass caused by replacing In atoms with Ga. CIS and Cu_xSe can coexist if Cu deposition is excessive and has a peak at 260 cm^{-1} for Cu-Se compounds [58].

The ordered vacancy compounds have the prominent Raman peak in the range 152 - 154 cm^{-1} attributed to the Se atoms' symmetric vibration in the lattice, and maybe a broad peak array in the higher frequency range of 225 – 250 cm^{-1} [59]. Moreover, since the crystal cations have fixed positions, the frequency depends totally on the anion mass [60].

2.3.4 Electrical properties

The Van Der Pauw technique is commonly used for the measurements of resistivity (ρ), hall mobility (μ_p), and carrier concentration (N_p) for semiconducting materials [61]. The [Cu]/[In] ratio strongly influences the electrical properties. It shows that N_p increases with the increase of

Cu/(In+Ga) at%, which is related to increased carrier concentration for stoichiometric CIGSe films with a possibility of higher ρ and lower N_p for Cu-poor films due to the absence of metal-like $Cu_{2-x}Se$ phase [62].

The broadening of the bandgap due to gallium inclusion in the gallium-rich phase causes an upward shift in the conduction-band minimum. It represents a potential barrier for injected electrons, which tend to recombine at the back contact. Consequently, the accumulation acts as a passivation layer, which reduces the recombination of electrons, thereby increasing V_{oc} and suppressing phototransistor effects. A barrier towards back-contact also reduces hole-transport to SCR caused by depletion of holes at the back-contact, leading to blocking of forward-current in the dark [35].

The improvement in device efficiency by incorporation of the lighter alkali metals (Na, K) is by the increase in V_{oc}, which can be estimated using the relation [63];

$$\Delta V_{oc} = \frac{2k_BT}{e} In\sqrt{\frac{N_a}{N_{ao}}} \qquad \textbf{(Eqn. 2. 12)}$$

with k_B being the Boltzmann constant, e the elemental charge, T the temperature, and the doping concentrations N_a and N_{ao}. The inclusion of heavier atoms displaces the lighter atoms during alkali atom causes a potential reduction in the V_{oc} [64]. However, a recovery of the V_{oc} is possible after a long treatment or annealing at a higher temperature, which creates the lighter alkali metals (Na, K) with the heavier ones [64,65]. The observed gain in the V_{oc} which estimated with the relation [64];

$$\Delta V_{oc} \leq \frac{k_BT}{e} In\frac{N_t}{N_{noPDT}} \qquad \textbf{(Eqn. 2. 13)}$$

for the sample with PDT after a duration, ***t*** comes from a combination of a reduced recombination rate in the bulk of the absorber layer and a reduced interface recombination velocity [66].

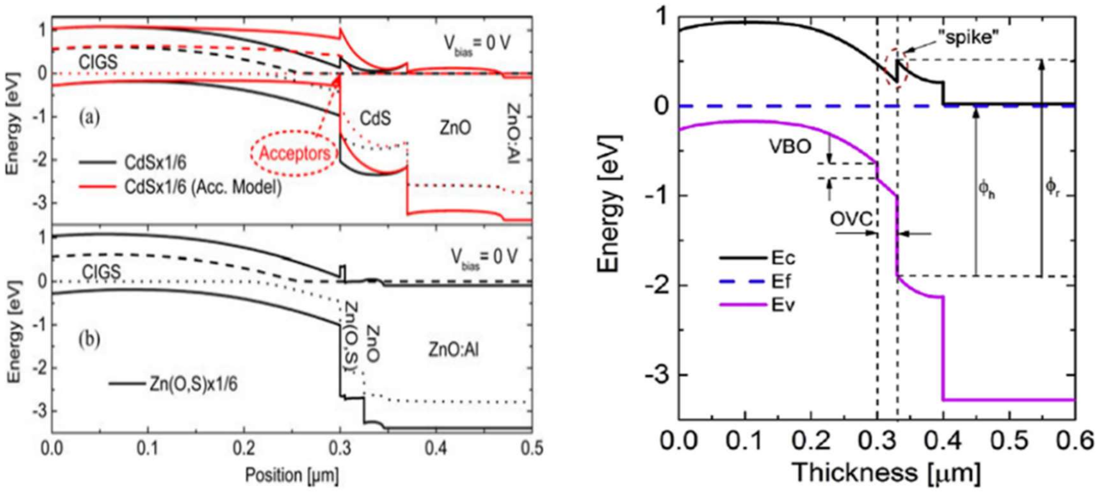

(a) (b)

Figure 2. 7 *Band diagrams of the three SCAPS models with 0.3 µm thick absorber layers. (a) the CdS models with and without interface acceptors and the Zn(O, S) model where the dashed and dotted lines show the quasi-Fermi levels of electrons and holes* [67]*, (b) with a 10 nm thick OVC layer The conduction band alignment at the OVC/CdS interface represented as a "spike." VBO, φ_h, and φ_r represent the valence band offset between the CIGSe and OVC layers, the potential hole barrier, and the recombination barrier at the OVC/buffer interface, respectively* [68]

In a standard 1.6 µm thick CIGSe device, the V_{oc} and FF values can increase with reduced thickness (to about half of its standard value) [67]. Beyond which, there is a significant decrease in V_{oc} and FF. However, there is an associated steady loss in J_{sc} while reducing the CIGSe thickness associated with a decrease in spectral response, especially at long wavelengths [67]. Also, there is a limitation to the device V_{oc} due to recombination in the CIGSe layer. The presence of alkali metals at the surface of CIGSe films creates the OVC layer's presence between the absorber and buffer layers. The OVC layer's introduction produces a positive downward-shifted valence band at the CIGSe surface [68].

The positive valence band offset (VBO) increases both φ_h and φ_r making the OVC layer inverted (Fig. 2.7), thereby reducing the hole concentration at the absorber/buffer interface and forming a buried electronic junction away from the interface. The reduced recombination in the space charge region (SCR) and the interface causes the minority-carrier electrons generated within the bulk CIGSe to become majority carriers in the buffer layer's neighborhood. The increased V_{oc} is primarily attributed to significantly reduced interface recombination [69]. The thickness of the OVC layer to an optimal is crucial since its increase increases V_{oc} due to the contributions generated by electron-hole pairs. A very thin layer causes the contribution of the OVC layer to the total generation to be lower. Beyond an optimal thickness, it becomes too thick. It starts to reduce the carrier collection from the CIGSe bulk due to the reduced band bending within the SCR, leading to a reduction in the device's efficiency [68].

Table 2. 1 *J-V parameter from measurements of substandard CIGSe device (0.3 µm) simulations with the same parameters with* [68] *and without* [67] *OVC layers*

	V_{oc} *(mV)*	J_{sc} *(mA/cm^2)*	*FF (%)*	*Efficiency, η (%)*	*Ref.*
CIGSe (without OVC)	672	16.7	74.6	8.3	[67]
CIGSe (with OVC)	666	20.1	76.0	10.2	[68]

A comparison of the J-V parameters of two simulated devices with the same parameters (Table 2.1) showed an increase in the CIGSe device's efficiency with an OVC layer due to J_{sc} and FF's increases, although the V_{oc} reduced.

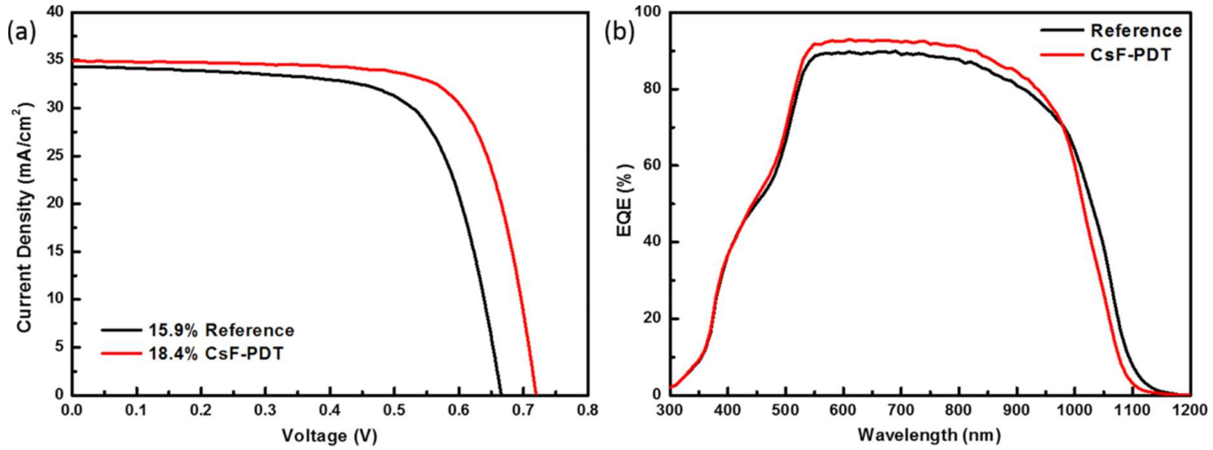

Figure 2. 8 *(a) Current–Voltage (J–V) characterization. (b) External quantum efficiency (EQE) spectra of CIGSe solar cells with and without CsF-PDT* [65].

A comparison of the J–V characterization and EQE (Fig. 2.8) showed some increment in the power conversion efficiency (PCE) to the reference device after alkali treatment. The sample exhibits higher EQE values in the 550–1000 nm region attributed to active charge collection nearly throughout the absorber layer. However, excess of the alkali metals severely degrades the FF of the devices [65].

2.3.5 Selenization and sulfurization

The different elements in the absorber layer diffuse in different directions during selenization/sulfurization. Cu and Ga diffuse out from the bulk to its surface of CIGSSe in the metallic element diffusion, with the diffusion of Cu being speedy compared to Ga during the reaction and leaving Ga's distribution at the bottom interface. Elemental S and Se, introduced as gas phase, diffuse into the bulk through the grain boundaries and the bulk with S supplied at the final phases of sequential processing residing typically at the surface [70].

During selenization, the Se atoms preferentially react with In, which could be due to the lower reaction energy of In than Ga. The average size of the CIG precursor grains before selenization significantly influences the thin-film characteristics [31]. The formation of a tiny layer of a nearly ideal ohmic contact $MoSe_2$ between Mo and CIGSe, influenced by the density of the Mo layer [71], with a bandgap of (1.41 eV), which is broader than that of the CIGSe absorber and as such forms a back-surface field (BSF) that can suppress the recombination of electrons and holes [72]. Similarly, the formation of MoS_2 has even a wider bandgap of 1.69 eV.

The presence and grading of sulfur (S) within the absorber layer influence the solar cell's valence and conduction bands [73]. The introduction of sulfur, usually in the final step of deposition, widens the effective bandgap at the space charge region (SCR) and leads to a sulfur-rich layer in the surface region. However, the bulk of the absorber, which controls photocurrent collection, remains virtually unaffected; this incorporation reduces the non-radiative recombination rate in the SCR, controls the devices' V_{oc}. So, the ideality factors appear to reduce for a front-grading with sulfur incorporation [35]. The layer of MoS_2 reportedly improves the V_{oc} of CIGSe solar cells by about 50 mV because of reduced leaky behavior and recombination occurring at the CIGSe/Mo interface [47]. The improvement on the V_{oc} could be due to band alignment modification, which appears to be wider than $MoSe_2$ by approximately 0.2 eV [74]. With Mo/MoS_2 having a conduction band offset at the interface being more significant than that of the Mo/$MoSe_2$, that reportedly helps to repel electrons and consequently reduce the recombination at the CIGSe and Mo interface [75]. The presence of a small quantity of sulfur also helps in surface passivation. However, the passivation appears limited due to a defect density of CIGSe known to increase with S content increases [73]. However, the formation of MoS_2 does not significantly affect the microstructure of CIGSe films [75], and excess and uncontrolled S incorporation can cause poor device performance [76].

2.3.6 Surface treatments and annihilation of defects

The microstructural features such as point defects significantly govern the electronic performance of materials, including the CIGSe devices [77]. The presence of defects, which may form part of larger defect complexes in the crystals, largely depends on the energetics of the vacancies and the interstitials within the structure and favors the defects with lower formation energy out of the different possible paths [37]. The common types of defects in ionic crystals are (1) cation and anion vacancies (Schottky pairs) and (2) cation vacancies and interstitial cations (Frenkel pairs) [39]. In the CIGSe structures, these defects include three vacancies, three interstitials, and six antisites [37]. The transport mechanism for each elemental component varies depending on the stoichiometry and temperature [77]. The defects usually lead to intrinsic doping and formation of trap levels in the absorber layer, Fermi level pinning, acting as recombination centers, and limiting the device performance [78]. However, the recombination occurring through these defects under normal conditions suppresses certain saturated conditions and suitable conduction band alignment at the heterointerface [79].

These defects' studies are mainly theoretical models, primarily employing the first-principles calculations within density functional theory [77]. However, some experimental results exist to corroborate the theoretical results [37].

Both copper vacancies (V_{Cu}) and interstitials (Cu_i) can coexist and mediate mass transport in the material, with V_{Cu} and Cu_i having lower migration barriers [80] and a high probability of forming deep-donor defect In_{Cu} in the extremely Cu-poor growth process [37]. Concerning the thermal activation energies, selenium appears to diffuse faster than indium but second to copper via dumbbells and more favorable under Se-rich conditions. Similar mass transport mechanisms exit for Se-poor conditions. However, the preferred mechanism does not depend on temperature [80], and selenium-related defects can create transition levels within the bandgap [81]. The ease of diffusion of V_{Cu}, Cu_i, and Se dumbbell depends primarily on their low migration barriers. The lesser concentrations of indium vacancies (V_{in}) and interstitials (In_i) are due to their high formation energies. They tend to occupy a nearest-neighbor copper site, which has a lesser energy barrier than replacing another indium site, which does not add to long-range mass transport [80]. The In_{Cu} appears to be a shallow donor, while Ga_{Cu} is a deep donor, and shallow V_{Cu} acceptors compensate both [78]. The Ga_{Cu} electron traps also add to the dominant intrinsic recombination centers, and high-gallium in CIGSe, above approximately 50% gallium, constitutes a minority carrier trap [78].

The presence of other defects in the CIGSe devices, such as exhibition of a shallow defect contribution with an activation energy $E_A \approx 100$ meV known as the N_1 defect, in order to distinguish it from more profound defect state contribution, N_2, with an activation energy $E_A \approx$ 250– 300 meV also continues interest from many researchers [82].

The alkali metal distribution in CIGSe is not homogenous, independent of the alkali metals used, and their concentration at grain boundaries is much higher than that inside the grains [83], while the concept of the immiscibility of phases (spinodal decomposition) explains the secondary phase formation with alkali atoms. The alkali atoms can occupy some vacancies but never fully become a part of the CIGSe compound. The type of binary or ternary alkali metal compounds formed during the chalcopyrite layer processing is dependent on the kinetics and the Gibbs function G(x, T) of the defined equilibria. The quantification of their reactions uses the Gibbs energy of mixing, ΔG_{mix}, to measure the spontaneity of a reaction to so-called critical temperature T_c, the lowest required temperature for a phase formation [83].

Exothermic reactions with a negative enthalpy allow for Cu's substitution by alkali atoms in a spontaneous reaction. A reversal endothermic reaction to displace the alkali metal by Cu will require a positive enthalpy and no longer a spontaneous process due to higher energy requirements. It is therefore easier to form $AInSe_2$ from $CuInSe_2$ (A= an alkali atom) than to regenerate $CuInSe_2$ once $AInSe_2$ has formed [83]. Na's presence within the CIGSe layer reduces Cu mass transport due to the occupation of V_{Cu} by Na_{Cu} defects; it impedes V_{Cu}-related cluster formation, leading to quantifiable effects on defect distribution within the material [84].

The heavier alkali atoms significantly reduce the number of deep donor-like defects (e.g., V_{Se}, In_{Cu}) and deep-level acceptor-like defects (e.g., V_{In}, Cu_{In}). These effects that the heavy atoms passivates point defects in CIGSe and modify their electrical environments by increasing the energy level of V_{Cu} [65]. Other surface treatment, using KCN removes the excess copper selenide content responsible for this quasi-epitaxial overgrowth [85].

2.3.7 Effects of alkali metals on the absorber layer - a review

The presence of alkali metals initially reported by Hedstrom et al. emphasized the beneficial effects of sodium (Na) on the grain growth of CIGSe thin-films and the improvement of V_{oc} and solar cell efficiency for cells fabricated on soda-lime glasses [86]. The report spurred increasing studies on the effects of various alkali species on CIGSe thin-film solar cells. According to some reports, alkali metals' presence passivates defects at grain boundaries, eliminating photocurrent hysteresis effects [87], and the passivation tends to reduce non-radiative recombination, thereby improve device efficiencies [88]. The soda-lime glasses (SLG) used as the substrate for fabricating solar cells serve as the conventional source for adding about 10 % sodium concentration reported for improving the efficiency of the solar cells [89]. However, the conventional methods for incorporation of alkali metals to CIGSe absorber layers are (i) pre-deposition from the substrates or a thin layer of alkali fluoride before absorber layer deposition [90], (ii) co-evaporation within the stages of deposition [91], and (iii) post-deposition as alkali fluorides [92]. Whereas pre-incorporation and co-evaporation methods can efficiently add Na and K to the CIGSe layers, the heavier alkali metals usually employ post-deposition techniques. Subsequently, post-deposition treatments (PDT) of the as-grown absorber commonly serve as the method of depositing thin layers of alkali metals, usually as fluorides. They have been a valid path to supply other alkali species aside from Na diffusing from the SLG substrate. The process creates several effects, including modifications in the surface composition and alkali content throughout the film, a shift in CIGSe absorber layer parameters, and the potential to apply a reduced minimal thickness of the CdS buffer layer [93].

Some studies also report the combination of alkali metals during PDT to harness the seemingly different benefits for improving the solar cells, which tends to report higher efficiencies than single alkali metal [94]. The lithium (Li) choice is not typical for the alkali metal inclusion for solar cell improvements. The reason may stem from Li is not being a component of soda-lime glass commonly used for solar cell fabrications. Although it reportedly has some improvement over alkali-free solar cells, its result is not as good as Na's application. It is not very useful for achieving improvement in the carrier concentration, and the desired effects on the CIGSe layer are less pronounced compared with the Na application [95]. The properties of Li may also impair the performance of CIGSe solar cells [96]. Consequently, most of the studies for high efficiencies of

CIGSe solar cells employ the alkali-metal heavier than Na during PDT, which promises to boost the device performance.

The presence of alkali metals within the bulk of the absorber layer has varying effects that improve the CIGSe layer's properties (especially the charge carrier potentials) and at the surface to improve the interface with the buffer layer. The different alkali metals yield some unique and shared effects for alkali elements on absorbers. The relative weights of the atoms, light (Na and Li) and heavy (Rb and Cs), also affect the properties of the CIGSe absorber layer through different types of processes [97] and have different drifting properties [98]. While Na and K improve, among other things, the electrical properties of the CIGSe absorber layer, the improvement by the heavier alkali metals is primarily due to the passivation of the interface with the buffer layer [99]. Whereas the light alkali metal atoms may act as impurities at the grain boundaries, the heavier (Cs and Rb) atoms might have more definite tendencies to form secondary phases ($RbInSe_2$ and $CsInSe_2$) at grain boundaries or close to the surface [97], which helps to reduce surface recombination. K laying in between alkali metals' position gives it the tendency to adopt either of both roles partially [27].

Some instances of surface passivation include the formation of intermediate layers (e.g., KIn_xSe_y) [100] or the creation of a suppressed PN homojunction heightened by either the Cd_{Cu} replacement [101]. Another potential effect is the possible Cu-depletion of the absorber layer surface, leading to band-bending and creating a higher potential barrier for holes to recombine at the interface [102]. The depletion of Cu or Ga at the absorber layer's top surface appears to be the reason for improving junction properties [103] with potential redistribution effects due to temperature [104]. The Cu depletion at the grain boundaries proposedly causes a lower valence band edge and leads to a reduction of hole concentration at the boundaries [105].

The considerable reduction of typical high surface recombination velocity observed at the surfaces and interfaces using passivation layers prevents charge carriers from getting trapped by surface or interface electronic defects. However, the passivation layers have some required micron-sized openings, which allow the transport of the photo-generated charge carriers toward the external circuit. Consequently, the absorber surface's passivation, reducing defective junction area to a minimum, promises an approach to increase the devices' efficiency [106].

Suitable surface treatment of the alkali-fluoride PDT may be essential before the deposition of buffer layers to remove soluble salts from the CIGSe surface or etch away the alkali-In-Se abundant surface phases [107]. These salts' presence may lead to some current blocking J-V behavior at the interface with the buffer layer, and the removal creates a reportedly significant diode quality improvement. However, completely etching away the alkali-modified surfaces causes a complete loss of the beneficial effects [107].

2.2.7.1 Influence of lighter alkali (Na and K) atoms

Sodium (Na) 's beneficial effects on device performance are primarily due to recombination defects' passivation. Its presence and varying composition due to doping affect the absorber layers' microstructure, optical properties, and electrical properties. Proper adjustments of the Na concentration can enhance the grain growth and improve thin films' crystalline and electrical conductivity [108]. The Na atoms usually migrate along the grain boundaries and accumulate at the interface to form intermediate products (Na_2O_x or Na_2Se_x) or form point defects (Na_{Cu}) at high temperatures [109], increasing the concentration of V_{Cu} acceptors [110].

They improve the V_{oc} by increasing the net acceptor concentration and decreasing resistivity [111] and increase the free carrier concentration by reducing the number of In_{Cu}^{2+} (or Ga_{Cu}^{2+}) donor-like defects [112]. The enhancement of the morphology, usually by increasing the grain size, reduces defect, leading to increased mobility and effective coalescence while reducing the hillock-like defects [113]. Wei et al. [41] theoretically reported Na's influence in the $CuInSe_2$ structure, with a small concentration of Na replacing In_{Cu} antisite defects, increasing carrier concentration. However, as the Na concentration rises to the level of replacing most of the In_{Cu} defects, it starts to remove the acceptor (Cu vacancy), thereby decreasing the carrier concentration and thus the hole density.

The averaged Na increases with an increase in the I(220/204)/I(112) ratio because of the decrease in CIGSe grain size, which influences the usual location of Na at the grain boundaries to an optimal beneficial value [26]. Thus, the optimal I(220/204)/I(112) ratio of the CIGSe film gives rise to the highest carrier concentration for high V_{OC} of the device [26].

The use of potassium (K) serves as an alternative or complement to Na in the solar cells. The application through potassium fluoride (KF) PDT, or the alternatively proposed so-called IKF-

PDT, which involves additional evaporation of indium during the treatment [100], serves as a primary source of K that enabled the fabrication of CIGSe thin-film solar cells on flexible substrates [101]. However, IKF-PDT releases detrimental elemental Se due to the CIGSe surface reaction, responsible for the FF losses with standard KF-PDT [100].

Similar to the effects of Na, the presence of K during PDT influences several bulk properties, including alkali distribution [114], the net doping [115], and minority carrier lifetime of charges [63]. It creates an increase in the open-circuit voltage (V_{oc}), the fill factor (FF) values, and the short-circuit current density (J_{sc}) [116]. The presence of K may also create some passivation of defects and grain boundaries [115]. It influences several bulk properties, such as a decrease in the interface recombination with the CdS layers, which in turn results in enhancement of CIGSe devices performance [103], minority carrier lifetime [115], alkali distribution [114], and the net doping [115].

The surface modification improves diode quality with the buffer layer. During KF-PDT, it produces a copper-depleted surface region in a depth of approximately 0–30 nm [115], which supposedly reduces the CIGSe valence band maximum near the surface [34] due to less repulsion between selenium p- and copper d-orbitals [28]. The lowering of the CIGSe valence band maximum at the surface due to copper depletion results in less recombination near the CIGSe/buffer interface due to lower hole concentration [102]. Another proposal is to form a K-In-Se abundant surface phase that passivates the CIGSe surface or the formation of $CdInS_2$ during CdS deposition using the chemical bath deposition (CBD) technique, which also yields beneficial interface properties [100]. An increase in the concentration of K at the surface supposedly changes the properties of the surficial layer. It enhances the diffusion of Cd atoms into the absorber, which is favorable to the formation of Cd_{Cu} during the subsequent fabrication of the device. Furthermore, the supposed increase of the Cd_{Cu} level leads to the change of band structure and enhancing p-n junction [103]. These modifications allow for thinner CdS buffer layers, which presents a minor optical loss and reduced parasitic light absorption with excellent device efficiencies [93,99].

Nicoara et al. [117] reported a resulting increase in the work function for CIGSe and CIGSe/CdS after KF-PDT due to the difference in charge carrier concentration, which causes a change in the Fermi level, a different band bending through different surface defects or surface charging, among other effects. Other causative effects include a surface dipole due to a change in electron affinity, a bandgap widening, and different surface material through a direct change in the work function.

However, K's introduction can lead to Na's replacement and a significant increase of K at the top surface in the CIGSe layer due to the ion-exchange mechanism of alkali elements; thus, K repelling Na adjusts the hole concentration [103]. Furthermore, K's use has permitted high-performing CIGSe devices on flexible substrates [101].

2.2.7.2 Influence of more massive (Cs and Rb) atoms

The application of alkali PDT shows an improvement in the carrier lifetime of the bulk, which tends to improve with the heaviness of the alkali metals (no alkali < K < heavy alkali atoms) [118]. This improvement is due to the modification of grain interior by K [119] and passivated grain boundary defects in the SCR and the bulk material [118]. Moreover, alkali metals' combination reportedly exhibits longer carrier lifetimes than a single alkali metal [118].

The mechanism for positive effects of Rb at the CIGSe surface is either bulk- or grain-boundary-induced effect, and in some cases, both. Through the so-called ion exchange mechanism, the introduction of heavier alkali elements through PDT displaces the lighter alkalis (i.e., Na and K), which may be present in the material, especially at the grain boundaries [92]. Rb's effects show a strong dependence on the GGI value in the CIGSe film, and the effect of elemental Rb on CIGSe seems closer to elemental K than Na. Post-deposition incorporation concentrates on the grain boundaries and the dislocation defects in the CIGSe grain interior, suggesting a modification of the structural and electrical properties of CIGSe at the CIGSe/CdS interface [120].

After PDT with Rb, Hauschild et al. [121] reported that the absorber band edges shift downward while the surface band gap remains relatively constant. There is an additional downward band bending at the CIGSe/CdS interface, which accounts for the reduced interface recombination after PDT of chalcopyrite surfaces.

The use of cesium (Cs) for PDT, like other alkali metals, boosts V_{OC} and J_{SC} in CIGSe [109], with a record efficiency of 22.9% [122] and 23.35% [13] for the CIGSe thin-film solar cells. It shares several features similar to Rb, as a heavy alkali metal, displacing the lighter alkalis already present in the material (Na and K) [123]. Surface treatment with Cs supposedly produces a Cs-contained compound at the grain-boundaries, with a Cu-deficient grain surface surrounded by Na [124]. That causes a possible grain boundary reconstruction mechanism on the CIGSe thin films.

Cs possess a relatively higher ionic radius and high formation energy of Cs_{Cu}, reducing the possibility of substituting the Cu vacancies [97,124]. It, however, has a more potent chemical affinity to In and Se and displaces Cu. Thus, the more significant Cs ion migrates toward the grain boundaries due to its loose atomics arrangement and relatively low chemical potential, staying on the grain surface and creating a "grain boundary segregation." Subsequent displacement of Cu by the Cs atoms, causing Cu-deficient grain surfaces, leads to $CsInSe_2$ or Cs-In(Ga)-Se compound at the grain boundaries with In, Ga, and Se [124]. Also, the relatively low enthalpies of the alkali-$InSe_2$ compounds can account for their abilities to displace Cu [97]. With Cs' presence at the grain surface, the deposition of CdS can lead to the formation of $Cd(In, Ga)_x(S, Se)_y$ layer as a result of Cd and S diffusing into the Cs-induced grain surface.

The improvement due to Cs-induced grain boundaries effectively reduces the recombination at the interface and the SCR region, thereby substantially causing a long carrier lifetime at the junction area [124]. The more prominent Cs-contained grain boundaries act as a significant barrier to block the outflow of Na. However, thermal activation can cause Cs-induced depletion and thermally activated flow of Na [124].

The different deposition techniques used for alkali metal incorporation aim at minimal and possible avoidance of including impurities during the process, providing a percentage of alkali concentration that reportedly improves solar cells' efficiency [89]. The stage of deposition, pre-deposition [90], co-evaporation [32], and post-deposition [86], during device fabrication, can serve to distinguish the methods for alkali deposition. This study adopts the post-deposition technique in a non-vacuum environment to deposit the heavier alkali metals on the CIGSe layer.

2.4 Buffer layer

Among many cadmium sulfide applications (CdS), it is commonly employed as buffer layer material for high-efficiency CIGSe solar cells, grown commonly by the so-called chemical bath deposition (CBD) technique. Some techniques for the thin film deposition with varying structural, electrical, and optical properties include [125]; RF sputtering, pulsed DC magnetron sputtering (PDCMS), close space sublimation (CSS), spray pyrolysis, metalorganic vapor phase epitaxy, thermal evaporation, chemical vapor deposition, close space vapor transport (CSVT), and molecular beam epitaxy. The resulting properties of the CdS layer influence the CIGSe/buffer interface plays a crucial role in the recombination, interdiffusion, and formation of the p-n junction for the CIGSe solar cell parameters [126]. The Cd-free high-efficiency solar cells employ the deposition of buffer layers of other materials, typically Zn(O, S) [13] and double buffer layers, e.g., $Zn(O, S, OH)_x/Zn_{0.8}Mg_{0.2}O$ as alternatives to the conventional CdS buffer layer [13].

Comparatively, the CdS films can possess a hexagonally oriented crystalline structure with columnar grain growth or possess a cubic structure showing small grainy crystallite, depending on the deposition technique employed [127]. Sputtering techniques tend to produce a faster deposition rate than CBD with better uniformity and slightly varying optical bandgap between the films produced with different techniques. The sputtered films exhibited a higher refractive index and slightly higher absorption with optimized sputtering conditions and temperature, suggesting increased grain size, increased density, and enhanced crystallinity compared to the CBD films [127]. Nevertheless, a chemical bath's CdS buffer layer shows suitable band alignment and interface quality with CIGSe [106]. The potential for the formation of other beneficial phases can add to the endearing of the CBD method.

The nature of the surface (e.g., lattice properties, polarity, orientation) influences the buffer layer's uniformity and coverage. It presents the bonding partners and different surface energies of CIGSe grains with different orientations [126]. The buffer layer's crystal structure and the resulting lattice mismatch on different CIGSe planes determine the possible growth of epitaxial, polycrystalline, amorphous, or nanocrystalline structures. The (220/204)-oriented CIGSe absorbers with optimal I(220/204)/I(112)ratio (~ 1.8) allow more Cd atoms to diffuse into absorber surfaces to form a favorable p/n homojunction but causes a decrease in V_{OC} above this value due probably from excess Cd-doping. It also accounts for the increase in the carrier concentration resulting from p/n homojunction quality (more Cd diffusing into absorbers). However, excess leads to decreased carrier concentration, too small CIGSe size, and excess Cd- doping into the CIGSe surface. Consequently, the orientation of the crystals in the CIGSe absorbers greatly influences the cell performance, particularly the V_{OC} [26]

Nonetheless, the Zn (O, S) performance is susceptible to the CIGSe surface chemistry before buffer layer deposition with ALD. The sensitivity is not as pronounced for CBD-grown CdS buffer layers, probably because the CBD solution modifies the CIGSe-alkali surface during the CBD growth nucleation [107] and potentially forms other phases [13]. The presence of low surface energy for the {112} CIGSe surface [128] and the type of atoms (Cu/In/Ga or Se) serve as bonding associates for Zn(O, S) and CdS. The type of nucleation at the CIGSe surface after reconstruction considerably influences the final CBD buffer layer's growth behavior and density [126].

Some significant differences exist between CdS and Zn(O, S) growth from solution in terms of growth kinetics and a difference in the solubility products between the corresponding hydroxides and sulfides, resulting in a high amount of $Zn(OH)_2$ in the Zn-containing buffer, compared with $Cd(OH)_2$ in CdS [126].

The presence of thin alkali fluoride layers on CIGSe, usually after PDT, causes a modification of the surface. There is an apparent majority dissolution of the present alkali metals in the CBD [129]. The presumed promoted ion-exchange processes that occur during the early stages of the chemical bath may increase buffer transparency in corresponding solar cell devices without compromising a high-quality interface, thereby preventing open-circuit voltage losses. Also, there could be a formation of alkali-In-Se type compounds and a graded Cd-In-(O, OH, S, Se) mixed layer during the initial phase of the CBD-CdS process. The subsequent more transparent buffer layer produces a substantial reduction of parasitic absorption by employing thinner buffer layers and improves the short-circuit current, which is one of the significant advantages of incorporating heavy alkali PDT [130]. At the interface, the alkali metal presence also enhances the diffusion of Cd atoms into the absorber. It is favorable to the formation of Cd_{Cu} during the subsequent fabrication of devices. The Cd_{Cu} level increase supposedly led to band structure change and improved p-n junction [103]. The reported large offsets in the valence and conduction band at the interface between the suggested alkali– induced alkali-In-Se – type surface species and the CIGSe absorber tend to limit charge carriers' transport and, consequently, recombination [131].

2.5 Back-contact

The choice of a suitable back-contact electrode for charge collection essentially requires a material with very low resistivity, high reflectivity, and excellent homogeneity. It should possess chemical inertness to the elements deposited above it. Among the several highly conducting metals with potentials for a back-contact electrode for CIGSe solar cell, molybdenum (Mo) is the promising material to serve as the ohmic contact for the high-efficient chalcopyrite solar cell [40].

Mo possesses a good chemically stability to the CIGSe absorber with a thermal expansion coefficient (5.8×10^{-6} K^{-1}) near to CISe (9.5×10^{-6} K^{-1}) and a relatively high melting point [40].

Mo's desirable attributes include relative stability at the processing temperature, resistance to alloying (with copper and indium), and strong bonding with the glass surface, making it reliable adhesion to substrates [132]. The Mo film also acts as a reflective layer in the CIGSe solar cells. In tandem cells, CIGSe HTM films adjacent to the back-contact layer enhance the function of Mo's back metal-electrode contact material as an optical reflector.

Like other thin-film materials, the deposition technique and parameters considerably influence the Mo layer [40]. Some techniques for Mo deposition include low-pressure chemical vapor deposition (LPCVD), electrodeposition, chemical vapor deposition (CVD), pulsed laser deposition, atomic layer deposition (ALD), sputtering. The Mo layer also acts as a diffusion barrier to substrates' elements moving into the absorber layer from the substrates or any sub-layer [8]. The film's density, crystallite size, number of crystallites per unit area, and dislocation density significantly influence the barrier's efficacy [133].

During selenization, Mo tends to form molybdenum-diselenide ($MoSe_2$) film, significantly affecting the Mo/CIGSe interface [134]. It also forms MoO_x in the presence of oxygen. The thickness of the $MoSe_2$ film increased with a higher annealing temperature (>550 ◦C). However, the $MoSe_2$ film's characteristics rely on the technique for CIGSe deposition and annealing conditions since the $MoSe_2$ film does not form under copper-rich conditions [90].

2.6 Window layer

The suitable window layers for high-efficient solar cells constitute materials with larger bandgaps (>3.3 eV) and high lateral conductance, typically transparent conducting oxides (TCO), which allow for the transference of photo-generated current to the electrical contacts without significant losses.

Conventional TCOs (e.g., In_2O_3: Sn-ITO; SnO_2: F-FTO; and ZnO: Al-ZnO) suffer from inherent transparency loss, which reduces the photons reaching the bottom cell, especially in tandem cells [135]. The use of a relatively thin layer of the TCO for small-scale devices, aided by metal grids, can help moderate the TCO's parasitic absorption. However, that might not be useful for upscaled larger modules since the thicker TCO electrode is required to decrease the resistive loss due to the lateral transportation of the current through the TCO. The parasitic absorption resulting from the thicker TCO is quite severe and limits the potential for high efficiency. To improve the TCO layer's transparency without conceding conductivity, a high-mobility TCO is desirable since the conductivity of TCOs depends on the carrier concentration and mobility [135].

For the CIGSe solar cells, the commonly used aluminum-doped zinc oxide (AZO) film serves as the TCO layer for the devices. Indium tin oxide (ITO) possesses some desirable properties, including less thickness-dependent resistivity. However, indium-associated health risks due to toxicity and the potential high cost have made indium tin oxide (ITO) films a less desirable choice. ITO is also not ideal for low thermal budget fabrication, more flexibility, and stability against stretching and bending forces [136]. Also, fluorine volatility significantly hampers the number of ways for depositing fluorine tin oxide (FTO). The choice of doping with aluminum among the other group III elements (Al, Ga, and In) is due primarily to its low raw material cost and comparable electrical and optical properties to ITO [137].

Several techniques for depositing AZO thin films [136] aim at low-temperature growth, industrial applicability, relatively excellent uniformity, and reproducibility. The reported resistivity values of AZO films for TCO solar cell applications range between 1×10^{-4} to 10 Ω cm with the lower resistivity values attained with some post-deposition treatment, usually by annealing at elevated temperatures up to 500°C [136]. The deposition methods and post-deposition affect the structure and morphology of the films. Aluminum (Al) concentrations for doping ZnO range between 1 and 3 at%, reportedly affecting the electrical, optical, and morphological properties [138].

The presence of a thin layer of intrinsic ZnO deposited between the buffer layer and the AZO layer provides isolation and prevents the diffusion of Al into the absorber layer. Also, exposure to moisture tends to degrade AZO films' quality, making long-term stability a considerable challenge in CIGSe solar cells [139].

2.7 Substrate and deposition temperature selections

The solar cell structure of the CIGSe devices adopts the substrate structure, which allows light to enter through the top of the cell and a highly reflective back-contact at the base next to the substrate [22]. The structure allows the advantage of employing a range of materials to deposition thin films from the commonly used soda-lime glass to flexible metals and polymeric foils. The substrate's choice can also influence the thin films' grain size and orientation [140].

Although the substrate is a passive component of the solar cell, it may still be essential to the device's efficiency. The preferred choice of soda-lime glass is due primarily to its thermal expansion coefficient, which is well-suited to the layers of the devices and Na content needed. However, it has some limitations due to its weight, rigidity, and predisposition to breaking.

Due to aesthetics and eliminate some limitations of using glass, solar cell processing carried out at high temperatures is possible and modified low-temperature techniques to accommodate fabrications on flexible polymer and metal substrates. These new sets of potential substrates are relatively lightweight, flexible, and valuable for the emerging building integrated photovoltaic (BIPV) applications [133].

2.8 Grid ohmic contacts

One technique to improve the carrier collection and reduce the ohmic losses is putting metal grids on the TCO, which is the standard technique employed in the CIGSe solar cell industry. Some of the significant losses associated with high-efficiency solar cells include the resistive loss associated with majority carriers' lateral conduction at the grids and recombination at metal contacts [141]. However, the TCO layers' sheet resistance is much larger than the grid electrode's resistance, and the geometric grid design for optimal performance depends on the sheet resistance.

The solar cell grid's ideal considerations include a uniform current generation over the cell area, with lateral dimensions much larger than the TCO layer's thickness. The flow of current in the layer is ohmic. An essential requirement for TCO applications is the low electrical resistivity, typically the sheet resistance, which significantly influences the grid spacing to minimize power loss. An estimated grid spacing is related to sheet resistivity and power loss by the relation [142];

$$s = \sqrt{\frac{12V_{mp} \times P_{loss}}{\rho_s \times J_{mp}}} \quad \textbf{(Eqn. 2. 14)}$$

s is the grid spacing, P_{loss} is the power loss (typically < 4%), V_{mp} maximum voltage, and J_{mp} maximum current density. A varying grid pattern is possible. The smallest grid unit's repetition can produce the entire grid pattern, choose grid geometries, and project total series resistance from the active region's resultant shading [143]. A protective layer covers the metal grids to prevent unwanted corrosion, usually by redox electrolyte.

2.9 CIGSe and Tandem solar cells

World energy still depends significantly on fossil fuels despite the advances made in alternate energy sources, especially in photovoltaics in the past few decades. It is necessary to advance solar cells' efficiencies at a comparatively lower cost to achieve the next coming decades' energy goals. The crystalline silicon (c-Si) solar cells still dominate the photovoltaics market for several decades, with a high percentage of the current market share. An approach for exceeding the fundamental limit of a single absorber solar cell is employing solar cells with multiple junctions and joining absorber materials that harvest a broad range of the solar spectrum and improve the device efficiency. This approach's adoption reduces thermalization and transmission losses in a single-junction solar cell with successful implementation for different technologies, applications, and locations [144].

The concept of tandem or stacked solar cells comprising different bandgap material, a larger bandgap (∼1.5−1.8 eV) solar cell stacked on a smaller bandgap (∼0.9−1.2 eV) [145], offers the possibility to fabricate devices with power conversion exceeding the Shockley-Queisser efficiency limit of 30% without light concentration [146]. The solar cell at the top converts high-energy photons with reduced thermalization loss and transmits the near-infrared (NIR) portion of the solar spectrum into the cell's bottom part [145].

Several tandems solar cells already exist, combining the different single-junction solar cells and the potential of achieving almost 40% with some new materials. The theoretical limiting conversion efficiency under standard test conditions in a tandem configuration is 46.1% (with bandgaps of 1.73 and 0.94eV) and 45.7% (with bandgaps of 1.60 and 0.94eV) for a four-terminal and two-terminal device, respectively [144]. The reported lower efficiencies might be experimentally due to a lack of high-performing high-bandgap solar cells on the top. It could also be due to sub-bandgap transparency from the top cell, which is reduced due to parasitic absorption and inhibits the realization of the bottom cell's high efficiencies. Quantitatively, the transmission and bandgap, especially the top layer, play vital roles in the tandem cells' efficiency. The top cell should be highly transparent below its bandgap [147].

The optical-current characteristics of $Cu(In, Ga)Se_2$ materials render it a desirable candidate as the hole-transporting material (HTM) in a tandem configuration with other active absorbing material for multi-junction device fabrication. Furthermore, p-type inorganic HTMs as alternatives to the tandems' organic ones offer long-term stability and lower cost. In combination with perovskites, CIGSe material replaces the conventional acidic PEDOT: PSS hole-transporting material, which can erode ITO, thereby decreasing the perovskite solar reliability cells [148]. The CIGSe material is also successful in tandem with semi-transparent dye-sensitized solar cell (DSSC) to improve the solar cell [149].

Summary

We reviewed the advances made with the CIGSe chalcopyrite material for solar cell applications, from its discovery to the recent advances to improve the devices' efficiency. The review highlights some comparative advantages over the market-dominant Si devices and the CIGSe absorber layers' properties. A review of the alkali metals elucidated the unique effects of different alkali elements (i.e., heavier and lighter alkali metals) on the absorber layers and their potential functions, providing insights into the reasons for efficiency improvements using the alkali metals.

The chapter also reviews the contacts on the CIGSe solar cell devices, Mo back contacts, and the AZO layers, exploring the fundamental properties (e.g., resistivity) needed for device fabrications and consideration grid formation. The review on the buffer layer focused on the CdS material commonly employed for high-efficient CIGSe devices. It also highlighted other potentials factors affecting the device fabrication, e.g., substrate and deposition temperatures, and the potentials for this second-generation material in tandem devices.

References

[1] J.L. Shay, S. Wagner, H.M. Kasper, Efficient CuInSe 2 /CdS solar cells, Appl. Phys. Lett. 27 (1975) 89–90. https://doi.org/10.1063/1.88372.

[2] U.S.G. Survey, Rare Earth Elements — Critical Resources for High Technology, (2002) 1–11. https://pubs.usgs.gov/fs/2002/fs087-02/fs087-02.pdf (accessed February 5, 2020).

[3] V.M. Fthenakis, End-of-life management and recycling of PV modules, Energy Policy. 28 (2000) 1051–1058. https://doi.org/10.1016/S0301-4215(00)00091-4.

[4] M.T. Bishop, M. Tomatis, W. Zhang, C. Peng, G.Z. Chen, J. He, D. Hu, Assessment of toxicity reduction in ZnS substituted CdS:P3HT bulk heterojunction solar cells fabricated using a single-source precursor deposition, Sustain. Energy Fuels. 3 (2019) 948–955. https://doi.org/10.1039/C9SE00123A.

[5] M. Tammaro, J. Rimauro, V. Fiandra, A. Salluzzo, Thermal treatment of waste photovoltaic module for recovery and recycling: Experimental assessment of the presence of metals in the gas emissions and in the ashes, Renew. Energy. 81 (2015) 103–112. https://doi.org/10.1016/j.renene.2015.03.014.

[6] Y. Tang, Copper Indium Gallium Selenide Thin Film Solar Cells, in: Nanostructured Sol. Cells, InTech, 2017. https://doi.org/10.5772/65291.

[7] Y. Mori, O. Terakado, M. Hirasawa, Evaporation Behaviors of Cu(In,Ga)Se_2 Semiconductor Compound via Pyrometallurgical Chlorination Process Utilizing Ammonium Chloride, Mater. Trans. 56 (2015) 883–888. https://doi.org/10.2320/matertrans.M2015043.

[8] P. Reinhard, A. Chirila, P. Blosch, F. Pianezzi, S. Nishiwaki, S. Buechelers, A.N. Tiwari, Review of progress toward 20% efficiency flexible CIGS solar cells and manufacturing issues of solar modules, in: 2012 IEEE 38th Photovolt. Spec. Conf. PART 2, IEEE, 2013: pp. 1–9. https://doi.org/10.1109/PVSC-Vol2.2013.6656789.

[9] B. Dimmler, CIGS and CdTe based thin film PV modules, an industrial r/evolution, in: 2012 38th IEEE Photovolt. Spec. Conf., IEEE, 2012: pp. 002494–002499. https://doi.org/10.1109/PVSC.2012.6318101.

[10] U.S. Department of Energy, Copper indium gallium diselenide, (2016) 1–3.

http://energy.gov/eere/sunshot/copper-indium-gallium-diselenide (accessed February 4, 2020).

[11] M.A. Green, E.D. Dunlop, D.H. Levi, J. Hohl-Ebinger, M. Yoshita, A.W.Y. Ho-Baillie, Solar cell efficiency tables (version 54), Prog. Photovoltaics Res. Appl. 27 (2019) 565–575. https://doi.org/10.1002/pip.3171.

[12] M.J. (Mariska) de Wild-Scholten, Energy payback time and carbon footprint of commercial photovoltaic systems, Sol. Energy Mater. Sol. Cells. 119 (2013) 296–305. https://doi.org/10.1016/j.solmat.2013.08.037.

[13] M. Nakamura, K. Yamaguchi, Y. Kimoto, Y. Yasaki, T. Kato, H. Sugimoto, Cd-Free Cu(In,Ga)(Se,S) 2 Thin-Film Solar Cell With Record Efficiency of 23.35%, IEEE J. Photovoltaics. 9 (2019) 1863–1867. https://doi.org/10.1109/JPHOTOV.2019.2937218.

[14] M.F. Azeumo, G. Conte, N.M. Ippolito, F. Medici, L. Piga, S. Santilli, Photovoltaic module recycling, a physical and a chemical recovery process, Sol. Energy Mater. Sol. Cells. 193 (2019) 314–319. https://doi.org/10.1016/j.solmat.2019.01.035.

[15] LabPro, How Recycling CIGS Solar Cell Waste Materials Can Help The Environment and Your Bottom Line, (2020) 2–5. https://labproinc.com/blog/laboratory-safety-lab-efficiency-11/post/how-recycling-cigs-solar-cell-waste-materials-can-help-the-environment-and-your-bottom-line-60 (accessed February 7, 2020).

[16] US Department of Energy - Energy Efficiency and Renewable Energy, What is the energy payback for PV?, Int. J. (2004) 1–2. https://doi.org/DOE/GO-102004-1847.

[17] CIGS White Paper 2019, 2019. https://cigs-pv.net/wortpresse/wp-content/uploads/2019/04/CIGS_White_Paper_2019_online.pdf.

[18] Solar Cell Structure | PVEducation, (n.d.). https://www.pveducation.org/pvcdrom/solar-cell-operation/solar-cell-structure (accessed May 6, 2020).

[19] Spectral Irradiance | PVEducation, (n.d.). https://www.pveducation.org/pvcdrom/properties-of-sunlight/spectral-irradiance (accessed May 6, 2020).

[20] N.A.C. Lah, M.N.M. Zubir, M.A. Samykano, Engineered Nanomaterial in Electronics and Electrical Industries, in: C.B.T. Mustansar Hussain (Ed.), Handb. Nanomater. Ind. Appl.,

Elsevier, 2018: pp. 324–365. https://doi.org/10.1016/B978-0-12-813351-4.00064-X.

[21] G. Regmi, A. Ashok, P. Chawla, P. Semalti, S. Velumani, S.N. Sharma, H. Castaneda, Perspectives of chalcopyrite-based CIGSe thin-film solar cell: a review, J. Mater. Sci. Mater. Electron. (2020). https://doi.org/10.1007/s10854-020-03338-2.

[22] J. Ramanujam, U.P. Singh, Copper indium gallium selenide based solar cells – a review, Energy Environ. Sci. 10 (2017) 1306–1319. https://doi.org/10.1039/C7EE00826K.

[23] I.I.S. Garcia, H.A. Calderon, TEM Characterization of Ball Milled Synthesized CIGS, CIS and CGS Nanoparticles for Energy Applications, Microsc. Microanal. 24 (2018) 2008–2009. https://doi.org/10.1017/S1431927618010528.

[24] Z. Ning, Z. Da-Ming, Z. Gong, An investigation on preparation of CIGS targets by sintering process, Mater. Sci. Eng. B. 166 (2010) 34–40. https://doi.org/10.1016/j.mseb.2009.09.026.

[25] S.K. Deb, H. Okamoto, M. Kondo, Y. Hamakawa, Thin-Film Solar Cells, Springer Berlin Heidelberg, Berlin, Heidelberg, 2014. https://doi.org/10.1007/978-3-662-10549-8.

[26] J. Chantana, T. Watanabe, S. Teraji, K. Kawamura, T. Minemoto, Effect of crystal orientation in Cu(In,Ga)Se 2 fabricated by multi-layer precursor method on its cell performance, Appl. Surf. Sci. 314 (2014) 845–849. https://doi.org/10.1016/j.apsusc.2014.06.186.

[27] G.F. Novikov, M.V. Gapanovich, Third generation Cu-In-Ga-(S,-Se) based solar inverters, Uspekhi Fiz. Nauk. 187 (2017) 173–191. https://doi.org/10.3367/UFNr.2016.06.037827.

[28] J.E. Jaffe, A. Zunger, Anion displacements and the band-gap anomaly in ternary ABC2 chalcopyrite semiconductors, Phys. Rev. B. 27 (1983) 5176–5179. https://doi.org/10.1103/PhysRevB.27.5176.

[29] J.S. Park, Z. Dong, S. Kim, J.H. Perepezko, CuInSe2 phase formation during Cu2Se/In2Se3 interdiffusion reaction, J. Appl. Phys. 87 (2000) 3683–3690. https://doi.org/10.1063/1.372400.

[30] T. Walter, H.W. Schock, Crystal growth and diffusion in Cu(In, Ga)Se2 chalcopyrite thin films, Thin Solid Films. 224 (1993) 74–81. https://doi.org/10.1016/0040-6090(93)90461-W.

[31] S.-U. Park, R. Sharma, K. Ashok, S. Kang, J.-K. Sim, C.-R. Lee, A study on composition,

structure and optical properties of copper-poor CIGS thin film deposited by sequential sputtering of CuGa/In and In/(CuGa+In) precursors, J. Cryst. Growth. 359 (2012) 1–10. https://doi.org/10.1016/j.jcrysgro.2012.08.013.

[32] J.M. Raguse, C.P. Muzzillo, J.R. Sites, L. Mansfield, Effects of Sodium and Potassium on the Photovoltaic Performance of CIGS Solar Cells, IEEE J. Photovoltaics. 7 (2017) 303–306. https://doi.org/10.1109/JPHOTOV.2016.2621343.

[33] R. Caballero, V. Izquierdo-Roca, X. Fontané, C.A.A. Kaufmann, J. Álvarez-García, A. Eicke, L. Calvo-Barrio, A. Pérez-Rodríguez, H.W.W. Schock, J.R.R. Morante, Cu deficiency in multi-stage co-evaporated Cu(In,Ga)Se2 for solar cells applications: Microstructure and Ga in-depth alloying, Acta Mater. 58 (2010) 3468–3476. https://doi.org/10.1016/j.actamat.2010.02.021.

[34] P. Pistor, D. Greiner, C.A. Kaufmann, S. Brunken, M. Gorgoi, A. Steigert, W. Calvet, I. Lauermann, R. Klenk, T. Unold, M.C. Lux-Steiner, Experimental indication for band gap widening of chalcopyrite solar cell absorbers after potassium fluoride treatment, Appl. Phys. Lett. 105 (2014). https://doi.org/10.1063/1.4892882.

[35] T. Lavrenko, T. Ott, T. Walter, Impact of sulfur and gallium gradients on the performance of thin film Cu(In,Ga)(Se,S) 2 solar cells, Thin Solid Films. 582 (2015) 51–55. https://doi.org/10.1016/j.tsf.2014.11.024.

[36] W. Liu, J.G. Tian, Q. He, F.Y. Li, C.J. Li, Y. Sun, Effect of metallic precursors on the thin film thickness and reaction resistances in the selenization process, Curr. Appl. Phys. 11 (2011) 327–330. https://doi.org/10.1016/j.cap.2010.07.028.

[37] H.-H. Sung, D.-C. Tsai, Z.-C. Chang, T.-J. Chung, S.-C. Liang, E.-C. Chen, F.-S. Shieu, The structural evolution of Cu(In,Ga)Se 2 thin film and device performance prepared through a three-stage process, Mater. Sci. Semicond. Process. 41 (2016) 519–528. https://doi.org/10.1016/j.mssp.2015.10.024.

[38] C.-Y. Su, W.-H. Ho, H.-C. Lin, C.-Y. Nieh, S.-C. Liang, The effects of the morphology on the CIGS thin films prepared by CuInGa single precursor, Sol. Energy Mater. Sol. Cells. 95 (2011) 261–263. https://doi.org/10.1016/j.solmat.2010.04.072.

[39] M. Marudachalam, R.W. Birkmire, H. Hichri, J.M. Schultz, A. Swartzlander, M.M. Al-Jassim, Phases, morphology, and diffusion in CuInxGa1−xSe2 thin films, J. Appl. Phys. 82

(1997) 2896–2905. https://doi.org/10.1063/1.366122.

[40] O. Nwakanma, P. Reyes, S. Velumani, Electrical, structural, and topographical properties of direct current (DC) sputtered bilayer molybdenum thin films, J. Mater. Sci. Mater. Electron. 29 (2018) 15671–15681. https://doi.org/10.1007/s10854-018-9165-2.

[41] S.-H. Wei, S.B. Zhang, A. Zunger, Effects of Na on the electrical and structural properties of CuInSe2, J. Appl. Phys. 85 (1999) 7214–7218. https://doi.org/10.1063/1.370534.

[42] Q. Han, Y.T. Hsieh, L. Meng, J.L. Wu, P. Sun, E.P. Yao, S.Y. Chang, S.H. Bae, T. Kato, V. Bermudez, Y. Yang, High-performance perovskite/ Cu(In,Ga)Se2 monolithic tandem solar cells, Science (80-.). (2018). https://doi.org/10.1126/science.aat5055.

[43] H. Joachim Möller, Semiconductors for solar cell applications, Prog. Mater. Sci. 35 (1991) 205–418. https://doi.org/10.1016/0079-6425(91)90001-A.

[44] H. Ru Hsu, S. Chun Hsu, Y. Liu, Improvement of V oc and J sc in CuInGaSe 2 solar cells using a novel sandwiched CuGa/CuInGa/In precursor structure, Appl. Phys. Lett. 100 (2012) 233903. https://doi.org/10.1063/1.4705297.

[45] M.A. Green, Solar cells—Operating principles, technology and system applications, 1982. https://doi.org/10.1016/0038-092X(82)90265-1.

[46] A. Morales-Acevedo, A simple model of graded band-gap CuInGaSe2 solar cells, Energy Procedia. 2 (2010) 169–176. https://doi.org/10.1016/j.egypro.2010.07.024.

[47] A. Han, X. Wang, X. Liu, Y. Huang, F. Meng, Z. Liu, Improvement of Ga distribution in Cu(In, Ga)(S, Se)2 film by pretreated Mo back contact, Sol. Energy. 162 (2018) 109–116. https://doi.org/10.1016/j.solener.2018.01.015.

[48] A. Han, Y. Sun, Y. Zhang, X. Liu, F. Meng, Z. Liu, Comparative study of the role of Ga in CIGS solar cells with different thickness, Thin Solid Films. 598 (2016) 189–194. https://doi.org/10.1016/j.tsf.2015.12.020.

[49] N. E. Gorji, M. D. Perez, U. Reggiani, L. Sandrolini, A New Approach to Valence and Conduction Band Grading in CIGS Thin Film Solar Cells, Int. J. Eng. Technol. 4 (2012) 573–576. https://doi.org/10.7763/IJET.2012.V4.435.

[50] J. Mattheis, P.J. Rostan, U. Rau, J.H. Werner, Carrier collection in Cu(In,Ga)Se2 solar cells with graded band gaps and transparent ZnO:Al back contacts, Sol. Energy Mater. Sol. Cells.

91 (2007) 689–695. https://doi.org/10.1016/j.solmat.2006.12.014.

[51] S.K. Chattopadhyaya, V.K. Mathur, Carrier distribution in graded-band-gap semiconductors under asymmetric band-edge gradients, Phys. Rev. B. 9 (1974) 3517–3523. https://doi.org/10.1103/PhysRevB.9.3517.

[52] M. Topič, F. Smole, J. Furlan, Band-gap engineering in CdS/Cu(In,Ga)Se 2 solar cells, J. Appl. Phys. 79 (1996) 8537–8540. https://doi.org/10.1063/1.362533.

[53] J. Song, S.S. Li, C.H. Huang, O.D. Crisalle, T.J. Anderson, Device modeling and simulation of the performance of Cu(In1−x,Gax)Se2 solar cells, Solid. State. Electron. 48 (2004) 73–79. https://doi.org/10.1016/S0038-1101(03)00289-2.

[54] I.-H. Choi, Raman spectroscopy of CuIn1−xGaxSe2 for in-situ monitoring of the composition ratio, Thin Solid Films. 519 (2011) 4390–4393. https://doi.org/10.1016/j.tsf.2011.02.058.

[55] O. Cojocaru-Mirédin, P.-P. Choi, D. Abou-Ras, S.S. Schmidt, R. Caballero, D. Raabe, Characterization of Grain Boundaries in Cu(In,Ga)Se\$_{\bf 2}\$ Films Using Atom-Probe Tomography, IEEE J. Photovoltaics. 1 (2011) 207–212. https://doi.org/10.1109/JPHOTOV.2011.2170447.

[56] H. Tanino, T. Maeda, H. Fujikake, H. Nakanishi, S. Endo, T. Irie, Raman spectra of CuInSe2, Phys. Rev. B. 45 (1992) 13323–13330. https://doi.org/10.1103/PhysRevB.45.13323.

[57] H. Tanino, H. Deai, H. Nakanishi, Raman Spectra of CuGa x In 1- x Se 2, Jpn. J. Appl. Phys. 32 (1993) 436. https://doi.org/10.7567/JJAPS.32S3.436.

[58] W. Witte, R. Kniese, M. Powalla, Raman investigations of Cu(In,Ga)Se2 thin films with various copper contents, Thin Solid Films. 517 (2008) 867–869. https://doi.org/10.1016/j.tsf.2008.07.011.

[59] S. Nomura, S. Ouchi, S. Endo, Raman Spectra of Ordered Vacancy Compounds in the Cu-In-Se System, Jpn. J. Appl. Phys. 36 (1997) L1075–L1077. https://doi.org/10.1143/JJAP.36.L1075.

[60] A.N. Tiwari, S. Blunier, M. Filzmoser, H. Zogg, D. Schmid, H.W. Schock, Characterization of heteroepitaxial CuIn3Se5 and CuInSe2 layers on Si substrates, Appl. Phys. Lett. 65

(1994) 3347–3349. https://doi.org/10.1063/1.112387.

[61] T. Matsumura, Y. Sato, A Theoretical Study on Van Der Pauw Measurement Values of Inhomogeneous Compound Semiconductor Thin Films, J. Mod. Phys. 01 (2010) 340–347. https://doi.org/10.4236/jmp.2010.15048.

[62] H.-J. Ko, G.-H. Lee, H.-J. Kim, M.-S. Han, C.-H. Jeong, J.-H. Lee, H.-S. Kim, J.-H. Kim, K.-B. Kim, S.-H. Lee, Investigation of high-quality CuInSe2 films with various Cu/In ratios, J. Cryst. Growth. 322 (2011) 91–94. https://doi.org/10.1016/j.jcrysgro.2011.02.043.

[63] A. Laemmle, R. Wuerz, M. Powalla, Efficiency enhancement of Cu(In,Ga)Se 2 thin-film solar cells by a post-deposition treatment with potassium fluoride, Phys. Status Solidi - Rapid Res. Lett. 7 (2013) 631–634. https://doi.org/10.1002/pssr.201307238.

[64] T. Kodalle, M.D. Heinemann, D. Greiner, H.A. Yetkin, M. Klupsch, C. Li, P.A. van Aken, I. Lauermann, R. Schlatmann, C.A. Kaufmann, Elucidating the Mechanism of an RbF Post Deposition Treatment in CIGS Thin Film Solar Cells, Sol. RRL. 2 (2018) 1800156. https://doi.org/10.1002/solr.201800156.

[65] H. Lee, Y. Jang, S.-W. Nam, C. Jung, P.-P. Choi, J. Gwak, J.H. Yun, K. Kim, B. Shin, Passivation of Deep-Level Defects by Cesium Fluoride Post-Deposition Treatment for Improved Device Performance of Cu(In,Ga)Se 2 Solar Cells, ACS Appl. Mater. Interfaces. 11 (2019) 35653–35660. https://doi.org/10.1021/acsami.9b08316.

[66] M.D. Heinemann, T. Kodalle, C. Hages, M. Klupsch, D. Greiner, L. Korte, S. Levcenco, T. Unold, R. Schlatmann, C.A. Kaufmann, Evaluation of recombination losses in thin film solar cells using an LED sun simulator - The effect of RbF post-deposition on CIGS solar cells, EPJ Photovoltaics. 9 (2018). https://doi.org/10.1051/epjpv/2018006.

[67] J. Pettersson, T. Torndahl, C. Platzer-Bjorkman, A. Hultqvist, M. Edoff, The Influence of Absorber Thickness on Cu(In,Ga)Se2 Solar Cells With Different Buffer Layers, IEEE J. Photovoltaics. 3 (2013) 1376–1382. https://doi.org/10.1109/JPHOTOV.2013.2276030.

[68] X. Zheng, W. Li, A.G. Aberle, S. Venkataraj, Efficiency enhancement of ultra-thin Cu(In,Ga)Se2 solar cells: optimizing the absorber bandgap profile by numerical device simulations, Curr. Appl. Phys. 16 (2016) 1334–1341. https://doi.org/10.1016/j.cap.2016.07.002.

[69] N. Devi, A. Aziz, S. Datta, Numerical modelling of CIGS/CdS solar cell, in: AIP Conf. Proc., 2018: p. 100031. https://doi.org/10.1063/1.5032967.

[70] J. Nam, Y. Kang, D. Lee, J. Yang, Y.-S. Kim, C.B. Mo, S. Park, D. Kim, Achievement of 17.9% efficiency in 30 × 30 cm 2 Cu(In,Ga)(Se,S) 2 solar cell sub-module by sulfurization after selenization with Cd-free buffer, Prog. Photovoltaics Res. Appl. 24 (2016) 175–182. https://doi.org/10.1002/pip.2653.

[71] Y.-C. Lin, M.T. Shen, Y.-L. Chen, H.-R. Hsu, C.-H. Wu, A study on MoSe2 layer of Mo contact in Cu(In,Ga)Se2 thin film solar cells, Thin Solid Films. 570 (2014) 166–171. https://doi.org/10.1016/j.tsf.2014.04.016.

[72] N. Kohara, S. Nishiwaki, Y. Hashimoto, T. Negami, T. Wada, Electrical properties of the Cu(In,Ga)Se2/ MoSe2/Mo structure, Sol. Energy Mater. Sol. Cells. 67 (2001) 209–215. https://doi.org/10.1016/S0927-0248(00)00283-X.

[73] K. Kim, H. Park, G.M. Hanket, W.K. Kim, W.N. Shafarman, Composition and bandgap control in Cu(In,Ga)Se 2 -based absorbers formed by reaction of metal precursors, Prog. Photovoltaics Res. Appl. 23 (2015) 765–772. https://doi.org/10.1002/pip.2494.

[74] A.H. Reshak, S. Auluck, Band structure and optical response of 2H-MoX2 compounds (X=S, Se, and Te), Phys. Rev. B. 71 (2005) 155114. https://doi.org/10.1103/PhysRevB.71.155114.

[75] Kihwan Kim, Peipei Xin, Jaeho Yun, W.N. Shafarman, VOC enhancement of sub-micron CIGS solar cells by sulfization of the Mo surface, in: 2015 IEEE 42nd Photovolt. Spec. Conf., IEEE, 2015: pp. 1–4. https://doi.org/10.1109/PVSC.2015.7355621.

[76] U.P. Singh, W.N. Shafarman, R.W. Birkmire, Surface sulfurization studies of Cu(InGa)Se2 thin film, Sol. Energy Mater. Sol. Cells. 90 (2006) 623–630. https://doi.org/10.1016/j.solmat.2005.04.037.

[77] L.E. Oikkonen, M.G. Ganchenkova, A.P. Seitsonen, R.M. Nieminen, Formation, migration, and clustering of point defects in CuInSe2 from first principles, J. Phys. Condens. Matter. 26 (2014). https://doi.org/10.1088/0953-8984/26/34/345501.

[78] J. Pohl, K. Albe, Intrinsic point defects in CuInSe2 and CuGaSe2 as seen via screened-exchange hybrid density functional theory, Phys. Rev. B. 87 (2013) 245203.

https://doi.org/10.1103/PhysRevB.87.245203.

[79] X. Hu, A. Gupta, T. Sakurai, A. Yamada, S. Ishizuka, S. Niki, K. Akimoto, Investigation of deep-level defects in Cu(In,Ga)Se 2 thin films by two-wavelength excitation photo-capacitance spectroscopy, Appl. Phys. Lett. 103 (2013) 163905. https://doi.org/10.1063/1.4826144.

[80] L.E. Oikkonen, M.G. Ganchenkova, A.P. Seitsonen, R.M. Nieminen, Mass transport in CuInSe2 from first principles, J. Appl. Phys. 113 (2013). https://doi.org/10.1063/1.4799064.

[81] L.E. Oikkonen, M.G. Ganchenkova, A.P. Seitsonen, R.M. Nieminen, Redirecting focus in CuInSe 2 research towards selenium-related defects, Phys. Rev. B - Condens. Matter Mater. Phys. 86 (2012) 1–5. https://doi.org/10.1103/PhysRevB.86.165115.

[82] T. Eisenbarth, R. Caballero, M. Nichterwitz, C.A. Kaufmann, H.-W. Schock, T. Unold, Characterization of metastabilities in Cu(In,Ga)Se 2 thin-film solar cells by capacitance and current-voltage spectroscopy, J. Appl. Phys. 110 (2011) 094506. https://doi.org/10.1063/1.3656453.

[83] D. Hariskos, M. Powalla, Thermodynamic limitations for alkali metals in Cu(In,Ga)Se2, J. Mater. Res. 32 (2017). https://doi.org/10.1557/jmr.2017.394.

[84] L.E. Oikkonen, M.G. Ganchenkova, A.P. Seitsonen, R.M. Nieminen, Effect of sodium incorporation into CuInSe2 from first principles, J. Appl. Phys. 114 (2013). https://doi.org/10.1063/1.4819105.

[85] J. Chantana, T. Watanabe, S. Teraji, T. Minemoto, Influence of minimum position in [Ga]/([Ga]+[In]) profile of Cu(In,Ga)Se2 on flexible stainless steel substrate on its photovoltaic performances, Sol. Energy Mater. Sol. Cells. 157 (2016) 750–756. https://doi.org/10.1016/j.solmat.2016.07.048.

[86] D. Colombara, F. Werner, T. Schwarz, I. Cañero Infante, Y. Fleming, N. Valle, C. Spindler, E. Vacchieri, G. Rey, M. Guennou, M. Bouttemy, A.G. Manjón, I. Peral Alonso, M. Melchiorre, B. El Adib, B. Gault, D. Raabe, P.J. Dale, S. Siebentritt, Sodium enhances indium-gallium interdiffusion in copper indium gallium diselenide photovoltaic absorbers, Nat. Commun. 9 (2018) 1–12. https://doi.org/10.1038/s41467-018-03115-0.

[87] Y. Shao, Z. Xiao, C. Bi, Y. Yuan, J. Huang, Origin and elimination of photocurrent hysteresis by fullerene passivation in CH3NH3PbI3 planar heterojunction solar cells, Nat. Commun. 5 (2014) 5784. https://doi.org/10.1038/ncomms6784.

[88] Z.Y. Liu, F.P. Zhang, J.X. Zhang, X. Zhang, Q.M. Lu, X.Y. Yang, Enhanced electrical transport by texture modulation and co-doping for Ca3Co4O9+δ materials, Results Phys. 6 (2016) 203–208. https://doi.org/10.1016/j.rinp.2016.04.008.

[89] S. Ye, X. Tan, M. Jiang, B. Fan, K. Tang, S. Zhuang, Impact of different Na-incorporating methods on Cu(In;Ga)Se2 thin film solar cells with a low-Na substrate, Appl. Opt. 49 (2010) 1662–1665. https://doi.org/10.1364/AO.49.001662.

[90] Q. Luo, H. Ma, Q. Hou, Y. Li, J. Ren, X. Dai, Z. Yao, Y. Zhou, L. Xiang, H. Du, H. He, N. Wang, K. Jiang, H. Lin, H. Zhang, Z. Guo, All-Carbon-Electrode-Based Endurable Flexible Perovskite Solar Cells, Adv. Funct. Mater. (2018). https://doi.org/10.1002/adfm.201706777.

[91] D. Guttler, A. Chirila, S. Seyrling, P. Blosch, S. Buecheler, X. Fontane, V. Izquierdo-Roca, L. Calvo-Barrio, A. Perez-Rodriguez, J.R. Morante, A. Eicke, A.N. Tiwari, Influence of NaF incorporation during Cu(In,Ga)Se<inf>2</inf> growth on microstructure and photovoltaic performance, in: 2010 35th IEEE Photovolt. Spec. Conf., IEEE, 2010: pp. 003420–003424. https://doi.org/10.1109/PVSC.2010.5614564.

[92] P. Schöppe, S. Schönherr, P. Jackson, R. Wuerz, W. Wisniewski, M. Ritzer, M. Zapf, A. Johannes, C.S. Schnohr, C. Ronning, Overall Distribution of Rubidium in Highly Efficient Cu(In,Ga)Se2 Solar Cells, ACS Appl. Mater. Interfaces. 10 (2018) 40592–40598. https://doi.org/10.1021/acsami.8b16040.

[93] T.M. Friedlmeier, P. Jackson, A. Bauer, D. Hariskos, O. Kiowski, R. Wuerz, M. Powalla, Improved Photocurrent in Cu(In,Ga)Se2Solar Cells: From 20.8% to 21.7% Efficiency with CdS Buffer and 21.0% Cd-Free, IEEE J. Photovoltaics. 5 (2015) 1487–1491. https://doi.org/10.1109/JPHOTOV.2015.2458039.

[94] S. Kim, J. Nishinaga, Y. Kamikawa, S. Ishizuka, T. Nagai, T. Koida, H. Tampo, H. Shibata, K. Matsubara, S. Niki, Reduced recombination in a surface-sulfurized Cu(InGa)Se 2 thin-film solar cell, Jpn. J. Appl. Phys. 57 (2018) 055701. https://doi.org/10.7567/JJAP.57.055701.

[95] M. Bodeg Ård, K. Granath, L. Stolt, Growth of Cu(In,Ga)Se 2 thin films by coevaporation using alkaline precursors, Thin Solid Films. 361–362 (2000) 9–16. https://doi.org/10.1016/S0040-6090(99)00828-7.

[96] T. Maeda, A. Kawabata, T. Wada, First-principles study on alkali-metal effect of Li, Na, and K in CuInSe2 and CuGaSe2, Jpn. J. Appl. Phys. 54 (2015). https://doi.org/10.7567/JJAP.54.08KC20.

[97] M. Malitckaya, H.P. Komsa, V. Havu, M.J. Puska, Effect of Alkali Metal Atom Doping on the CuInSe2-Based Solar Cell Absorber, J. Phys. Chem. C. 121 (2017) 15516–15528. https://doi.org/10.1021/acs.jpcc.7b03083.

[98] R. Wuerz, W. Hempel, P. Jackson, Diffusion of Rb in polycrystalline Cu(In,Ga)Se2 layers and effect of Rb on solar cell parameters of Cu(In,Ga)Se2 thin-film solar cells, J. Appl. Phys. 124 (2018) 165305. https://doi.org/10.1063/1.5044629.

[99] O. Donzel-Gargand, T. Thersleff, J. Keller, T. Törndahl, F. Larsson, E. Wallin, L. Stolt, M. Edoff, Deep surface Cu depletion induced by K in high-efficiency Cu(In,Ga)Se2 solar cell absorbers, Prog. Photovoltaics Res. Appl. 26 (2018) 730–739. https://doi.org/10.1002/pip.3010.

[100] T. Lepetit, S. Harel, L. Arzel, G. Ouvrard, N. Barreau, Co-evaporated KInSe 2 : A fast alternative to KF post deposition treatment in high efficiency Cu(In,Ga)Se 2 thin film solar cells, 2017 IEEE 44th Photovolt. Spec. Conf. PVSC 2017. 6 (2017) 1–4. https://doi.org/10.1109/PVSC.2017.8366832.

[101] A. Chirilă, P. Reinhard, F. Pianezzi, P. Bloesch, A.R. Uhl, C. Fella, L. Kranz, D. Keller, C. Gretener, H. Hagendorfer, D. Jaeger, R. Erni, S. Nishiwaki, S. Buecheler, A.N. Tiwari, Potassium-induced surface modification of Cu(In,Ga)Se 2 thin films for high-efficiency solar cells, Nat. Mater. 12 (2013) 1107–1111. https://doi.org/10.1038/nmat3789.

[102] J.A. Aguiar, A. Stokes, C.-S. Jiang, T. Aoki, P.G. Kotula, M.K. Patel, B. Gorman, M. Al-Jassim, Revealing Surface Modifications of Potassium-Fluoride-Treated Cu(In,Ga)Se 2 : A Study of Material Structure, Chemistry, and Photovoltaic Performance, Adv. Mater. Interfaces. 3 (2016) 1600013. https://doi.org/10.1002/admi.201600013.

[103] X. Lyu, D. Zhuang, M. Zhao, Q. Gong, L. Zhang, R. Sun, Y. Wei, X. Peng, Y. Wu, G. Ren, An investigation on performance enhancement for KF post deposition treated CIGS solar

cells fabricated by sputtering CIGS quaternary targets, Vacuum. 151 (2018) 233–236. https://doi.org/10.1016/j.vacuum.2018.02.023.

[104] Y. Kamikawa, J. Nishinaga, S. Ishizuka, T. Tayagaki, H. Guthrey, H. Shibata, K. Matsubara, S. Niki, Effect of thermal annealing on the redistribution of alkali metals in Cu(In,Ga)Se2 solar cells on glass substrate, J. Appl. Phys. 123 (2018) 093101. https://doi.org/10.1063/1.5016949.

[105] M. Hafemeister, S. Siebentritt, J. Albert, M.C. Lux-Steiner, S. Sadewasser, Large neutral barrier at grain boundaries in chalcopyrite thin films, Phys. Rev. Lett. 104 (2010) 14–17. https://doi.org/10.1103/PhysRevLett.104.196602.

[106] P. Reinhard, B. Bissig, F. Pianezzi, H. Hagendorfer, G. Sozzi, R. Menozzi, C. Gretener, S. Nishiwaki, S. Buecheler, A.N. Tiwari, Alkali-templated surface nanopatterning of chalcogenide thin films: A novel approach toward solar cells with enhanced efficiency, Nano Lett. 15 (2015) 3334–3340. https://doi.org/10.1021/acs.nanolett.5b00584.

[107] F. Larsson, O. Donzel-Gargand, J. Keller, M. Edoff, T. Törndahl, Atomic layer deposition of Zn(O,S) buffer layers for Cu(In,Ga)Se2 solar cells with KF post-deposition treatment, Sol. Energy Mater. Sol. Cells. 183 (2018) 8–15. https://doi.org/10.1016/j.solmat.2018.03.045.

[108] X. He, J. Liu, Q. Ye, K. Luo, Y. Jiang, C. Liao, L. Ouyang, D. Zhuang, J. Mei, W. Lau, The role of Na incorporation in the low-temperature processed CIGS thin film solar cells using post deposition treatment, J. Alloys Compd. 658 (2016) 12–18. https://doi.org/10.1016/j.jallcom.2015.10.181.

[109] L. Qi, Y. Yang, D. Jiang, C. Tu, L. Wan, X. Chen, Z. Li, Factors associated with the duration of viral shedding in adults with COVID-19 outside of Wuhan, China: a retrospective cohort study, Int. J. Infect. Dis. 96 (2020) 531–537. https://doi.org/10.1016/j.ijid.2020.05.045.

[110] Z.K. Yuan, S. Chen, Y. Xie, J.S. Park, H. Xiang, X.G. Gong, S.H. Wei, Na-Diffusion Enhanced p-type Conductivity in Cu(In,Ga)Se2: A New Mechanism for Efficient Doping in Semiconductors, Adv. Energy Mater. 6 (2016) 1–7. https://doi.org/10.1002/aenm.201601191.

[111] A. Romeo, M. Terheggen, D. Abou-Ras, D.L. Bätzner, F.-J. Haug, M. Kälin, D. Rudmann, A.N. Tiwari, Development of thin-film Cu(In,Ga)Se2 and CdTe solar cells, Prog.

Photovoltaics Res. Appl. 12 (2004) 93–111. https://doi.org/10.1002/pip.527.

[112] K. Zhang, C. Yang, L. Yin, Z. Liu, Q. Song, H. Luo, Z. Xiong, M. Xu, X. Xiao, Fabricating highly efficient Cu(In,Ga)Se2 solar cells at low glass-substrate temperature by active gallium grading control, Sol. Energy Mater. Sol. Cells. 120 (2014) 253–258. https://doi.org/10.1016/j.solmat.2013.09.012.

[113] P.S. Vasekar, N.G. Dhere, Effect of sodium addition on Cu-deficient CuIn1-xGaxS2 thin film solar cells, Sol. Energy Mater. Sol. Cells. 93 (2009) 69–73. https://doi.org/10.1016/j.solmat.2008.04.013.

[114] L.M. Mansfield, R. Noufi, C.P. Muzzillo, C. Dehart, K. Bowers, B. To, J.W. Pankow, R.C. Reedy, K. Ramanathan, Enhanced performance in Cu(In,Ga)Se2 solar cells fabricated by the two-step selenization process with a potassium fluoride postdeposition treatment, IEEE J. Photovoltaics. 4 (2014) 1650–1654. https://doi.org/10.1109/JPHOTOV.2014.2354259.

[115] I. Khatri, H. Fukai, H. Yamaguchi, M. Sugiyama, T. Nakada, Effect of potassium fluoride post-deposition treatment on Cu(In,Ga)Se2 thin films and solar cells fabricated onto sodalime glass substrates, Sol. Energy Mater. Sol. Cells. 155 (2016) 280–287. https://doi.org/10.1016/j.solmat.2016.06.023.

[116] M. RUCKH, D. SCHMID, M. KAISER, R. SCHAFFLER, T. WALTER, H. SCHOCK, Influence of substrates on the electrical properties of Cu(In,Ga)Se2 thin films, Sol. Energy Mater. Sol. Cells. 41–42 (1996) 335–343. https://doi.org/10.1016/0927-0248(95)00105-0.

[117] N. Nicoara, T. Lepetit, L. Arzel, S. Harel, N. Barreau, S. Sadewasser, Effect of the KF post-deposition treatment on grain boundary properties in Cu(In, Ga)Se 2 thin films, Sci. Rep. 7 (2017) 1–7. https://doi.org/10.1038/srep41361.

[118] S. Kim, H. Tampo, H. Shibata, K. Matsubara, S. Niki, Effect of Combined Alkali (KF + CsF) Post-Deposition Treatment on Cu(InGa)Se2 Solar Cells, Phys. Status Solidi - Rapid Res. Lett. 12 (2018) 1–5. https://doi.org/10.1002/pssr.201800372.

[119] C.P. Muzzillo, Review of grain interior, grain boundary, and interface effects of K in CIGS solar cells: Mechanisms for performance enhancement, Sol. Energy Mater. Sol. Cells. 172 (2017) 18–24. https://doi.org/10.1016/j.solmat.2017.07.006.

[120] S. Ishizuka, N. Taguchi, J. Nishinaga, Y. Kamikawa, S. Tanaka, H. Shibata, Group III

Elemental Composition Dependence of RbF Postdeposition Treatment Effects on Cu(In,Ga)Se 2 Thin Films and Solar Cells, J. Phys. Chem. C. 122 (2018) 3809–3817. https://doi.org/10.1021/acs.jpcc.8b00079.

[121] D. Hauschild, D. Kreikemeyer-Lorenzo, P. Jackson, T.M. Friedlmeier, D. Hariskos, F. Reinert, M. Powalla, C. Heske, L. Weinhardt, Impact of a RbF Postdeposition Treatment on the Electronic Structure of the CdS/Cu(In,Ga)Se2 Heterojunction in High-Efficiency Thin-Film Solar Cells, ACS Energy Lett. 2 (2017) 2383–2387. https://doi.org/10.1021/acsenergylett.7b00720.

[122] T. Kato, J.-L. Wu, Y. Hirai, H. Sugimoto, V. Bermudez, Record Efficiency for Thin-Film Polycrystalline Solar Cells Up to 22.9% Achieved by Cs-Treated Cu(In,Ga)(Se,S) 2, IEEE J. Photovoltaics. 9 (2019) 325–330. https://doi.org/10.1109/JPHOTOV.2018.2882206.

[123] P. Jackson, R. Wuerz, D. Hariskos, E. Lotter, W. Witte, M. Powalla, Effects of heavy alkali elements in Cu(In,Ga)Se2 solar cells with efficiencies up to 22.6%, Phys. Status Solidi - Rapid Res. Lett. 10 (2016) 583–586. https://doi.org/10.1002/pssr.201600199.

[124] T.-Y. Lin, I. Khatri, J. Matsuura, K. Shudo, W.-C. Huang, M. Sugiyama, C.-H. Lai, T. Nakada, Alkali-induced grain boundary reconstruction on Cu(In,Ga)Se2 thin film solar cells using cesium fluoride post deposition treatment, Nano Energy. 68 (2020) 104299. https://doi.org/10.1016/j.nanoen.2019.104299.

[125] A. Ashok, G. Regmi, A. Romero-Núñez, M. Solis-López, S. Velumani, H. Castaneda, Comparative studies of CdS thin films by chemical bath deposition techniques as a buffer layer for solar cell applications, J. Mater. Sci. Mater. Electron. 31 (2020) 7499–7518. https://doi.org/10.1007/s10854-020-03024-3.

[126] W. Witte, D. Abou-Ras, D. Hariskos, Chemical bath deposition of Zn(O,S) and CdS buffers: Influence of Cu(In,Ga)Se 2 grain orientation, Appl. Phys. Lett. 102 (2013) 051607. https://doi.org/10.1063/1.4788717.

[127] F. Lisco, P.M. Kaminski, A. Abbas, K. Bass, J.W. Bowers, G. Claudio, M. Losurdo, J.M. Walls, The structural properties of CdS deposited by chemical bath deposition and pulsed direct current magnetron sputtering, Thin Solid Films. 582 (2015) 323–327. https://doi.org/10.1016/j.tsf.2014.11.062.

[128] S.B. Zhang, S.-H. Wei, Reconstruction and energetics of the polar (112) and (¯1¯1¯2)

versus the nonpolar (220) surfaces of CuInSe2, Phys. Rev. B. 65 (2002) 081402. https://doi.org/10.1103/PhysRevB.65.081402.

[129] P. Reinhard, B. Bissig, F. Pianezzi, E. Avancini, H. Hagendorfer, D. Keller, P. Fuchs, M. Döbeli, C. Vigo, P. Crivelli, S. Nishiwaki, S. Buecheler, A.N. Tiwari, Features of KF and NaF Postdeposition Treatments of Cu(In,Ga)Se2 Absorbers for High Efficiency Thin Film Solar Cells, Chem. Mater. 27 (2015) 5755–5764. https://doi.org/10.1021/acs.chemmater.5b02335.

[130] P. Yang, R.G. Wilks, W. Yang, M. Bär, Interface Formation between CdS and Alkali Postdeposition-Treated Cu(In,Ga)Se2 Thin-Film Solar Cell Absorbers - Key to Understanding the Efficiency Gain, ACS Appl. Mater. Interfaces. 12 (2020) 6688–6698. https://doi.org/10.1021/acsami.9b20327.

[131] E. Handick, P. Reinhard, J.H. Alsmeier, L. Köhler, F. Pianezzi, S. Krause, M. Gorgoi, E. Ikenaga, N. Koch, R.G. Wilks, S. Buecheler, A.N. Tiwari, M. Bär, Potassium Postdeposition Treatment-Induced Band Gap Widening at Cu(In,Ga)Se2 Surfaces - Reason for Performance Leap?, ACS Appl. Mater. Interfaces. 7 (2015) 27414–27420. https://doi.org/10.1021/acsami.5b09231.

[132] M.M. Aqil, M.A. Azam, M.F. Aziz, R. Latif, Deposition and characterization of molybdenum thin film using direct current magnetron and atomic force microscopy, J. Nanotechnol. 2017 (2017). https://doi.org/10.1155/2017/4862087.

[133] K.H. Ong, R. Agileswari, B. Maniscalco, P. Arnou, C.C. Kumar, J.W. Bowers, M.B. Marsadek, Review on substrate and molybdenum back contact in CIGS thin film solar cell, Int. J. Photoenergy. 2018 (2018). https://doi.org/10.1155/2018/9106269.

[134] J. Álvarez-García, A. Pérez-Rodríguez, A. Romano-Rodríguez, J.R. Morante, L. Calvo-Barrio, R. Scheer, R. Klenk, Microstructure and secondary phases in coevaporated CuInS2 films: Dependence on growth temperature and chemical composition, J. Vac. Sci. Technol. A Vacuum, Surfaces, Film. 19 (2001) 232–239. https://doi.org/10.1116/1.1329123.

[135] G. Yin, A. Steigert, P. Manley, R. Klenk, M. Schmid, Enhanced absorption in tandem solar cells by applying hydrogenated In 2 O 3 as electrode, Appl. Phys. Lett. 107 (2015) 211901. https://doi.org/10.1063/1.4936328.

[136] S.O. El hamali, W.M. Cranton, N. Kalfagiannis, X. Hou, R. Ranson, D.C. Koutsogeorgis,

Enhanced electrical and optical properties of room temperature deposited Aluminium doped Zinc Oxide (AZO) thin films by excimer laser annealing, Opt. Lasers Eng. 80 (2016) 45–51. https://doi.org/10.1016/j.optlaseng.2015.12.010.

[137] K. Ellmer, Past achievements and future challenges in the development of optically transparent electrodes, Nat. Photonics. 6 (2012) 809–817. https://doi.org/10.1038/nphoton.2012.282.

[138] H. ming Zhou, D. qing Yi, Z. ming Yu, L. rong Xiao, J. Li, Preparation of aluminum doped zinc oxide films and the study of their microstructure, electrical and optical properties, Thin Solid Films. 515 (2007) 6909–6914. https://doi.org/10.1016/j.tsf.2007.01.041.

[139] J. Pan, L. Kerr, X. Li, H.J. Gulley-Stahl, A.J. Sommer, Investigation of aluminum induced degradation in sputtered Al:ZnO for CIGS solar cells applications, in: 2009 34th IEEE Photovolt. Spec. Conf., IEEE, 2009: pp. 000345–000349. https://doi.org/10.1109/PVSC.2009.5411667.

[140] R. Klenk, T. Walter, H.-W. Schock, D. Cahen, A model for the successful growth of polycrystalline films of CuInSe2 by multisource physical vacuum evaporation, Adv. Mater. 5 (1993) 114–119. https://doi.org/10.1002/adma.19930050209.

[141] A.W. Blakers, Shading losses of solar-cell metal grids, J. Appl. Phys. 71 (1992) 5237–5241. https://doi.org/10.1063/1.350580.

[142] R. Corkish, M.A. Green, M.E. Watt, S.R. Wenham, Applied Photovoltaics, Second, Routledge, 2013. https://doi.org/10.4324/9781849770491.

[143] N. Convers Wyeth, Sheet resistance component of series resistance in a solar cell as a function of grid geometry, Solid. State. Electron. 20 (1977) 629–634. https://doi.org/10.1016/0038-1101(77)90103-4.

[144] C.D. Bailie, M.G. Christoforo, J.P. Mailoa, A.R. Bowring, E.L. Unger, W.H. Nguyen, J. Burschka, N. Pellet, J.Z. Lee, M. Grätzel, R. Noufi, T. Buonassisi, A. Salleo, M.D. McGehee, Semi-transparent perovskite solar cells for tandems with silicon and CIGS, Energy Environ. Sci. 8 (2015) 956–963. https://doi.org/10.1039/C4EE03322A.

[145] L. Kranz, A. Abate, T. Feurer, F. Fu, E. Avancini, J. Löckinger, P. Reinhard, S.M. Zakeeruddin, M. Grätzel, S. Buecheler, A.N. Tiwari, High-Efficiency Polycrystalline Thin

Film Tandem Solar Cells, J. Phys. Chem. Lett. 6 (2015) 2676–2681. https://doi.org/10.1021/acs.jpclett.5b01108.

[146] M.A. Green, Third Generation Photovoltaics Advanced Solar Energy Conversion, First, Springer-Verlag Berlin Heidelberg, New York, 2006.

[147] M. Schmid, R. Klenk, M.C. Lux-Steiner, Quantitative analysis of cell transparency and its implications for the design of chalcopyrite-based tandems, Sol. Energy Mater. Sol. Cells. 93 (2009) 874–878. https://doi.org/10.1016/j.solmat.2008.10.008.

[148] Z. Li, T.R. Klein, D.H. Kim, M. Yang, J.J. Berry, M.F.A.M. Van Hest, K. Zhu, Scalable fabrication of perovskite solar cells, Nat. Rev. Mater. 3 (2018) 1–20. https://doi.org/10.1038/natrevmats.2018.17.

[149] W.-S. Jeong, J.-W. Lee, S. Jung, J.H. Yun, N.-G. Park, Evaluation of external quantum efficiency of a 12.35% tandem solar cell comprising dye-sensitized and CIGS solar cells, Sol. Energy Mater. Sol. Cells. 95 (2011) 3419–3423. https://doi.org/10.1016/j.solmat.2011.07.038.

Chapter Three: Experimental procedures and Alkali Halide post-deposition treatments (PDT)

3.1 Introduction

The fabrication of thin-film devices using any innovative techniques aims to improve the device's efficiency at a simultaneous lower cost and short fabrication time. The deposition using either physical vapor deposition (PVD) or chemical vapor deposition (CVD) for vacuum depositions or some non-vacuum methods [1–3] depends on the nature of the elements and the desired quality of the thin-films commonly affected by the deposition techniques used. The deposition processes involve the production of appropriate atomic, ionic, or molecular species and the transport through a medium of these species for condensation on the substrate, either directly or via a chemical or electrochemical reaction [4].

Understanding the fundamental behavior of the elements and compositions aids in the development of technology for large area industrial-scale applications and addresses the production costs. For every layer of the thin-film device, the physical properties, e.g., stack density, surface roughness, and crystallinity, depend on the deposition methods and affect the resulting solar cell device's quality. Furthermore, although some deposition techniques can yield a higher level of purity of the layers and potentially higher efficiencies, they are relatively more costly and challenging to scale up for industrial applications. The absorber layer appears to be the essential layer in the solar cell, with the properties, e.g., structural, surface, optical, and electrical, significantly influencing the device's performance and efficiency, accounting for the much attention given to this layer of the solar cell. Other device layers and the adopted fabrication methods and surface treatments of each layer after deposition also affect the device performance, especially the interfaces.

This chapter presents a preview of the experimental methods employed for depositing the separate layers of the solar cell. Finally, it proposed a non-vacuum method for alkali-halide deposition for PDT.

3.2 Molybdenum back-contact deposition

Molybdenum (Mo), among other choices of conductive materials such as gold (Au), platinum (Pt), silver (Ag), copper (Cu), nickel (Ni), and aluminum (Al), forms an essential ohmic back-contact of the CIGSe thin-film solar cells with low-resistivity, high reflectivity and inertness to chemically reacting and alloying with copper and indium from the CIGSe layer [5–9]. The unabsorbed photons get reflected into the absorber layer owing to their high reflectivity [10]. The deposited Mo thin-films' structure and density, which are greatly influenced by the deposition techniques [11,12], serve as a barrier and effective medium to control impurities' diffusion from the sub-layer. Therefore, Mo serves as a barrier for controlled diffusion of elements, usually Na from SLG [12], in composite with other thin layer materials to reduce/block unwanted impurities (e.g., iron and chromium from flexible stainless-steel substrates) [7,13–18]. It also possesses excellent adhesion to the substrates, with the deposition technique significantly influencing the homogeneity [6–8].

Mo possesses a good chemically stability to the CIGSe absorber and a relatively high melting point, with a thermal expansion coefficient (5.8×10^{-6} K^{-1}) close to CISe (9.5×10^{-6} K^{-1}) [5,19], making it amenable to several thin-film deposition techniques[20–26]. However, its high melting point (2896 K) and low vapor pressure (3.47 Pa at 3000 K) make it ideal for sputtering [25].

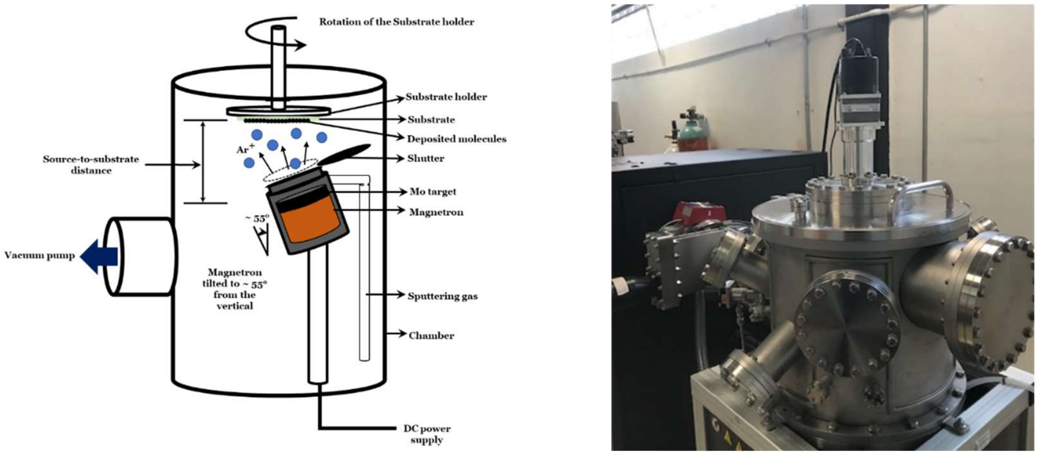

(a) *(b)*

Figure 3. 1 *(a) A schematic diagram for a direct-current sputtering system (b) An image of the DC sputtering equipment for Mo back-contact deposition.*

Sputtering refers to particles' ejection (atoms, ions, and clusters) from a surface bombarded by energetic ions [27,28]. In this case, physical sputtering with ionized Ar gases involving a gaseous plasma generated in a confined chamber containing the deposited material. Ionized Ar gases impact and erode the target surface with high energies (dependent on the sputtering power and pressure). The fraction of atoms that intersect the surface with energies exceeding the binding energy eject from the surface without melting and evaporation of the source material. Typically, the chamber is first evacuated to a high vacuum level, the base pressure, to abate any background gases and possible contaminants' partial pressures. Some of the incident Ar ions scatter off the target surface and do not contribute to the effective sputtering process. Combined with magnetic fields (hence the expression "magnetron"), the generated plasma's electrons get confined near the target's surface. The improved "sputtering yield," using this technique, has a broader range of applications for the deposition of several thin-film materials [28,29].

The sputter yield describes the number of sputtered atoms (including the material ejected as ions, molecules, and clusters) per incoming particle, thereby measuring the target material's efficiency to the respective incoming particle mass [28]. The direct-current (DC) magnetron sputtering offers an easy-to-control and low-cost method for metal deposition. The different sputtering parameters such as power, argon (Ar) pressure, substrate temperature, and deposition time significantly affect the electrical, mechanical, structural, and adhesion properties of Mo back contact. The technique and parameters also influence the thin film's grain sizes and crystal orientations [6]. A compelling advantage of sputtering lies with the sputtered atomic species' energy on the substrate's surface. The ejected atoms or molecules attach to the substrate with kinetic energy higher than conventional evaporation and produce denser layers and improve the substrate's mechanical attachment [30].

The different deposition parameters (sputtering power, argon (Ar) pressure, deposition time, the incident angle of bombarding ions [31]) significantly affect the structural, electrical, and mechanical properties of the deposited Mo contacts [26,32–34], which seems to improve with high-temperature treatment [35]. The use of optimized source-to-substrate distance and low rotation-per-minute substrates ensures excellent uniformity over a given surface area. The deposited film structure also influences the diffusion of atoms through the back-contact into the absorber layer [33,34,36,37], with significant dependence on the density, number of crystallites per unit area, and crystallite size, as well as dislocation density of the film [7,26,38,39].

Different optimal layer parameters allow for the deposition of thin-films multi-layers that show better qualities than a single-layer deposition. For example, Mo films deposited at relatively higher power and lower pressures exhibit better conductivity; however, with smaller grain sizes and higher densities, which can inhibit Na's desired moderate inclusion from the SLG. Higher deposition powers can also result in more kinetic energies of the sputtered ionic species leading to potential impregnation of the existing layers instead of the desired deposition. On the other hand, lower deposition power and higher pressures lead to the deposition of lesser dense films, which are usually more resistive and more transparent. The combination of optimized parameters to combine more than one layer of Mo allows for the thin-films with superior qualities than a single-layer, either by variation of power at constant pressure or the variation of the sputtering pressure [11,12].

This study proposes a bilayer deposition of Mo back contact thin film using parameters from optimized sputtering conditions (power, pressure) with fixed optimized source-to-substrate and rpm conditions.

3.3 CIGSe fabrication

Thermal evaporation presents a simple physical vapor deposition technique that allows for the atoms or molecules' significant ejection from a heated surface. The evaporated particles through joule heating condense on a substrate where they nucleate together to form a thin film coating, usually in a vacuum environment below 1×10^{-5} Torr (1.3×10^{-3} Pa) [4,40]. A high vacuum is essential to reduce the mean free path of the gas molecules (greater than 1 meter below 10^{-5} Torr), making the evaporation highly directional. It also ensures greatly improved film purity, reducing background gases and possible contamination (e.g., oxygen, moisture) [41].

Comparatively, the energy of the impinging ions from thermal evaporation to the substrate's surface is lower than sputtering, necessitating applying a specific quantity substrate temperature to improve the microstructure of the thin-film during growth. Consequently, the deposited layers generally present a microstructure, which is widely different from the bulk material evaporated [30].

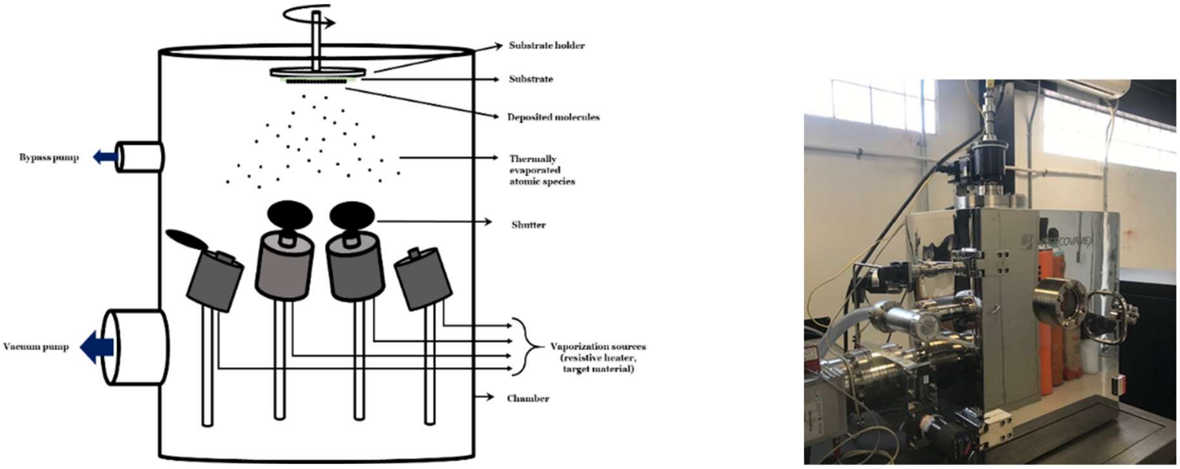

(a) *(b)*

Figure 3. 2 *(a) A schematic diagram for a thermal evaporation system (b) Co-evaporation equipment with four sources. for depositing the CI(G)Se absorber layer*

The properties of a given thin-film material (e.g., crystallographic, microstructure, and topographical) depend on the growth kinetics of and some parameters, including the source and substrate temperature, energy of atomic/molecular species, the topography of the substrate, and presence of ambient gases among other possible factors [31,42]. These factors affect the thin-films' initial nucleation stages' density, determining the crystallite sizes or the lateral grain sizes. Subsequent annealing after depositions can influence recrystallization and may affect the grain parameters.

The co-evaporation technique is more versatile and economical than several other methods (e.g., MBE, ALD) to prepare binary and ternary compound thin films. It taps into the advantages of thermal evaporation to evaporate to or more metal sources in vapor conditions. In comparison to other thin-film deposition techniques, it offers other advantages, which include:

a. Comparatively inexpensive and non-tedious metallurgy for preparing thin-films and direct introduction dopants in their elemental form with doping level easily controlled
b. Employs the vapor pressures of the elements which are high enough at low temperatures (50 < T < 1500 °C) to evaporate the materials
c. The control of stoichiometry of the films by varying the evaporation rates of separate elements allows for better control of the carrier density and the type of conductivity of the compound

d. Since various elements have different vapor pressures for evaporation, this offers a degree of purification even from non-purified sources during deposition

It offers better control of film thicknesses in low vacuum and deposition conditions, and the growth can be started and stopped abruptly. These advantages allow for the deposition of a wide variety of materials with reasonable control of homogeneity and stoichiometry.

3.3.1 Three-stage co-evaporation and selenization

The three-stage method adopts the advantages of co-evaporation for the stepwise deposition of metallic precursors for the absorber layer fabrication [43,44]. The adopted steps in the presence of selenium continually evaporated are;

a. co-evaporation of In, Ga, and Se in the first stage
b. the second step involving the co-evaporation of Cu and Se, preferentially at a higher temperature to allow for diffusion and intermixing of the elements;
c. in the final step, In, Ga, and Se's deposition, the overall composition is Cu deficient.

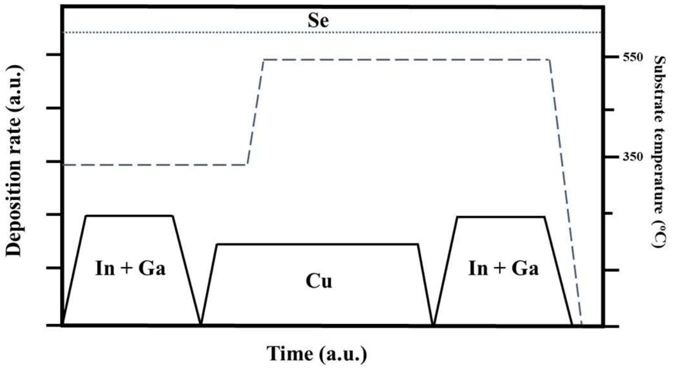

Figure 3. 3 *Schematic of the adopted 3-stage deposition (not to scale) for the CIGSe absorber, with the application of substrate temperatures. The deposition rates vary, and the deposition time adjusted to obtained desired thickness and compositions within the layer, with selenium constantly evaporated throughout the deposition.*

Typical high-efficiency CIGSe absorbers possess a preferential (112) or 220/(204) orientation required for high-efficiency devices, and the surfaces of the Cu deficient CIGSe compound presents an ordered defect compound (ODC), characteristically with a stoichiometry of Cu(In,

$Ga)_3Se_5$ [45]. The ODC is n-type and forms a p–n homojunction at the interface between the chalcopyrite and the ODC, reducing the interface recombination [46,47].

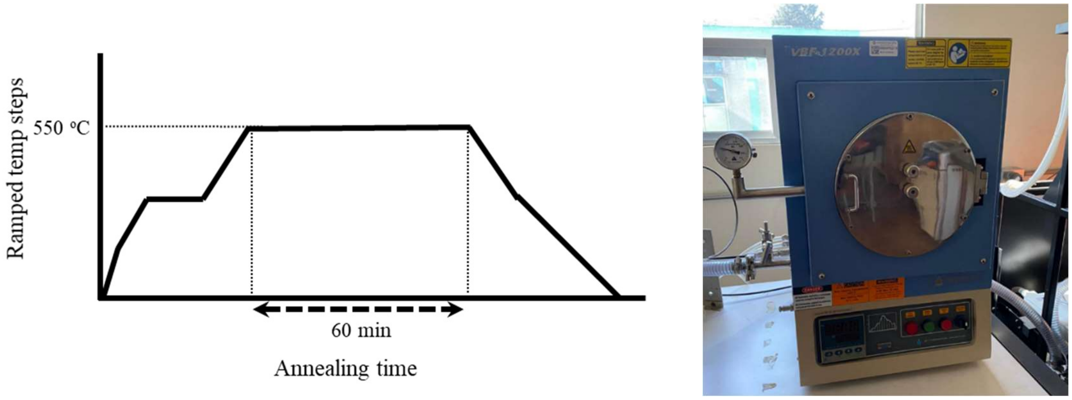

(a) *(b)*

Figure 3. 4 *(a) Schematic diagram of the ramped selenization method in argon (Ar) atmosphere (b) vacuum selenization equipment for thermal treatments in Ar atmosphere*

In addition to Na, other impurities in the absorber layer, e.g., oxygen, can also influence the solar cell's performance. The oxygen reportedly enhances the absorber's net p doping and reduces grain boundary recombination, thereby improving the intergrain transport [48,49]. The absorber layer fabrication was interrupted after the three-stage co-evaporation and exposed to an open-air atmosphere before further selenization using the ramped technique (Fig. 3.4) in a controlled argon environment at a temperature of 550 °C for 60 minutes.

3.3.2 Post-deposition treatments with alkali halides using non-vacuum spin-coating method

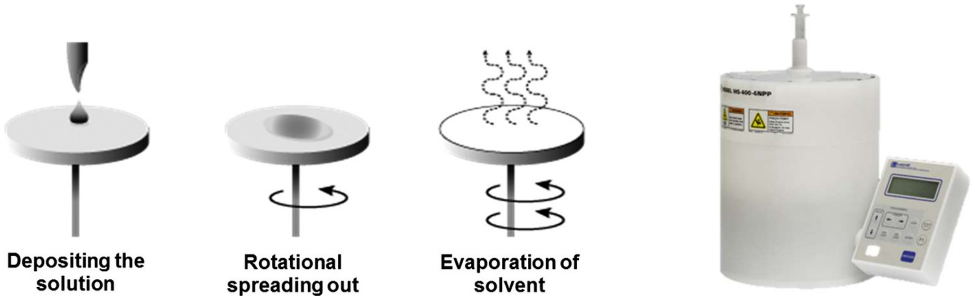

(a) *(b)*

Figure 3. 5 *(a) The schematic diagram for the spin-coating process and (b) spin coater (Laurell Model WS-400-6NPP) used for alkali PDT*

The recent advances and improvements in chalcopyrite CIGSe solar cells' efficiencies are mainly due to incorporating alkali metals through post-deposition treatments (PDT) [50–56]. Although not completely understood, the mechanisms for the improvements by these alkali metals reportedly vary from mainly bulk effects for the lighter alkali atoms to surface effects for the heavier alkali atoms. The conventional method for the PDT is the evaporation of the alkali fluorides in the vacuum, which allows for the evaporation of the volatile fluorine component leaving behind the alkali metals. The evaporation and low thickness of the alkali metal layers needed (<100 nm) may be challenging to obtain in the vacuum, especially over larger surfaces. Vacuum systems are also relatively more expensive than their non-vacuum contemporaries.

The non-vacuum spin-coating method's significant advantage is relatively low-cost due to its less complex and inherently low investment requirements for device fabrication and comparative cost-to-efficiency ratios. Although lacking comparative advantage against vacuum systems in structures, high purity, and degree of horizontal molecular orientation, it offers higher throughput and substantial area uniformity, with better material utilization and potentially lower energy requirements [57]. Presenting some results that described the performance of spin-coated materials as "deteriorated" compared with vacuum-deposited films, Shibata et al. [56] showed that performance degradation could improve with conditioning with viability for application in device fabrication. The contamination by oxygen and other ambient gases is removed by depositing within the inert Ar atmosphere or nitrogen (N_2) environment. Approximate thermal treatments aids in removing residual solvent and probable carbon contaminants, which have adverse effects on the absorber layer [57].

3.4 Cadmium sulfide (CdS) deposition and characterization

The immense interest from several researchers in the use of cadmium sulfide (CdS) semiconductor material spans over a wide range of engineering and industrial applications [58–62] and mostly as a buffer material in high-efficient solar cell applications [63–65]. It is the preferred choice for CIGSe thin-film solar cells, among other choices, e.g., In_2S_3, TiO_2, $In(OH)_3$, ZnSe, (Zn, Mg)O, $InZnSe_x$, ZnS [66–72] due to the comparatively improved interactions through better lattice matching and conduction band alignment, also chemical compatibility [73–76].

The deposited thin-films properties also tend to vary marginally depending on the adopted deposition technique and present complexing agents used in chemical methods [77–80]. Several physical and chemical optimized deposition techniques, e.g., sputtering, chemical bath deposition (CBD) [81–90], used to deposit the CdS buffer layer, aim at reducing the losses at the heterojunctions (e.g., recombination losses) and associated with the thickness (e.g., V_{oc} losses) within the buffer layer. Moderately optimized thickness of the thin-film allows for the sufficient passage of light with desirable transparency and minimal attenuation accompanying very thick layers. At the same time, too thin layers cause short-circuits within the solar cell device. Most studies on (CdS) buffer layers attempt to overcome the open-voltage limitation of about 1.0V, which may be due to the bulk properties of the intrinsic layer (Urbach edges), junction recombination, or the properties of the p- and n-layers used (built-in potential) [91,92].

The CBD technique often used for the high-efficient solar cells offers several advantages, including low-temperature processing, easily scalable for industrial applications, comparatively lower cost. During the growth process, the released cadmium and sulfur ions, with a complexing agent's help, condense on the substrate. Effectively controlling the ions' release can influence the thin-film properties, preferably creating Cd excess or S vacancies [93]. The nucleation stages also influence the formation of favorable Cd_{Cu} during device fabrication, which improves the p-n junction [94]. Nucleation and subsequent growth during CBD depend on the parameters, including the molarity (concentration) of the precursor material, bath temperature, deposition time, pH of the solution, speed of stirrer, nature (surface) of the substrate, and presence of complexing agents [78].

The CBD technique often used for the high-efficient solar cells offers several advantages, including low-temperature processing, easily scalable for industrial applications, comparatively lower cost. During the growth process, the released cadmium and sulfur ions, with a complexing agent's help, condense on the substrate. Effectively controlling the ions' release can influence the thin-film properties, preferably creating Cd excess or S vacancies [93]. The nucleation stages also influence the formation of favorable Cd_{Cu} during device fabrication, which improves the p-n junction [94]. Nucleation and subsequent growth during CBD depend on the parameters, including the molarity (concentration) of the precursor material, bath temperature, deposition time, pH of the solution, speed of stirrer, nature (surface) of the substrate, and presence of complexing agents [78].

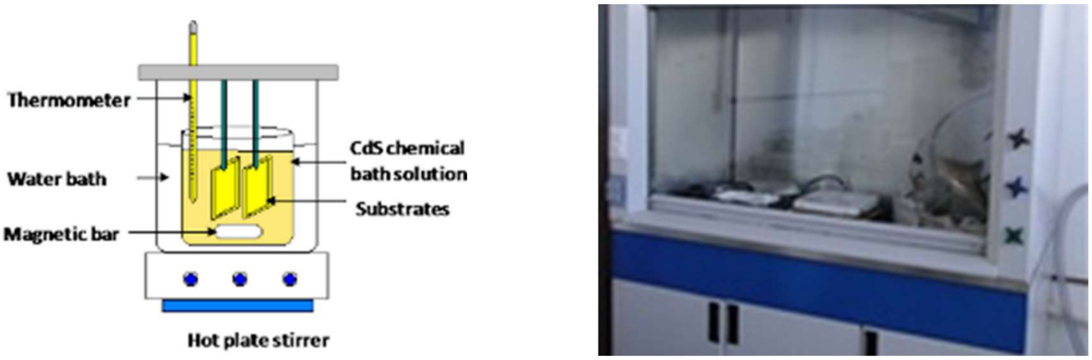

(a) *(b)*

Figure 3. 6 *(a) Schematic diagram of a CdS chemical bath deposition system [95] (b) chemical bath deposition hood for CdS deposition*

3.5 Transparent conducting oxide (TCO) deposition

The essential requirements for the materials used for TCO materials include low electrical (sheet) resistivity and high optical transmittance for efficient collection of the photo-generated charges. Aluminum-doped zinc oxide (AZO) provides a viable alternative to indium tin oxide (ITO) to avoid the toxicity and potentially high cost associated with indium. Other considerations include low thermal budget fabrication, flexibility, and stability against stretching and bending forces to which ITO is not ideally applicable [96,97]. For solar cell applications, the AZO layer is by vacuum or solution thin-film deposition techniques, e.g., pulsed-laser deposition, atomic layer deposition, magnetron sputtering, chemical vapor deposition, spray pyrolysis, and the sol-gel process [96,98–102].

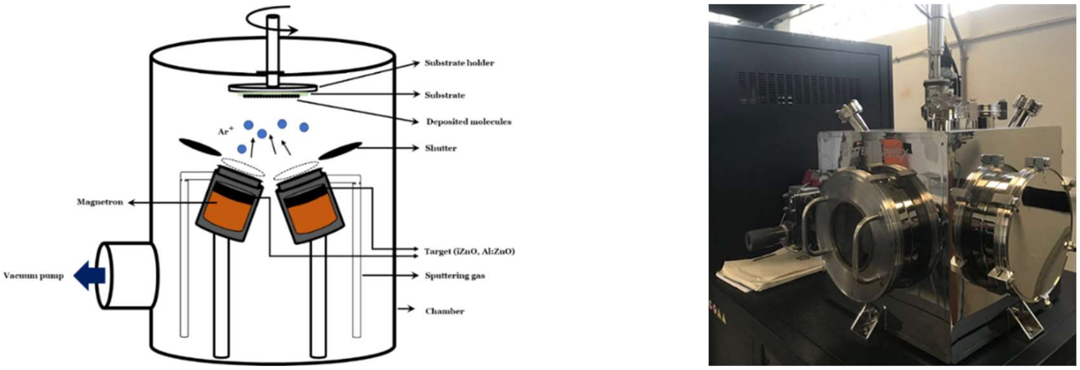

(a) *(b)*

Figure 3. 7 *(a) A schematic diagram for a radio-frequency sputtering system. (b) radio-frequency sputtering machine for depositing metals, metal oxides, and ceramics, used for TCO layer deposition on the solar cell*

The AZO deposition using radio-frequency (RF) offers some advantages, including the potential for low-temperature growth, industrial applicability, relatively excellent uniformity, and reproducibility. Comparatively, direct current (DC) sputtering has twice the deposition rate as RF but shows reduced transmission at room temperatures. In contrast, RF sputtering gives an excellent transfer at all temperatures, and the deposition rate is independent of deposition temperature [97,103].

Optimized deposition parameters allow for deposition of low thickness AZO thin-films with low resistivity (high carrier concentration) and high optical transmittance. AZO thin films' reported values for solar cell application ranges between 1×10^{-4} to 10 Ω-cm. The lower resistivity values are attained with post-deposition treatment, usually by annealing at elevated temperatures up to 500°C [96,102,104]. Isherwood [97] reported that thin films deposited with temperatures of 200 °C and less had comparably lower resistivities than films deposited at higher temperatures. Furthermore, the elevated temperatures, which can help reduce the films' resistivity and improve grain growths, can cause degradation of the CdS layer in the device and Zn's possible diffusion into the buffer layer.

The inclusion of Al^+ dopant concentration as impurities in ZnO changes the resistivity by increasing the carrier concentrations, bandgap energy, and photoelectrical properties [105,106]. The Al concentration between 1 and 3 at% reported better electrical, optical, and morphological properties [102]. Also, recent reports on high-efficiency solar cells with low thickness, ca. 100 nm produces better excellent efficiency in comparison with the commonly deposited thick layers [101].

The performance with different thicknesses, transparency, and resistivity, can be quantitatively evaluated using a quality factor (QF) (similar to the figure of merit (FOM defined by [107]):

$$\text{QF} = \text{transmittance x sheet conductance} = \text{transmittance / sheet resistance} \qquad \textbf{(Eqn. 3. 1)}$$

The better conditions should give QF's higher value, which requires a low sheet resistance and high transparency. A sufficiently thin layer is required to achieve a high transmittance, which inversely causes a higher sheet resistance in the thin films. Thus, the above inverse relation puts a limit on the QF value. Potentially high QF values have been achieved with ITO thin films with high conductivity [108,109]. However, their low transparency, around 78%, is much lower than the essential requirement for transparent conductors (T > 85%), and the disadvantages associated with ITO also pose additional problems [110].

The AZO thin film deposition using an RF-magnetron sputtering system with an operating frequency between 50-60 Hz allows for better control of the power and pressure, influencing the sputtered films' properties. The target-to-substrate distance was adjusted to about 6.0 cm and tilted to about 55° to the horizontal as these conditions affect physical deposition techniques [111]. The base pressure for all film depositions at approximately 5.0×10^{-6} Torr helps eliminate the potential contaminants' deposition chamber. The variation of the argon (Ar) flux at different sccm rates controls the sputtering pressure. The zinc oxide with alumina target (ZnO/Al_2O_3, 98/2 wt%; 3.00" (76.2 mm) diameter and 0.250" (6.35 mm) thickness with 99.999% pure part) from Kurt J. Lesner was the target for the sputtering, and Argon (Ar, 99.99%) from Infra group-Mexico (Industrial line standards) serving as the sputtering gas. The variation of deposition power between 50 W to 135 W with low reflected power, less than 3 W, accommodates the limits of the maximum power density, 20 W/inch^2 of the AZO target, and optimizing the sputtering power. The working pressures varied from 5.0 mTorr to 25 mTorr. The depositions carried out at ambient had the temperatures rise to about 43 ºC due to non-intentional heating and up to 200 ºC applied substrate temperatures. A substrate rotation of about 0.05 rpm was maintained in depositions to ensure the film's uniformity over 100 cm^2 surface area.

3.6 Samples characterization

We characterized the thin-films with no further sample preparations and ambient conditions existing within the characterizing equipment.

An essential characteristic of thin-film devices is the thickness, which ranges in the order of nanometers to a few microns, and profilometry, in which a probe, mechanical (contact) or optical (non-contact), is passed across the surface, offers a method to measure the thickness of the layers and devices. The substrates' rotation during deposition ensures uniformity of the grain cluster growth in the vertical direction and, consequently, the films' thickness. The probe follows the contours at different points on the surface, and the average recorded heights of the probe at different points on the sample or device gives the thickness of the measurement [112]. The thickness of the deposited thin-films was measured by Bruker's DektakXT® Stylus surface profiler in the mechanical contact mode using the step created during the deposition.

X-ray diffraction, based on Bragg's law (nλ = 2dsinθ), presents a potent non-destructive, and commonly used method for characterizing crystalline materials providing information on the preferred crystal orientations (texture), structures, phases, and other structural parameters, e.g., average crystallite size, crystallinity, strain, stress, and some crystal defects [3,113].

The coherently diffracting domain (crystallite) sizes (Dp) calculated using the Scherrer equation (Eq. 2) from the full width at half maximum (β—FWHM) value is,

$$D_p = \frac{K\lambda}{\beta\, cos} \qquad \textbf{(Eqn. 3. 2)}$$

β is the X-ray peak's width, generally measured as the full-width at half-maximum (FWHM) after the correction of error due to instrumental broadening, θ is the Bragg angle, and K is the so-called Scherrer constant. K depends on the crystallite shape and the size distribution, and the indexes of the diffraction line. K also depends on the definition used for β, whether FWHM or integral breadth, the total area under the diffraction peak divided by the maximum peak intensity. K can have values anywhere from 0.62 and 2.08. In the absence of any information on crystal shape, K ranges between 0.89–1. In the present work, K = 0.94, and the size calculations should be considered approximate. The results will have uncertainties arising from the uncertainty in K, as discussed in [114]. The resulting strain (*e*) on the films and the microstrain (ε) on the films is given by equations (3.3) [115] and (3.4) [116],

$$e = \frac{a - a_{bulk}}{a_{bulk}} \qquad \textbf{(Eqn. 3. 3)}$$

a and a_{bulk} are the measured and bulk lattice parameter values, respectively.

$$\varepsilon = \frac{\beta \cot \theta}{4} \qquad \textbf{(Eqn. 3. 4)}$$

Williamson and Smallman's formula [117] estimates the dislocation density (δ), using the equation (3.5)

$$\delta = \frac{1}{D_p^2} \qquad \textbf{(Eqn. 3. 5)}$$

while the number of crystallites/unit area (N) for a given thickness (t) is given by (3.6) [118]

$$N = \frac{t}{D_p^3} \qquad \textbf{(Eqn. 3. 6)}$$

The surface morphology studies using scanning electron microscopy (SEM) avails a technique for obtaining high-resolution electronic images of different materials' surfaces. SEM studies offer clear, high-resolution images of the grain sizes and surface texture of particles. The analytical technique of energy-dispersive X-ray spectroscopy (EDS), usually accompanying the SEM, allows obtaining information about the elemental composition of supposed particles based on X-rays emitted from different points of the surface of the sample [119].

The scanning probe technique using atomic force microscopy (AFM) gives the profiles of the sample surfaces with an excellent horizontal and vertical resolution (~ 0.2 and 0.01 nm, respectively) [120]. The topography of the thin-films substantially influences the bulk properties of the material [112]. The topographical studies AFM carried out using NT-MDT, NTEGRA Spectra were in semi-contact mode. The images can be affected by the piezoelectric material's hysteresis and cross-talk between the (x, y, z) axes that may require software enhancement and filtering. Such filtering could 'flatten' out real topographical features. The images obtained in ambient conditions with no special sample preparation were analyzed using the IA-P9 software.

The electrical properties of thin-film layers in the form of resistivity of the contacts and the charge properties (e.g., concentration, mobility) of the semiconducting layers are vital to the device's performance. The sheet resistance (or surface resistivity) measures resistance across the surface of a conducting material. For thin-films (with thickness is less than 40% of the probe spacing), the sheet resistance, R_s (in Ω/□) is given by,

$$R_S = \frac{\pi}{In\,2} \times \frac{V}{I} = \frac{resistivity\ (\rho)}{thickness\ (t)} \qquad \textbf{(Eqn. 3. 7)}$$

However, the standard four-point probe cannot provide information concerning the semiconducting materials' carrier properties [121]. The Hall effect measurements is a method to determine the carrier concentration, carrier type, and when attached with a resistivity measurement, the mobility of a material [122,123]. All Hall measurements for the semiconducting samples were carried out in ambient conditions with a magnetic field of 5500G and using Au ohmic contacts.

UV–Visible (UV–Vis) spectrophotometer (Jasco V-670) used to measure the optical properties of the films within the UV-Vis spectral region (200 nm to 800 nm) provided information on the transmittance, reflectance, and bandgap of the measure materials. Spectral characterization for the films' composition and the structure was carried out with photoluminescence (PL) measurements using JOBIN YVON HORIBA SPEX MSD2 spectrometer with UV Laser (325nm) excitation, providing a non-destructive and non-contact method for analyzing the electronic structure of materials. Raman spectroscopy, based on an inelastic scattering process, is a vital tool in the field of vibrational spectroscopy with the change in the wavelength of the photon scattered by the sample's molecule, known as the "Raman shift" characteristic of the molecules in the incident light it interacts with [124,125]. The information from the spectra proves useful in knowing the bonds and vibrational modes present in a material.

The surface characterization using atomic force microscopy (AFM) (NT-MDT, NTEGRA Spectra) allowed for surface analysis in a non-contact mode for the thin films' topographical information, which plays a significant role in the interface. Analysis of the obtained 2D and 3D micrographs was analyzed using the IA-P9 software, and images were taken in ambient conditions with no special sample preparation. The most commonly used parameters to analyze the surface texture include roughness, waviness, lay, and flows. These parameters represent the random variations of the grains found in the films [6,126].

The depth profile using the secondary ion mass spectroscopy (SIMS) provides a composite of mass spectra collected from each level within the sample [127]. The depth profile measurements of the structures carried out using the ION TOF TOF-SIMS5 Time-of-Flight Secondary Ion Mass Spectrometer (TOF-SIMS) in-depth profile mode employing Cs^+ ion gun provided an analytical technique for chemical identification and determination of elemental concentrations of the elements.

References

[1] M. Ohring, The Materials Science of Thin Films, ACADEMIC PRESS LIMITED, London, 1992.

[2] D.S. Ginley, J.D. Perkins, Handbook of Transparent Conductors, Springer US, Boston, MA, 2011. https://doi.org/10.1007/978-1-4419-1638-9.

[3] K.L. Chopra, Thin film phenomena, McGraw-Hill, New York, 1969. http://www.uniprot.org/uniprot/P00441.

[4] K. Wasa, M. Kitabatake, H. Adachi, Thin Film Processes, in: Thin Film Mater. Technol., Elsevier, 2004: pp. 17–69. https://doi.org/10.1016/b978-081551483-1.50003-4.

[5] J.A. Shields, Applications of Molybdenum Metal and its Alloys, 2013. www.imoa.info (accessed May 2, 2020).

[6] M.M. Aqil, M.A. Azam, M.F. Aziz, R. Latif, Deposition and characterization of molybdenum thin film using direct current magnetron and atomic force microscopy, J. Nanotechnol. 2017 (2017). https://doi.org/10.1155/2017/4862087.

[7] J.-H. Yoon, S. Cho, W.M. Kim, J.-K. Park, Y.-J. Baik, T.S. Lee, T.-Y. Seong, J. Jeong, Optical analysis of the microstructure of a Mo back contact for Cu(In,Ga)Se2 solar cells and its effects on Mo film properties and Na diffusivity, Sol. Energy Mater. Sol. Cells. 95 (2011) 2959–2964. https://doi.org/10.1016/j.solmat.2011.02.030.

[8] R. Syed, S.K. Ghosh, P.U. Sastry, G. Sharma, R.C. Hubli, J.K. Chakravartty, Electrodeposition of thick metallic amorphous molybdenum coating from aqueous electrolyte, Surf. Coatings Technol. 261 (2015) 15–20. https://doi.org/10.1016/j.surfcoat.2014.11.073.

[9] R.J. Matson, O. Jamjoum, A.D. Buonaquisti, P.E. Russell, L.L. Kazmerski, P. Sheldon, R.K. Ahrenkiel, Metal contacts to CuInSe2, Sol. Cells. 11 (1984) 301–305. https://doi.org/10.1016/0379-6787(84)90019-X.

[10] Y. Osman, M. Fedawy, M. Abaza, M.H. Aly, Solar cell performance enhancement with optimized CIGS absorber bandgap and buffer layer, J. Phys. Conf. Ser. 1447 (2020) 012057. https://doi.org/10.1088/1742-6596/1447/1/012057.

[11] J.H. Scofield, A. Duda, D. Albin, B.L. Ballard, P.K. Predecki, Sputtered molybdenum

bilayer back contact for copper indium diselenide-based polycrystalline thin-film solar cells, Thin Solid Films. 260 (1995) 26–31. https://doi.org/10.1016/0040-6090(94)06462-8.

[12] P.M.P. Salomé, J. Malaquias, P.A. Fernandes, A.F. da Cunha, Mo bilayer for thin film photovoltaics revisited, J. Phys. D. Appl. Phys. 43 (2010) 345501. https://doi.org/10.1088/0022-3727/43/34/345501.

[13] C.Y. Shi, Y. Sun, Q. He, F.Y. Li, J.C. Zhao, Cu(In,Ga)Se 2 solar cells on stainless-steel substrates covered with ZnO diffusion barriers, Sol. Energy Mater. Sol. Cells. 93 (2009) 654–656. https://doi.org/10.1016/j.solmat.2008.12.004.

[14] C.-W. Kim, H.J. Kim, J.H. Kim, C. Jeong, Characterization of Flexible CIGS Thin Film Solar Cells on Stainless Steel with Intrinsic ZnO Diffusion Barriers, J. Nanosci. Nanotechnol. 16 (2016) 5124–5127. https://doi.org/10.1166/jnn.2016.12198.

[15] P. Blösch, F. Pianezzi, A. Chirilă, P. Rossbach, S. Nishiwaki, S. Buecheler, A.N. Tiwari, Diffusion barrier properties of molybdenum back contacts for Cu(In,Ga)Se2 solar cells on stainless steel foils, J. Appl. Phys. 113 (2013). https://doi.org/10.1063/1.4789616.

[16] K. Herz, A. Eicke, F. Kessler, R. Wächter, M. Powalla, Diffusion barriers for CIGS solar cells on metallic substrates, Thin Solid Films. 431–432 (2003) 392–397. https://doi.org/10.1016/S0040-6090(03)00259-1.

[17] W.-S. Liu, H.-C. Hu, N.-W. Pu, S.-C. Liang, Developing flexible CIGS solar cells on stainless steel substrates by using Ti/TiN composite structures as the diffusion barrier layer, J. Alloys Compd. 631 (2015) 146–152. https://doi.org/10.1016/j.jallcom.2014.12.189.

[18] A. Rockett, J.S. Britt, T. Gillespie, C. Marshall, M.M. Al Jassim, F. Hasoon, R. Matson, B. Basol, Na in selenized Cu(In,Ga)Se2 on Na-containing and Na-free glasses: distribution, grain structure, and device performances, Thin Solid Films. 372 (2000) 212–217. https://doi.org/10.1016/S0040-6090(00)01028-2.

[19] S. Bini, B. Spataro, A. Marcelli, S. Sarti, V.A. Dolgashev, S. Tantawi, A.D. Yeremian, Y. Higashi, M.G. Grimaldi, L. Romano, F. Ruffino, R. Parodi, G. Cibin, C. Marrelli, M. Migliorati, C. Caliendo, Molybdenum sputtering film characterization for high gradient accelerating structures, Chinese Phys. C. 37 (2013) 097005. https://doi.org/10.1088/1674-1137/37/9/097005.

[20] N. Lifshitz, Selective Molybdenum Deposition by LPCVD, J. Electrochem. Soc. 134 (1987) 2061. https://doi.org/10.1149/1.2100820.

[21] T.J. Morley, L. Penner, P. Schaffer, T.J. Ruth, F. Bénard, E. Asselin, The deposition of smooth metallic molybdenum from aqueous electrolytes containing molybdate ions, Electrochem. Commun. 15 (2012) 78–80. https://doi.org/10.1016/j.elecom.2011.11.026.

[22] W. Zhu, T. Low, Y.-H. Lee, H. Wang, D.B. Farmer, J. Kong, F. Xia, P. Avouris, Electronic transport and device prospects of monolayer molybdenum disulphide grown by chemical vapour deposition, Nat. Commun. 5 (2014) 3087. https://doi.org/10.1038/ncomms4087.

[23] A.T.T. Mostako, A. Khare, Molybdenum thin films via pulsed laser deposition technique for first mirror application, Laser Part. Beams. 30 (2012) 559–567. https://doi.org/10.1017/S0263034612000560.

[24] D.H. Kwon, Z. Jin, S. Shin, W.-S. Lee, Y.-S. Min, A comprehensive study on atomic layer deposition of molybdenum sulfide for electrochemical hydrogen evolution, Nanoscale. 8 (2016) 7180–7188. https://doi.org/10.1039/C5NR09065B.

[25] A. Morán, O. Nwakanma, S. Velumani, H. Castaneda, Comparative study of optimised molybdenum back-contact deposition with different barriers (Ti, ZnO) on stainless steel substrate for flexible solar cell application, J. Mater. Sci. Mater. Electron. 31 (2020) 7524–7538. https://doi.org/10.1007/s10854-020-03058-7.

[26] O. Nwakanma, P. Reyes, S. Velumani, Electrical, structural, and topographical properties of direct current (DC) sputtered bilayer molybdenum thin films, J. Mater. Sci. Mater. Electron. 29 (2018) 15671–15681. https://doi.org/10.1007/s10854-018-9165-2.

[27] J. Sarkar, Sputtering Targets and Sputtered Films for the Microelectronic Industry, in: Sputtering Mater. VLSI Thin Film Devices, Elsevier, 2014: pp. 1–92. https://doi.org/10.1016/b978-0-8155-1593-7.00001-1.

[28] M. Braun, Magnetron Sputtering Technique, in: Handb. Manuf. Eng. Technol., Springer London, London, 2015: pp. 2929–2957. https://doi.org/10.1007/978-1-4471-4670-4_28.

[29] Magnetron Sputtering Overview, (n.d.). https://angstromengineering.com/tech/magnetron-sputtering/ (accessed June 5, 2020).

[30] C. Grèzes-besset, G. Chauveau, Optical coatings for large facilities, in: Opt. Thin Film.

Coatings, Elsevier, 2013: pp. 695–717. https://doi.org/10.1533/9780857097316.4.695.

[31] W. Kiyotaka, K. Isaku, K. Hidetoshi, Handbook of Sputter Deposition Technology: Fundamentals and Applications for Functional Thin Films, 2012.

[32] K. Sun, F. Liu, J. Huang, C. Yan, N. Song, H. Sun, C. Xue, Y. Zhang, A. Pu, Y. Shen, J.A. Stride, M. Green, X. Hao, Flexible kesterite Cu 2 ZnSnS 4 solar cells with sodium-doped molybdenum back contacts on stainless steel substrates, Sol. Energy Mater. Sol. Cells. 182 (2018) 14–20. https://doi.org/10.1016/j.solmat.2018.02.036.

[33] W.J. Lee, D.H. Cho, J.H. Wi, W.S. Han, J. Kim, Y.D. Chung, Na effect on flexible Cu(In,Ga)Se2 photovoltaic cell depending on diffusion barriers (SiOx, i-ZnO) on stainless steel, Mater. Chem. Phys. 147 (2014) 783–787. https://doi.org/10.1016/j.matchemphys.2014.06.021.

[34] G.L. Agawane, S.W. Shin, S.A. Vanalakar, M.P. Suryawanshi, A. V. Moholkar, J.H. Kim, Investigations on chemo-mechano stabilities of the molybdenum thin films deposited by DC-sputter technique, Zeitschrift Fur Phys. Chemie. (2015). https://doi.org/10.1515/zpch-2014-0624.

[35] E. Moons, T. Engelhard, D. Cahen, Ohmic Contacts to p-CulnSe 2 Crystals, J. Electron. Mater. 22 (1993) 275–280. https://doi.org/10.1007/BF02661377.

[36] C. Yan, J. Huang, K. Sun, S. Johnston, Y. Zhang, H. Sun, A. Pu, M. He, F. Liu, K. Eder, L. Yang, J.M. Cairney, N.J. Ekins-Daukes, Z. Hameiri, J.A. Stride, S. Chen, M.A. Green, X. Hao, Cu2ZnSnS4 solar cells with over 10% power conversion efficiency enabled by heterojunction heat treatment, Nat. Energy. 3 (2018) 764–772. https://doi.org/10.1038/s41560-018-0206-0.

[37] S.M. Pandharkar, S.R. Rondiya, A. V. Rokade, B.B. Gabhale, H.M. Pathan, S.R. Jadkar, Synthesis and Characterization of Molybdenum Back Contact Using Direct Current-Magnetron Sputtering for Thin Film Solar Cells, Front. Mater. (2018). https://doi.org/10.3389/fmats.2018.00013.

[38] J. Li, S. Glynn, L. Mansfield, M. Young, Y. Yan, M. Contreras, R. Noufi, F.L. Terry, D. Levi, Density profiles in sputtered molybdenum thin films and their effects on sodium diffusion in Cu(In xGa 1-x)Se 2 photovoltaics, Conf. Rec. IEEE Photovolt. Spec. Conf. (2011) 002749–002752. https://doi.org/10.1109/PVSC.2011.6186516.

[39] K.H. Ong, R. Agileswari, B. Maniscalco, P. Arnou, C.C. Kumar, J.W. Bowers, M.B. Marsadek, Review on substrate and molybdenum back contact in CIGS thin film solar cell, Int. J. Photoenergy. 2018 (2018). https://doi.org/10.1155/2018/9106269.

[40] D.M. Mattox, Handbook of Physical Vapor Deposition (PVD) Processing, Elsevier, 2010. https://doi.org/10.1016/C2009-0-18800-1.

[41] Resistive Thermal Evaporation | Angstrom Engineering, (n.d.). https://angstromengineering.com/tech/resistive-thermal-evaporation/ (accessed June 8, 2020).

[42] K. Wasa, S. Hayakawa, Handbook of sputter deposition technology, 1992. https://doi.org/10.1073/pnas.0703993104.

[43] M.A. Contreras, J. Tuttle, A. Gabor, A. Tennant, K. Ramanathan, S. Asher, A. Franz, J. Keane, L. Wang, R. Noufi, High efficiency graded bandgap thin-film polycrystalline Cu(In,Ga) Se2-based solar cells, Sol. Energy Mater. Sol. Cells. 41–42 (1996) 231–246. https://doi.org/10.1016/0927-0248(95)00145-X.

[44] A.M. Gabor, J.R. Tuttle, D.S. Albin, M.A. Contreras, R. Noufi, A.M. Hermann, High-efficiency CuIn x Ga 1− x Se 2 solar cells made from (In x ,Ga 1− x) 2 Se 3 precursor films, Appl. Phys. Lett. 65 (1994) 198–200. https://doi.org/10.1063/1.112670.

[45] C. Xu, H. Zhang, J. Parry, S. Perera, G. Long, H. Zeng, A single source three-stage evaporation approach to CIGS absorber layer for thin film solar cells, Sol. Energy Mater. Sol. Cells. 117 (2013) 357–362. https://doi.org/10.1016/j.solmat.2013.06.006.

[46] J. Hedstrom, H. Ohlsen, M. Bodegard, A. Kylner, L. Stolt, D. Hariskos, M. Ruckh, H.-W. Schock, ZnO/CdS/Cu(In,Ga)Se/sub 2/ thin film solar cells with improved performance, in: Conf. Rec. Twenty Third IEEE Photovolt. Spec. Conf. - 1993 (Cat. No.93CH3283-9), IEEE, 1993: pp. 364–371. https://doi.org/10.1109/PVSC.1993.347154.

[47] M.A. Contreras, M.J. Romero, R. Noufi, Characterization of Cu(In,Ga)Se2 materials used in record performance solar cells, Thin Solid Films. 511–512 (2006) 51–54. https://doi.org/10.1016/j.tsf.2005.11.097.

[48] U. Rau, D. Braunger, R. Herberholz, H.W. Schock, J.F. Guillemoles, L. Kronik, D. Cahen, Oxygenation and air-annealing effects on the electronic properties of Cu(In,Ga)Se2 films

and devices, J. Appl. Phys. 86 (1999) 497–505. https://doi.org/10.1063/1.370758.

[49] L. Kronik, U. Rau, J.F. Guillemoles, D. Braunger, H.W. Schock, D. Cahen, Interface redox engineering of Cu(In,Ga)Se2-based solar cells: Oxygen, sodium, and chemical bath effects, Thin Solid Films. 361 (2000) 353–359. https://doi.org/10.1016/S0040-6090(99)00768-3.

[50] E. Handick, P. Reinhard, J.H. Alsmeier, L. Köhler, F. Pianezzi, S. Krause, M. Gorgoi, E. Ikenaga, N. Koch, R.G. Wilks, S. Buecheler, A.N. Tiwari, M. Bär, Potassium Postdeposition Treatment-Induced Band Gap Widening at Cu(In,Ga)Se2 Surfaces - Reason for Performance Leap?, ACS Appl. Mater. Interfaces. 7 (2015) 27414–27420. https://doi.org/10.1021/acsami.5b09231.

[51] D. Shin, J. Kim, T. Gershon, R. Mankad, M. Hopstaken, S. Guha, B.T. Ahn, B. Shin, Effects of the incorporation of alkali elements on Cu(In,Ga)Se2 thin film solar cells, Sol. Energy Mater. Sol. Cells. 157 (2016) 695–702. https://doi.org/10.1016/j.solmat.2016.07.015.

[52] P. Jackson, D. Hariskos, R. Wuerz, W. Wischmann, M. Powalla, Compositional investigation of potassium doped Cu(In,Ga)Se2 solar cells with efficiencies up to 20.8%, Phys. Status Solidi - Rapid Res. Lett. 8 (2014) 219–222. https://doi.org/10.1002/pssr.201409040.

[53] P. Reinhard, B. Bissig, F. Pianezzi, E. Avancini, H. Hagendorfer, D. Keller, P. Fuchs, M. Döbeli, C. Vigo, P. Crivelli, S. Nishiwaki, S. Buecheler, A.N. Tiwari, Features of KF and NaF Postdeposition Treatments of Cu(In,Ga)Se2 Absorbers for High Efficiency Thin Film Solar Cells, Chem. Mater. 27 (2015) 5755–5764. https://doi.org/10.1021/acs.chemmater.5b02335.

[54] R. Wuerz, W. Hempel, P. Jackson, Diffusion of Rb in polycrystalline Cu(In,Ga)Se2 layers and effect of Rb on solar cell parameters of Cu(In,Ga)Se2 thin-film solar cells, J. Appl. Phys. 124 (2018) 165305. https://doi.org/10.1063/1.5044629.

[55] D. Kreikemeyer-Lorenzo, D. Hauschild, P. Jackson, T.M. Friedlmeier, D. Hariskos, M. Blum, W. Yang, F. Reinert, M. Powalla, C. Heske, L. Weinhardt, Rubidium Fluoride Post-Deposition Treatment: Impact on the Chemical Structure of the Cu(In,Ga)Se 2 Surface and CdS/Cu(In,Ga)Se 2 Interface in Thin-Film Solar Cells, ACS Appl. Mater. Interfaces. 10 (2018) 37602–37608. https://doi.org/10.1021/acsami.8b10005.

[56] S. Kim, H. Tampo, H. Shibata, K. Matsubara, S. Niki, Effect of Combined Alkali (KF +

CsF) Post-Deposition Treatment on Cu(InGa)Se2 Solar Cells, Phys. Status Solidi - Rapid Res. Lett. 12 (2018) 1–5. https://doi.org/10.1002/pssr.201800372.

[57] A.R. Uhl, C. Fella, A. Chirilă, M.R. Kaelin, L. Karvonen, A. Weidenkaff, C.N. Borca, D. Grolimund, Y.E. Romanyuk, A.N. Tiwari, Non-vacuum deposition of Cu(In,Ga)Se2 absorber layers from binder free, alcohol solutions, Prog. Photovoltaics Res. Appl. 20 (2012) 526–533. https://doi.org/10.1002/pip.1246.

[58] A.A. Yadav, E.U. Masumdar, Photoelectrochemical investigations of cadmium sulphide (CdS) thin film electrodes prepared by spray pyrolysis, J. Alloys Compd. 509 (2011) 5394–5399. https://doi.org/10.1016/j.jallcom.2011.02.061.

[59] J. Zhang, D. Li, R. Chen, Q. Xiong, Laser cooling of a semiconductor by 40 kelvin, Nature. 493 (2013) 504–508. https://doi.org/10.1038/nature11721.

[60] S.D. Naik, S.K. Apte, R.S. Sonawane, U.P. Mulik, B.B. Kale, Nanostructured CdS/CdSSe glass composite for photonic application, Pramana. 65 (2005) 707–712. https://doi.org/10.1007/BF03010458.

[61] N. Zhu, A. Zhang, P. He, Y. Fang, Cadmium sulfide nanocluster-based electrochemical stripping detection of DNA hybridization, Analyst. 128 (2003) 260–264. https://doi.org/10.1039/b211987k.

[62] A. Dandia, V. Parewa, K.S. Rathore, Synthesis and characterization of CdS and Mn doped CdS nanoparticles and their catalytic application for chemoselective synthesis of benzimidazoles and benzothiazoles in aqueous medium, Catal. Commun. 28 (2012) 90–94. https://doi.org/10.1016/j.catcom.2012.08.020.

[63] J. Britt, C. Ferekides, Thin-film CdS/CdTe solar cell with 15.8% efficiency, Appl. Phys. Lett. 62 (1993) 2851–2852. https://doi.org/10.1063/1.109629.

[64] T. Wada, Microstructural characterization of high-efficiency Cu(In,Ga)Se2 solar cells, Sol. Energy Mater. Sol. Cells. 49 (1997) 249–260. https://doi.org/10.1016/S0927-0248(97)00201-8.

[65] A. Gupta, A.D. Compaan, All-sputtered 14% CdS⁄CdTe thin-film solar cell with ZnO:Al transparent conducting oxide, Appl. Phys. Lett. 85 (2004) 684–686. https://doi.org/10.1063/1.1775289.

[66] A. Ennaoui, M. Weber, R. Scheer, H.. Lewerenz, Chemical-bath ZnO buffer layer for CuInS2 thin-film solar cells, Sol. Energy Mater. Sol. Cells. 54 (1998) 277–286. https://doi.org/10.1016/S0927-0248(98)00079-8.

[67] A.M. Chaparro, C. Maffiotte, M.T. Gutiérrez, J. Herrero, J. Klaer, K. Siemer, D. Bräunig, Characterisation of CuInS2/ZnSe junctions by XPS and electroreflectance, Thin Solid Films. 387 (2001) 104–107. https://doi.org/10.1016/S0040-6090(00)01716-8.

[68] G. Gordillo, C. Calderón, CIS thin film solar cells with evaporated InSe buffer layers, Sol. Energy Mater. Sol. Cells. 77 (2003) 163–173. https://doi.org/10.1016/S0927-0248(02)00319-7.

[69] N. Naghavi, S. Spiering, M. Powalla, B. Cavana, D. Lincot, High-efficiency copper indium gallium diselenide (CIGS) solar cells with indium sulfide buffer layers deposited by atomic layer chemical vapor deposition (ALCVD), Prog. Photovoltaics Res. Appl. 11 (2003) 437–443. https://doi.org/10.1002/pip.508.

[70] P. Genevée, A. Darga, C. Longeaud, D. Lincot, F. Donsanti, Atomic layer deposition of ZnIn x S y buffer layers for Cu(In,Ga)Se 2 solar cells, J. Renew. Sustain. Energy. 7 (2015) 013116. https://doi.org/10.1063/1.4906912.

[71] R.A. Devi, M. Latha, S. Velumani, G. Oza, P. Reyes-Figueroa, M. Rohini, I.G. Becerril-Juarez, J.-H. Lee, J. Yi, Synthesis and Characterization of Cadmium Sulfide Nanoparticles by Chemical Precipitation Method, J. Nanosci. Nanotechnol. 15 (2015) 8434–8439. https://doi.org/10.1166/jnn.2015.11472.

[72] J. Sterner, J. Malmström, L. Stolt, Study on ALD In 2 S 3 /Cu(In,Ga)Se 2 interface formation, Prog. Photovoltaics Res. Appl. 13 (2005) 179–193. https://doi.org/10.1002/pip.595.

[73] D. Abou-Ras, G. Kostorz, A. Romeo, D. Rudmann, A.N. Tiwari, Structural and chemical investigations of CBD- and PVD-CdS buffer layers and interfaces in Cu(In,Ga)Se2-based thin film solar cells, Thin Solid Films. 480–481 (2005) 118–123. https://doi.org/10.1016/j.tsf.2004.11.033.

[74] T. Minemoto, T. Matsui, H. Takakura, Y. Hamakawa, T. Negami, Y. Hashimoto, T. Uenoyama, M. Kitagawa, Theoretical analysis of the effect of conduction band offset of window/CIS layers on performance of CIS solar cells using device simulation, Sol. Energy

Mater. Sol. Cells. 67 (2001) 83–88. https://doi.org/10.1016/S0927-0248(00)00266-X.

[75] S. Ishizuka, K. Sakurai, A. Yamada, K. Matsubara, P. Fons, K. Iwata, S. Nakamura, Y. Kimura, T. Baba, H. Nakanishi, T. Kojima, S. Niki, Fabrication of wide-gap Cu(In1−xGax)Se2 thin film solar cells: a study on the correlation of cell performance with highly resistive i-ZnO layer thickness, Sol. Energy Mater. Sol. Cells. 87 (2005) 541–548. https://doi.org/10.1016/j.solmat.2004.08.017.

[76] C. Persson, Y.-J. Zhao, S. Lany, A. Zunger, n-type doping of CuInSe2 and CuGaSe2, Phys. Rev. B. 72 (2005) 035211. https://doi.org/10.1103/PhysRevB.72.035211.

[77] F. Göde, İ.A. Kariper, E. Güneri, S. Ünlü, Effect of Complexing Agent on the Structural, Optical and Electrical Properties of Polycrystalline Indium Sulfide Thin Films Deposited by Chemical Bath Deposition, Acta Phys. Pol. A. 132 (2017) 527–530. https://doi.org/10.12693/APhysPolA.132.527.

[78] A. Ashok, G. Regmi, A. Romero-Núñez, M. Solis-López, S. Velumani, H. Castaneda, Comparative studies of CdS thin films by chemical bath deposition techniques as a buffer layer for solar cell applications, J. Mater. Sci. Mater. Electron. 31 (2020) 7499–7518. https://doi.org/10.1007/s10854-020-03024-3.

[79] G. Pérez-Hernández, J. Pantoja-Enríquez, B. Escobar-Morales, D. Martinez-Hernández, L.L. Díaz-Flores, C. Ricardez-Jiménez, N.R. Mathews, X. Mathew, A comparative study of CdS thin films deposited by different techniques, Thin Solid Films. 535 (2013) 154–157. https://doi.org/10.1016/j.tsf.2012.11.092.

[80] A.A.A.B.D. El-raady, A.M. Abo-bakr, ON THE EFFECT OF COMPLEXING AGENTS ON THE STRUCTURAL AND OPTICAL PROPERTIES OF CdS NANOCRYSTALS, Chalcogenide Lett. 10 (2013) 55–62.

[81] B.-S. Moon, J.-H. Lee, H. Jung, Comparative studies of the properties of CdS films deposited on different substrates by R.F. sputtering, Thin Solid Films. 511–512 (2006) 299–303. https://doi.org/10.1016/j.tsf.2005.11.080.

[82] P.P. Sahay, R.K. Nath, S. Tewari, Optical properties of thermally evaporated CdS thin films, Cryst. Res. Technol. 42 (2007) 275–280. https://doi.org/10.1002/crat.200610812.

[83] K. Sivaramamoorthy, S. Asath Bahadur, M. Kottaisamy, K.R. Murali, Properties of CdS

films deposited by the electron beam evaporation technique, J. Alloys Compd. 503 (2010) 170–176. https://doi.org/10.1016/j.jallcom.2010.04.227.

[84] D.W. Niles, H. Höchst, Strain-induced changes in the electronic valence-band structure of a cubic CdS(100) film, Phys. Rev. B. 44 (1991) 10965–10968. https://doi.org/10.1103/PhysRevB.44.10965.

[85] N. V. Hullavarad, S.S. Hullavarad, Synthesis and characterization of monodispersed CdS nanoparticles in SiO2 fibers by sol–gel method, Photonics Nanostructures - Fundam. Appl. 5 (2007) 156–163. https://doi.org/10.1016/j.photonics.2007.03.001.

[86] J. Nishino, S. Chatani, Y. Uotani, Y. Nosaka, Electrodeposition method for controlled formation of CdS films from aqueous solutions, J. Electroanal. Chem. 473 (1999) 217–222. https://doi.org/10.1016/S0022-0728(99)00250-8.

[87] J. Patel, F. Mighri, A. Ajji, D. Tiwari, T.K. Chaudhuri, Spin-coating deposition of PbS and CdS thin films for solar cell application, Appl. Phys. A. 117 (2014) 1791–1799. https://doi.org/10.1007/s00339-014-8659-x.

[88] M. Shaban, M. Mustafa, A.A.P. Khan, Hexagonal diameter in cadmium sulfide/anodic alumina nanoporous bi-layer membrane by a sol–gel spin coating and their sensing application, Appl. Phys. A. 126 (2020) 268. https://doi.org/10.1007/s00339-020-3371-5.

[89] A.A. Yadav, M.A. Barote, E.U. Masumdar, Studies on nanocrystalline cadmium sulphide (CdS) thin films deposited by spray pyrolysis, Solid State Sci. 12 (2010) 1173–1177. https://doi.org/10.1016/j.solidstatesciences.2010.04.001.

[90] H. Uda, H. Yonezawa, Y. Ohtsubo, M. Kosaka, H. Sonomura, Thin CdS films prepared by metalorganic chemical vapor deposition, Sol. Energy Mater. Sol. Cells. 75 (2003) 219–226. https://doi.org/10.1016/S0927-0248(02)00163-0.

[91] R.S. Crandall, E.A. Schiff, The correlation of open-circuit voltage with bandgap in amorphous silicon-based pin solar cells, in: AIP Conf. Proc., AIP, 1996: pp. 101–108. https://doi.org/10.1063/1.49397.

[92] B. Von Roedern, G.H. Bauer, Material requirements for buffer layers used to obtain solar cells with high open circuit voltages, Mater. Res. Soc. Symp. - Proc. 557 (1999) 761–766.

[93] P. Reyes, S. Velumani, Structural and optical characterization of mechanochemically

synthesized copper doped CdS nanopowders, Mater. Sci. Eng. B. 177 (2012) 1452–1459. https://doi.org/10.1016/j.mseb.2012.03.002.

[94] X. Lyu, D. Zhuang, M. Zhao, Q. Gong, L. Zhang, R. Sun, Y. Wei, X. Peng, Y. Wu, G. Ren, An investigation on performance enhancement for KF post deposition treated CIGS solar cells fabricated by sputtering CIGS quaternary targets, Vacuum. 151 (2018) 233–236. https://doi.org/10.1016/j.vacuum.2018.02.023.

[95] M. Estela, M. L., M. Tufino-Velazquez, G. Contreras-Puente, A. Morales-Acevedo, Chemical Bath Deposited CdS for CdTe and Cu(In,Ga)Se2 Thin Film Solar Cells Processing, in: Sol. Cells - Thin-Film Technol., InTech, 2011: pp. 116–124. https://doi.org/10.5772/21934.

[96] S.O. El hamali, W.M. Cranton, N. Kalfagiannis, X. Hou, R. Ranson, D.C. Koutsogeorgis, Enhanced electrical and optical properties of room temperature deposited Aluminium doped Zinc Oxide (AZO) thin films by excimer laser annealing, Opt. Lasers Eng. 80 (2016) 45–51. https://doi.org/10.1016/j.optlaseng.2015.12.010.

[97] P.J.M. Isherwood, M. Gona, J.W. Bowers, N. Neves, P. Newbatt, J.M. Walls, Comparison of DC and RF sputtered aluminium-doped zinc oxide for photovoltaic applications, in: 2015 IEEE 42nd Photovolt. Spec. Conf., IEEE, 2015: pp. 1–5. https://doi.org/10.1109/PVSC.2015.7355900.

[98] B.J. Babu, S. Velumani, J. Arenas-Alatorre, A. Kassiba, J. Chavez, H. Park, S.Q. Hussain, J. Yi, R. Asomoza, Structural Properties of Ultrasonically Sprayed Al-Doped ZnO (AZO) Thin Films: Effect of ZnO Buffer Layer on AZO, J. Electron. Mater. 44 (2014) 699–705. https://doi.org/10.1007/s11664-014-3541-3.

[99] S.J. Henley, M.N.R. Ashfold, D. Cherns, The growth of transparent conducting ZnO films by pulsed laser ablation, Surf. Coatings Technol. 177–178 (2004) 271–276. https://doi.org/10.1016/j.surfcoat.2003.09.005.

[100] T.M.K. Thandavan, S.M.A. Gani, C.S. Wong, R.M. Nor, Enhanced photoluminescence and Raman properties of Al-doped ZnO nanostructures prepared using thermal chemical vapor deposition of methanol assisted with heated brass, PLoS One. 10 (2015) 1–18. https://doi.org/10.1371/journal.pone.0121756.

[101] S. Paetel, Roadmap CIGS towards 25 % Efficiency, Zent. Für Sonnenenergie- Und

Wasserstoff-Forsch. Baden-Württemb. (2016).

[102] H. ming Zhou, D. qing Yi, Z. ming Yu, L. rong Xiao, J. Li, Preparation of aluminum doped zinc oxide films and the study of their microstructure, electrical and optical properties, Thin Solid Films. 515 (2007) 6909–6914. https://doi.org/10.1016/j.tsf.2007.01.041.

[103] K. S, J.J. Ríos-Ramírez, S. Chakaravarthy, V. S, Electrical, optical, and topographical properties of RF magnetron sputtered aluminum-doped zinc oxide (AZO) thin films complemented by first-principles calculations, J. Mater. Sci. Mater. Electron. 29 (2018) 15383–15395. https://doi.org/10.1007/s10854-018-8920-8.

[104] T.R. Ramireddy, V. Venugopal, J.B. Bellam, A. Maldonado, J. Vega-Pérez, S. Velumani, M.D.L.L. Olvera, Effect of the milling time of the precursors on the physical properties of sprayed aluminum-doped zinc oxide (ZnO: Al) thin films, Materials (Basel). 5 (2012) 1404–1412. https://doi.org/10.3390/ma5081404.

[105] J.-Y. Noh, H. Kim, Y.-S. Kim, C.H. Park, Electron doping limit in Al-doped ZnO by donor-acceptor interactions, J. Appl. Phys. 113 (2013) 153703. https://doi.org/10.1063/1.4801533.

[106] M.D. McCluskey, C.D. Corolewski, J. Lv, M.C. Tarun, S.T. Teklemichael, E.D. Walter, M.G. Norton, K.W. Harrison, S. Ha, Acceptors in ZnO, J. Appl. Phys. 117 (2015) 112802. https://doi.org/10.1063/1.4913827.

[107] G. Haacke, New figure of merit for transparent conductors, J. Appl. Phys. 47 (1976) 4086–4089. https://doi.org/10.1063/1.323240.

[108] S. Seki, Y. Sawada, M. Ogawa, M. Yamamoto, Y. Kagota, A. Shida, M. Ide, Highly conducting indium-tin-oxide transparent films prepared by dip-coating with an indium carboxylate salt, Surf. Coatings Technol. 169–170 (2003) 525–527. https://doi.org/10.1016/S0257-8972(03)00170-1.

[109] U. Betz, M. Kharrazi Olsson, J. Marthy, M.F. Escolá, F. Atamny, Thin films engineering of indium tin oxide: Large area flat panel displays application, Surf. Coatings Technol. 200 (2006) 5751–5759. https://doi.org/10.1016/j.surfcoat.2005.08.144.

[110] Z. Chen, W. Li, R. Li, Y. Zhang, G. Xu, H. Cheng, Fabrication of highly transparent and conductive indium-tin oxide thin films with a high figure of merit via solution processing, Langmuir. 29 (2013) 13836–13842. https://doi.org/10.1021/la4033282.

[111] D.M. Mattox, Handbook of Physical Vapor Deposition (PVD) Processing, in: Handb. Phys. Vap. Depos. Process., Elsevier, 1998: p. 746. https://doi.org/10.1016/B978-081551422-0.50001-2.

[112] H. Assender, How Surface Topography Relates to Materials' Properties, Science (80-.). 297 (2002) 973–976. https://doi.org/10.1126/science.1074955.

[113] E.L. Ed, X-ray Characterization of Materials, Wiley, 1999. https://doi.org/10.1002/9783527613748.

[114] V. Uvarov, I. Popov, Metrological characterization of X-ray diffraction methods at different acquisition geometries for determination of crystallite size in nano-scale materials, Mater. Charact. 85 (2013) 111–123. https://doi.org/10.1016/j.matchar.2013.09.002.

[115] F. Nemla, D. Cherrad, Metallic amorphous electrodeposited molybdenum coating from aqueous electrolyte: Structural, electrical and morphological properties under current density, Appl. Surf. Sci. 375 (2016) 1–8. https://doi.org/10.1016/j.apsusc.2016.01.012.

[116] S.K. Ghosh, T. Bera, O. Karacasu, A. Swarnakar, J.G. Buijnsters, J.P. Celis, Nanostructured MoSx-based thin films obtained by electrochemical reduction, Electrochim. Acta. (2011). https://doi.org/10.1016/j.electacta.2010.10.065.

[117] G.K. Williamson, R.E. Smallman, III. Dislocation densities in some annealed and cold-worked metals from measurements on the X-ray Debye-Scherrer spectrum, Philos. Mag. (1956). https://doi.org/10.1080/14786435608238074.

[118] S. Velumani, S.K. Narayandass, D. Mangalaraj, Structural characterization of hot wall deposited cadmium selenide thin films, Semicond. Sci. Technol. (1998). https://doi.org/10.1088/0268-1242/13/9/009.

[119] J.C.H. Spence, High-Resolution Electron Microscopy, Fourth, Oxford University Press, Oxford, United Kingdom, 2013. https://doi.org/10.1093/acprof:oso/9780199668632.001.0001.

[120] C.N.R. Rao, K. Biswas, Characterization of Nanomaterials by Physical Methods, Annu. Rev. Anal. Chem. 2 (2009) 435–462. https://doi.org/10.1146/annurev-anchem-060908-155236.

[121] C.A. Bishop, Process Diagnostics and Coating Characteristics, in: Vac. Depos. onto Webs,

Film. Foils, Elsevier, 2011: pp. 81–114. https://doi.org/10.1016/B978-1-4377-7867-0.00005-2.

[122] J. Lindemuth, Hall Effect Measurement Handbook A Fundamental Tool for Semiconductor Material Characterization, Lake Shore Cryotronics, Incorporated, 2020.

[123] R. Chwang, B.J. Smith, C.R. Crowell, Contact size effects on the van der Pauw method for resistivity and Hall coefficient measurement, Solid. State. Electron. 17 (1974) 1217–1227. https://doi.org/10.1016/0038-1101(74)90001-X.

[124] D.D. Le Pevelen, NIR FT-raman, in: Encycl. Spectrosc. Spectrom., Elsevier, 2016: pp. 98–109. https://doi.org/10.1016/B978-0-12-409547-2.12150-X.

[125] K. Chen, Y.H. Ong, C. Yuen, Q. Liu, Surface-Enhanced Raman Spectroscopy for Intradermal Measurements, in: Imaging in Dermatology, Elsevier, 2016: pp. 141–154. https://doi.org/10.1016/B978-0-12-802838-4.00013-3.

[126] M. Gandais, Characterization in silicon processing, Int. J. Miner. Process. 42 (1994) 137. https://doi.org/10.1016/0301-7516(94)90025-6.

[127] R.J. MacDonald, B. V. King, SIMS — Secondary Ion Mass Spectrometry, in: 2003: pp. 127–154. https://doi.org/10.1007/978-3-662-05227-3_5.

Chapter Four: Deposition and characterization of Molybdenum back-contact

4.1 Introduction

A vital phase in the fabrication of a device is optimizing the component layers and subsequent surface treatments to improve the layers' interface.

The molybdenum (Mo) thin films deposited using direct current (DC) sputtering system ion argon (Ar) ion allows for better control of the thickness (through deposition rate and rpm) and uniformity of the deposited film. The deposition parameters (e.g., sputtering power, argon (Ar) pressure) affect the structural, mechanical, and electrical properties. Furthermore, the structural and morphological properties help to control the desired controlled diffusion of Na through the soda-lime glass and in tandem with other layers to block the diffusion of undesired impurities (e.g., Iron (Fe) and Chromium (Cr)) through stainless steel (SS) into the absorber layer [1–8]. Some common barriers employed to control/block the influx of impurities from the flexible substrates include intrinsic zinc oxide (ZnO) [3,8], molybdenum (Mo) [7], Al_2O_3 [9], and even composites, e.g., Ti/TiN [2]. A primary physical property considered for the choice of substrate, which affects the back-contact, mainly for CIGSe solar cells, is the coefficient of thermal expansion (CTE) favorable in the range between 8 x 10^{-6} K^{-1} to 11 x 10^{-6} K^{-1}[10]. A significant difference in CTE values creates an increase in stress on the thin films deposited on the substrate, sometimes resulting in the substrate's CIGSe layers' delamination [11,12]. The concomitant increase in the density of defects within the CIGSe layer usually occurs during cooling after the growth process. The. The CTE value for glass ~8 x 10^{-6} K^{-1} [13] and ~ 10.4 x 10^{-6} K^{-1} for SS 430 [14].

The following section (4.1) presents the analysis of Mo thin-films deposited on soda-lime glass. The following section (4.2) contains the deposition and analysis of Mo deposited on a flexible substrate, in tandem with Ti and ZnO layers as efficient barriers to the diffusion of impurity ions from stainless steel.

4.2 Mo thin films on soda-lime glass

This study on the molybdenum (Mo) back-contact layer for solar cell applications optimizes the parameters for deposition on SLG and stainless steel substrates using direct-current (dc) sputtering with varying sputtering powers (100 to 800 W) and pressures (5 to 20 mTorr). We made the depositions for 10 minutes. A target-to-substrate distance is 5.5 cm for the dc sputtering, with the magnetron tilted to about 55°. The base pressure maintained for all the depositions at ambient temperatures was ~ 4.0 × 10^{-6} Torr with the substrate rotation of about 0.05 rpm to ensure the film's uniformity.

4.2.1 Structural analysis

Structural characterization of the dc deposited thin films using X-ray diffraction between 2θ values ranging from 20 to 80° (Fig. 4.1) shows preferential (110) and (211) orientation of the Mo characteristic planes (ICDD No. 03-065-7442). The varying intensities of the (110) and (211) peaks depend on the sputtering power and Ar pressure, which affects the sputtered ionic species' settling on the substrate.

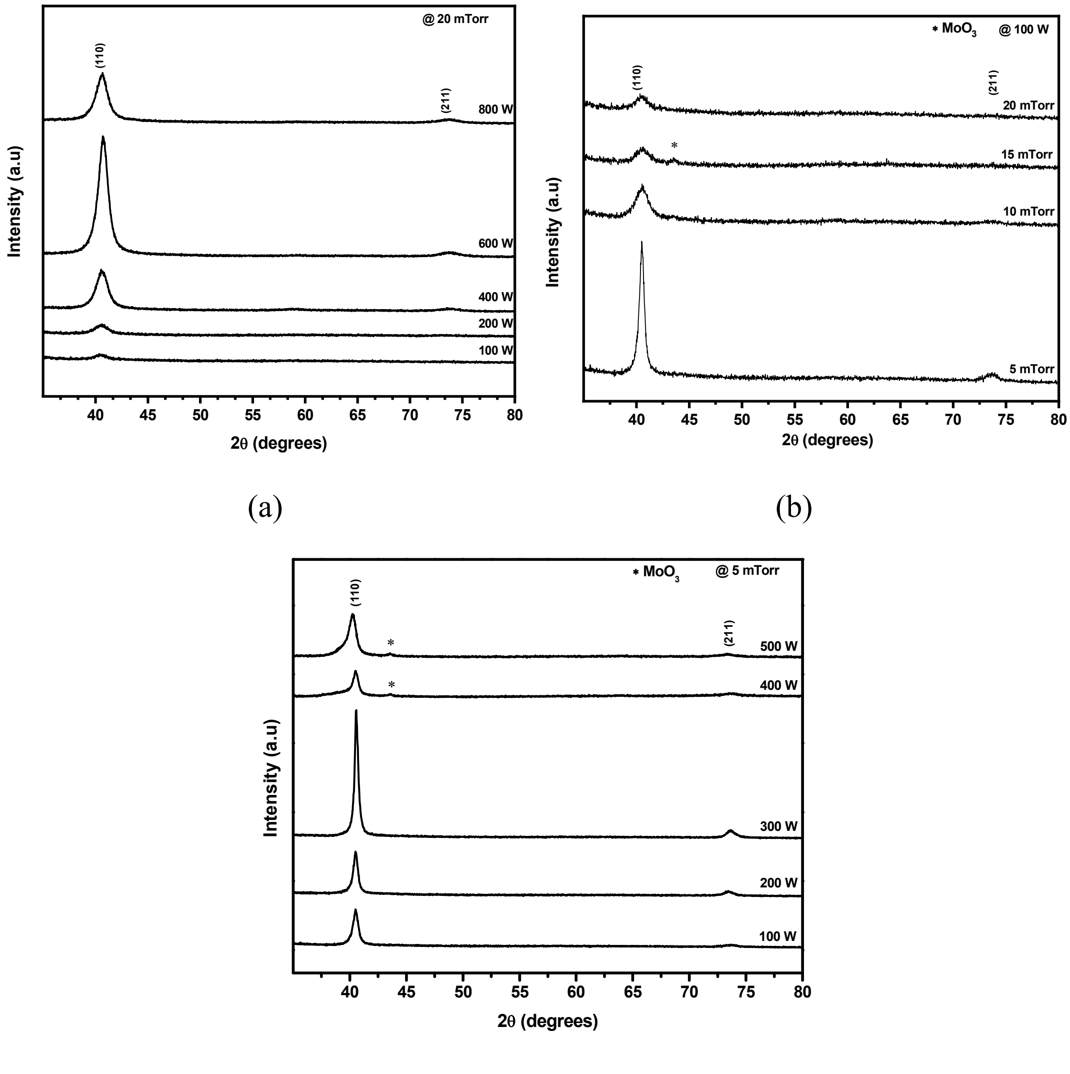

(a) (b)

(c)

Figure 4. 1 *XRD patterns of the Mo films at (a) various deposition powers at 20 mTorr, (b) various working pressures at 100 W, and (c) various deposition powers at constant 5 mTorr*

A variation of the sputtering power at a constant pressure of 20 mTorr (Fig. 4.1a) increases the kinetic energy of the ejected Mo particles from the target as the power of Ar ions bombarding the target increases. Thus, the deposition rate increases with the increasing sputtering power [15], resulting in a possible increase in the deposited films' thickness if more Mo particles arrive at the substrate. The intensity of (110) peak orientation increases with sputtering power, from 100 W to 600 W. However, a further increase in power (to 800 W) results in a reduction in the peak intensity, maybe due to very high kinetic energy inhibiting the crystallization of the Mo atoms on the substrate. Also, the Mo thin films deposited with 800 W on the substrate appear flaked partly along the edges and some parts of the substrate, which may be due to Mo's fast deposition rate on the substrate that inhibits proper sticking to the thin films [16].

The sputtering pressure influences the properties of sputtered thin films [15] as it significantly affects the mean free path (λ) of the dislodged Mo ions from the target and the resultant sputter yield [17]. Using constant sputtering power of 100 W, the variation of sputtering pressure (Fig. 4.1b) shows a decrease of the (110) peak intensity as the pressure increases. The increase in λ resulting from increased pressure and thus entropy inside the chamber leads to more collisions among sputtering Ar ions and sputtered Mo particles. The observed decrease in peak intensity suggesting crystalline degradation of Mo film with an increase in pressure results in low crystallization due to an increase in λ, suggesting that lower sputtering pressures are ideal for the deposition. Attempts at depositions with lower pressures below 5 mTorr were unsuccessful due to loss of sputtering flux inside the chamber, resulting in the lack of deposition. The (MoO_3) peaks corresponding to the oxidized phase in some depositions could be due to exposure of the films to the ambient atmosphere.

Since lower powers are ideal for sputtering to avoid potential embedding of the sputtered ions on the sublayer or damaging the substrate, depositions with a constant pressure of 5 mTorr (Fig. 4.1c) and varying sputtering power from 100 to 500 W produced films with varying degrees of crystallinity typified by the varying intensity of (110) peak and shape (i.e., FWHM). The intensity of the primary peak increased with increased sputtering power from 100 to 300 W, attributed to better deposition and increased thickness. However, further increase in sputtering power (400 to 500 W) resulted in the reduction of crystallinity, previously discussed for depositions between 600 and 800 W.

The observed shifts in peak position with a variation of sputtering parameters reflect changes in the lattice parameters, e.g., strain. For instance, thin films' calculated stress values may be negative and positive, representing compressive or tensile stress, respectively [18,19]. The lattice parameters calculated from the most intense peaks in comparison with the reference (ICDD file No: 03-065-7442) confirmed a cubic structure, with lattice constant (***a***) ranging between 3.1408–3.1733 Å, in good agreement with the literature [19,20]. Other parameters calculated from the structural characterizations using XRD show variations with deposition parameters, i.e., power and pressure.

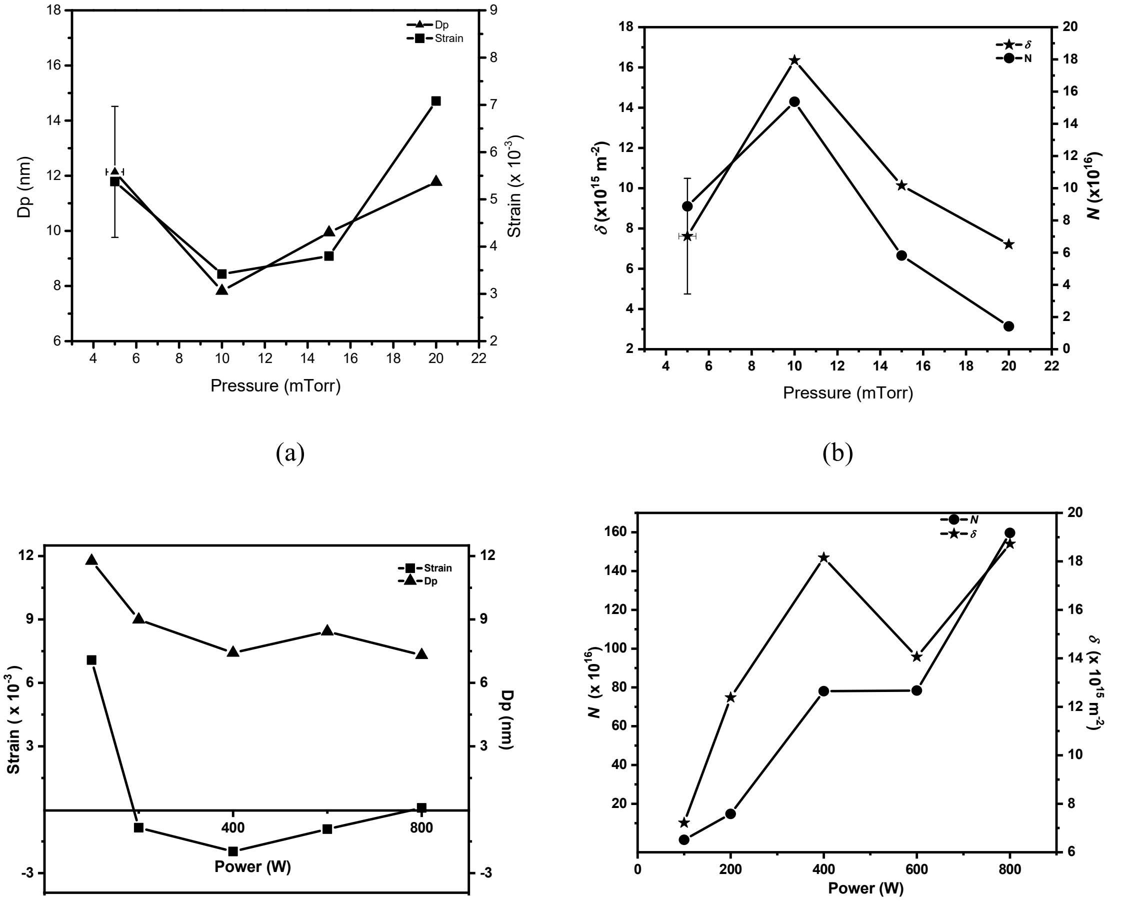

(a) (b)

(c) (d)

Figure 4. 2 *Variations of strain, the crystallite size (Dp), dislocation density (δ), and the number of crystallites per unit area (N) as functions of deposition power and pressure: (a) and (b) at 100 W, (c) and (d) at 20 mTorr*

The calculated crystallite parameters estimated from the X-ray diffractogram (strain, dislocation density, crystallite sizes, and the number of crystallites per unit area) show some variations with the deposition parameters. With a constant 100 W deposition power, the estimated crystallite size (D_p) and strain appear to decrease with an initial increase in pressure from 5 mTorr to 10 mTorr, with a corresponding increase in dislocation density (δ) and the number of crystallites per unit area (N) (Fig. 2 a and b). Increasing the pressure to 15 mTorr and above shows an increase in D_p with a reversal in the δ and N values trend.

Since the pressure controls the entropy within the chamber, and thus the mean free path of the sputtered ionic species, the seemingly increase in crystallite sizes may be due to fewer particles arriving at the substrate for proper settling and growth of the crystals. However, fewer sputtered ionic species arriving at the substrate may result in poor film formation, leading to resistive films in metallic materials. All estimated values of strain are positive, with a similar pattern of variation as D_p.

For a constant sputtering pressure of 20 mTorr (Fig. 4.2 b and c), increasing sputtering power from 100 W to 800 W produces higher kinetic energy resulting in enhanced atomic peening, which produces denser films. However, D_p appeared to decrease with increasing power, even with the increase in the deposited film's thickness. The higher kinetic energy acquired at increasing power inhibits the proper settling of the Mo atoms on the substrate, resulting in the film's poor crystallization, which results in the observed decrease in D_p and observed compressive stress in the films. The deposited films' microstrain (ε) values varied between 6.68×10^{-3} and 15.43×10^{-3}. The depositions (at 20 mTorr, 800 W) produced highly energetic particles with a correspondingly high value of entropy within the chamber, affecting the settling of the sputtered Mo ionic species and inhibited good attaching to the thin films. Also, deposition with a higher power (e.g., 800 W) during sputtering on a small substrate can damage the surface and result in implantation rather than a deposition.

The results (Fig. 4.2) confirm that depositions at lower pressures [18], and considering the potential effects of power, yield Mo films with desirable structural properties for a back-contact, with a better density, which tends to decrease with an increase in sputtering pressure. Further depositions with a constant lower pressure of 5 mTorr and varying sputtering power (Fig. 4.3) produced thin films with little tensile stress, fluctuating to compressive at 400 W and tensile at 500 W.

Dp's estimated value appears to increase with power from 100 W to 200 W, marginally decreasing with a further increase in power. The associated variations in δ and N show a similar variation pattern, reducing initially from 100 W to 200 W, increasing with further power. The thin films' calculated microstrain (ε) range between 6.0x 10^{-3} to 22 x10^{-3}.

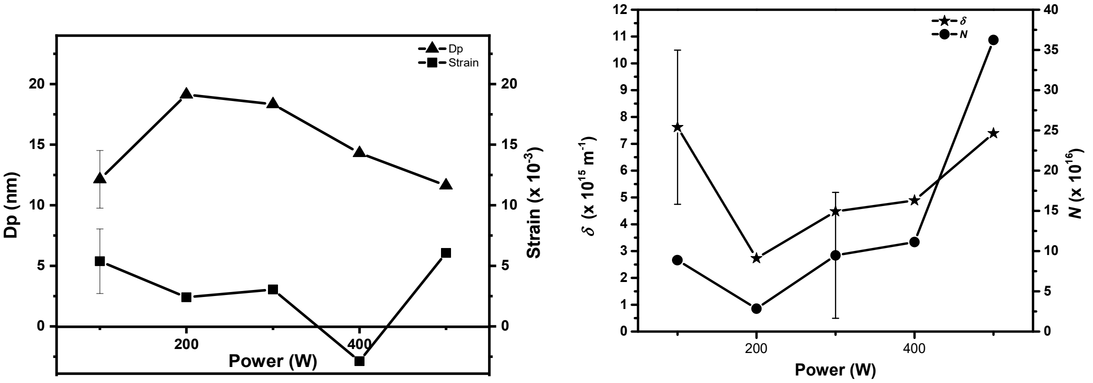

(a) (b)

Figure 4. 3 *Variations of strain, crystallite size, dislocation density, and the number of crystallites per unit area with power at 5 mTorr*

4.2.2 Resistivity analysis

The four-point probe method (using the Veeco FPP 5000 probe located in SEES-CINVESTAV) provides a vital technique for characterizing metals and semiconductors [21], especially the sheet resistance (and resistivity) of the ohmic contacts used in the device fabrication. The Veeco FPP 5000 simplifies the measurements of resistive properties of semiconductors and resistive thin-films with a measurement range displaying sheet resistivity up to 450k ohm/sq and down to a resolution of 10^{-3} milliohm/Sq. The variation of sputtering parameters, reflecting in the structural properties, also significantly affects the thin films' resistive properties.

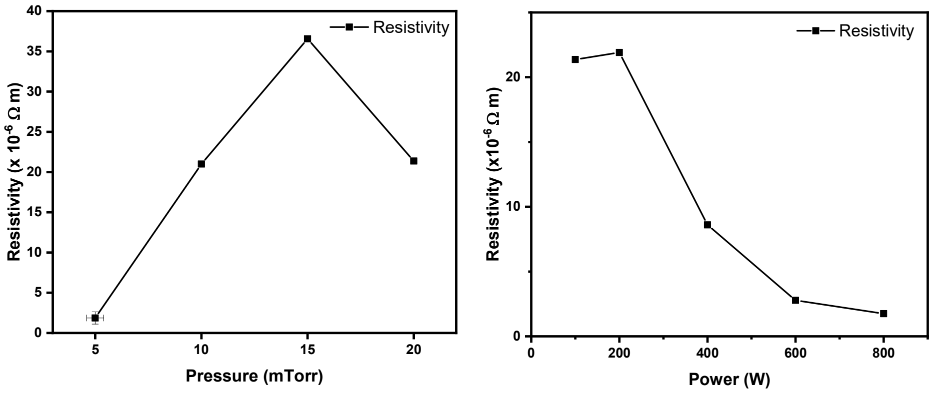

(a) (b)

Figure 4. 4 *The resistivity of the deposited Mo films with different deposition power and pressure: (a) at 100 W, and (b) at 20 mTorr*

The increase in working pressure (Fig. 4.4a) causes an increase in thin films' resistivity. As observed from the structural characterizations, increasing the pressure causes the mean free path to decrease due to entropy in the system and poorer crystallization, leading to increasing resistivity. On the contrary, increasing the power (Fig. 4.4b), which potentially sputter more Mo particles, reduces the thin film's resistivity. Depositing with a constant lower pressure of 5 mTorr (Fig. 4.5) produces Mo thin films with reduced sheet resistance with increasing sputtering power. The apparent lack of further reduction in resistance (between 400 and 500 W) may be due to the effect of the thickness (resistivity = sheet resistance x thickness) and crystallization effects previously discussed in **Section 4.2**.

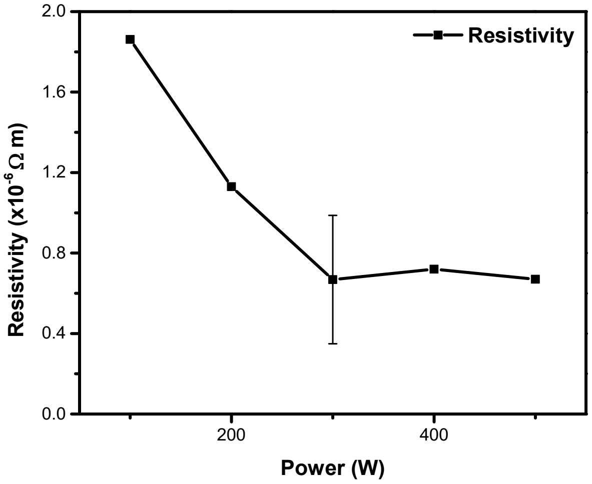

Figure 4. 5 *Resistivity of the deposited Mo films with different deposition power and at 5 mTorr*

At a pressure of 5 mTorr and 300 W sputtering power, we measured a low resistivity of 0.66 x 10^{-6} Ω m after depositing for 10 minutes. As previously noted, the deposition was ceiled at 500 W to avoid any damage to the SLG or the possibility of ion implantation at higher deposition powers. Also, there occurs a loss of flux at such a low pressure and higher powers, above 500 W, because the lower pressures could not support sputtering at such powers.

4.2.3 Bilayer deposition of Mo

A combination of deposition parameters allows for achieving desirable qualities of the thin films, thereby possibly joining together two or more layers and improving the obtained layer's properties over the combined individual layers. In Mo's case and using either DC and RF sputtering, a combination of different sputtering power and pressures used for depositing separate layers allows for joining the layers [15,18,22,23]. For the choice of Mo back-contacts, we desired to obtain very low resistivities (~10^{-6} **Ω** m) and dense columnar structures that allow for controlled diffusion of alkali metals (e.g., Na, K) into the absorber layer. For thin films on the substrate, the existence of compressive or tensile stress is desirable close to a zero value. Considering the results on the optimized deposition parameters (i.e., power, pressure, source-to-substrate distance, time), we choose a constant sputtering pressure of 5 mTorr and sputtering power of 300 W for the first layer and 100 W for the second in fabricating the bilayer. The bottom (first) layer deposited at higher power (300 W) ensured better adhesion and improved conductivity through a reduction in the resistivity value, and the top (second) layer deposited at lower power (100 W) to improve the quality of the crystallites. Joining two layers together is likened to a parallel combination, and the effective resistance of the layers combined in parallel.

4.2.3.1 Structural and electrical values

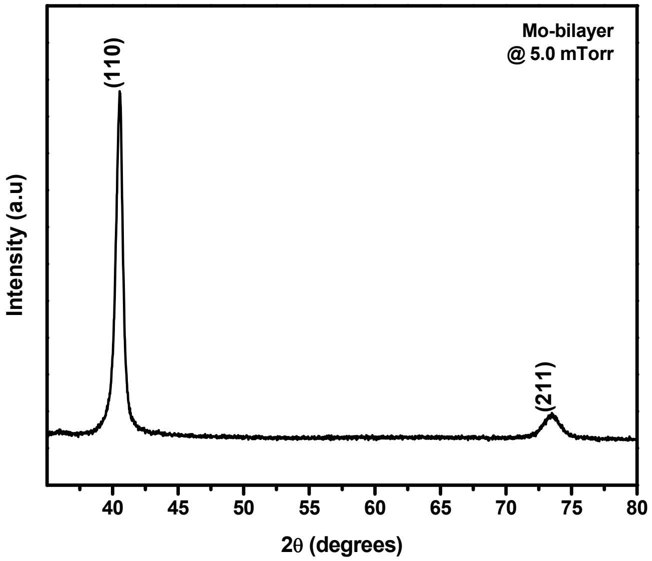

Figure 4. 6 *XRD patterns for bilayer Mo deposited at 300 and 100 W for first and second layers at 5 mTorr*

The X-ray diffractogram for the Mo bilayer (Fig. 4.6) exhibited 2θ peaks at 40.536° and 73.505° corresponding to (110) and (211) cubic characteristic planes of Mo (ICDD file No:03-065-7442). The calculated average crystallite size is 14.56 nm, with a lattice parameter of 3.1490 Å and a comparably low tensile strain. The estimated structural parameters and resistivity values presented in Table 4.1 are comparable to literature values and ideal for the back-contact properties of a CIGSe solar cell.

Table 4. 1 *The sputtering, electrical, and structural parameters of the Mo bilayer deposition*

Layers	**Power (W)**	**Pressure (mTorr)**	**ρ ($\times 10^{-6}$ Ω m)**	**D_p (nm)**	**Strain (x 10^{-3})**	**ε (x 10^{-3})**	**δ (x 10^{15})**	**N (x 10^{16})**	**Deposition time (min)**
1	300	5.0	0.60	14.56	0.62	7.34	4.72	21.69	10
2	100								25

4.2.3.2 Morphological characterization

The cross-sectional view of the bilayer Mo film (Fig. 4.7) shows a columnar structure [24] in the arrangement. Increasing the deposition rate with higher power (300W) results in densely packed structures with excellent adhesion, and reducing the deposition power allows for depositing less dense structures [25].

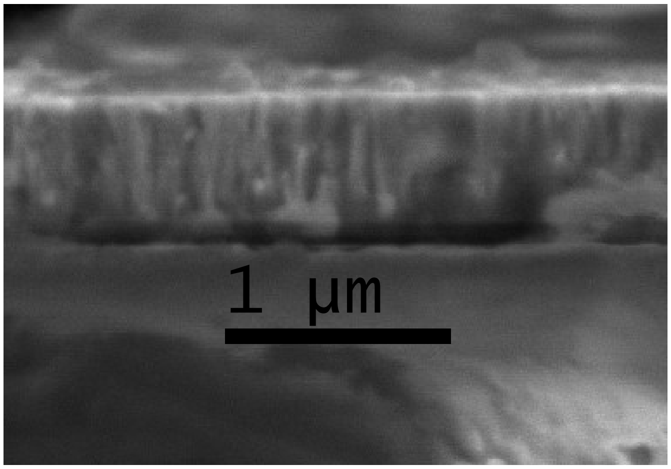

Figure 4. 7 *SEM cross-section of the bilayer Mo deposition at 300 W (Layer-1) and 100 W (Layer-2)*

The columnar structures of the Molybdenum layers allow for the controlled diffusion of Na through the layers. The blurry remnants on the top of the film result from the uneven cutting of the substrate. Besides providing good adhesion for the thin film, the higher deposition also reduces the thin film resistivity, as noted with the parallel combination of the resistivity values. The average thickness of the deposited film obtained is 670 nm as measured using Gatan Inc., Digital Micrograph software.

4.2.3.3 Topographical measurements

A deposited thin film's surface properties contribute to mechanical and electrical transport properties as it has a tangible impact on device performance. Standard surface parameters measured from atomic force microscopy (AFM) for the roughness include the average (Ra) and the root mean square (RMS-Rq) values. Ra is a measure of the vertical deviation, representing the variation of the mean height at the surface area according to the reference plane, and RMS-Rq measures the root mean square deviation of a profile used in calculating the skew kurtosis parameter [26]. The surface skewness (Rsk) characterizes the symmetry of distribution where a positive value of R_{sk} indicates that peaks are dominant in the distribution while the negative shows that valleys become dominant. The skewness parameter also indicates if the peak distribution is symmetrical, while the kurtosis parameter determines whether the distribution of height is Gaussian.

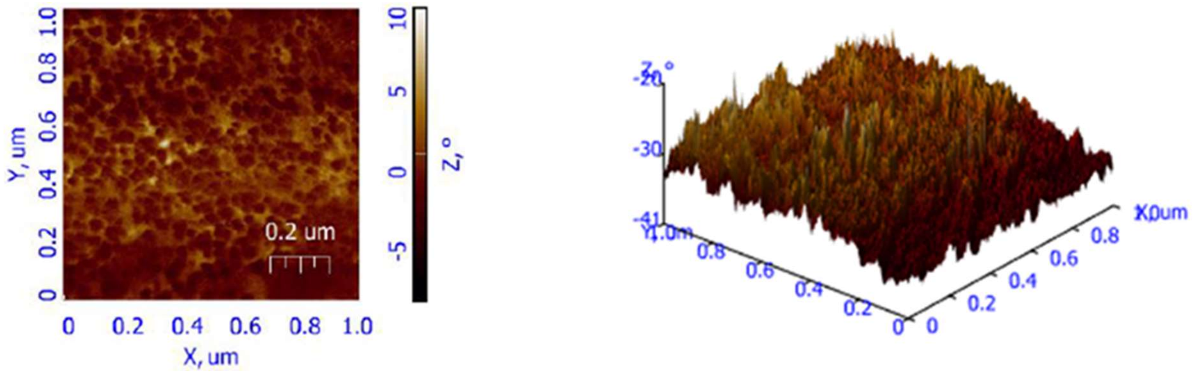

(a) (b)

Figure 4. 8 *AFM measurement of the surface morphology of a bilayer molybdenum film in (a) 2D and 3D*

A two- and three-dimensional images of the Mo bilayer film (Fig. 4.8) showed the presence of random variation of smaller granular shapes and a slightly rougher surface. The surface micrographs (using NT-MDT, NTEGRA Spectra) in the non-contact mode were analyzed using the IA-P9 software. The imaging carried out in an ambient condition had no special sample preparation. The analysis (Table 4.2) shows a roughness value of 1.365 nm, with the height distribution of the surface tending towards a Gaussian distribution if Rq/Ra (=1.204) with dominant peaks as depicted by the positive value of R_{sk}.

Table 4. 2 *Surface parameters for the bilayer Mo film from AFM measurement.*

Sample	R_a (nm)	R_q (nm)	Rq / Ra	R_{max} (nm)	R_{sk}	R_{ka}
Bilayer Mo	1.365	1.644	1.204	6.589	0.442	2.704

4.3 Mo thin films on stainless steel

The fabrication of CIGSe solar cells on flexible substrates, e.g., stainless steel, has some primary challenges, including diffusion of harmful impurities from the substrate (e.g., Cr, Fe), the surface roughness of the substrate, which adversely impacts the efficiency of the device. The effects of surface roughness can reduce by polishing the SS surface. Devices fabricated on polished surfaces showed a significant increase in efficiency as the concentration of unwanted ions decreases with polishing and reduced roughness [27–29]. Cleaned industrially polished SS 430 flexible substrates (composition given in Table 4.3) had barriers deposited to block the absorber layers' influx of impurity ions.

Table 4. 3 *The nominal composition of alloy 430 stainless steel*

Composition	C	Mn	P	S	Si	Cr	Ni	N	Fe
Min	-	-	-	-	-	16.0	-	-	-
Max	0.12	1.00	0.04	0.03	1.00	18.0	0.75	-	Bal

We optimized the dc sputtering conditions for Mo on ZnO and Ti's diffusion barriers in ZnO/Mo and Ti/Mo tandem structures. We considered the effects of temperature during absorber layer depositions and selenization on impurity diffusion, annealing the samples at a temperature of 550ºC in vacuum conditions (~ 7.0 x10^{-6} Torr) to check the efficacy of the barrier/back-contact structure. The Mo layer's microstructure analyzed through the structural, morphological, and topological properties significantly impact the elemental diffusion through the thin film layer and the cell's performance.

4.3.1 Barrier fabrication and Mo film deposition

The material and deposition technique adopted can determine the required thickness [4,5,7,9] with usual considerations, including residual stress, causing a structural deformation or micro-cracking of the thin films. We deposited 50nm thickness of ZnO using optimized conditions [30] at ambient and slightly elevated temperatures of 100ºC for the barrier layer using radio-frequency (RF) sputtering. We deposited 100nm thickness of Ti in a vacuum (~ 2.5 x 10^{-6} Torr) for the barrier layer using e-beam evaporation (128 mA, 4.13 kV with a deposition rate of 1.5 Å/s).

The molybdenum thin films deposited using varying powers (100 to 300 W) and pressures (5 to 10 mTorr) allow for optimizing the sputtering parameters. The choice of parameters aims to have better growth and obtain good crystallinity with more crystallites packed in a given area (i.e., a higher number of crystallites per unit area) to impede impurities' diffusion. In tandem with other barrier layers (Ti, ZnO), we comparatively analyzed the Mo/barrier layer's effectiveness for application with Mo.

4.3.2 Structural analysis

The X-ray diffractogram of the thin films showed the preferential (110) and (211) orientation characteristic of cubic Mo structures, with varying peak intensities indicative of the dc sputtering parameters. We pegged the maximum deposition at power at 300 W to avoid any implantation or to cause any damages to previously deposited layers and all depositions for a constant duration of 20 minutes. We deposited on SLG substrates with the same parameters on the SS with and without barriers as a reference.

At a constant power of 300 W, the working pressure variation from 5 to 10 mTorr (Fig. 4.9a) showed that the prominent peak (110) increased at 7.5 mTorr, but reduced slightly with a further pressure increase to 10 mTorr. As previously noted (with Fig. 4.1b), the increase in working pressure can lead to more collision within the chamber among the sputtering Ar gas and the ejected Mo ions, resulting in the crystallinity's depreciation. The depositions at a constant lower pressure of 5 mTorr and varying dc power from 100 W to 300 W (Fig. 4.9a inset) resulted in increased peak intensity as power increases. As previously, we did not carry out further depositions with sputtering powers above 300 W.

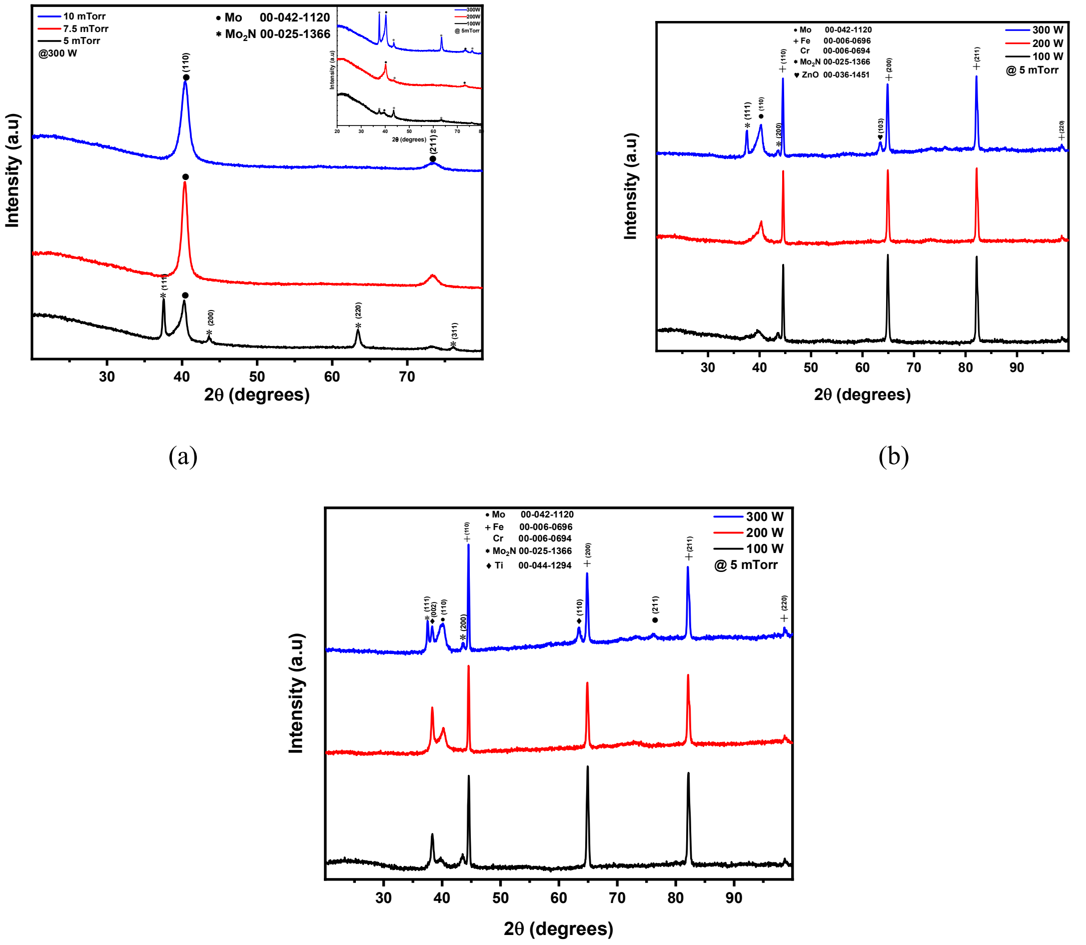

(a)

(b)

(c)

Figure 4. 9 *XRD patterns of the Mo films at (a) constant power of 300W and different pressures (inset graph of deposition with the constant pressure of 5mTorr and different powers) and deposition with a constant pressure of 5mTorr and different powers for (b) ZnO barrier and (c) Ti barrier.*

The depositions on SS with ZnO barrier and SS with Ti barrier (Fig. 4.9 b and c) with varying sputtering powers from 100 to 300 W and constant pressure of 5 mTorr all showed an increase in crystallinity as power increases, as can be inferred from the intensity of the Mo peaks. We observed intense high peaks of Fe/Cr in the depositions, dwarfing the peaks of Mo. We also identified peaks corresponding to ZnO (Fig. 4.9b) and Ti (Fig 4.9c), which probably come from the barrier materials. The observed Ti and ZnO peaks may come from the penetrating X-ray passing through the Mo layer and hitting the underlying barrier and maybe the substrate. The controlled thickness of the Mo layer, and therefore, the density, can determine the intensity of the underlying materials.

The observed peaks corresponding to Mo₂N in some depositions could be due to the films' immediate exposure to nitrogen during cleaning or substrate preparation.

Depositing with a constant power of 300W on SS without a barrier (Fig. 4.10a) and with ZnO (Fig. 4.10b) and Ti barriers (Fig. 4.10c), the crystallinity of the Mo films increased with an increase in pressure from 5 mTorr to 7.5 mTorr. Further increase in pressure to 10 mTorr resulted in a decrease in the crystallinity as typified with a decrease in peak intensity [31]. From the diffractogram (Fig. 4.10), we observe that the intensity of the prominent peak of (110) is more significant than Fe/Cr peaks in all depositions with 7.5 mTorr and 300 W.

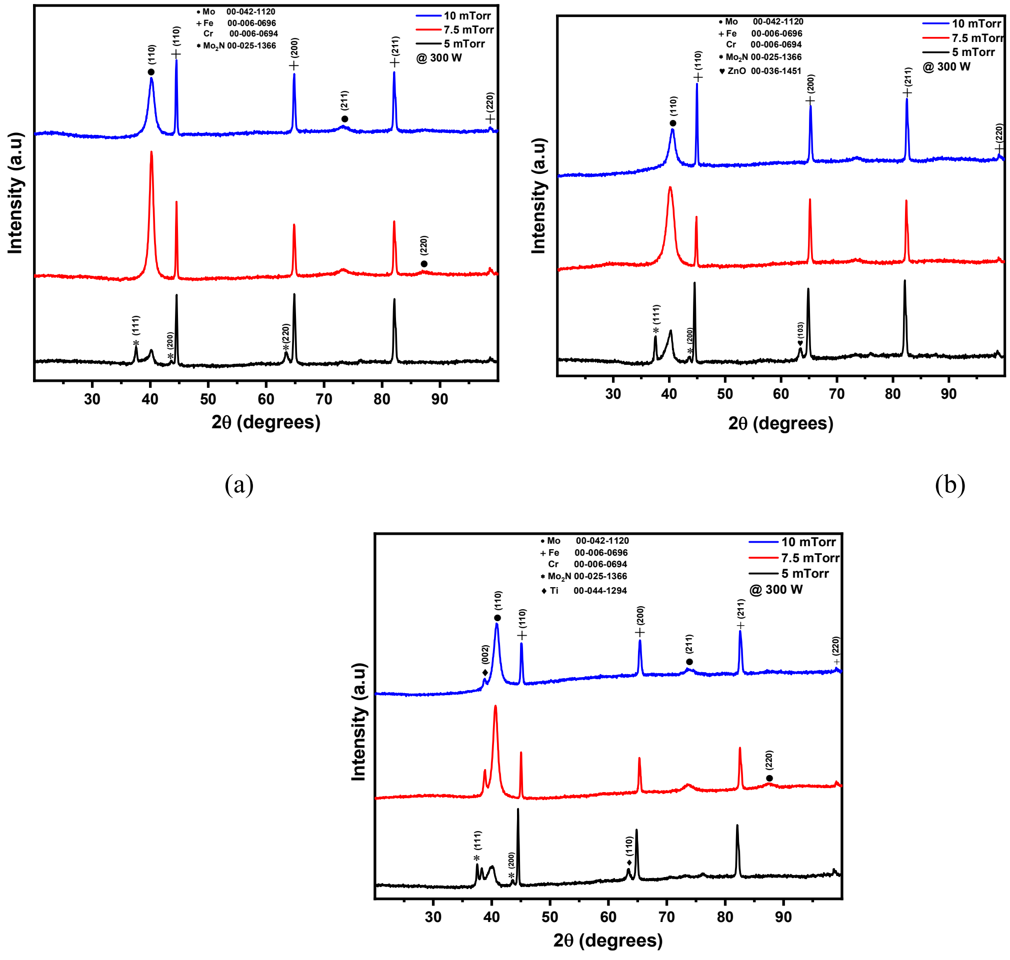

(a)

(b)

(c)

Figure 4. 10 *XRD patterns of the Mo films at a constant power of 300W and different pressures on (a) only SS (b) with ZnO barrier and (c) with Ti barrier.*

The estimated lattice parameter, ***a***, for the Mo thin films varied between 3.108–3.182 Å, comparable to reported literature values [31]. Comparatively, thin films deposited with a constant power of 300 W and varying sputtering pressures produced better depositions than working with varying powers at constant pressure.

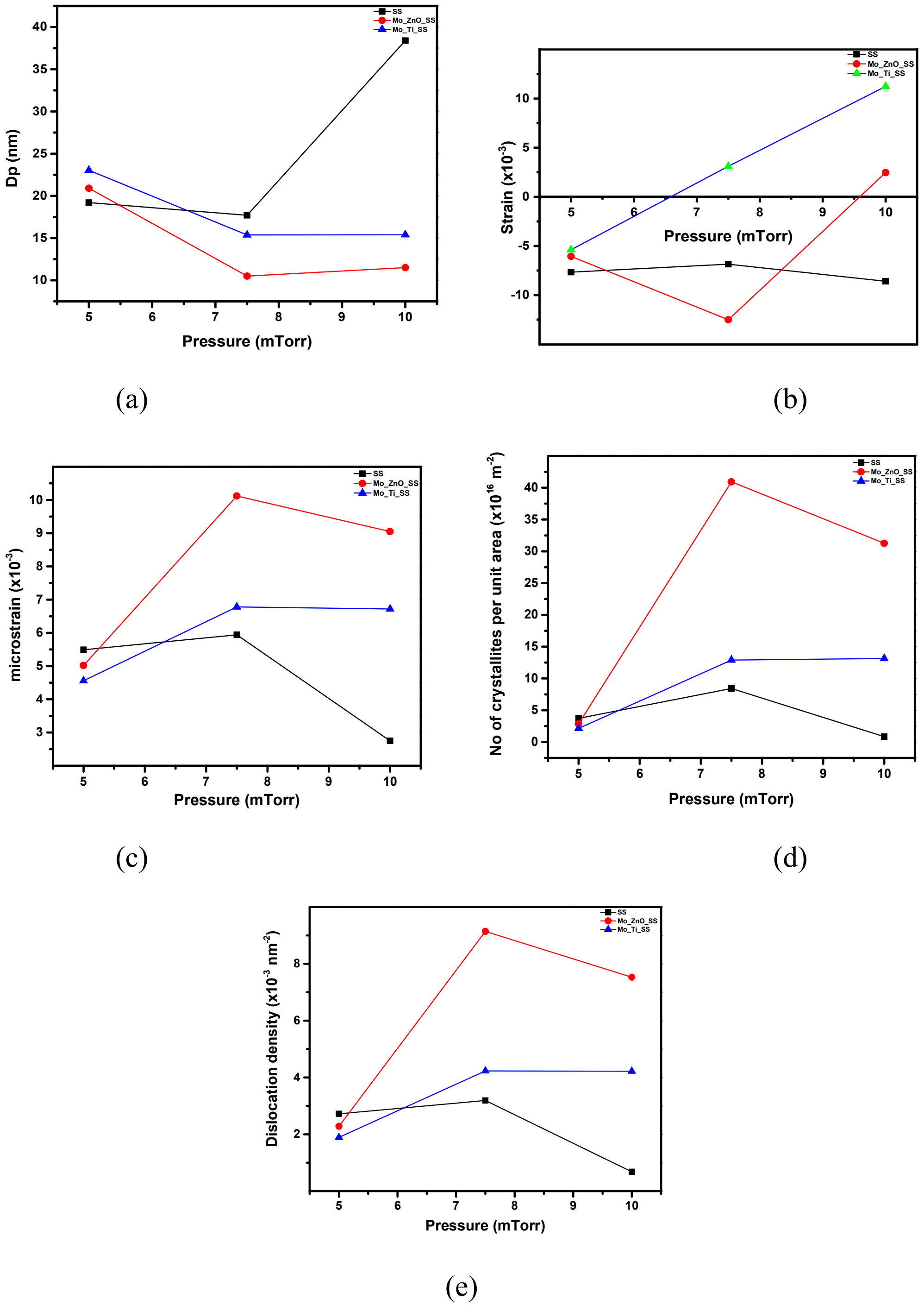

(a) (b)

(c) (d)

(e)

Figure 4. 11 *A comparative plot of lattice parameters of (a) Dp, (b) strain, (c) microstrain, (d) no of crystallites per unit area, and (e) dislocation density of Mo films at deposited at a constant power of 300W and different pressures on SS and with Ti/ ZnO*

The crystallite sizes showed a slight decrease with increased pressure for Mo films deposited on bare SS substrate from 5 mTorr to 7.5 mTorr but increased as pressure increases to 10 mTorr. The crystallite sizes showed a similar trend in variation for films deposited on both ZnO and Ti barriers, decreasing with increased pressure but showed a minimal increase with further increase in pressure. Many Mo sputtered ions arriving at the substrate may inhibit crystallite growth, resulting in reduced D_p. Higher pressures reportedly produce larger entropies in the sputtering chambers, and though the crystallite sizes appear to increase, the number of crystallites in a unit area decreases (Fig. 4.11d).

The calculated values of strain for Mo films deposited on the Ti barrier changed from compressive (negative) to tensile (positive) as the pressure increased while on the ZnO barrier becomes more negative (5 to 7.5 mTorr) but changed to tensile (positive) as pressure increased to 10 mTorr. The presence of compressive stress can result from the incorporation of metallic impurities [32–34] in this case, probably Fe or Cr. Although the deposition at 7.5 mTorr and 300W gave a good crystalline peak, as shown by the XRD diffractogram, it showed a higher stress value in the ZnO barrier. Strain in the reference SS substrate without any barrier remained compressive for all film deposition conditions due to a higher influx of impurity ions in the film [18]. The microstrain, the number of crystallites per unit area, and dislocation density (Fig. 4.11 c-e) show the same variation trend, increasing with depositions pressures from 5 mTorr to 7.5 mTorr and reducing with further increase in pressure to 10 mTorr.

The absorber layer depositions are usually carried out with a substrate temperature to improve crystallinity, and also, most annealing and post-deposition treatments usually above 450°C [12]. Therefore, it will be significant to subject the depositions to thermal treatment and determine the Mo/barrier composite's efficacy. Although crystallization is known to increase with annealing temperature, the temperature gradient also tends to increase impurities' diffusion into the barrier layer, and Fe reportedly has a higher diffusion coefficient. Thus, it is impossible to annihilate Fe contamination at high temperatures [36,37] perfectly.

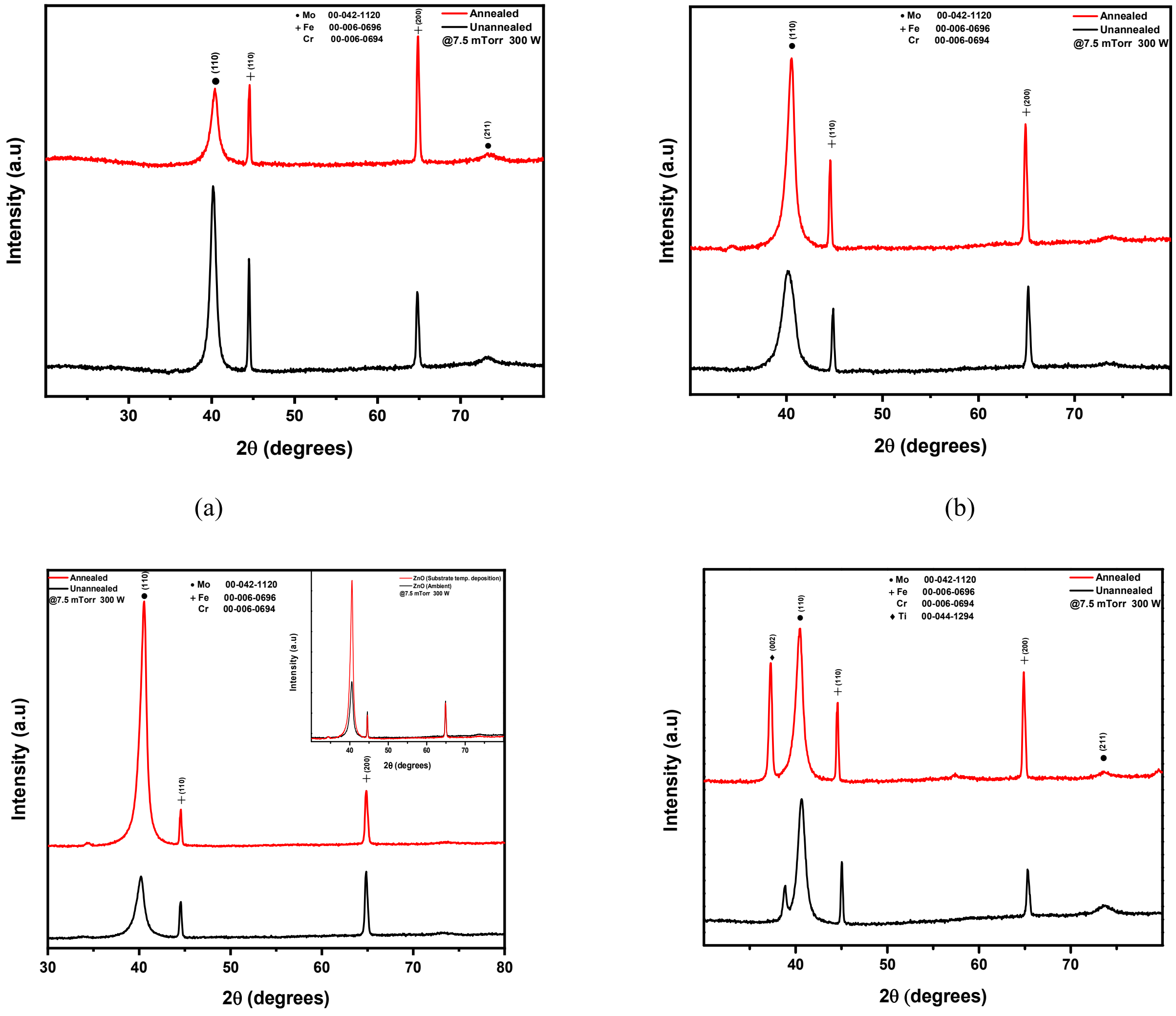

(a)

(b)

(c)

(d)

Figure 4. 12 *XRD pattern of as-deposited and annealed (at 550°C) Mo films (a) SS without a barrier (b) SS with ZnO barrier deposited at ambient (c) SS with ZnO barrier deposited at a substrate temperature of 100°C (inset graph comparing annealed samples with ZnO barriers deposited at ambient and 100°C) and (d) SS with Ti barrier*

We observed a significant reduction in the Mo peak intensity for depositions without a barrier (Fig. 4. 12a). However, there is no change in the preferred orientation. The reduction in peaks could result from the more significant infusion of impurities into the Mo structure, mainly Fe and Cr, as evident from the increase in their peaks' intensity. Mo films deposited on barriers appear to have increased crystallinity with temperature [35], as the peak intensities appear to increase after annealing with reduced peak widths. For comparison, we deposited the ZnO barrier with a substrate temperature of 100°C. Mo films' intensity on the ZnO barrier deposited with substrate temperature significantly increased, appearing to have better intensity than the ZnO barrier deposited at ambient.

Table 4. 4 *lattice parameters; Dp, strain, microstrain, no of crystallites per unit area and dislocation density of annealed (at 550ºC) Mo films on SS (Mo_SS) without barriers, and Mo_Ti_SS for deposition with titanium barrier, (Mo_ZnO(A)_SS) for ZnO deposited at ambient and Mo_ZnO(100) for ZnO deposited at 100ºC substrate temperature*

		Dp (nm)	**Strain x10^{-3}**	**Microstrain x10^{-3}**	**Dislocation density (x10^{-3} nm^{-2})**	**No of crystallites per unit area x10^{16}**
Mo_ SS	As-deposited	17.7	-6.85	5.94	3.19	8.43
	Annealed	46.1	-4.24	2.28	0.47	0.48
Mo_Ti_SS	As-deposited	15.4	3.11	6.78	4.23	17.89
	Annealed	19.2	-1.36	5.45	2.71	6.61
Mo_ZnO(A)_SS	As-deposited	10.5	-12.5	10.1	9.14	40.94
	Annealed	16.5	1.21	6.34	3.69	10.5
Mo_ZnO(100)_SS	Annealed	17.7	2.23	5.88	3.18	8.40

The estimated lattice parameters of the Mo films before and after annealing (Table 4.4) showed an increase in the crystallite sizes after annealing, causing a reduction in the number of crystallites per unit area. Even with the considerable increase in Mo films' crystallite size deposited without a barrier after annealing, the value of stress remained the most negative (compressive) compared to other films that were closer to zero value.

The films deposited on the Ti barrier showed a change from tensile (positive) to a slightly compressive (negative) stress, which may be due to Ti's diffusion into the layer evident from the increase in the Ti intensity peak after annealing. The stress values for films on ZnO barriers reduced marginally to tensile after annealing, which may be due to improved crystallinity of the underlying barrier.

4.3.3 Morphological analysis

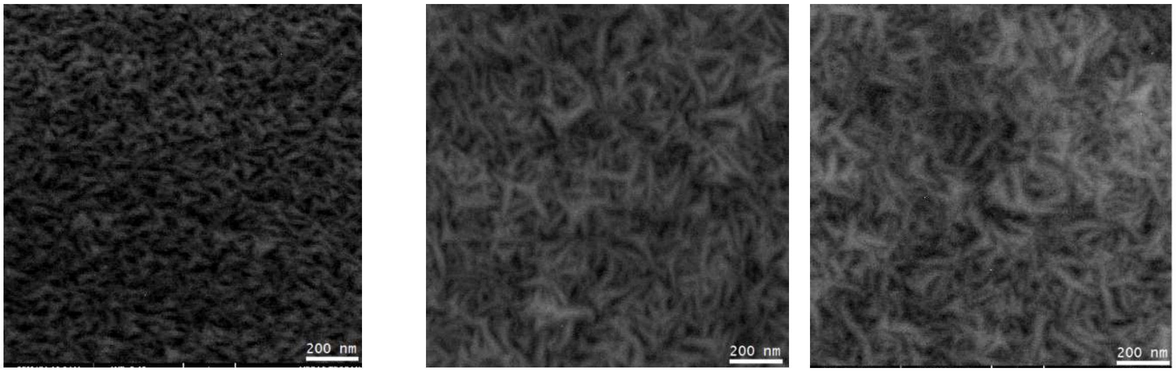

(a) (b) (c)

Figure 4. 13 *SEM Micrographs of Mo films deposited with 300 W power and 7.5 mTorr pressure on (a) SS, (b) with Ti barrier, and (c) ZnO barrier, both showing fiber-like structures.*

Mo films' micrographs deposited on SS without a barrier (Fig. 4.13a) appeared triangular [34,36]. In contrast, depositions on barriers appeared more fiber-like (Fig. 4.13 b and c) [37,38]. Depositing at lower pressure values, which reportedly produce densely packed grains [38], may help create larger grains with annealing [36] and help inhibit impurity diffusion.

Table 4. 5 *Comparative elemental compositions of the elements in the Mo layer, as-deposited and annealed, and the % reduction of impurities after annealing with barriers to a deposition without a barrier*

	Sample condition	*% Fe*	*% Cr*	*% Mo*	*% Zn*	*% O*	*% Ti*	*% Reduction with barrier*	
								Fe	**Cr**
SS_Mo	Annealed	28.51	6.30	65.19				-	-
SS_Ti_Mo	As deposited	3.34	0.72	95.29	-	-	0.65	-	-
	Annealed	19.63	4.15	69.05	-	-	7.18	31.15	34.13
SS_ZnO(A)_Mo	As deposited	17.19	3.65	61.44	0	17.34	-	-	-
	Annealed	26.34	5.80	49.15	2.00	16.73	-	7.61	7.94
SS_ZnO(100)_Mo	As deposited	2.93	0.69	76.00	0.72	19.66	-	-	-
	Annealed	16.79	3.93	56.87	1.60	20.82	-	41.11	37.62

We measured the elemental compositions of the Mo/barrier depositions using EDS studies. Elemental compositions of the composite Mo/barrier structures showed that the ZnO barrier deposited at a substrate temperature of 100°C provided about 40% more reduction in Fe and Cr impurity atoms, and the Mo/Ti tandem structure gave about 31% reduction for Fe and 34% for Cr atoms. The minimum barrier performance was by ZnO deposited at the ambient condition with a reduction of approximately 8% for Fe and Cr. The improvement in the ZnO barrier's performance deposited at a substrate temperature can be attributed to the improvement in crystalline quality, as shown in the X-ray diffractogram.

4.3.4 Resistivity measurements

The electrical sheet resistance and Mo's associated resistivity, which play vital roles in back-contact fabrication, are rarely considered since SS is highly conductive with resistivity in the order of 10^{-6} **Ω** m. The focus of most studies is based on the fabrication of potential barriers instead. However, assuming a parallel combination of resistance between the SS substrate, the barrier, and the Mo layer, we can calculate the effective resistance of the back-contact using the relation;

$$\frac{1}{R_{eff}} = \frac{1}{R_{SS}} + \frac{1}{R_{barrier}} + \frac{1}{R_{Mo}} \qquad \textbf{(Eqn. 4. 1)}$$

where R_{eff} is the effective resistance

R_{SS} is the resistance of the SS

$R_{barrier}$ is the resistance of the barrier

R_{Mo} is the resistance of the Mo layer

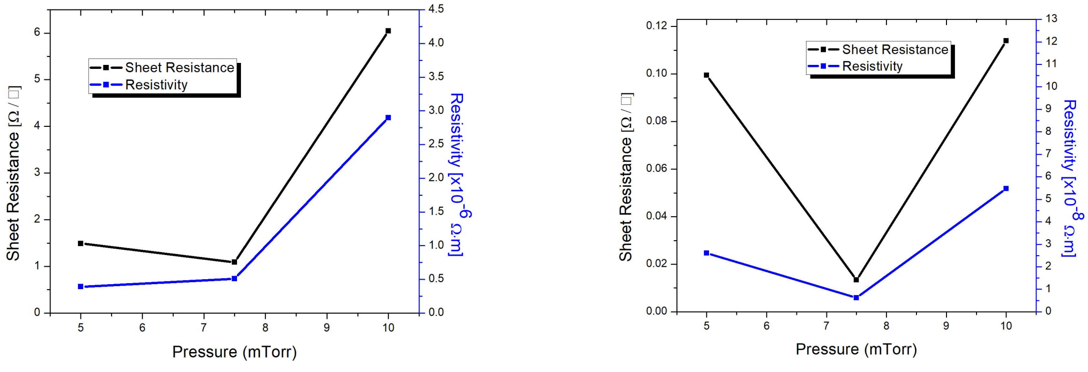

(a) (b)

Figure 4. 14 *Sheet Resistance and resistivity of molybdenum films on a) glass and b) SS with ambient ZnO barrier*

The effective resistance from the combination of resistances from Mo and SS, Mo, Ti, and SS was below our equipment's capacity to measure as they were lower in values. A layer of ZnO, which is a ceramic [39], has a higher resistivity, and thus we can measure the resistance of the Mo layer deposited on the ZnO barrier. The variation in crystallite properties with pressure affects the thin films (Fig. 10) and the resistivity. With annealing, the Mo/barrier structure shows an improvement in crystallinity, evident from the XRD characterization, and reduction in the resistivity. The Mo films' sheet resistance and the calculated resistivity (Fig. 14) showed a decrease in value with an increase in pressure from 5 to 7.5 mTorr. Further increase in the pressure can reduce the crystalline quality (Fig. 4.10), reflecting resistance increase.

4.3.5 SIMS characterization

The depth profile analysis of the Mo/barrier layers using the SIMS technique provides information on the elemental distribution moving into the film from the top, with sensitivity for even trace elements and capacity for sub-nanometer depth resolution. Although this technique provided the tool for analysis of the composition, the SIMS signal is not quantitative. The relative intensities of the secondary ion peaks in SIMS do not directly reflect the species' relative concentrations in the sample. The depth profile's goal is to understand the distribution of elements as a depth function [40,41].

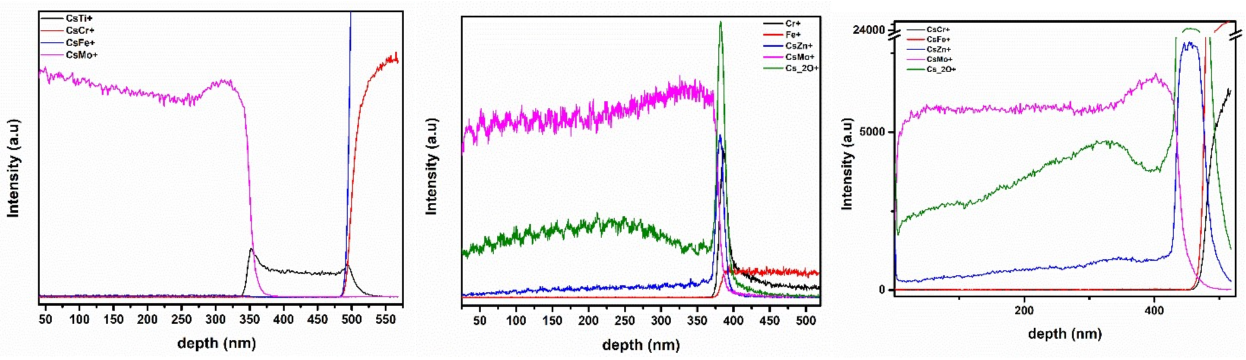

(a) (b) (c)

Figure 4. 15 *Depth profile of as-deposited Mo thin films on (a) SS with Ti barrier, (b) with ZnO barrier, and (c) with ZnO (deposited at 100°C substrate temperature) barrier*

The intensities of Mo in all samples (Fig. 4.15) without annealing showed a relatively uniform signal down the depth towards the interface. The oxygen intensity appears higher in intensity at the barrier layer because of the lower mass-to-charge value than the other elements. The Fe and Cr signals are suppressed in all samples, depicting a significant blockage of the impurity atoms.

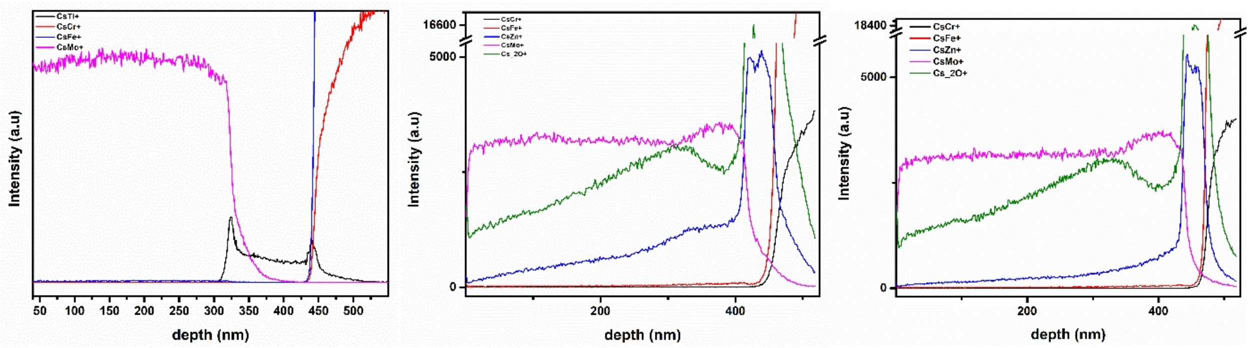

(a) (b) (c)

Figure 4. 16 *Depth profile of annealed Mo on (a) SS with Ti barrier, (b) with ZnO barrier, and (c) with ZnO (deposited at 100°C substrate temperature) barrier*

We observed a relatively steady Mo intensity signal after annealing until the Mo/barrier interface (Fig. 4.16). Fe and Cr's signals did not appear within the Mo layer's depth, up till the barrier layers, inferring the impurity atoms' effective shielding.

Thus, in all the profiles, as-deposited (Fig. 4.15) and annealed (Fig. 4.16), we observed that impurity signals are suppressed at the upper layers of the samples and only increased down the depth within the barriers. Since SIMS functions based on mass (per unit charge), that could account for the high-intensity signals of oxygen atoms observed for the ZnO barrier profiles since oxygen has a lower mass than Cs. Oxygen is also known to have a relatively high sensitivity factor. As earlier observed in unannealed samples, the shape of Mo profile intensity showed a relatively constant density distribution, which only decayed at the interface with the barrier materials, as observed from the profiles.

Summary

We optimized the dc sputtering conditions and successfully deposited a bilayer of Mo film with 300 W and 100 W power for layer-1 and layer- 2, respectively, at the constant pressure of 5 mTorr. The SEM image revealed a densely formed layer-1 and sparsely packed upper layer that formed with columnar structures. The bilayer film thickness was ca. 670 nm, as measured from the SEM cross-sectional image. AFM measurements showed granular structures with an RMS roughness (Rq) value of 1.644 nm for the bilayer film surface. As measured from the four-point probe technique, the Mo bilayer film's resistivity was 0.60×10^{-6} Ω m.

We optimized the parameters for depositing Mo/barrier layer for stainless steel substrate on the flexible substrate. Structural characterization showed better crystallinity at a dc sputtering power of 300 W and 7.5 mTorr. SEM micrographs showed fiber-like structures for the Mo layer deposited on a barrier. The elemental analysis using EDS showed a reduction of impurities with the ZnO barrier deposited at a substrate temperature of 100 °C (about 40%) and the Ti barrier (about 30%) and the minimum reduction by ZnO deposited at the ambient condition (about 8%). As-deposited and annealed, SIMS profiles for the samples showed a relatively uniform deposition of the Mo density and suppressed intensity of impurity atoms on the back-layer.

References

[1] W.-S. Liu, H.-C. Hu, N.-W. Pu, S.-C. Liang, Using a Ti/TiN composite structure as the diffusion barrier layer for CIGS solar cell application on stainless steel substrates, in: 2014 21st Int. Work. Act. Flatpanel Displays Devices, IEEE, 2014: pp. 245–248. https://doi.org/10.1109/AM-FPD.2014.6867182.

[2] W.S. Liu, H.C. Hu, N.W. Pu, S.C. Liang, Developing flexible CIGS solar cells on stainless steel substrates by using Ti/TiN composite structures as the diffusion barrier layer, J. Alloys Compd. 631 (2015) 146–152. https://doi.org/10.1016/j.jallcom.2014.12.189.

[3] C.Y. Shi, Y. Sun, Q. He, F.Y. Li, J.C. Zhao, Cu(In,Ga)Se 2 solar cells on stainless-steel substrates covered with ZnO diffusion barriers, Sol. Energy Mater. Sol. Cells. 93 (2009) 654–656. https://doi.org/10.1016/j.solmat.2008.12.004.

[4] D. Bae, S. Kwon, J. Oh, J. Lee, W. Kim, Fabrication of high efficiency flexible CIGS solar cell with ZnO diffusion barrier on stainless steel substrate, Mater. Res. Soc. Symp. Proc. 1324 (2012) 115–120. https://doi.org/10.1557/opl.2011.966.

[5] D. Bae, S. Kwon, J. Oh, W.K. Kim, H. Park, Investigation of Al2O3 diffusion barrier layer fabricated by atomic layer deposition for flexible Cu(In,Ga)Se2 solar cells, Renew. Energy. 55 (2013) 62–68. https://doi.org/10.1016/j.renene.2012.12.024.

[6] K.-B. Kim, Effect of Metal Barrier Layer for Flexible Solar Cell Devices on Tainless Steel Substrates, Appl. Sci. Converg. Technol. 26 (2017) 16–19. https://doi.org/10.5757/asct.2017.26.1.16.

[7] P. Blösch, F. Pianezzi, A. Chirilă, P. Rossbach, S. Nishiwaki, S. Buecheler, A.N. Tiwari, Diffusion barrier properties of molybdenum back contacts for Cu(In,Ga)Se2 solar cells on stainless steel foils, J. Appl. Phys. 113 (2013). https://doi.org/10.1063/1.4789616.

[8] C.-W. Kim, H.J. Kim, J.H. Kim, C. Jeong, Characterization of Flexible CIGS Thin Film Solar Cells on Stainless Steel with Intrinsic ZnO Diffusion Barriers, J. Nanosci. Nanotechnol. 16 (2016) 5124–5127. https://doi.org/10.1166/jnn.2016.12198.

[9] K. Herz, A. Eicke, F. Kessler, R. Wächter, M. Powalla, Diffusion barriers for CIGS solar cells on metallic substrates, Thin Solid Films. 431–432 (2003) 392–397. https://doi.org/10.1016/S0040-6090(03)00259-1.

[10] T.U.Pv.-Z.B. für M. und E. (HZB) C. A. Kaufmann, D. Greiner, S. Harndt, R. Klenk, S. Brunken, R. Schlatmann, M. Nichterwitz, H.-W. Schock, FLEXIBLE Cu(In, Ga)Se2 THIN FILM SOLAR CELLS FOR SPACE APPLICATIONS - RECENT RESULTS FROM A GERMAN JOINT PROJECT (PIPV2), in: 29th Eur. Photovolt. Sol. Energy Conf. Exhib., n.d.: pp. 1439–1443. https://doi.org/10.1017/CBO9781107415324.004.

[11] F. Kessler, D. Rudmann, Technological aspects of flexible CIGS solar cells and modules, Sol. Energy. 77 (2004) 685–695. https://doi.org/10.1016/j.solener.2004.04.010.

[12] S. Niki, M. Contreras, I. Repins, M. Powalla, K. Kushiya, S. Ishizuka, K. Matsubara, CIGS absorbers and processes, Prog. Photovoltaics Res. Appl. 18 (2010) 453–466. https://doi.org/10.1002/pip.969.

[13] J.W. Martin, Glasses and ceramics, in: Mater. Eng., Elsevier, 2006: pp. 133–158. https://doi.org/10.1533/9781845691608.2.133.

[14] B.W. D'Andrade, A.Z. Kattamis, P.F. Murphy, Flexible organic electronic devices on metal foil substrates for lighting, photovoltaic, and other applications, in: Handb. Flex. Org. Electron. Mater. Manuf. Appl., Elsevier Inc., 2015: pp. 315–341. https://doi.org/10.1016/B978-1-78242-035-4.00013-0.

[15] Z.-H. Li, E.-S. Cho, S.J. Kwon, Molybdenum thin film deposited by in-line DC magnetron sputtering as a back contact for Cu(In,Ga)Se2 solar cells, Appl. Surf. Sci. 257 (2011) 9682–9688. https://doi.org/10.1016/j.apsusc.2011.06.101.

[16] A.E.H.B. Kashyout, H.M.A. Soliman, H.A. Gabal, P.A. Ibrahim, M. Fathy, Preparation and characterization of DC sputtered molybdenum thin films, Alexandria Eng. J. 50 (2011) 57–63. https://doi.org/10.1016/j.aej.2011.01.009.

[17] W. Kiyotaka, K. Isaku, K. Hidetoshi, Handbook of Sputter Deposition Technology: Fundamentals and Applications for Functional Thin Films, 2012.

[18] J.H. Scofield, A. Duda, D. Albin, B.L. Ballard, P.K. Predecki, Sputtered molybdenum bilayer back contact for copper indium diselenide-based polycrystalline thin-film solar cells, Thin Solid Films. 260 (1995) 26–31. https://doi.org/10.1016/0040-6090(94)06462-8.

[19] F. Nemla, D. Cherrad, Metallic amorphous electrodeposited molybdenum coating from aqueous electrolyte: Structural, electrical and morphological properties under current

density, Appl. Surf. Sci. 375 (2016) 1–8. https://doi.org/10.1016/j.apsusc.2016.01.012.

[20] S.K. Ghosh, T. Bera, O. Karacasu, A. Swarnakar, J.G. Buijnsters, J.P. Celis, Nanostructured MoSx-based thin films obtained by electrochemical reduction, Electrochim. Acta. (2011). https://doi.org/10.1016/j.electacta.2010.10.065.

[21] Y. SINGH, ELECTRICAL RESISTIVITY MEASUREMENTS: A REVIEW, Int. J. Mod. Phys. Conf. Ser. 22 (2013) 745–756. https://doi.org/10.1142/s2010194513010970.

[22] S.-F. Chen, S.-J. Wang, W.-D. Lee, M.-H. Chen, C.-N. Wei, H.-Y.Y. Bor, Preparation and Characterization of Molybdenum Thin Films by Direct-Current Magnetron Sputtering, Atlas J. Mater. Sci. 2 (2017) 54–59. https://doi.org/10.5147/ajms.v2i1.123.

[23] S.F. Wang, H.C. Yang, C.F. Liu, H.Y.Y. Bor, Characteristics of bilayer molybdenum films deposited using Rf sputtering for back contact of thin film solar cells, Adv. Mater. Sci. Eng. 2014 (2014) 1–6. https://doi.org/10.1155/2014/531401.

[24] L. Assmann, J.C. Bernède, A. Drici, C. Amory, E. Halgand, M. Morsli, Study of the Mo thin films and Mo/CIGS interface properties, Appl. Surf. Sci. 246 (2005) 159–166. https://doi.org/10.1016/j.apsusc.2004.11.020.

[25] R. Syed, S.K. Ghosh, P.U. Sastry, G. Sharma, R.C. Hubli, J.K. Chakravartty, Electrodeposition of thick metallic amorphous molybdenum coating from aqueous electrolyte, Surf. Coatings Technol. 261 (2015) 15–20. https://doi.org/10.1016/j.surfcoat.2014.11.073.

[26] B. Bhushan, Surface Roughness Analysis and Measurement Techniques, Mod. Tribol. Handb. 1 (2001) 49–120.

[27] X. Hu, Z. Song, W. Liu, F. Qin, Z. Zhang, H. Wang, Chemical mechanical polishing of stainless steel foil as flexible substrate, Appl. Surf. Sci. 258 (2012) 5798–5802. https://doi.org/10.1016/j.apsusc.2012.02.100.

[28] L. Jiang, Y. He, Y. Yang, J. Luo, Chemical Mechanical Polishing of Stainless Steel as Solar Cell Substrate, ECS J. Solid State Sci. Technol. 4 (2015) P162–P170. https://doi.org/10.1149/2.0171505jss.

[29] S.J. Lee, Y.H. Chen, S.C. Hu, Y.C. Lin, J.W. Chang, T.L. Poon, W.C. Ke, Improved performance of amorphous Si thin-film solar cells on 430 stainless steel substrate by an

electrochemical mechanical polishing process, J. Alloys Compd. 558 (2013) 95–98. https://doi.org/10.1016/j.jallcom.2013.01.044.

[30] G. Regmi, M. Rohini, P. Reyes-Figueroa, A. Maldonado, M. de la Luz Olvera, S. Velumani, Deposition and characterization of ultrathin intrinsic zinc oxide (i-ZnO) films by radio frequency (RF) sputtering for propane gas sensing application, J. Mater. Sci. Mater. Electron. 29 (2018) 15682–15692. https://doi.org/10.1007/s10854-018-9166-1.

[31] O. Nwakanma, P. Reyes, S. Velumani, Electrical, structural, and topographical properties of direct current (DC) sputtered bilayer molybdenum thin films, J. Mater. Sci. Mater. Electron. 29 (2018) 15671–15681. https://doi.org/10.1007/s10854-018-9165-2.

[32] H. Windischmann, R.W.W. Collins, J.M.M. Cavese, Effect of hydrogen on the intrinsic stress in ion beam sputtered amorphous silicon films, J. Non. Cryst. Solids. 85 (1986) 261–272. https://doi.org/10.1016/0022-3093(86)90001-3.

[33] I. Blech, U. Cohen, Effects of humidity on stress in thin silicon dioxide films, J. Appl. Phys. 53 (1982) 4202–4207. https://doi.org/10.1063/1.331244.

[34] T. Yamaguchi, R. Miyagawa, Effects of oxygen on the properties of sputtered molybdenum thin films, Jpn. J. Appl. Phys. 30 (1991) 2069–2073. https://doi.org/10.1143/JJAP.30.2069.

[35] Y. Kim, M.S. Kim, H.J. Yun, S.Y. Ryu, B.J. Choi, Effect of growth temperature on AlN thin films fabricated by atomic layer deposition, Ceram. Int. 44 (2018) 17447–17452. https://doi.org/10.1016/j.ceramint.2018.06.212.

[36] H. Zhao, J. Xie, A. Mao, A. Wang, Y. Chen, T. Liang, D. Ma, Effects of Heating Mode and Temperature on the Microstructures, Electrical and Optical Properties of Molybdenum Thin Films, Materials (Basel). 11 (2018) 1634. https://doi.org/10.3390/ma11091634.

[37] J.-H. Cha, K. Ashok, N.J.S. Kissinger, Y.-H. Ra, J.-K. Sim, J.-S. Kim, C.-R. Lee, Effect of Thermal Annealing on the Structure, Morphology, and Electrical Properties of Mo Bottom Electrodes for Solar Cell Applications, J. Korean Phys. Soc. 59 (2011) 2280–2285. https://doi.org/10.3938/jkps.59.2280.

[38] W. Li, X. Yan, A.G. Aberle, S. Venkataraj, Effect of deposition pressure on the properties of magnetron-sputter-deposited molybdenum back contacts for CIGS solar cells, Jpn. J. Appl. Phys. 54 (2015) 08KC14. https://doi.org/10.7567/JJAP.54.08KC14.

[39] A. Sedky, T.A. El-Brolossy, S.B. Mohamed, Correlation between sintering temperature and properties of ZnO ceramic varistors, J. Phys. Chem. Solids. (2012). https://doi.org/10.1016/j.jpcs.2011.11.035.

[40] R. Wuerz, A. Eicke, M. Frankenfeld, F. Kessler, M. Powalla, P. Rogin, O. Yazdani-Assl, CIGS thin-film solar cells on steel substrates, Thin Solid Films. 517 (2009) 2415–2418. https://doi.org/10.1016/j.tsf.2008.11.016.

[41] D.S. McPhail, Applications of Secondary Ion Mass Spectrometry (SIMS) in materials science, J. Mater. Sci. 41 (2006) 873–903. https://doi.org/10.1007/s10853-006-6568-x.

Chapter Five: Deposition and characterization of optimized CI(G)Se absorber layer fabrication with alkali metals PDT

5.1 Introduction

The absorber layer's performance, an essential component of the solar cell, is greatly influenced by the structural, electrical, and optical properties, dependent on the growth method. Additionally, several studies focus on post-deposition treatments [1–6] to improve the absorber layers' properties within the grains, boundaries, and the layers' interface.

Among the several vacuum and non-vacuum methods available, the fabrication cost considered alongside the efficiency (i.e., cost-to-efficiency ratio) affects deposition method choice. The vacuum methods that tend to yield better-performing thin-films are more cost-intensive and may require specialized equipment with concerns relating to material utilization. Comparatively, the non-vacuum methods may produce lower efficiencies, offer better material utilization, and reduce costs.

For the deposition, we adopted the novel three-stage co-evaporation method for the absorber layer deposition. Section 5.1 presents the deposition parameters that play vital roles in the absorber layer's composition. The following sections (5.2) present the deposition and characterization of the copper-indium-selenium (CISe) layer and (5.3) copper-indium-gallium-selenium (CIGSe). Section 5.4 presented the non-vacuum spin-coating method used for PDT and the results from the proposed CIGSe with non-vacuum PDT in section 5.5.

5.2 Evaporation parameters and deposition rates

The distinct evaporation methods in vacuum conditions depending on the steps (e.g., one-shot, 2, 3- stages) or the presence of a crystalline phase (e.g., Cu-rich or poor) during the device formation affect the device performance. During evaporation, the total evaporated flux within the chambers depends on the vapor pressures and surface temperature of the sources, which may be loosely modeled by the relation [7],

$$In(R) = \frac{A}{T_s} + B \qquad \textbf{(Eqn. 5. 1)}$$

R is the evaporation rate, while **A** and **B** are constants, with **T_s** representing the surface temperature. The evaporated flux arriving on the substrate also depends on the distance between the flux beam's source and shape (ϕ). On arrival, the atoms either stick (i.e., adsorb) to the substrate or get re-evaporated. The atoms (**N**) ratio of adsorbed to the impinging gives the sticking coefficient, **S_c** [8].

$$S_c = \frac{N_{adsorbed}}{N_{impinging}} \qquad \textbf{(Eqn. 5. 2)}$$

The sticking coefficients of copper, gallium, and indium are close to one. The depositions carried out in an excess continuous selenium environment allow for the constant replacement of Se in the absorber layer and maintain its stoichiometry. Assuming the value of S_c equals one within a small chamber, highly focused evaporation sources with optimized source-to-substrate distance, each material's evaporation rate is assumed to be approximately equal to the deposition rate. The deposition rates (Table 5.1) allow for controlling the approximate thickness and each precursor's quantity in the layer.

Table 5. 1 *Evaporation parameters of the sources (with source-to-substrate distance ~25 cm)*

	Source Temp (Deg)	**Av. Thickness (µm)**	**Dep. Rate (Å/s)**	**Dep. Rate (nm/s)**
Cu	1250	0.1216	0.6755	0.0676
	1275	0.2021	1.1225	0.1123
	1300	0.2825	1.5695	0.1570
In	850	1.5950	8.8611	0.8861
	950	13.003	72.239	7.2239
Ga	900	0.6216	3.4531	0.3453
	1000	10.328	57.378	5.7378
Se	200	6.3132	35.073	3.5073

The co-evaporation technique, and adopted in this study, the novel three-stage method, requires the evaporating indium (In) and gallium (Ga) together in the deposition's first and final stages (refer to sec. 3.2.1). The base pressure for all depositions is ~ 6.0 x 10^{-6} Torr.

We theoretically estimate the absorber layer's composition using the deposition temperatures (i.e., deposition rates) (Table 5.2). Although it does not provide the absorber layer's actual composition due to substrate temperature effects and other ambient factors, it can guide a close approximation to the desired stoichiometry.

Table 5. 2 *Estimation of the fractional ratio with deposition rates*

	Source Temp (Deg)	**$\tau_{In}/(\tau_{In}+\tau_{Ga})$**	**$\tau_{Ga}/(\tau_{In}+\tau_{Ga})$**
In **Ga**	850 1000	0.134	0.866
In **Ga**	950 900	0.954	0.045
In **Ga**	950 950	0.704	0.296
In **Ga**	950 1000	0.557	0.443

The source temperatures for the elemental evaporations are; Cu ~ 1300 ºC, In ~ 900 ºC, Ga~ 1000 ºC and Se ~ 200 ºC. We carried out no surface treatment (e.g., with KCN) on the CIGSe layer after the deposition to avoid any extra element at the layer's surface. The composition ratios of the elements in the absorber layer are commonly denoted by;

$$x = \frac{Ga}{In+G} \qquad \textbf{(Eqn. 5. 3)}$$

The letter x represents the Ga elemental composition, and (1-x) gives the In composition. Gallium possesses smaller radium to indium ($r_{Ga}/r_{In} \approx 0.75$), and partial replacement of Ga with In distorts the lattice parameters. The tetragonal distortion magnitude is u = 2 - c/a (c/a = 2 for undistorted structure), varying linearly with Ga content and modifying the optical-electrical properties [9,10]. The Cu composition, represented by y, is given by;

$$y = \frac{Cu}{In+Ga} \qquad \textbf{(Eqn. 5. 4)}$$

We deposited the absorber layers using the three-stage, which consists primarily of the steps;

1. The deposition of an (In, Ga)Se thin film
2. Deposition of Cu in the presence of Se yielding a Cu-rich phase with a stoichiometry >1 (i.e., y=[Cu]/([In]+[Ga])>1)
3. In the final stage, the deposition of (In, Ga) adjusted to the desired thickness and stoichiometry to obtain preferably a Cu composition ranging between 0.8 < y < 1.2.

Selenium flux (Fig. 3.3) is continuously evaporated during deposition to provide a stoichiometric supply of Se. Its composition affects the morphology, structure, and electrical properties of the absorber layer and defects [11–13]. During the evaporations, some phases of the elemental combinations occur, which metamorphosizes into the CI(G)Se compounds, usually due to the temperature gradients available during synthesis. The basic properties of the probable intermediate phases that could form during the deposition, i.e., CuSe and In(Ga)Se, were highlighted in section 2.3.1. The participating critical $Cu_{2-x}Se$ phase (i.e., second stage) related to the growth of CI(G)Se at Cu-rich condition favors the achievement of CIGSe with large grains. Due to a comparative higher diffusion rate of copper (~10^{-9} cm^2/s at 400 °C) to those of indium and gallium (~10^{-13} -10^{-12} cm^2/s) [14,15], the probable mechanism for CI(G)Se formation is the diffusion of Cu atoms into the $(In, Ga)_2Se_3$ and the corresponding counter diffusion of vacancies into Cu_xSe, characteristic of atomic transport via vacancies.

When the layer is Cu-rich, the recrystallization phenomenon enables the reconstruction of the layers by a grain boundary migration mechanism [16] and changing the structures from small to large grains while minimizing crystalline defects in the grains.

5.3 Alkali halide deposition

The conventional method for alkali metal deposition during the post-deposition treatments has been through controlled evaporation of varying thicknesses in vacuum conditions [17–20]. However, using an optimized non-vacuum technique can also present a viable and scalable alternative for tapping into the advantages of employing alkali metals on CIGSe solar cells.

We prepared an optimized 0.3M solution of cesium fluoride (CsF) and rubidium fluoride (RbF) in isopropyl alcohol. The optimized molarity allows for the deposition of a thin layer (<70nm) of the alkali material, with proper drying without forming a gel. The thin films also appear to be hygroscopic, causing a thicker film to readily absorb moisture from the atmosphere, which may be detrimental to fabrication. The solvent evaporates faster with thermal treatment, leaving behind the constituents of the solute. The thickness of the spin-coated layers also depends on the fluid's viscosity and rotation speed (rpm). All depositions were done in a nitrogen atmosphere using the optimized spin-coating parameters: 2000 rpm, <18% humidity for 45 secs. The films are dried at 350 °C in the chamber within the nitrogen atmosphere.

Table 5. 3 *The EDS analysis of the average composition of alkali halides deposited on a glass substrate*

Alkali halides	Composition			
	Cs	F	O	C
CsF	99.00	0.06	0.93	0.01
	Rb	F	O	C
RbF	99.04	0.06	0.90	0.01

The elemental composition of the alkali fluoride film on the glass after deposition and annealing (Table 5.3) showed a high content of the alkali metals—the presence of carbon and oxygen, maybe from the organic solvent used during preparation. The relatively large amount of alkali metals obtained from the method substantiates the inclusion of the alkali metal layer in the solar cell and not as a halide. The approximate thickness of the films on a simple glass substrate measure with a profilometer is 39.73±1.86 nm.

5.4 CuIn(Ga)Se_2 absorber deposition and characterization

5.4.1 Structural properties

We studied the crystalline properties of the deposited thin films using X-ray diffraction (XRD). The diffractogram obtained after normalization shows that more prominent peaks of the CISe structures ((112), (204), (116/312)) (indexed with ICDD No. 00-040-1487) shifted to higher angles for CIGSe characterization (ICDD 00-035-1102), and confirming an ordered chalcopyrite structure. The peak positions marked with asterisks (*) are due to $K_{\alpha 2}$ radiations during the XRD measurements.

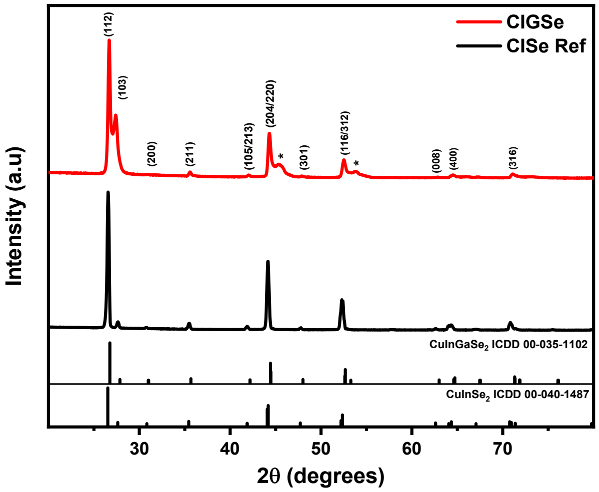

(a)

Figure 5. 1 *XRD patterns of the (a) CISe/CIGSe thin films annealed at 550 °C for 60 minutes.*

The observed shift in 2θ angles (e.g., from 26.57° in CISe to 26.68° in CIGSe for 112-plane) (Fig. 5.1) with Ga inclusion corresponds to a change in lattice parameters to a smaller unit cell probably due to the smaller atomic radius of Ga compared to In. It can also lead to more defects in the CuInSe lattice structure. Other parameters besides the deposition rates (e.g., excess Cu during second stage deposition, final thickness) can also influence the absorber layers' morphological and structural properties deposited by the three-stage procedure [9,21,22].

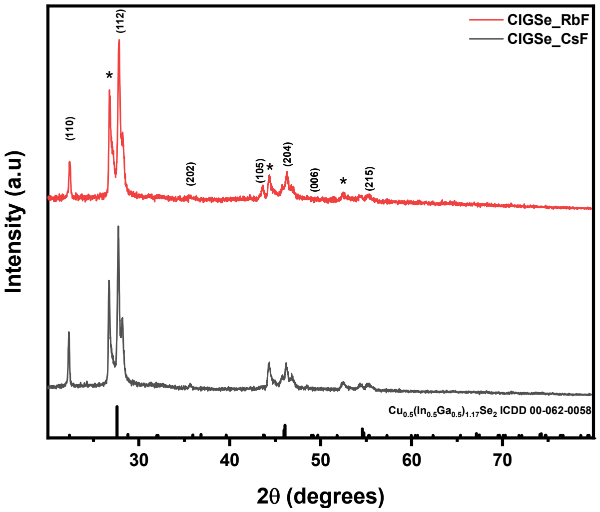

Figure 5. 2 *X-ray diffractogram of CIGSe absorber thin films with CsF and RbF PDT*

The X-ray diffractogram after PDT (Fig. 5.2) maintained the chalcopyrite structure. However, we observed a change of phase and other phases like copper-indium-selenide due to further recrystallization. After PDT, the observed peak (112) intense peaks coincide with Cu poor phases, which may be due to Ga and Cu's depletion at the surfaces due to alkali metal incorporations [23–26]. We observed no phases belonging to the alkali metals after PDT, consistent with the concept of the immiscibility of phases [27].

The chalcopyrite structures exhibited a preferential (112) orientation, typically promoted by Na's diffusion (from the SLG) into the absorber layer. The Lotgering factor (LF) proves a simple and easy calculation method of representation for the orientation degree. The computed LF is from the intensities of XRD peaks using the typical θ/2θ scan mode and defined by the equation [28,29];

$$LF = \frac{P-P_o}{1-P_o} \qquad \textbf{(Eqn. 5. 5)}$$

P denotes the ratio of the summation of the peak intensities corresponding to the preferred orientation axis to the sum of all diffraction peaks in particle-oriented materials. P_o originates from the reference data. The LF varies between zero to unity; LF = 0 relates to random orientation, while LF = 1 to a perfect orientation. If an orientation has an LF >|0.2|, and others are less than |0.2|, then the crystallites are assumed to have a preferential orientation in the corresponding (hkl) direction. Thus, films with LF ≤ |0.2| are considered to have a random texture. The thin films all appear to have a (112) preferential orientation (Table 5.4).

Table 5. 4 *LF factors for CIGSe thin films as-deposited and with PDT using Cs and Rb.*

	CIGSe	**CIGSe_Cs**	**CIGSe_Rb**
LF_{112}	0.27	0.50	0.51
LF_{204}	0.10	0.19	0.17

The lattice parameters (Table 5.5) showed the variations with Ga inclusion in CIGSe, increasing the tetragonal lattice distortion, u. As noted earlier, the atomic radius of Ga is smaller than In. Thus, partial inclusion and replacement of indium atoms cause a decrease in the lattice parameters ‘c’ and ‘a’ and the corresponding ‘c/a’ ratio. Ga reportedly preferentially diffuses towards the back contact. The addition and potential displacement of light alkali metals by heavy alkali metals may account for the further increase in u. The marginal difference in the lattice parameters of the as-deposited and PDT samples may also originate from the change in phases, i.e., stoichiometric to Cu poor phases, and the presence of other phases.

Table 5. 5 *Calculated lattice parameters for reference CIS thin film and CIGSe thin films as-deposited and with PDT using Cs and Rb.*

Sample	2θ (112)	FWHM	Dp	c	a	u
CISe Ref	26.6064	0.2303	37.02	11.5856	5.8009	0.0028
CIGSe	26.6870	0.1919	44.44	11.5460	5.7851	0.0042
CIGSe_Cs	27.7611	0.1771	48.26	10.8692	5.6283	0.0688
CIGSe_Rb	27.8336	0.1771	48.27	10.8998	5.5979	0.0529

5.4.2 Morphological properties

The grain sizes of polycrystalline materials in thin-film solar cells play vital roles in the devices' efficiency, proposing comparatively better efficiency/cost ratios to crystalline material-based solar cells. The morphological modifications on the absorber layers' surface area due to the accumulation of the alkali metals, which may situate within or in the grain boundaries at the absorber layer [30–32], passivates the absorber surfaces [33].

The PDT process creates several effects, including modifications in the surface composition and alkali content throughout the film, allowing the potential application of reduced minimal thickness of the CdS buffer layer [34]. The presence of alkali metals at the CIGSe surfaces, which reportedly causes the depletion of Cu content at the surface [24], aids Cd's diffusion into the CIGSe surface region during buffer layer deposition, leading to an improved junction quality [24]. The effects of alkali metal atoms on the absorber layers vary within the bulk and surface, depending on the concentration and depositing factors [35,36]. However, their relative atomic weights affect the migration properties through different process types [32] and different atomic drifting [37].

The effects of heavier atoms (Rb, Cs) mainly occur due to modifying the absorber interface and may influence the polycrystalline thin films' general grain parameters. The passivation effects improve the absorber layers' quality, adopting the description of “quality” to mean improved crystallite sizes, more considerable mobility, and diffusion length of carriers within the grains [38]. The enhancement of the morphology, usually by increasing the grain size, reduces crystalline defects and may increase mobility and effective coalescence while reducing the hillock-like defects [39].

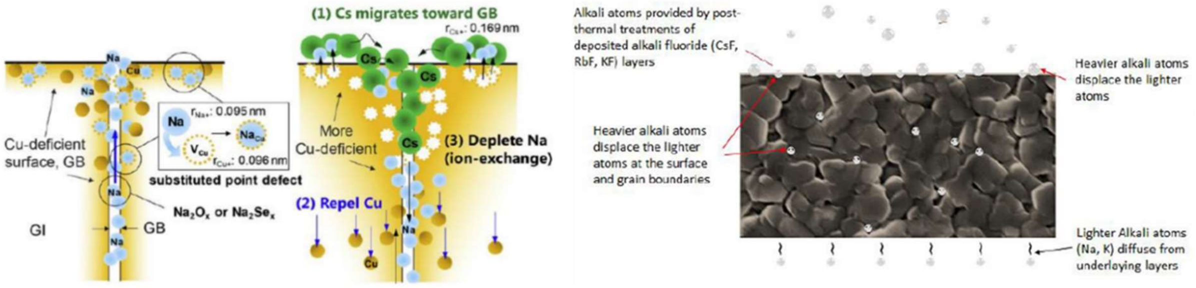

(a) (b)

Figure 5. 3 *Schematic diagrams of CIGSe thin-film with and without Cs-deposition (GI: grain interior; GB: grain boundary) [2]. The illustration shows the migration of alkali metals through the absorber layer exhibiting the ion displacement mechanism and the potential Cu-depletion at the layer's surface.*

The alkali metals cause some modifications on the absorber surface (Fig. 5.3), causing an increase of Cu-depleted regions explained by the out-diffusion of Cu atoms and in-diffusion alkali metal atoms [40]. The effects at the CIGSe surface are either bulk- or grain-boundary-induced effects, and in some cases, both. The introduction of heavier alkali elements through PDT displaces the lighter alkalis (i.e., Na and K), which may be present in the material, especially at the grain boundaries [24,31,37,41,42], through the so-called ion-exchange mechanism.

That causes a possible grain boundary reconstruction mechanism on the CIGSe thin films. They possess a relatively higher ionic radius and high formation energy, reducing the possibility of substituting the Cu vacancies [2,32]. They, however, have a more potent chemical affinity to In and Se and displace Cu. Thus, the more significant heavier alkali ions migrate toward the grain boundaries due to their loose atomic arrangement and relatively low chemical potential, creating a "grain boundary segregation." Subsequent displacement of Cu by the alkali atoms, causing Cu-deficient grain boundaries, leads to $AlkInSe_2$ or Alk-In(Ga)-Se compounds (Alk = alkali) at the grain boundaries with In, Ga, and Se [2]. Also, the relatively low enthalpies of alkali-$InSe_2$ compounds can account for their abilities to displace Cu [32].

We carried out the deposited films' surface characterization with a JEOL 6400 F scanning electron microscopy (SEM) equipped with an energy-dispersive X-ray detector (acceleration voltage of 20 kV) to study the morphology of films and estimate the atomic composition of the thin films.

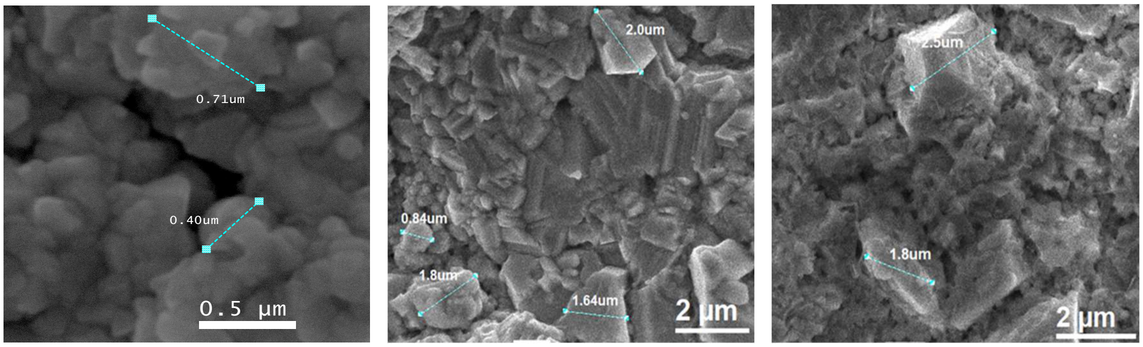

(a) (b) (c)

Figure 5. 4 *SEM images of CIGSe absorber thin films (a) as-deposited (b) Cs-PDT and (c) Rb-PDT*

The morphology (Fig. 5.4) shows a random distribution of grains with increased sizes after PDT and some smaller grains. The increase attributed to alkali metals getting fixated at the grain boundaries accounts for reducing grain boundaries. The overall compositions of the elements (Table 5.6) measured with EDS showed a reduction of Cu and marginally Ga's composition on the surfaces after PDT.

Table 5. 6 *Elemental compositions of the different materials using EDS analysis*

	%Cu	**%In**	**%Ga**	**%Se**	**%Alk**	**Cu/ (In+Ga)**	**In/ (In+Ga)**	**Ga/ (In+Ga)**
CIGSe	27.10	15.94	9.04	47.92	--	1.085	0.638	0.362
CIGSe_Cs	22.73	16.67	8.46	44.61	2.44	0.904	0.663	0.337
CIGSe_Rb	22.52	18.63	4.93	44.27	2.57	0.956	0.791	0.209

The decrease of Cu content with PDT, from slightly Cu-rich (>1) in as-deposited films to slightly Cu-poor (<1), supports the depletion at the surface and is consistent with the properties of OVC layers. The average In content increases marginally with a slight reduction of Ga content after PDT, more significant with RbF [4]. Selenized films with Ga/Ga+In ratios less than 0.6 may contain a phase-separated mixture of $CuInSe_2$ and $CuGaSe_2$ near the Mo/film interface [43], consistent with the observation in XRD.

5.4.3 Topographical analysis

The PDT, especially using heavier alkali metals, primarily influences the surface of the CIGSe layer. Therefore, a quantitative topological characterization, using at least three parameters, e.g., roughness profile parameters, skewness, and kurtosis, may be useful in the surfaces' architecture [44]. The surface structure plays a vital role in the interactions between this layer with the buffer layer and may significantly affect the surface's adherence [45].

We scanned all samples with a 10 µm × 10 µm field of view (data not shown) to obtain an even surface coverage and selected 1 µm × 1 µm areas for scanning and analysis to avoid damaged and contaminated areas. The images (2- and 3-dimensions) and cross-section line profiles (Fig. 5.5) generated for each of the surfaces allowed for roughness and statistical analysis and the subsequent plot of x-translation against height data (Fig. 5.5 iii).

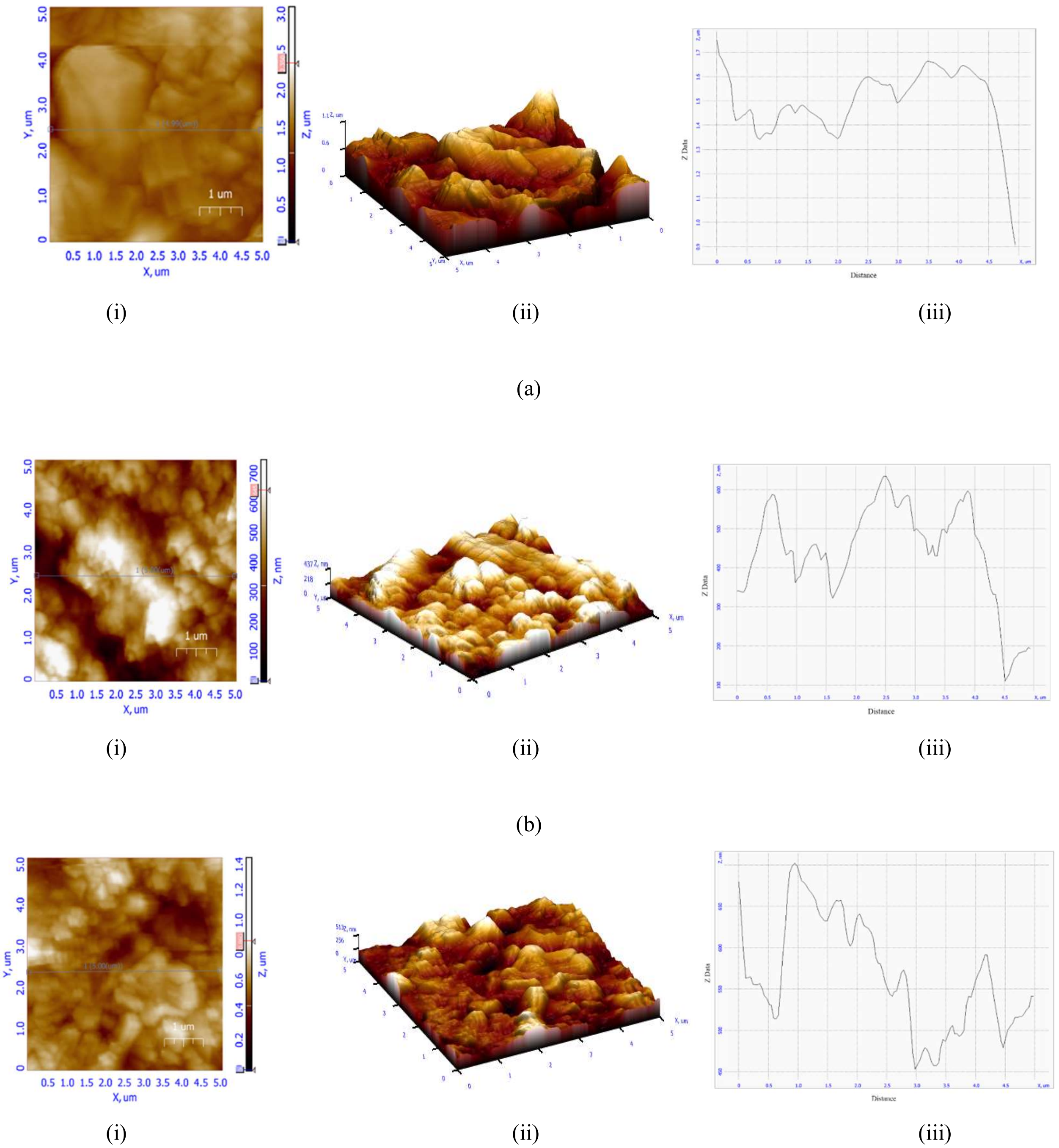

(i) (ii) (iii)

(a)

(i) (ii) (iii)

(b)

(i) (ii) (iii)

(c)

Figure 5. 5 *AFM images in two and three- dimensions images, cross-sectional profiles, and x- against Z data plot of CIGSe films (a) as-deposited (b) Cs_PDT and (c) Rb_PDT*

The PDT films showed a well reduced peak-to-peak value, which could be due to alkali metals' presence at the surfaces. To quantitatively assess roughness, some roughness parameters were calculated with the average roughness ranging between 103 nm for the as-deposited and reducing to 97 nm and 56 nm for Cs- and Rb-PDT films, respectively, and an image of the reduced surface roughness observed from the 3-dimensional images (Fig. 5.5).

Table 5. 7 *Surface parameters from AFM measurements of CIGSe samples*

	RMS, R_q (μm)	**Av. Roughness, R_a (μm)**	**Peak-to-peak, R_{max} (μm)**	**Skewness, R_{skw}**	**Kurtosis, R_{kur}**
CIGSe	0.138	0.103	0.863	-1.577	7.209
CIGSe_Cs	0.120	0.097	0.473	-0.364	2.241
CIGSe_Rb	0.67	0.056	0.249	-0.235	1.859

Using the roughness analysis parameters (Table 5.7), R_a, R_q, and R_{max} describe the vertical dimensions along the surface's x-direction. In contrast, R_{skw} and R_{kur} describe the horizontal dimensions along the z-direction. The R_{max} values, depicting the difference between the highest and lowest points on a surface and significantly affected by surface damage or contamination, reduced with PDT, presumably due to the alkali metals' attachment. R_a and the more sensitive R_q measured the spread of the height values around the mean value and reduced after PDT, almost to halve after treatment with Rb, and useful in skew and kurtosis computations.

The roughness skewness describes the surface profile variations' symmetry about the mean plane, being sensitive to occasional deep valleys or high peaks. The kurtosis value measures the distribution of spikes above and below the mean line. It is > 3 for spiky surfaces, < 3 for bumpy surfaces, and equals 3 for utterly random surfaces. A plot of x-translation against Z data and the corresponding simple statistics showed that the surfaces possess a negative skew, which reportedly is a criterion for a good bearing surface [46] with bumpy surfaces after PDT.

5.4.4 Electrical measurements

For polycrystalline materials, the migration of carriers through the intergrain barriers can be in either of the three ways: (a) tunneling, (b) thermionic emission, and (c) ohmic conduction. Furthermore, with PDT, the presence of alkali materials at the grain (e.g., Na) and intergrain boundaries (e.g., Cs, Rb) and possible secondary phase formations (e.g., AlkInSe) may induce some differences in the electrical properties due to properties such as effective mass or mobility, electron band structure (i.e., bandgap) and permittivity [47]. The grain boundaries act as potential barriers, impeding charges' flow through the thin-film semiconductors [48–50]. The Hall effect and resistivity measurements in van der Pauw configuration provide a vital technique to directly obtain a samples' conductive charge carrier concentration and mobility [50].

The Hall measurements on polycrystalline material usually yield an acceptable approximation of the grain boundaries' ingrained properties and contributions. The effective properties reduce to the in-grain values if the grain boundary properties get depleted (i.e., less conductive than the grains). The transport barrier at the grain boundary is not too significant.

The thin films' average thickness, measured with a profilometer, is 3.15 μm. We employed a current (1-2 μA) on the sample with an applied constant magnetic field of 5500G to the sample surface for the electrical characterization in ambient conditions.

Table 5. 8 *Resistivity, carrier concentration, and mobility of CIGSe samples*

	Resistivity (Ω cm)	**Carrier conc. (cm^{-3})**	**Mobility (cm^2/V s)**
CIGSe	19.3	1.8×10^{17}	1.77
CIGSe_Cs	104	7.6×10^{14}	78.6
CIGSe_Rb	537	2.0×10^{14}	57.11

The Cu depletion at the surfaces after PDT [Cu/(Ga + In) < 1], and the possible formation Alk–In–Se compound, (e.g., $CsInSe_2$ and $RbInSe_2$) on the CIGSe film surface due to the PDT [5,51] accounts for the increase in resistivity and reduction in carrier concentration [50,52].

The carriers' mobility within the thin films after PDT comes through contributions from the CIGSe grains and the alkali atoms occupying the grain boundaries. The relation may describe the contributions,

$$\frac{1}{\mu_{eff}} = \frac{1}{\mu_b} + \frac{1}{\mu_{gb}} \qquad \textbf{(Eqn. 5. 6)}$$

μ_b comes from the grain bulks and μ_{gb} from the grain boundaries [50,53]. Also, alkali atoms' ion-displacement mechanism accounts for Na's potential removal at the absorber layers' surface, contributing to the reduced carrier concentration (Table 5.8). However, the heavier alkali metals and passivation of the surface result in a tremendous increase in carrier mobility after PDT.

With optimized temperature treatment, the displaced lighter atoms (e.g., Na) can migrate and reattach themselves to the surface with the more massive atoms, resulting in increased mobility and carrier concentration [4,54].

5.4.5 Raman characterizations

Surface characterizations using Raman spectroscopy yield valuable results in the study of surfaces and of heterointerfaces between the constituent layers of low-dimensional structures. The technique depends on the Raman effect, according to which when incident light (wavelength 750–850 nm) excites constituents in the thin films, they will reflect light in a different wavelength. For CIGSe materials, using excitation wavelength measurements under UV (325 nm) may show an evolution of spectra related to the amorphous Se phase [55], denoting decomposition of the alkali-$InSe_2$ compound under UV excitation [56].

The Raman spectroscopy technique characterizing the vibrational, rotational, and other low-frequency modes in a system determines the single or poly-type structures and secondary phases in a sample. The peaks associated with longitudinal vibrations became more intense than those associated with transversal vibrations due to the Fröhlich electron−phonon interaction as the excitation light approaches resonance. The relative intensity of the peaks relates to the different types of vibrations, longitudinal or transversal, that originate such peaks interact with the excitation light [57]. The reflected light's wavelength is also characteristic of various chemical components and possible compositions.

The presence of alkali metal secondary phases on top of the CIGSe was not possible using XRD but requires advanced characterization techniques, e.g., X-ray photoelectron spectroscopy

(XPS) or high-resolution transmission electron microscopy (TEM). However, the fast and non-destructive Raman characterization technique provides reliable detection, identification, and characterization for thin layers of alk-$InSe_2$ on the $CIGSe_2$-based absorber layers [56].

The typical Raman spectrum of CISe has a high-intensity peak corresponding to the A1 optical phonon mode of the chalcopyrite structures and several less intense peaks (e.g., the weaker B_2/E mode), typically less than 10% of the primary peak intensity outside of the resonant conditions in the low wavenumber range below 80 cm^{-1} and within the high wavenumber range above 200 cm^{-1} [58–60]. The shifts in peak positions for CISe-base material are commensurate with the Ga content. The detection of alk-$InSe_2$ can also be more difficult in CIGSe materials where Ga incorporation leads to a shift of the compound's prominent peak to higher wavenumbers [57,61–63].

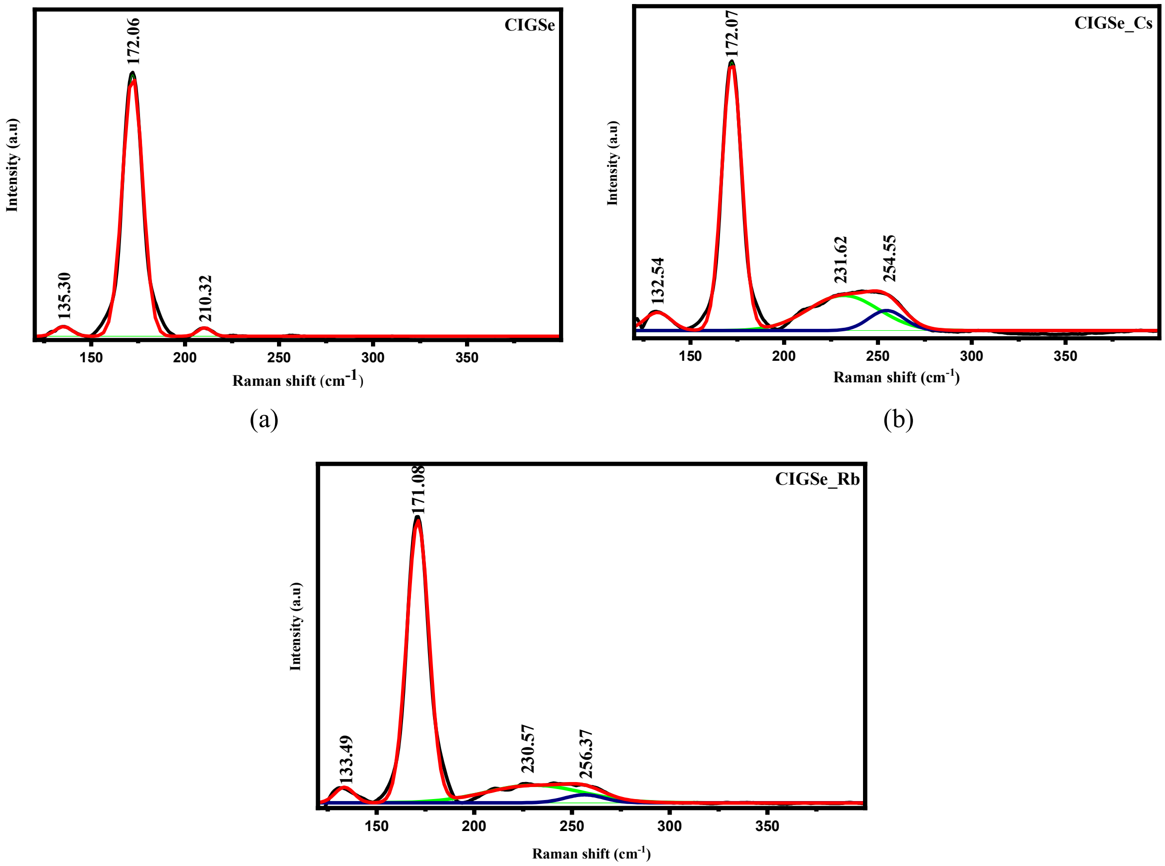

(a)

(b)

(c)

Figure 5. 6 *Raman spectra of CIGSe films as-deposited and with PDT*

All the characterized CIGSe films (Fig. 5.6) exhibited an intense scattering peak corresponding to the A1 optical phonon mode of the chalcopyrite structures and the weaker B_2/E mode for CIGSe absorber with no PDT. The presence of peaks at lower frequencies below the A1 characteristic phonon mode may be due to the ordered defect compounds' formation mechanism (ODCs) commonly present in high-efficiency CIGSe absorber materials [64]. Minor discrepancies exist between the frequency reported in this study and measured literature vibrational modes are below 5 cm^{-1}.

The slight variation in the positions may be due to the difference in the CISe material's composition. The observed broadened peak may be due to the OVC layer's presence or overlapping peaks created by alkali metals' addition (RbInSe, CsInSe) [65]. The deconvolution of broad peaks and shoulders applied to the analysis of different materials [66,67] allows the resolution of low intensity and highly overlapped peaks. Upon deconvolution, the observed Raman peaks at 254.55 cm^{-1} (Fig. 5.6 b) and 256.37 cm^{-1} (Fig. 5.6 c) may be due to the presence of $CsInSe_2$ and $RbInSe_2$ [56], respectively.

Summary

We carried out a PDT of CIGSe absorber layers using heavy alkali metals deposited in a non-vacuum environment. The XRD studies showed a successful deposition of the alkali metal layer without any structural modifications. This result corroborated by Raman studies showed the major chalcopyrite vibration modes and a slight shoulder, attributable to the presence of OVC layers. Surface modifications can improve the grain structures, leading to reduced recombination losses, as shown by the SEM studies. AFM results show an enhancement of the surface topographical properties, improving the interface with the buffer layer. The reduction in the Cu content and potential displacement of Na from the surface leads to a reduction in the carrier concentration, as shown by Hall effect characterization. However, there is an increase in the mobility of the carriers after the PDT. Raman characterization on all the CIGSe films showed the A1 optical phonon mode of the chalcopyrite structures and peaks at lower frequencies belonging to the ODCs. The deconvolution of the broad peaks on CIGSe films with PDT displayed peaks confirming the formation of alk-$InSe_2$ phases on top of the absorber layer.

The results show that the proposed method will be successful for alkali metals PDT in CIGSe solar cells, with great potential for improved efficiencies. Further studies will focus on the fabrication of CIGSe solar cell devices using this PDT processing.

References

[1] K. Kim, I. Jeong, Y. Cho, D. Shin, S. Song, S.K. Ahn, Y.J. Eo, A. Cho, C. Jung, W. Jo, J.H. Kim, P.P. Choi, J. Gwak, J.H. Yun, Mechanisms of extrinsic alkali incorporation in CIGS solar cells on flexible polyimide elucidated by nanoscale and quantitative analyses, Nano Energy. 67 (2020). https://doi.org/10.1016/j.nanoen.2019.104201.

[2] T.-Y. Lin, I. Khatri, J. Matsuura, K. Shudo, W.-C. Huang, M. Sugiyama, C.-H. Lai, T. Nakada, Alkali-induced grain boundary reconstruction on Cu(In,Ga)Se2 thin film solar cells using cesium fluoride post deposition treatment, Nano Energy. 68 (2020) 104299. https://doi.org/10.1016/j.nanoen.2019.104299.

[3] D. Kreikemeyer-Lorenzo, D. Hauschild, P. Jackson, T.M. Friedlmeier, D. Hariskos, M. Blum, W. Yang, F. Reinert, M. Powalla, C. Heske, L. Weinhardt, Rubidium Fluoride Post-Deposition Treatment: Impact on the Chemical Structure of the Cu(In,Ga)Se 2 Surface and CdS/Cu(In,Ga)Se 2 Interface in Thin-Film Solar Cells, ACS Appl. Mater. Interfaces. 10 (2018) 37602–37608. https://doi.org/10.1021/acsami.8b10005.

[4] T. Kodalle, M.D. Heinemann, D. Greiner, H.A. Yetkin, M. Klupsch, C. Li, P.A. van Aken, I. Lauermann, R. Schlatmann, C.A. Kaufmann, Elucidating the Mechanism of an RbF Post Deposition Treatment in CIGS Thin Film Solar Cells, Sol. RRL. 2 (2018) 1800156. https://doi.org/10.1002/solr.201800156.

[5] E. Handick, P. Reinhard, R.G. Wilks, F. Pianezzi, T. Kunze, D. Kreikemeyer-Lorenzo, L. Weinhardt, M. Blum, W. Yang, M. Gorgoi, E. Ikenaga, D. Gerlach, S. Ueda, Y. Yamashita, T. Chikyow, C. Heske, S. Buecheler, A.N. Tiwari, M. Bär, Formation of a K-In-Se surface species by NaF/KF postdeposition treatment of Cu(In,Ga)Se2 thin-film solar cell absorbers, ACS Appl. Mater. Interfaces. 9 (2017) 3581–3589. https://doi.org/10.1021/acsami.6b11892.

[6] I. Khatri, H. Fukai, H. Yamaguchi, M. Sugiyama, T. Nakada, Effect of potassium fluoride post-deposition treatment on Cu(In,Ga)Se2 thin films and solar cells fabricated onto sodalime glass substrates, Sol. Energy Mater. Sol. Cells. 155 (2016) 280–287. https://doi.org/10.1016/j.solmat.2016.06.023.

[7] Wiley-VCH, ed., Ullmann’s Chemical Engineering and Plant Design, Wiley, 2004. https://books.google.com.mx/books?id=q0lOAQAACAAJ.

[8] K.N. (King-N. Tu, Electronic thin film science : for electrical engineers and materials scientists, Macmillan, New York, 1996.

[9] D. Abou-Ras, R. Caballero, C.A. Kaufmann, M. Nichterwitz, K. Sakurai, S. Schorr, T. Unold, H.W. Schock, Impact of the Ga concentration on the microstructure of CuIn1–xGaxSe2, Phys. Status Solidi – Rapid Res. Lett. 2 (2008) 135–137. https://doi.org/10.1002/pssr.200802059.

[10] S.-H. Wei, S.B. Zhang, A. Zunger, Effects of Ga addition to CuInSe2 on its electronic, structural, and defect properties, Appl. Phys. Lett. 72 (1998) 3199–3201. https://doi.org/10.1063/1.121548.

[11] K.H. Kim, K.H. Yoon, J.H. Yun, B.T. Ahn, Effects of Se Flux on the Microstructure of Cu(In,Ga)Se[sub 2] Thin Film Deposited by a Three-Stage Co-evaporation Process, Electrochem. Solid-State Lett. 9 (2006) A382. https://doi.org/10.1149/1.2208011.

[12] S. Chaisitsak, A. Yamada, M. Konagai, Preferred orientation control of Cu(In1-x Gax)Se2 (x ≈ 0.28) thin films and its influence on solar cell characteristics, Japanese J. Appl. Physics, Part 1 Regul. Pap. Short Notes Rev. Pap. 41 (2002) 507–513. https://doi.org/10.1143/jjap.41.507.

[13] S. Ishizuka, A. Yamada, P. Fons, S. Niki, Texture and morphology variations in (In,Ga) 2 Se 3 and Cu(In,Ga)Se 2 thin films grown with various Se source conditions, Prog. Photovoltaics Res. Appl. 21 (2013) 544–553. https://doi.org/10.1002/pip.1227.

[14] D.J. Schroeder, G.D. Berry, A.A. Rockett, Gallium diffusion and diffusivity in CuInSe 2 epitaxial layers, Appl. Phys. Lett. 69 (1996) 4068–4070. https://doi.org/10.1063/1.117820.

[15] K. Gartsman, L. Chernyak, V. Lyahovitskaya, D. Cahen, V. Didik, V. Kozlovsky, R. Malkovich, E. Skoryatina, V. Usacheva, Direct evidence for diffusion and electromigration of Cu in CuInSe2, J. Appl. Phys. 82 (1997) 4282–4285. https://doi.org/10.1063/1.366252.

[16] N. Barreau, T. Painchaud, F. Couzinié-Devy, L. Arzel, J. Kessler, Recrystallization of CIGSe layers grown by three-step processes: A model based on grain boundary migration, Acta Mater. 58 (2010) 5572–5577. https://doi.org/10.1016/j.actamat.2010.06.025.

[17] H. Lee, Y. Jang, S.-W. Nam, C. Jung, P.-P. Choi, J. Gwak, J.H. Yun, K. Kim, B. Shin, Passivation of Deep-Level Defects by Cesium Fluoride Post-Deposition Treatment for

Improved Device Performance of Cu(In,Ga)Se 2 Solar Cells, ACS Appl. Mater. Interfaces. 11 (2019) 35653–35660. https://doi.org/10.1021/acsami.9b08316.

[18] S. Zahedi-Azad, M. Maiberg, R. Clausing, R. Scheer, Influence of heavy alkali post deposition treatment on wide gap Cu(In,Ga)Se 2, Thin Solid Films. 669 (2019) 629–632. https://doi.org/10.1016/j.tsf.2018.11.041.

[19] M. Raghuwanshi, A. Vilalta-Clemente, C. Castro, S. Duguay, E. Cadel, P. Jackson, D. Hariskos, W. Witte, P. Pareige, Influence of RbF post deposition treatment on heterojunction and grain boundaries in high efficient (21.1%) Cu(In,Ga)Se2 solar cells, Nano Energy. 60 (2019) 103–110. https://doi.org/10.1016/j.nanoen.2019.03.028.

[20] E. Avancini, R. Carron, T.P. Weiss, C. Andres, M. Bürki, C. Schreiner, R. Figi, Y.E. Romanyuk, S. Buecheler, A.N. Tiwari, Effects of Rubidium Fluoride and Potassium Fluoride Postdeposition Treatments on Cu(In,Ga)Se 2 Thin Films and Solar Cell Performance, Chem. Mater. 29 (2017) 9695–9704. https://doi.org/10.1021/acs.chemmater.7b03412.

[21] D. Abou-Ras, M.A. Contreras, R. Noufi, H.W. Schock, Impact of the Se evaporation rate on the microstructure and texture of Cu(In,Ga)Se2 thin films for solar cells, Thin Solid Films. 517 (2009) 2218–2221. https://doi.org/10.1016/j.tsf.2008.10.133.

[22] N. Barreau, J. Lähnemann, F. Couzinié-Devy, L. Assmann, P. Bertoncini, J. Kessler, Impact of Cu-rich growth on the CuIn1-xGaxSe2 surface morphology and related solar cells behaviour, Sol. Energy Mater. Sol. Cells. 93 (2009) 2013–2019. https://doi.org/10.1016/j.solmat.2009.08.004.

[23] E. Ghorbani, P. Erhart, K. Albe, Energy level alignment of Cu(In, Ga)(S, Se)2 absorber compounds with In2S3, NaIn5S8, and CuIn5S8 Cd-free buffer materials, Phys. Rev. Mater. 3 (2019) 075401. https://doi.org/10.1103/PhysRevMaterials.3.075401.

[24] A. Chirilă, P. Reinhard, F. Pianezzi, P. Bloesch, A.R. Uhl, C. Fella, L. Kranz, D. Keller, C. Gretener, H. Hagendorfer, D. Jaeger, R. Erni, S. Nishiwaki, S. Buecheler, A.N. Tiwari, Potassium-induced surface modification of Cu(In,Ga)Se 2 thin films for high-efficiency solar cells, Nat. Mater. 12 (2013) 1107–1111. https://doi.org/10.1038/nmat3789.

[25] P. Pistor, D. Greiner, C.A. Kaufmann, S. Brunken, M. Gorgoi, A. Steigert, W. Calvet, I. Lauermann, R. Klenk, T. Unold, M.C. Lux-Steiner, Experimental indication for band gap

widening of chalcopyrite solar cell absorbers after potassium fluoride treatment, Appl. Phys. Lett. 105 (2014). https://doi.org/10.1063/1.4892882.

[26] M. Mezher, L.M. Mansfield, K. Horsley, M. Blum, R. Wieting, L. Weinhardt, K. Ramanathan, C. Heske, KF post-deposition treatment of industrial Cu(In, Ga)(S, Se) 2 thin-film surfaces: Modifying the chemical and electronic structure, Appl. Phys. Lett. 111 (2017) 071601. https://doi.org/10.1063/1.4998445.

[27] D. Hariskos, M. Powalla, Thermodynamic limitations for alkali metals in Cu(In,Ga)Se2, J. Mater. Res. 32 (2017). https://doi.org/10.1557/jmr.2017.394.

[28] Z.Y. Liu, F.P. Zhang, J.X. Zhang, X. Zhang, Q.M. Lu, X.Y. Yang, Enhanced electrical transport by texture modulation and co-doping for Ca3Co4O9+δ materials, Results Phys. 6 (2016) 203–208. https://doi.org/10.1016/j.rinp.2016.04.008.

[29] R. Furushima, S. Tanaka, Z. Kato, K. Uematsu, Orientation distribution-Lotgering factor relationship in a polycrystalline material - As an example of bismuth titanate prepared by a magnetic field, J. Ceram. Soc. Japan. 118 (2010) 921–926. https://doi.org/10.2109/jcersj2.118.921.

[30] P. Schöppe, S. Schönherr, R. Wuerz, W. Wisniewski, G. Martínez-Criado, M. Ritzer, K. Ritter, C. Ronning, C.S. Schnohr, Rubidium segregation at random grain boundaries in Cu(In,Ga)Se2 absorbers, Nano Energy. 42 (2017) 307–313. https://doi.org/10.1016/j.nanoen.2017.10.063.

[31] P. Jackson, R. Wuerz, D. Hariskos, E. Lotter, W. Witte, M. Powalla, Effects of heavy alkali elements in Cu(In,Ga)Se2 solar cells with efficiencies up to 22.6%, Phys. Status Solidi - Rapid Res. Lett. 10 (2016) 583–586. https://doi.org/10.1002/pssr.201600199.

[32] M. Malitckaya, H.P. Komsa, V. Havu, M.J. Puska, Effect of Alkali Metal Atom Doping on the CuInSe2-Based Solar Cell Absorber, J. Phys. Chem. C. 121 (2017) 15516–15528. https://doi.org/10.1021/acs.jpcc.7b03083.

[33] S. Kim, H. Tampo, H. Shibata, K. Matsubara, S. Niki, Effect of Combined Alkali (KF + CsF) Post-Deposition Treatment on Cu(InGa)Se2 Solar Cells, Phys. Status Solidi - Rapid Res. Lett. 12 (2018) 1–5. https://doi.org/10.1002/pssr.201800372.

[34] T.M. Friedlmeier, P. Jackson, A. Bauer, D. Hariskos, O. Kiowski, R. Wuerz, M. Powalla,

Improved Photocurrent in Cu(In,Ga)Se2Solar Cells: From 20.8% to 21.7% Efficiency with CdS Buffer and 21.0% Cd-Free, IEEE J. Photovoltaics. 5 (2015) 1487–1491. https://doi.org/10.1109/JPHOTOV.2015.2458039.

[35] J. Hedstrom, H. Ohlsen, M. Bodegard, A. Kylner, L. Stolt, D. Hariskos, M. Ruckh, H.-W. Schock, ZnO/CdS/Cu(In,Ga)Se/sub 2/ thin film solar cells with improved performance, in: Conf. Rec. Twenty Third IEEE Photovolt. Spec. Conf. - 1993 (Cat. No.93CH3283-9), IEEE, 1993: pp. 364–371. https://doi.org/10.1109/PVSC.1993.347154.

[36] S. Ye, X. Tan, M. Jiang, B. Fan, K. Tang, S. Zhuang, Impact of different Na-incorporating methods on Cu(In;Ga)Se2 thin film solar cells with a low-Na substrate, Appl. Opt. 49 (2010) 1662–1665. https://doi.org/10.1364/AO.49.001662.

[37] R. Wuerz, W. Hempel, P. Jackson, Diffusion of Rb in polycrystalline Cu(In,Ga)Se2 layers and effect of Rb on solar cell parameters of Cu(In,Ga)Se2 thin-film solar cells, J. Appl. Phys. 124 (2018) 165305. https://doi.org/10.1063/1.5044629.

[38] A. Morales-Acevedo, Physical basis for the design of CdS/CdTe thin film solar cells, Sol. Energy Mater. Sol. Cells. 90 (2006) 678–685. https://doi.org/10.1016/j.solmat.2005.04.004.

[39] P.S. Vasekar, N.G. Dhere, Effect of sodium addition on Cu-deficient CuIn1-xGaxS2 thin film solar cells, Sol. Energy Mater. Sol. Cells. 93 (2009) 69–73. https://doi.org/10.1016/j.solmat.2008.04.013.

[40] F. Pianezzi, P. Reinhard, A. Chirilă, B. Bissig, S. Nishiwaki, S. Buecheler, A.N. Tiwari, Unveiling the effects of post-deposition treatment with different alkaline elements on the electronic properties of CIGS thin film solar cells, Phys. Chem. Chem. Phys. 16 (2014) 8843–8851. https://doi.org/10.1039/c4cp00614c.

[41] S. Ishizuka, N. Taguchi, J. Nishinaga, Y. Kamikawa, S. Tanaka, H. Shibata, Group III Elemental Composition Dependence of RbF Postdeposition Treatment Effects on Cu(In,Ga)Se 2 Thin Films and Solar Cells, J. Phys. Chem. C. 122 (2018) 3809–3817. https://doi.org/10.1021/acs.jpcc.8b00079.

[42] A. Vilalta-Clemente, M. Raghuwanshi, S. Duguay, C. Castro, E. Cadel, P. Pareige, P. Jackson, R. Wuerz, D. Hariskos, W. Witte, Rubidium distribution at atomic scale in high efficient Cu(In,Ga)Se2 thin-film solar cells, Appl. Phys. Lett. 112 (2018) 103105. https://doi.org/10.1063/1.5020805.

[43] M. Marudachalam, R.W. Birkmire, H. Hichri, J.M. Schultz, A. Swartzlander, M.M. Al-Jassim, Phases, morphology, and diffusion in CuInxGa1−xSe2 thin films, J. Appl. Phys. 82 (1997) 2896–2905. https://doi.org/10.1063/1.366122.

[44] H.K. Webb, V.K. Truong, J. Hasan, C. Fluke, R.J. Crawford, E.P. Ivanova, Roughness Parameters for Standard Description of Surface Nanoarchitecture, Scanning. 34 (2012) 257–263. https://doi.org/10.1002/sca.21002.

[45] V.K. Truong, R. Lapovok, Y.S. Estrin, S. Rundell, J.Y. Wang, C.J. Fluke, R.J. Crawford, E.P. Ivanova, The influence of nano-scale surface roughness on bacterial adhesion to ultrafine-grained titanium, Biomaterials. 31 (2010) 3674–3683. https://doi.org/10.1016/j.biomaterials.2010.01.071.

[46] B. Rajesh Kumar, T. Subba Rao, AFM studies on surface morphology, topography and texture of nanostructured zinc aluminum oxide thin films, Dig. J. Nanomater. Biostructures. 7 (2012) 1881–1889.

[47] V. Šnejdar, J. Jerhot, Electrical conductivity of polycrystalline semiconductors, Thin Solid Films. 37 (1976) 303–316. https://doi.org/10.1016/0040-6090(76)90600-3.

[48] S.B. Atakulov, To the problem of Hall “mobility” in polycrystalline thin films with potential barriers, Solid State Commun. 51 (1984) 415–419. https://doi.org/10.1016/0038-1098(84)90125-X.

[49] J. Jerhot, V. Šnejdar, Hall effect in polycrystalline semiconductors, Thin Solid Films. 52 (1978) 379–395. https://doi.org/10.1016/0040-6090(78)90181-5.

[50] F. Werner, Hall measurements on low-mobility thin films, J. Appl. Phys. 122 (2017) 135306. https://doi.org/10.1063/1.4990470.

[51] N. Taguchi, S. Tanaka, S. Ishizuka, Direct insights into RbInSe 2 formation at Cu(In,Ga)Se 2 thin film surface with RbF postdeposition treatment, Appl. Phys. Lett. 113 (2018) 113903. https://doi.org/10.1063/1.5044244.

[52] H.H. Sheu, Y.T. Hsu, S.Y. Jian, S.C. Liang, The effect of Cu concentration in the photovoltaic efficiency of CIGS solar cells prepared by co-evaporation technique, Vacuum. 131 (2016) 278–284. https://doi.org/10.1016/j.vacuum.2016.07.008.

[53] J.W. Orton, M.J. Powell, The Hall effect in polycrystalline and powdered semiconductors,

Reports Prog. Phys. 43 (1980) 1263–1307. https://doi.org/10.1088/0034-4885/43/11/001.

[54] R. Scheer, H.-W. Schock, Chalcogenide Photovoltaics, Wiley-VCH Verlag GmbH & Co. KGaA, Weinheim, Germany, 2011. https://doi.org/10.1002/9783527633708.

[55] V. V. Poborchii, A. V. Kolobov, K. Tanaka, An in situ Raman study of polarization-dependent photocrystallization in amorphous selenium films, Appl. Phys. Lett. 72 (1998) 1167–1169. https://doi.org/10.1063/1.121002.

[56] M. Guc, T. Kodalle, R. Kormath Madam Raghupathy, H. Mirhosseini, T.D. Kühne, I. Becerril-Romero, A. Pérez-Rodríguez, C.A. Kaufmann, V. Izquierdo-Roca, Vibrational Properties of RbInSe2: Raman Scattering Spectroscopy and First-Principle Calculations, J. Phys. Chem. C. 124 (2020) 1285–1291. https://doi.org/10.1021/acs.jpcc.9b08781.

[57] W. Kauschke, M. Cardona, Resonant Raman Scattering in Semiconductors, Phys. Scr. T25 (1989) 201–205. https://doi.org/10.1088/0031-8949/1989/T25/036.

[58] H. Tanino, T. Maeda, H. Fujikake, H. Nakanishi, S. Endo, T. Irie, Raman spectra of CuInSe2, Phys. Rev. B. 45 (1992) 13323–13330. https://doi.org/10.1103/PhysRevB.45.13323.

[59] C. Rincón, F.J. Ramírez, Lattice vibrations of CuInSe2 and CuGaSe2 by Raman microspectrometry, J. Appl. Phys. 72 (1992) 4321–4324. https://doi.org/10.1063/1.352195.

[60] V. Izquierdo-Roca, X. Fontané, E. Saucedo, J.S. Jaime-Ferrer, J. Álvarez-García, A. Pérez-Rodríguez, V. Bermudez, J.R. Morante, Process monitoring of chalcopyrite photovoltaic technologies by Raman Spectroscopy: An application to low cost electrodeposition based processes, New J. Chem. 35 (2011) 453–460. https://doi.org/10.1039/c0nj00794c.

[61] S.Y. Kim, J. Kim, Fabrication of CIGS thin films by using spray pyrolysis and post-selenization, J. Korean Phys. Soc. 60 (2012) 2018–2024. https://doi.org/10.3938/jkps.60.2018.

[62] C. Insignares-Cuello, C. Broussillou, V. Bermúdez, E. Saucedo, A. Pérez-Rodríguez, V. Izquierdo-Roca, Raman scattering analysis of electrodeposited Cu(In,Ga)Se 2 solar cells: Impact of ordered vacancy compounds on cell efficiency, Appl. Phys. Lett. 105 (2014) 021905. https://doi.org/10.1063/1.4890970.

[63] C. Insignares-Cuello, V. Izquierdo-Roca, J. López-García, L. Calvo-Barrio, E. Saucedo, S.

Kretzschmar, T. Unold, C. Broussillou, T. Goislard de Monsabert, V. Bermudez, A. Pérez-Rodríguez, Combined Raman scattering/photoluminescence analysis of Cu(In,Ga)Se2 electrodeposited layers, Sol. Energy. 103 (2014) 89–95. https://doi.org/10.1016/j.solener.2014.02.005.

[64] C.-M.M. Xu, X.-L.L. Xu, J. Xu, X.-J.J. Yang, J. Zuo, N. Kong, W.-H.H. Huang, H.-T.T. Liu, Composition dependence of the Raman A 1 mode and additional mode in tetragonal Cu–In–Se thin films, Semicond. Sci. Technol. 19 (2004) 1201–1206. https://doi.org/10.1088/0268-1242/19/10/006.

[65] M. Guc, T. Kodalle, R. Kormath Madam Raghupathy, H. Mirhosseini, T.D. Kühne, I. Becerril-Romero, A. Pérez-Rodríguez, C.A. Kaufmann, V. Izquierdo-Roca, Vibrational Properties of RbInSe 2 : Raman Scattering Spectroscopy and First-Principle Calculations, J. Phys. Chem. C. 124 (2020) 1285–1291. https://doi.org/10.1021/acs.jpcc.9b08781.

[66] M. Placidi, M. Dimitrievska, V. Izquierdo-Roca, X. Fontané, A. Castellanos-Gomez, A. Pérez-Tomás, N. Mestres, M. Espindola-Rodriguez, S. López-Marino, M. Neuschitzer, V. Bermudez, A. Yaremko, A. Pérez-Rodríguez, Multiwavelength excitation Raman scattering analysis of bulk and two-dimensional MoS 2 : vibrational properties of atomically thin MoS 2 layers, 2D Mater. 2 (2015) 035006. https://doi.org/10.1088/2053-1583/2/3/035006.

[67] P. Vidal-Fuentes, M. Guc, X. Alcobe, T. Jawhari, M. Placidi, A. Pérez-Rodríguez, E. Saucedo, V.I. Roca, Multiwavelength excitation Raman scattering study of Sb 2 Se 3 compound: fundamental vibrational properties and secondary phases detection, 2D Mater. 6 (2019) 045054. https://doi.org/10.1088/2053-1583/ab4029.

Chapter Six: Characterization of aluminum-doped Zinc oxide and buffer layers deposition

6.1 Introduction

Thin-film depositions of aluminum-doped zinc oxide (AZO) for TCO applications commonly aim to reduce the resistivity with some thick layers, which show detrimental effects to the transmittance property. However, some reports on high-efficiency solar cells show that low-thickness AZO layers can also provide excellent efficiency. Recent studies aimed at developing ultra-thin devices show that low thickness layers can also yield better efficiency [1–4]. The lower resistivity values attained with some post-deposition treatment, usually by annealing at elevated temperatures up to 500°C [5–7], may cause some detrimental effects during device fabrications (e.g., the diffusion of Al into the absorber layer) in the substrate configuration. The optimal deposition techniques and parameters [1,6–10] affect the deposited films' properties, influencing the solar cell device [11,12].

This study aims at depositing ultra-thin AZO films (~100 nm) with higher transmittance and comparatively low sheet resistances at moderate temperatures (< 200 °C) with no need for further post-deposition treatment. The physical deposition parameters and machine configurations enumerated in section 3.4 reportedly affect the thin films [13].

6.2 Optimizing the deposition parameters

All film depositions' base pressure was approximately 5.0×10^{-6} Torr to avoid contamination from any residue gas in the sputtering chamber with ambient deposition temperatures rising to ~43 °C due to non-intentional heating. A substrate rotation of about 0.05 rpm was maintained in depositions to ensure the film's uniformity over the surfaces and reflected power of less than 3 W for all depositions.

The optimization results on thickness and resistivity characterizations for AZO films (Table 6.1) deposited for 90 minutes at ambient temperatures showed variations with the working pressure and sputtering power. Increasing the sputtering power at a constant pressure value of 15 mTorr showed an accompanying reduction in resistivity and increased thickness. At a constant sputtering power of 125 W, increasing the operating pressure results in lesser thickness, and the resistivity of thin films tends to decrease with increasing pressure. Further increase in working pressure beyond 25 mTorr may present detrimental effects on the films, as evident in the low deposition rates commonly associated with RF sputtering [12].

The reduction in resistivity could be due to improved doping of the ZnO lattice with Al ions. Attempts at depositions with lower sputtering power (50 W or lesser) and higher pressure (≥15 mTorr) produce no measurable thickness and very high resistivity beyond our equipment scale. The poor deposition may be due to high entropy and less kinetic energy. We ignored a further increase in sputtering power (beyond 135 W) to accommodate the limits of the maximum power density of the target (20 W/inch^2).

Table 6. 1 *Thickness and resistivity for varying sputtering powers and pressures*

Power (W)	Pressure (mTorr)	Average thickness (nm)	Resistivity (Ω cm)
50	15	--	--
75		70.8	8400
125		120.1	4.61
135		139.9	3.62
125	5	141.8	--
	15	120.1	4.61
	20	27.6	0.516
	25	14.4	0.304

Contrary to the observations during sputtering at lower pressures, mainly for single elemental materials (e.g., Mo) [14–16], materials that require some doping tend to require some higher pressures to allow for incorporation of the dopant in the crystal structure. Adopting an optimal sputtering power (125 W) and pressure (20 mTorr), we increased the deposition time (150 minutes) to improve the thickness of the thin-film. The average thickness of the AZO thin films is 97 nm.

6.2.1 Structural characterization

The X-ray diffractogram of the AZO films (Fig. 1) showed characteristic peaks of a hexagonal wurtzite structure (ICCD 00-036-1451), with preferred orientation and peak intensities varying with deposition parameters and temperature effects.

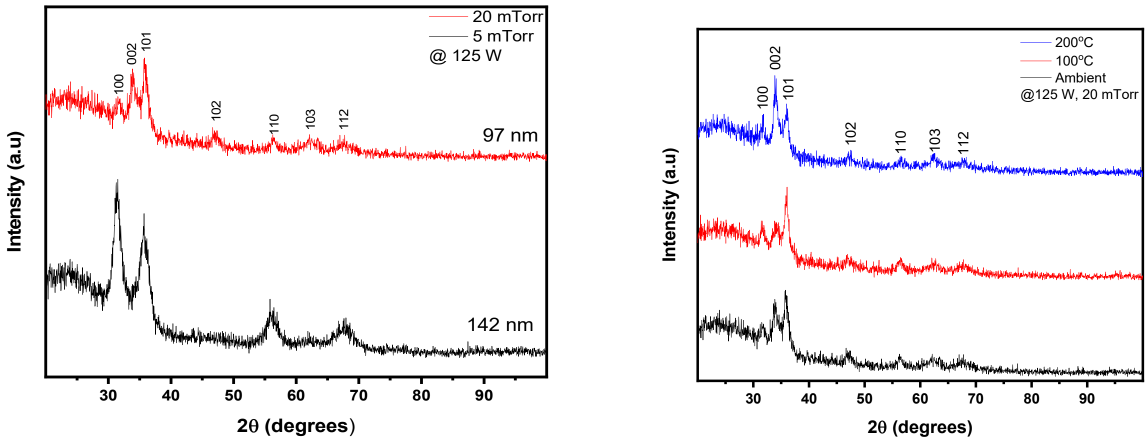

(a) (b)

Figure 6. 1 *XRD pattern of the AZO films deposited at (a) different pressures and the same power and (b) different temperatures*

We observed the (002) peak position previously lacking in depositions with lower working pressure (5 mTorr) (Fig. 6.1a) as the pressure increased (20 mTorr), which could be due to the greater incorporation of Al within the crystal lattice. At a constant power of 125 W and 20 mTorr working pressure, the increase in substrate temperature (Fig. 6.1b) seemed to increase the relative peak intensity and induce a change in the preferred orientation from (101) to (002) at a substrate temperature of 200 oC, consistent with an increase in the atomic ratio of Al [6,10,17]. Al also reflects the diffraction angle shift to a higher 2θ value and a marginal increase in the bond length, L (Table 6.2).

Table 6. 2 *Lattice parameters of AZO films deposited at 125 W and 20 mTorr at different temperatures: ambient, 100°C and 200°C*

Temp. (°C)	2θ (°)	FWHM (β)	D_p (nm)	a (Å)	c (Å)	c/a	L (Å)
Ambient	35.76	0.472	18.5	3.253	5.295	1.628	1.990
100	35.93	0.630	13.8	3.273	5.270	1.610	1.995
200	36.12	0.394	36.7	3.261	5.305	1.627	1.994

6.2.2 Morphological analysis

The surface morphology of the AZO films (Fig. 6.2) showed the presence of randomly oriented grains, which appears to increase with the effects of temperature. The temperature gradient application reduces ZnO's surface energy [18] and allows for more incorporation of Al [19]. The increase in grain sizes offer better compactness and helps to decrease optical scattering [12].

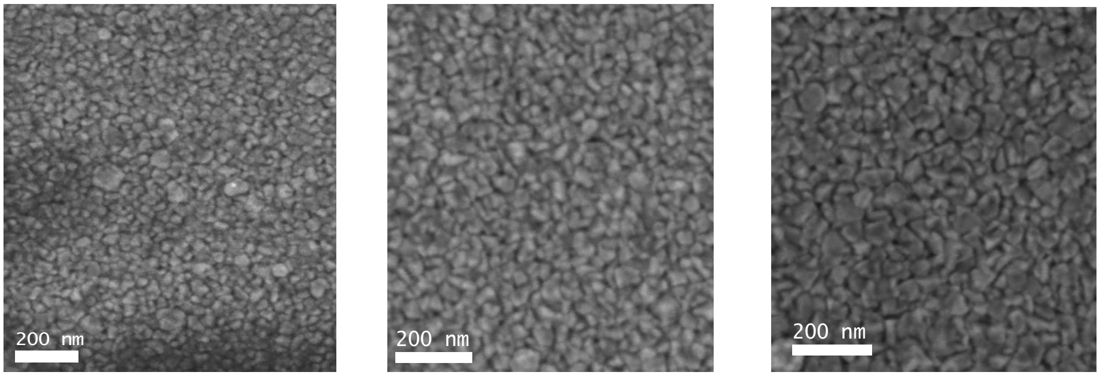

(a) (b) (c)

Figure 6. 2 *Surface micrograph using FE-SEM for films deposited using 125 W and 20 mTorr at (a) ambient (b) 100 ^oC and (c) 200 ^oC*

Elemental analysis for the percentage compositions in the AZO thin films using energy-dispersive spectroscopy (EDS) (Table 6.3) shows that Al's composition increases with temperature.

Table 6. 3 *Elemental compositions of the AZO thin films from EDS analysis*

	%Zn	**%Al**	**%O**	**Al/ (Al+Zn)**	**Zn/ (Al+Zn)**
Ambient	17.40	1.83	80.77	9.50	90.50
100 ^{o}C	16.05	1.89	82.06	10.5	89.5
200 ^{o}C	15.27	2.39	82.34	13.5	86.5

The high Al content can also account for a potential increased conductivity of the films and a possible shift in the films' band-edge.

6.2.3 Electrical measurements

The thin films' measured sheet resistance and calculated resistivity decrease as the working pressure increases [20] at constant deposition power (Table IV). The decrease could be due to Al's higher inclusion, causing improved electrical property and the changes in the thin film's structure and morphology reported in the previous sections. The increase in resistivity as the pressure increases from 20 mTorr to 25 mTorr could be due to poor crystallization and very little thickness deposited.

Table 6. 4 *Average thickness and electrical parameters films deposited in ambient using four-point probe measurement*

Power (W)	Pressure (mTorr)	Av. thickness (nm)	Sheet Resistance (10^2 Ω/□)	Resistivity (10^{-3} Ω cm)
125	5	367	569.6	2091
	10	246	6.412	15.75
	15	155	7.672	11.93
	20	97.9	4.276	4.186
	25	68.5	6.518	4.463

The characterization of thin films deposited at a constant power of 125 W and a pressure of 20 mTorr (Fig. 6.3) shows a variation in the resistivity values with temperature effects.

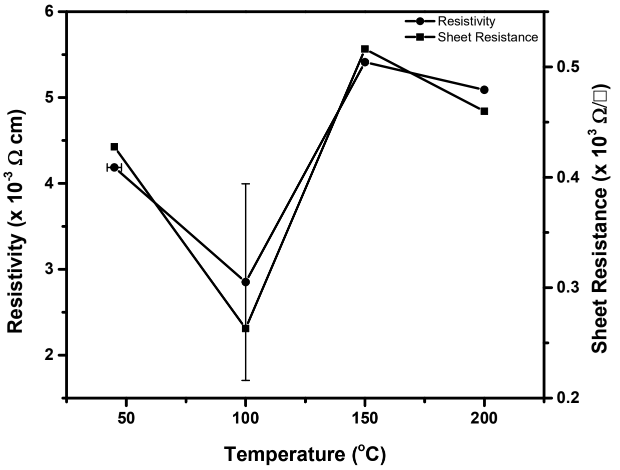

Figure 6.3 *Variation of sheet resistance (ρ_s) and resistivity (ρ) at different temperatures (with constant 125 W and 20 mTorr depositions)*

We measured a decrease in sheet resistance and the calculated resistivity from ambient to 100 °C depositions (Fig. 3). The increase in the resistivity at depositions with 200 °C substrate temperature could be due to a change in the crystal orientation and distortions in the lattice parameters with increased temperature [12]. The Hall characterization of the sample deposited with the 100 °C substrate temperature yielded 3.56 $cm^2/V\ s$ mobility, an n-type carrier concentration of 2×10^{21} $cm^{-3,}$ and a comparable resistivity of 1.01×10^{-3} Ω cm.

6.2.4 Optical characterizations

The optical transmittance for TCO layers, desirable > 85 %, typically decreases with increasing thickness [21,22]. Since the thin films' resistivity decreases with increasing thickness, there is a vital requirement to optimize the optical and electrical properties to minimize parasitic light absorption. The transmittance of the deposited AZO (Fig. 4) film showed relatively high values for all depositions. The deposition at a low pressure of 5 mTorr, which possesses a higher thickness, as can be seen from the interference pattern, has a lower transmittance than the depositions with a lesser thickness (i.e., 20 mTorr).

The transmittance values measured at 550 nm show that all the films deposited with the optimal condition (125 W and 20 mTorr), independent of the temperature, are above 90%.

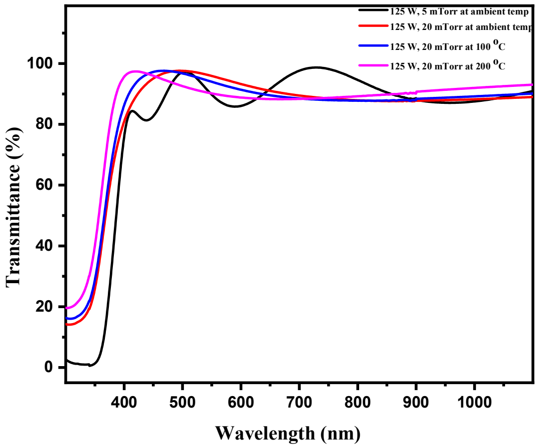

Figure 6.4 *The transmittance against wavelength for various AZO films (125 W, and varying pressures 5 to 20 mTorr) and varying temperatures*

6.2.5 Quality factor (QF) calculation

TCO's resistivity is a relevant parameter, and the sheet resistance depends on the resistivity and thickness, which also affects each film's optical transmittance. Therefore, all these parameters are interrelated. Then, there is a need to decide the best deposition conditions for applying the TCO to solar cells. Using Eqn 1, the better conditions should be those who give the highest value of QF. Using the mentioned equation (1), we calculated the quality factor for the AZO films.

Table 6. 5 *QF for the films deposited at 125 W, 20 mTorr at various temperatures: ambient, 100 °C and 200 °C*

Power (W)	Pressure (mTorr)	T (°C)	%T	ρ_s (10^2 Ω/□)	ρ (10^{-3} Ω cm)	QF (10^{-3} Ω^{-1})
125	20	Ambient	95.92	4.276	4.186	2.243
		100	94.02	2.630	2.851	3.575
		200	90.18	4.598	5.090	1.961

Several indications, taking into account the measurements made, point to the best deposition temperature being 200 °C: table 6.1 shows larger crystallite size, reduced dislocation density, and larger grain sizes from the SEM micrographs. However, the QF mentioned above and (Table 6.5) show that the better condition for deposition is at 100 °C, confirming that this is the best deposition temperature for solar cell applications.

6.3 CdS deposition and characterization

The cadmium sulfide thin films (thickness varying between 50 nm to 100 nm) commonly serve as a buffer layer for the CdTe and CIGSe solar cells, mainly due to their high electron affinity and excellent heterojunction partner for p-type absorber semiconductors [23]. Its more expansive range of bandgap (2.38 eV to 2.58 eV) than the absorber layer allows sufficient passage of incident photons to reach the absorber layer, and the potential high carrier density (~10^{17} cm^{-3}) makes it an excellent companion to the chalcopyrite semiconductor absorbers.

Contrary to the commonly idealized p-n junction at the interface between p-type CIGSe and n-type CdS responsible for the charge carrier creation and separation necessary to produce a solar cell current, some literature suggests that the actual p-n junction in the thin-film solar cell forms within the CIGSe absorber. A proposed inverted thin n-type CIGSe defect layer forms at the surface, existing between the bulk CIGSe layer and the CdS interface [24,25], with a nearly flat conduction band between CIGSe/CdS interface [24], and the idea of an abrupt CdS/CIGSe interface is incorrect [26]. The extension of the SCR into the absorber allows for a better collection of the photogenerated carriers.

The preferred structure of CdS films for the CIGSe solar cells is the hexagonal structure over the cubic counterpart, which possesses a wider optical bandgap. The thin films combine with CIGSe and the ZnO layer in three main ways; (i) electrically, e.g., band alignment, (ii) structurally, e.g., lattice mismatch, and (iii) chemically, e.g., interdiffusion. The lattice mismatch increases with Ga content. Other advantages of the buffer layer include the passivation of the surface states of the CIGSe layer and the elimination of surface oxides. It also protects the absorber layer from potential damage during the deposition of the ZnO window.

The deposition techniques used for CdS thin-films [27–34] affect the thin films' structural, optical, and electrical properties. The chemical bath deposition (CBD) method widely used for low-cost polycrystalline thin-film solar cells offers the advantages of economy, convenience, and extensive area deposition capability. It offers the possibility of preparing films at lower temperatures (near room) as compared to the classical evaporation methods (the lowest deposition temperature in the vapor phase being achieved by metal-organic chemical vapor deposition (MOCVD), with acceptable properties (optical properties, crystallization state). Compared to CVD, the precursors react in a metastable situation but a liquid phase instead of the vapor phase. Additionally, it is adaptable to large-area processing with low fabrication cost.

Common concerns for the deposition technique of CdS include environmental pollutions with waste management and disposal of the toxic components. The process may not be compatible with an inline vacuum deposition of CIGSe modules. The relatively small bandgap of ~ 2.4 eV may also lead to absorption in the blue spectra range, thus decreasing the short circuit current.

Many precursors serve as sources of complexing ions (mainly for the metal source) or decomposable molecules (such as thiourea and seleno-urea as sulfur and selenium sources, respectively), and CBD offers better performance when compared with the other deposition methods. During the deposition, the growth mechanism maybe by the (i) "ion by ion" process or (ii) "cluster by cluster" (or colloidal growth). For most CdS thin-film depositions, the film formation may usually be an ion by ion process for the formation of adherent specular layers, even in the presence of colloids in solution. It aids the formation of compact layers with little trapped electrolytes. Colloidal growth processes may control the kinetics of colloids' formation in solution and partly influence the substrate's activity.

During the deposition, the film's properties and coverage get influenced by some deposition parameters, such as bath temperature, deposition time, and [S]/[Cd] ratio in the solution (thiourea to cadmium chloride concentration) on the crystalline structure, surface morphology, chemical composition and optical properties [28] [35].

The adopted deposition methods and results for CdS in this study, published in [42], and ZnO published in [43] form the buffer layers in device fabrication.

Summary

We successfully optimized conditions for low thickness AZO thin films with no further high-temperature post-deposition treatment, providing explanations to the changes observed with the application of substrate temperatures. Structural characterizations of films obtained with the optimized deposition conditions using XRD confirmed a successful deposition of hexagonal wurtzite structure, with bond length L of 1.995 Å, accounted for by the successful doping of ZnO lattice by Al ions. The morphological studies showed the effects of temperature in the grain sizes and distribution with EDS analysis, showing Al's percentage inclusion as the temperature is varied. With a high transmittance of 94% and resistivity of 2.851 x 10^{-3} Ω cm, the QF for the AZO films was 3.575 10^{-3} Ω^{-1}.

References

[1] S. Paetel, Roadmap CIGS towards 25 % Efficiency, Zent. Für Sonnenenergie- Und Wasserstoff-Forsch. Baden-Württemb. (2016).

[2] G. Rajan, K. Aryal, S. Karki, P. Aryal, R.W. Collins, S. Marsillac, Characterization and Analysis of Ultrathin CIGS Films and Solar Cells Deposited by 3-Stage Process, J. Spectrosc. 2018 (2018) 1–9. https://doi.org/10.1155/2018/8527491.

[3] M. Boubakeur, A. Aissat, M. Ben Arbia, H. Maaref, J.P. Vilcot, Enhancement of the efficiency of ultra-thin CIGS/Si structure for solar cell applications, Superlattices Microstruct. 138 (2020) 106377. https://doi.org/10.1016/j.spmi.2019.106377.

[4] G. Yin, V. Brackmann, V. Hoffmann, M. Schmid, Enhanced performance of ultra-thin Cu(In,Ga)Se2 solar cells deposited at low process temperature, Sol. Energy Mater. Sol. Cells. 132 (2015) 142–147. https://doi.org/10.1016/j.solmat.2014.08.045.

[5] T.R. Ramireddy, V. Venugopal, J.B. Bellam, A. Maldonado, J. Vega-Pérez, S. Velumani, M.D.L.L. Olvera, Effect of the milling time of the precursors on the physical properties of sprayed aluminum-doped zinc oxide (ZnO: Al) thin films, Materials (Basel). 5 (2012) 1404–1412. https://doi.org/10.3390/ma5081404.

[6] S.O. El hamali, W.M. Cranton, N. Kalfagiannis, X. Hou, R. Ranson, D.C. Koutsogeorgis, Enhanced electrical and optical properties of room temperature deposited Aluminium doped Zinc Oxide (AZO) thin films by excimer laser annealing, Opt. Lasers Eng. 80 (2016) 45–51. https://doi.org/10.1016/j.optlaseng.2015.12.010.

[7] H. ming Zhou, D. qing Yi, Z. ming Yu, L. rong Xiao, J. Li, Preparation of aluminum doped zinc oxide films and the study of their microstructure, electrical and optical properties, Thin Solid Films. 515 (2007) 6909–6914. https://doi.org/10.1016/j.tsf.2007.01.041.

[8] B.J. Babu, S. Velumani, J. Arenas-Alatorre, A. Kassiba, J. Chavez, H. Park, S.Q. Hussain, J. Yi, R. Asomoza, Structural Properties of Ultrasonically Sprayed Al-Doped ZnO (AZO) Thin Films: Effect of ZnO Buffer Layer on AZO, J. Electron. Mater. 44 (2014) 699–705. https://doi.org/10.1007/s11664-014-3541-3.

[9] S.J. Henley, M.N.R. Ashfold, D. Cherns, The growth of transparent conducting ZnO films by pulsed laser ablation, Surf. Coatings Technol. 177–178 (2004) 271–276. https://doi.org/10.1016/j.surfcoat.2003.09.005.

[10] T.M.K. Thandavan, S.M.A. Gani, C.S. Wong, R.M. Nor, Enhanced photoluminescence and Raman properties of Al-doped ZnO nanostructures prepared using thermal chemical vapor deposition of methanol assisted with heated brass, PLoS One. 10 (2015) 1–18. https://doi.org/10.1371/journal.pone.0121756.

[11] K. S, J.J. Ríos-Ramírez, S. Chakaravarthy, V. S, Electrical, optical, and topographical properties of RF magnetron sputtered aluminum-doped zinc oxide (AZO) thin films complemented by first-principles calculations, J. Mater. Sci. Mater. Electron. 29 (2018) 15383–15395. https://doi.org/10.1007/s10854-018-8920-8.

[12] P.J.M. Isherwood, M. Gona, J.W. Bowers, N. Neves, P. Newbatt, J.M. Walls, Comparison of DC and RF sputtered aluminium-doped zinc oxide for photovoltaic applications, in: 2015 IEEE 42nd Photovolt. Spec. Conf., IEEE, 2015: pp. 1–5. https://doi.org/10.1109/PVSC.2015.7355900.

[13] D.M. Mattox, Handbook of Physical Vapor Deposition (PVD) Processing, in: Handb. Phys. Vap. Depos. Process., Elsevier, 1998: p. 746. https://doi.org/10.1016/B978-081551422-0.50001-2.

[14] O. Nwakanma, P. Reyes, S. Velumani, Electrical, structural, and topographical properties of direct current (DC) sputtered bilayer molybdenum thin films, J. Mater. Sci. Mater. Electron. 29 (2018) 15671–15681. https://doi.org/10.1007/s10854-018-9165-2.

[15] A. Morán, O. Nwakanma, S. Velumani, H. Castaneda, Comparative study of optimised molybdenum back-contact deposition with different barriers (Ti, ZnO) on stainless steel substrate for flexible solar cell application, J. Mater. Sci. Mater. Electron. 31 (2020) 7524–7538. https://doi.org/10.1007/s10854-020-03058-7.

[16] J.H. Scofield, A. Duda, D. Albin, B.L. Ballard, P.K. Predecki, Sputtered molybdenum bilayer back contact for copper indium diselenide-based polycrystalline thin-film solar cells, Thin Solid Films. 260 (1995) 26–31. https://doi.org/10.1016/0040-6090(94)06462-8.

[17] C. Jeong, H.S. Kim, D.R. Chang, K. Kamisako, Effect on Al 2 O 3 doping concentration of RF magnetronl sputtered ZnO:Al films for solar cell applications, Jpn. J. Appl. Phys. 47 (2008) 5656–5658. https://doi.org/10.1143/JJAP.47.5656.

[18] D. Raoufi, Synthesis and photoluminescence characterization of ZnO nanoparticles, J. Lumin. (2013). https://doi.org/10.1016/j.jlumin.2012.08.045.

[19] Y. Kajikawa, Texture development of non-epitaxial polycrystalline ZnO films, J. Cryst. Growth. (2006). https://doi.org/10.1016/j.jcrysgro.2005.11.089.

[20] M.A. Green, Solar cells—Operating principles, technology and system applications, Sol. Energy. 28 (1982) 447. https://doi.org/10.1016/0038-092X(82)90265-1.

[21] Z. Chen, W. Li, R. Li, Y. Zhang, G. Xu, H. Cheng, Fabrication of highly transparent and conductive indium-tin oxide thin films with a high figure of merit via solution processing, Langmuir. 29 (2013) 13836–13842. https://doi.org/10.1021/la4033282.

[22] U. Betz, M. Kharrazi Olsson, J. Marthy, M.F. Escolá, F. Atamny, Thin films engineering of indium tin oxide: Large area flat panel displays application, Surf. Coatings Technol. 200 (2006) 5751–5759. https://doi.org/10.1016/j.surfcoat.2005.08.144.

[23] I.O. Oladeji, L. Chow, Optimization of Chemical Bath Deposited Cadmium Sulfide Thin Films, J. Electrochem. Soc. 144 (1997) 2342–2346. https://doi.org/10.1149/1.1837815.

[24] D. Schmid, M. Ruckh, F. Grunwald, H.W. Schock, Chalcopyrite/defect chalcopyrite heterojunctions on the basis of CuInSe 2, J. Appl. Phys. 73 (1993) 2902–2909. https://doi.org/10.1063/1.353020.

[25] A. Morales-Acevedo, N. Hernández-Como, G. Casados-Cruz, Modeling solar cells: A method for improving their efficiency, Mater. Sci. Eng. B Solid-State Mater. Adv. Technol. 177 (2012) 1430–1435. https://doi.org/10.1016/j.mseb.2012.01.010.

[26] C. Heske, D. Eich, R. Fink, E. Umbach, T. van Buuren, C. Bostedt, L.J. Terminello, S. Kakar, M.M. Grush, T.A. Callcott, F.J. Himpsel, D.L. Ederer, R.C.C.C. Perera, W. Riedl, F. Karg, Observation of intermixing at the buried CdS/Cu(In, Ga)Se2 thin film solar cell heterojunction, Appl. Phys. Lett. 74 (1999) 1451–1453. https://doi.org/10.1063/1.123578.

[27] A. Punnoose, M. Marafi, G. Prabu, F. El-Akkad, F. El Akkad, CdS Thin Films Prepared by RF Magnetron Sputtering in Ar Atmosphere, Phys. Status Solidi. 177 (2000) 453–458. https://doi.org/10.1002/(SICI)1521-396X(200002)177:2<453::AID-PSSA453>3.0.CO;2-R.

[28] F. Ouachtari, A. Rmili, B. Elidrissi, A. Bouaoud, H. Erguig, P. Elies, Influence of Bath Temperature, Deposition Time and S/Cd Ratio on the Structure, Surface Morphology, Chemical Composition and Optical Properties of CdS Thin Films Elaborated by Chemical

Bath Deposition, J. Mod. Phys. 02 (2011) 1073–1082. https://doi.org/10.4236/jmp.2011.29131.

[29] A. Ashour, N. El-Kadry, S.A. Mahmoud, On the electrical and optical properties of CdS films thermally deposited by a modified source, Thin Solid Films. 269 (1995) 117–120. https://doi.org/10.1016/0040-6090(95)06868-6.

[30] N.I. Fainer, M.L. Kosinova, Y.M. Rumyantsev, E.G. Salman, F.A. Kuznetsov, Growth of PbS and CdS thin films by low-pressure chemical vapour deposition using dithiocarbamates, Thin Solid Films. 280 (1996) 16–19. https://doi.org/10.1016/0040-6090(95)08188-7.

[31] S. Petillon, A. Dinger, M. Grün, M. Hetterich, V. Kazukauskas, C. Klingshirn, J. Liang, B. Weise, V. Wagner, J. Geurts, Molecular beam epitaxy of CdS/ZnSe heterostructures, J. Cryst. Growth. 201–202 (1999) 453–456. https://doi.org/10.1016/S0022-0248(98)01374-8.

[32] A. Ashour, Physical Properties of Spray Pyrolysed CdS Thin Films, Turkish J. Phys. 27 (2003) 551–558.

[33] M.E. Rincón, M.W. Martínez, M. Miranda-Hernández, Structural, optical and photoelectrochemical properties of screen-printed and sintered (CdS)x(ZnS)1-x (0<x<1) films, Sol. Energy Mater. Sol. Cells. 77 (2003) 25–40. https://doi.org/10.1016/S0927-0248(02)00242-8.

[34] I. V. Demidenko, V.M. Ishimov, Electrodeposition of thin cadmium sulfide films from Na2SO3-based electrolyte, Russ. J. Appl. Chem. 90 (2017) 1225–1229. https://doi.org/10.1134/S1070427217080055.

[35] D. Lincot, R.O. Borges, Chemical Bath Deposition of Cadmium Sulfide Thin Films. In Situ Growth and Structural Studies by Combined Quartz Crystal Microbalance and Electrochemical Impedance Techniques, J. Electrochem. Soc. 139 (1992) 1880–1889. https://doi.org/10.1149/1.2069515.

Chapter Seven: Conclusions, Recommendation, and Future Work

7.1 Conclusions and recommendation

This study set out to optimize parameters for the deposition of copper-indium-gallium-selenium (CIGSe) absorber layer using the three-stage co-evaporation method and a novel non-vacuum post-deposition treatment (PDT) with alkali metals in a non-vacuum environment. It also proposes a bilayer model for the Mo back-contact on SLG and a Mo/barrier tandem structure for SS flexible substrates. It further posited an optimized deposition for the AZO window layer for TCO applications, with a proposed QF parameter to evaluate the layer's performance.

The proposed bilayer of Mo film on SLG under optimized conditions of 300 and 100 W for layer-1 and layer- 2, respectively, at the constant pressure of 5 mTorr revealed a densely formed layer-1 and a sparsely packed upper layer with columnar structures from the SEM micrographs. AFM measurements showed granular structures with an RMS roughness (Rq) value of 1.644 nm for the bilayer film surface. The obtained results showed the value of the surface's roughness and the sputtered film's grain parameters in good agreement with the literature for the optimal Mo back-contacts. As measured from the four-point probe technique, the Mo bilayer film's resistivity was 0.60×10^{-6} Ω m.

Further studies on the back-contact optimized a Mo/barrier tandem layer for application on flexible SS substrate. The XRD diffractogram showed better crystallinity at an optimized power of 300 W and 7.5 mTorr for fabrications on Mo/barrier layer for the SS substrate. The SEM micrographs on the surface showed fiber-like structures for the Mo layer deposited on a barrier. The roughness and other AFM parameters' values are in excellent compliance with the literature for the optimal Mo back-contacts. Comparative analysis of the barrier performance showed a better reduction of impurities with the ZnO barrier deposited at a substrate temperature of 100 °C (about 40%), followed by the Ti barrier (about 30%). The lowest performance was by ZnO deposited at the ambient condition (about 8%). The Mo films' structure for the optimized samples showed a (110) orientation plane corresponding to the body-centered cubic (bcc) structure. The intensity of the optimized peaks was higher than those from the barriers and impurities from the substrate. As-deposited and annealed, SIMS profiles for the samples showed a relatively uniform deposition of the Mo density and suppressed intensity of impurity atoms on the back-layer.

The studies on AZO thin films for TCO applications provided optimized conditions for low thickness thin-film deposition with desirable parameters and no need for further temperature treatments. The morphological analysis showed variation supporting aluminum incorporation with temperature, providing explanations for the changes observed with substrate temperatures. The optimized condition yielded an AZO film with ca. 100 nm thickness, high transmittance of 94% and resistivity of $2.851 \times 10^{-3}\ \Omega$ cm, and a QF of $3.575\ 10^{-3} \times \Omega^{-1}$.

The proposed novel PDT technique on the three-stage deposited CIGSe absorber layer explored the non-vacuum spin-coating method and offered an alternative for alkali metals deposition on the absorber layer. The studies showed that alkali metals using the proposed method cause no structural modifications, corroborated by Raman studies, which showed the major chalcopyrite vibration modes and a slight shoulder after PDT, attributed to the presence of OVC layers. The deconvoluted Raman peaks, however, showed the presence of alkali-In(Ga)-Se phase. According to the sem micrographs, the PDT films showed improvements in the grain after PDT, desirable for passivation. EDS analysis confirmed a slight reduction in the Cu content and successful incorporation of alkali metals on the absorber layer. AFM results showed some modifications on the topographical properties, which may be beneficial for interface with the buffer layer. The reduction in the Cu content and potential displacement of Na from the surface leads to a reduction in the carrier concentration, as shown by Hall effect characterization. However, there is an increase in the mobility of the carriers after the PDT. The measured carrier concentration reduced from $1.8\text{x}10^{17}$ cm^{-3} as-deposited CIGSe p-type thin films to 7.6×10^{14} cm^{-3} and 2.0×10^{14} cm^{-3} for Cs- and Rb- PDT p-type thin-films, and the mobility significantly increased from 1.77 cm^2/V s for non-PDT films to 78.6 and 57.1 cm^2/V s after PDT for Cs and Rb, respectively. The obtained results show that the proposed method will be successful for alkali metals PDT in CIGSe solar cells, with great potential for improved efficiencies.

The novel method for PDT developed in this study offers an efficiency improvement technique using alkali halides, an easily scalable and cost-effective non-vacuum method. The study is also recommendable for explaining the mechanisms involved with alkali treatments for enhancing device efficiencies.

7.2 Future Work

Further studies will focus on the complete fabrication and optimizing CIGSe solar cell device efficiencies using PDT processes, surface studies, and interface optimizations. Additionally, apply the novel PDT processes on other thin-film fabrication processes, e.g., the hybrid process. The quest for better-performing devices continues, and potentials for trapping into a broader range of the solar spectrum appear pretty enticing. Future work will consider incorporating the results from this study into standalone devices and tandem configurations to improve solar cell devices' efficiency.

Academic works

Patent (in process)

1. Proceso hibrido de tres etapas para formar peliculas absorbedoras en celda de pelicula delgada CIS y CIGS (Three-stage hybrid process to form CIS and CIGS thin film cell absorbent films). Inventores: Velumani S, Ashok Adhikari, Ganesh Regmi, **Onyekachi Michael Nwakanma**, Jorge Narro-Rios. March 2020

Articles

1. **O. Nwakanma**, S. Velumani, A. Morales-Acevedo, "Review on the effects due to alkali metals on Copper-Indium-Gallium-Selenide solar cells," Materials Today Energy, https://doi.org/10.1016/j.mtener.2020.100617
2. Babudurai, M., **Nwakanma, O.**, Romero-Nuñez, A. et al. Mechanical activation of TiO2/Fe2O3 nanocomposite for arsenic adsorption: effect of ball-to-powder ratio and milling time. J Nanostruct Chem (2021). https://doi.org/10.1007/s40097-021-00388-8
3. A. Morán, **O. Nwakanma**, S. Velumani, H. Castaneda, "Comparative study of optimised molybdenum back-contact deposition with different barriers (Ti, ZnO) on stainless steel substrate for flexible solar cell application," Journal of Materials Science: Materials in Electronics https://doi.org/10.1007/s10854-020-03058-7
4. **O. Nwakanma**, P. Reyes, S. Velumani, "Electrical, structural, and topographical properties of direct current (DC) sputtered bilayer molybdenum thin films," Journal of Materials Science: Materials in Electronics https://doi.org/10.1007/s10854-018-9165-2

Conferences Papers

1. **Onyekachi M Nwakanma**, Arturo Morales Acevedo, Velumani Subramaniam, "Study of the effects of non-vacuum deposited alkali-metals on copper-indium-gallium-selenide absorber layers for solar cells," 2020 IEEE virtual Photovoltaics Specialists Conference June 15th to August 21st, 2020.
2. **Onyekachi Michael Nwakanma**, Alan Enrique Moran Hernandez, Jorge Narro-Rios, Velumani S, "Comparative study of molybdenum back-contact deposition with different barriers (Ti, ZnO) on stainless steel substrate for flexible solar cell application," XXVIII International Materials Research Congress, Cancun August 2019
3. Alan Enrique Moran Hernandez, **Onyekachi Michael Nwakanma**, Jorge Narro-Rios, Velumani S, "Efficient barrier conditions and Molybdenum deposition conditions on stainless steel for solar cell applications," XXVIII International Materials Research Congress, Cancun August 2019
4. Ashok Adhikari, Jorge Narro-Rios, **Onyekachi Michael Nwakanma**, Ganesh Regmi, Velumani S, Fabián Andrés Pulgarín Agudelo, "Characterizations of a Selenized Cu(In1-xGax)Se2 Thin Film Absorber Layer Fabricated By a Three-Stage Hybrid Method", 15th International Conference on Electrical Engineering, Computing Science and Automatic Control (CCE), August 2018 10.1109/ICEEE.2018.8533902
5. Ganesh Regmi, Jorge Narro-Rios, Ashok Adhikari, **Onyekachi Michael Nwakanma**, Velumani S, Fabián Andrés Pulgarín Agudelo "Structural, Morphological, Topographical, and Electrical Properties of Selenized Stacked CIGSe Layers by Evaporation Technique," 15th International Conference on Electrical Engineering, Computing Science and Automatic Control (CCE), August 2018 10.1109/ICEEE.2018.8533910
6. Onyekachi Michael Nwakanma, Jorge Narro-Rios, Velumani S, "Effect of complexing agents on optimized deposition of CDS buffer layer for high-efficient CIGSe solar cells," XXVII International Materials Research Congress, Cancun, August 2018
7. **Onyekachi Michael Nwakanma**, Jorge Narro-Rios, Velumani S, "Morphology and optical properties of optimized radio-frequency sputtered aluminum-doped zinc oxide thin films for solar cell applications," XXVII International Materials Research Congress, Cancun, August 2018
8. **Onyekachi Michael Nwakanma**, Jaime Vega, Pablo Reyes, Velumani S, Rene Asomoza-Palacio, *Synthesis and characterization of CIGSe powders from compound precursors*, XXVI International Materials Research Congress, Cancun, August 2017
9. **Onyekachi Michael Nwakanma**, Jaime Vega, Pablo Reyes, Velumani S, *Electrical properties of dc sputtered molybdenum films: effect of sputtering power and pressure*, XXVI International Materials Research Congress, Cancun, August 2017

Conferences Attended

1. International E-Symposium on Advanced Techniques for Energy Harvesting and Storage Applications, July 08 – 10, 2020
2. 2020 IEEE virtual Photovoltaics Specialists Conference June 15th to August 21st, 2020.
3. XXVIII International Materials Research Congress, Cancun August 2019
4. 15th International Conference on Electrical Engineering, Computing Science and Automatic Control (CCE), August 2018
5. XXVII International Materials Research Congress, Cancun, August 2018
6. XXVI International Materials Research Congress, Cancun, August 2017